

Modeling Sea Level Rise Impact on Estuarine Morphodynamics

Elmilady, H.M.S.M.A.

DOI

[10.4233/uuid:f4475a82-30bf-49cc-af13-ccd6d993adc3](https://doi.org/10.4233/uuid:f4475a82-30bf-49cc-af13-ccd6d993adc3)

Publication date

2025

Document Version

Final published version

Citation (APA)

Elmilady, H. M. S. M. A. (2025). *Modeling Sea Level Rise Impact on Estuarine Morphodynamics*. [Dissertation (TU Delft), Delft University of Technology, IHE Delft Institute for Water Education]. IHE Delft Institute for Water Education. <https://doi.org/10.4233/uuid:f4475a82-30bf-49cc-af13-ccd6d993adc3>

Important note

To cite this publication, please use the final published version (if applicable). Please check the document version above.

Copyright

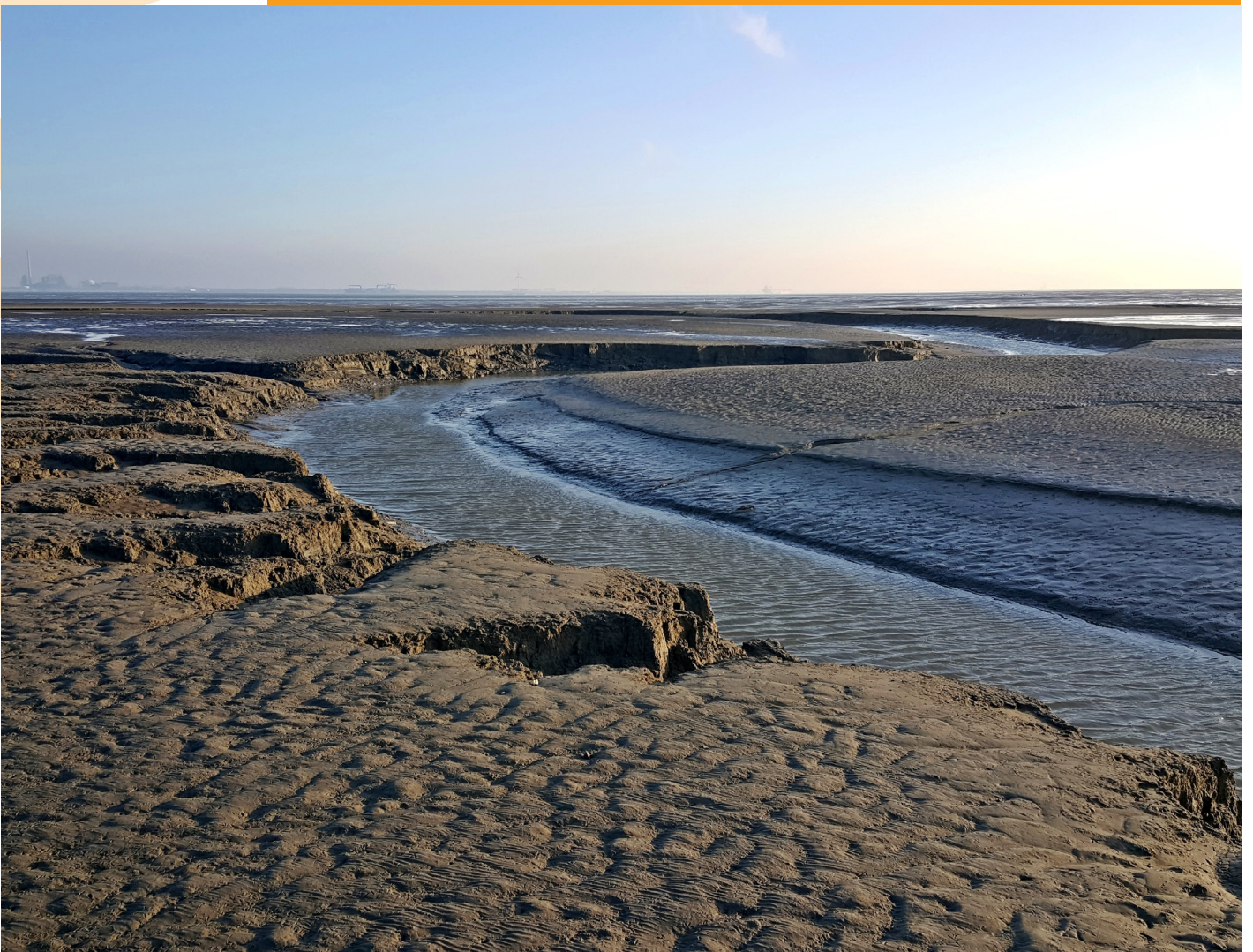
Other than for strictly personal use, it is not permitted to download, forward or distribute the text or part of it, without the consent of the author(s) and/or copyright holder(s), unless the work is under an open content license such as Creative Commons.

Takedown policy

Please contact us and provide details if you believe this document breaches copyrights. We will remove access to the work immediately and investigate your claim.

Hesham Mohamed Samy Elmilady

Modeling Sea Level Rise Impact on Estuarine Morphodynamics



MODELING SEA LEVEL RISE IMPACT ON ESTUARINE
MORPHODYNAMICS

Hesham Mohamed Samy Elmilady

MODELING SEA LEVEL RISE IMPACT ON ESTUARINE
MORPHODYNAMICS

DISSERTATION

for the purpose of obtaining the degree of doctor

at Delft University of Technology

by the authority of the Rector Magnificus Prof.dr.ir. T.H.J.J. van der Hagen,

chair of the Board for Doctorates

and

in fulfilment of the requirement of the Rector of IHE Delft

Institute for Water Education, Prof.dr. E.J. Moors,

to be defended in public on

Wednesday, 23 April 2025 at 10.00 hours

Modeling Sea Level Rise

by

Hesham Mohamed Samy ELMILADY

Master of Science in Water Science and Engineering

UNESCO-IHE Institute for Water Education, Delft, the Netherlands

born in Alexandria, Egypt

This dissertation has been approved by the (co)promotor.

Composition of the doctoral committee:

Rector Magnificus TU Delft	chairperson
Rector IHE Delft	vice-chairperson
Prof.dr.ir. J.A. Roelvink	TU Delft / IHE Delft, promotor
Dr.ir. M. van der Wegen	IHE Delft, copromotor
Independent members:	
Prof.dr.ir. Z.B. Wang	TU Delft
Prof.dr. M.G. Kleinhans	Utrecht University
Prof.dr. J. van de Koppel	University of Groningen
Prof.dr. G. Coco	University of Auckland, New Zealand
Prof.dr. I.I. Popescu	TU Delft / IHE Delft, reserve member

This research was conducted under the auspices of the Graduate School for Socio-Economic and Natural Sciences of the Environment (SENSE)

© 2025, Hesham Mohamed Samy Elmilady

Although all care is taken to ensure integrity and the quality of this publication and the information herein, no responsibility is assumed by the publishers, the author nor IHE Delft for any damage to the property or persons as a result of operation or use of this publication and/or the information contained herein.

A pdf version of this work will be made available as Open Access via <https://ihedelftrepository.contentdm.oclc.org/> This version is licensed under the Creative Commons Attribution-Non Commercial 4.0 International License, <http://creativecommons.org/licenses/by-nc/4.0/>

Published by IHE Delft Institute for Water Education
www.un-ihe.org
ISBN 978-90-73445-73-4

Dedicated to my beloved and supportive family.

ACKNOWLEDGEMENTS

I am grateful to the many people and institutions that contributed to the completion of this PhD thesis. This journey has been both challenging and rewarding, and it would not have been possible without your support. First, I would like to sincerely thank Dr.ir. Mick van der Wegen for his guidance, expertise, and constant support which were essential throughout this research. Your quick replies, insightful feedback, patience, and encouragement have been very helpful in shaping my work and guiding me through the complexities. You always made time for my questions, I sincerely appreciate the time and effort you invested in mentoring me. Also, for arranging the funding for this research and for keeping me involved with the research community through conferences, meetings, and various opportunities.

I am also grateful to Prof. dr.ir. Dano Roelvink for his expert guidance and feedback which enriched my research. Despite your busy schedule, you were always available whenever help was needed. I learned a lot from our discussions. After our meetings, if any topic remained open, you would always remember and get back to me later.

I would like to thank Dr. Ad van der Spek for taking part in my supervisory team and for his constructive critiques and valuable advice which contributed to this study.

This research is supported by the U.S. Geological Survey Priority Ecosystem Science and Coastal and Marine Geology Programs, and the California Delta Science Program as a part of the CASCaDE climate change project (contribution number 80). I would like to thank all the personnel involved. Special thanks to Dr. Bruce Jaffe for his time, and support with data, expertise, and guidance. Also, for being part of my supervisory team. Furthermore, on his hospitality when visiting the USGS office in Santa Cruz.

This study is partially funded by Deltares Research Funds as a part of their collaboration with the Rijkswaterstaat and the Vlaams-Nederlandse Scheldecommissie (VNSC). I would like to thank a lot of personnel from Deltares including, but not limited to, Marcel Taal and Björn Robke for their expert support.

Some of the modeling work in this research was carried out on the Dutch national e-infrastructure with the support of SURF Cooperative. I would like to thank Mr. Ander Astudillo for his support using the SURFsara HPC.

Special thanks to all my colleagues with whom I shared joyous moments and difficult times. I extend my appreciation to IHE Delft staff members of the CURR department and other personnel such as Jolanda Boots, Floor Felix, and Anique Karsten for their support.

Finally, on a personal note, I would like to thank my family for their unconditional support and encouragement throughout my PhD journey. Special thanks to my parents, my beloved wife and daughter, your constant motivation has been a source of strength.

SUMMARY

Estuaries are dynamic environments where riverine fresh water meets tidally forced marine saline water. They encompass unique ecosystems and provide natural buffers that protect economic livelihoods. Many estuaries face continuous pressure from urbanization, altered river flows and sediment supply, subsidence, and sea level rise (SLR).

Estuarine beds are dynamic, influenced by marine (waves, tides, salinity, sea level) and fluvial (discharges, sediment load) forces. Morphological development is key to sustainable estuarine ecosystems and human activities. SLR will trigger a long-term (century-and-beyond scale) morphodynamic adaptation that will significantly impact the future state of estuarine systems. There is an urgent need for an enhanced understanding of relevant morphodynamic processes and the development of skillful forecast tools to assess SLR impact.

This research aims to assess SLR impact on the long-term morphological development of the estuarine environment, focusing on intertidal area by applying a process-based, numerical model (Delft3D) to predict morphodynamic behaviour. Fundamental studies on idealized estuaries are performed to determine governing processes and model parameter settings. In particular, these include wind wave dynamics, sediment properties, and grid resolution. Further, the modeling approach is applied in two case studies, namely San Pablo Bay (USA) and the Western Scheldt Estuary (Netherlands). Hindcasts are validated against unique datasets covering a period from decades to 1.5 centuries, while forecasts cover a century timescale under various SLR scenarios.

Model results show that morphodynamic adaptation lags behind SLR. Despite accretion under SLR, intertidal areas decay. The adaptation time lag and intertidal area loss mainly depend on SLR rate and magnitude along with sediment supply and sediment properties. Extreme SLR scenarios (1.67 m and 3.02 m over a century) can result in a 91% and 54% loss of intertidal area for San Pablo Bay and the Western Scheldt, respectively.

The results of this study advance understanding of the SLR impact on the morphological evolution of estuaries. It also shows that, despite their complexity, process-based models are reliable and valuable tools for performing morphological forecasts. Delft3D-type models can be used in future studies to investigate potential adaptation measures or to determine and quantify parameters for more aggregated models.

SAMENVATTING

Estuaria zijn dynamische omgevingen waar rivierwater en getij gedreven zout water uit de zee elkaar ontmoeten. Ze omvatten unieke ecosystemen en bieden natuurlijke buffers die land en infrastructuur beschermen. Veel estuaria staan onder druk van verstedelijking, veranderde rivierstromen en sedimentaanvoer, bodemdaling en zeespiegelstijging (ZSS).

Estuariene bodems zijn dynamisch en worden beïnvloed door mariene (golven, getijden, zoutgehalte, zeeniveau) en fluviale (debiet, sediment toevoer) processen. Morfologische ontwikkeling vormt de basis voor duurzame estuariene ecosystemen en menselijke activiteiten. ZSS leidt tot een morfodynamische aanpassing van eeuwen (en langer) die een aanzienlijke impact heeft op de toekomstige staat van estuariene systemen. Er is een dringende behoefte aan een beter begrip van relevante morfodynamische processen en de ontwikkeling van betrouwbare instrumenten om ZSS impact te voorspellen.

Dit onderzoek richt zich op het beoordelen van de impact van ZSS op de morfologische ontwikkeling van estuaria, met een focus op het intergetijdengebied. Om het morfodynamisch gedrag te voorspellen wordt gebruik gemaakt van een op proces beschrijving gebaseerd, numeriek model (Delft3D). Fundamentele studies van geïdealiseerde estuaria worden uitgevoerd om dominante processen en essentiële model parameterinstellingen te bepalen. Deze omvatten met name rasterresolutie, windgolfdynamiek en sedimenteigenschappen. Verder wordt de modelleringsaanpak toegepast in twee casestudies, namelijk San Pablo Bay (VS) en het Westerschelde-estuarium (Nederland). Model resultaten worden gevalideerd tegen unieke datasets die een periode bestrijken van decennia tot 1.5 eeuw, terwijl voorspellingen een tijdschaal van een eeuw bestrijken onder verschillende ZSS-scenario's.

Modelresultaten tonen dat morfodynamische aanpassing achterloopt op ZSS. Ondanks verhoging onder ZSS neemt de hoeveelheid intergetijdengebied af. Het achterblijven en verlies van intergetijdengebied zijn voornamelijk afhankelijk van de snelheid en omvang van ZSS, samen met de sedimentaanvoer en sedimenteigenschappen. Extreme ZSS-scenario's (1,67 m en 3,02 m over een eeuw) kunnen resulteren in een verlies van 91% en 55% van het intergetijdengebied voor respectievelijk San Pablo Bay en de Westerschelde.

De resultaten van deze studie bevorderen het begrip van de ZSS-impact op de morfologische evolutie van estuaria. Het laat ook zien dat, ondanks de complexiteit, op processen gebaseerde modellen betrouwbare en waardevolle hulpmiddelen zijn voor het uitvoeren van morfologische voorspellingen. Delft3D type modellen kunnen worden gebruikt in toekomstige studies om mogelijke adaptatie maatregelen te onderzoeken of om parameters voor meer geschematiseerde modellen te bepalen en kwantificeren.

CONTENTS

Acknowledgements	vii
Summary	ix
Samenvatting.....	xi
Contents.....	xiii
1 Introduction.....	1
1.1 Estuaries	2
1.1.1 Intertidal area.....	3
1.2 Climate Change (Global Warming).....	4
1.3 Sea level Changes	6
1.3.1 Historical sea level changes	7
1.3.2 Current sea level rise.....	9
1.3.3 Sea level projections	11
1.4 Knowledge Gaps and Objectives.....	13
1.4.1 General Problem Identification	13
1.4.2 Specific Knowledge Gaps	16
1.4.3 Goals and Objectives	18
1.5 Development Relevance.....	19
1.6 Long-term Morphodynamic Modeling approaches	20
1.6.1 Behavior-based models.....	20
1.6.2 Process-based models	22
1.7 Methodology and Thesis Structure.....	23
2 Morphodynamic Evolution of a Fringing Sandy Shoal From Tidal Levees to Sea Level	25
2.1 Introduction	26
2.1.1 Modeling intertidal flats.....	27
2.1.2 Tidal levees	28
2.1.3 Sea level rise.....	28
2.1.4 Research Objective	29
2.2 Sandy Shoals Observations	29
2.2.1 Eastern Scheldt	30
2.2.2 Remote sensing at Western Scheldt and Wadden Sea.....	31
2.3 Numerical Model Setup	33
2.3.1 Model setup and forcing	33
2.3.2 Wave model.....	34

2.3.3	Sediment transport and morphodynamics.....	35
2.4	Model Results.....	36
2.4.1	Development towards equilibrium.....	36
2.4.2	Intratidal dynamics.....	37
2.4.3	Sensitivity analysis.....	40
2.5	Forcing Variations.....	41
2.5.1	Wave conditions.....	42
2.5.2	Sea level rise.....	43
2.6	Discussion.....	46
2.6.1	Observed and Modeled trends.....	46
2.6.2	Sea level rise.....	48
2.6.3	Future Research.....	50
2.7	Conclusions.....	50
	Appendix 1.....	52
3	Modeling the Morphodynamic Response of Estuarine Intertidal Shoals to Sea-Level Rise.....	59
3.1	Introduction.....	60
3.2	Model description.....	62
3.3	Model results.....	65
3.3.1	Morphology.....	65
3.3.2	Shear stresses.....	66
3.3.3	Sediment transport.....	67
3.3.4	Wave impact.....	68
3.4	Sea level Rise.....	69
3.4.1	Morphology.....	70
3.4.2	Hydrodynamics and Sediment transport.....	72
3.4.3	Sensitivity analysis.....	74
3.5	Discussion.....	83
3.5.1	Implications for real case studies.....	83
3.5.2	Future work.....	86
3.6	Conclusions.....	87
	Appendix 2.....	88
4	Intertidal Area Disappears Under Sea Level Rise 250 Years of Morphodynamic Modeling.....	101
4.1	Introduction.....	102
4.1.1	Previous Studies.....	103
4.1.2	Research Objective.....	104
4.2	Case Study.....	104

4.2.1	Setting	104
4.2.2	Morphology.....	105
4.2.3	Tides.....	106
4.2.4	Salinity	106
4.2.5	River Inflow	107
4.2.6	Waves and Wind.....	107
4.2.7	Sediment Characteristics.....	108
4.2.8	Sediment load.....	108
4.2.9	Regional Sea Level Rise	110
4.3	Modeling	110
4.4	Results	112
4.4.1	Hindcast	112
4.4.2	Forecast	116
4.5	Discussion	120
4.5.1	General Model Performance	120
4.5.2	Hindcast Sensitivity	121
4.5.3	Forecast Analysis.....	123
4.5.4	Modeling Approach.....	126
4.5.5	Application to Other Estuaries	127
4.5.6	Future Research and Recommendations.....	127
4.6	Conclusions	128
	Appendix 3	129
5	The impact of mud dynamics on long-term morphodynamic evolution of the Western Scheldt estuary under sea level rise.....	135
5.1	Introduction	136
5.2	Western Scheldt Estuary.....	139
5.2.1	Geometric Configuration	139
5.2.2	Morphological characteristics	140
5.2.3	Hydrodynamics.....	140
5.2.4	Sediment Characteristics.....	141
5.3	Modeling setup	143
5.4	Hindcast.....	147
5.5	Forecast	150
5.5.1	Forecast sensitivity	158
5.6	Discussion	161
5.6.1	Mud impact	161
5.6.2	Sediment balance.....	163
5.6.3	Relevance to other estuaries.....	165

5.6.4	Future research	165
5.7	Conclusions	166
	Appendix 4	168
6	Conclusions & Recommendations.....	171
6.1	Conclusions	172
6.1.1	Introduction	172
6.1.2	Answers to research questions	172
6.2	Recommendations.....	176
	References	179
	List of acronyms.....	205
	List of Tables.....	207
	List of Figures	209
	About the author.....	219

1

INTRODUCTION

This chapter provides a brief introduction to the estuarine environment and discusses the ongoing climate change (global warming) and its relevance to estuaries. Furthermore, it summarizes information regarding sea level rise (SLR) including the historical SLR, current SLR observations, and future predictions. This chapter also presents the knowledge gaps and research objectives. Furthermore, the general methodology and modeling approach used for achieving the goals are presented.

1.1 ESTUARIES

Estuaries (e.g., Figure 1.1) are semi-enclosed water bodies along the coast that serve as a transition zone from land to sea where riverine freshwater meets and mixes with oceanic saline water. They have a highly dynamic nature as they are constantly subjected to both marine and riverine forcing. Marine forcing is mainly exerted by waves, tides, currents, wind, and salt intrusion while riverine forcing includes the, highly variable, seasonal fresh water flows and sediment load. This interaction within estuaries creates life-supporting habitat for thousands of species and makes them one of the most productive and precious ecosystems in the world (e.g., Harvey et al., 1998), even more so than the oceans and rivers influencing them, and comparable to coral reefs and tropical rainforests.

The estuarine environment offers a variety of services along with the economic livelihood of many communities. It is a vital habitat for thousands of birds and fish species, invertebrates, and wildlife. Habitats within estuaries comprise river deltas, open waters, salt and freshwater marshes, mangroves, sandy and rocky beaches, shellfish flats, and swamps. Also, estuaries provide better water quality for people and organisms, for example, through the filtration process that occurs within the salt marshes. Moreover, they play an important role in maintaining the ocean's health as they continuously trap, filter, and recycle sediment and pollutants in the water before it is discharged into oceans (e.g., Ittekkot, 1988).



Figure 1.1. Aerial view of Murray River Estuary, Australia. Image source: www.freeaussiestock.com.

Estuaries additionally provide a wide range of ecosystem services that extend from simple recreational activities and tourism to huge industrial and economic activities. Their

protected waters support the development of important public infrastructure such as ports and harbors that are vital for transportation and shipping. They act like natural buffer zones between land and sea thus providing natural protection of human settlements from the continuous threat of storm surges and flooding. In addition, estuaries provide economic livelihood for a lot of communities (Mitsch & Gosselink, 2000) as the estuarine resources generate a huge number of job opportunities and a large income. For example, in the Massachusetts - Cape Cod Bay estuarine system, shipping and marinas earn about 1.9\$ billion/year while tourism and recreational activities earn about 1.5\$ billion/year and fishing generates about 240\$ million/year (USCG Aux, 2008).

The high economic and environmental value of the estuarine environment made it one of the most heavily populated environments in the world and throughout history. The continuously increasing human interest in utilizing the estuarine valuable resources impacted estuaries throughout the world which extended in some estuaries to almost complete alteration of the estuarine dynamics. One of the major threats to estuaries is the large-scale conversion by draining, damming, constructions, or dredging which leads to the destruction and loss of the natural habitat along with the alteration of the flows. Another important potential threat is climate change. Climatic-induced changes can already be observed in estuaries throughout the world through changes in sea level, riverine flows, sediment supply, water temperature, and extreme events. These changes are currently affecting the estuarine environment and its effect is expected to increase as climate change continues which could result in an undesirable impact. This raises the need for a better understanding of those changes to ensure the sustainability of the valuable estuarine environment.

1.1.1 Intertidal area

The intertidal zone is the region between high and low tide lines which is characterized by fluctuating conditions of submersion and exposure. It is a key component of many estuaries and tidal basins that provides flood protection, erosion control, and nutrient cycling (Narayan et al., 2017; Reed et al., 2018; Rios-Yunes et al., 2023), has significant recreational and cultural value (Wilson et al., 2005), and includes valuable habitats for fish, benthic species, and birds (e.g., Galbraith et al., 2002; Lipcius et al., 2013).

Worldwide, intertidal areas are experiencing a notable decline due to anthropogenic impact and climate change (Airoldi & Beck, 2007; N. J. Murray et al., 2014, 2019; Song et al., 2020). Pressure sources include urbanization (Lai et al., 2015; MacKinnon et al., 2012), changes in riverine flows and sediment supply (Blum & Roberts, 2009; Jaffe et al., 2007), and sea level rise (SLR; Lovelock et al., 2017; Passeri et al., 2015).

1.2 CLIMATE CHANGE (GLOBAL WARMING)

Climate change is occurring and the evidence is clear (e.g., IPCC, 2013). Earth is warming, a 143-year global surface temperature record (Figure 1.2), since recordkeeping began, showed that 2023 was the warmest on the record which is about 1.36 °C (or 2.45 ° F; Figure 1.3) warmer than in the late 19th century (NASA, 2023a). The 10 most recent years are the warmest on record. Also, each year in the past 47 years has been warmer than the global average surface temperature of the 20th century.

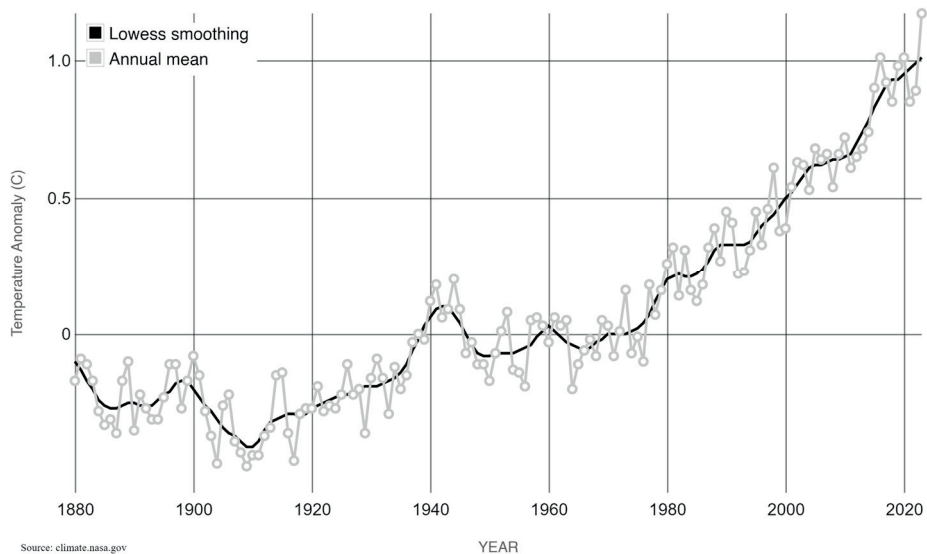


Figure 1.2. The change in the average global surface temperature (°C) from 1880 to 2023 compared to the long-term average from 1951 to 1980. Figure source: NASA (2023a).

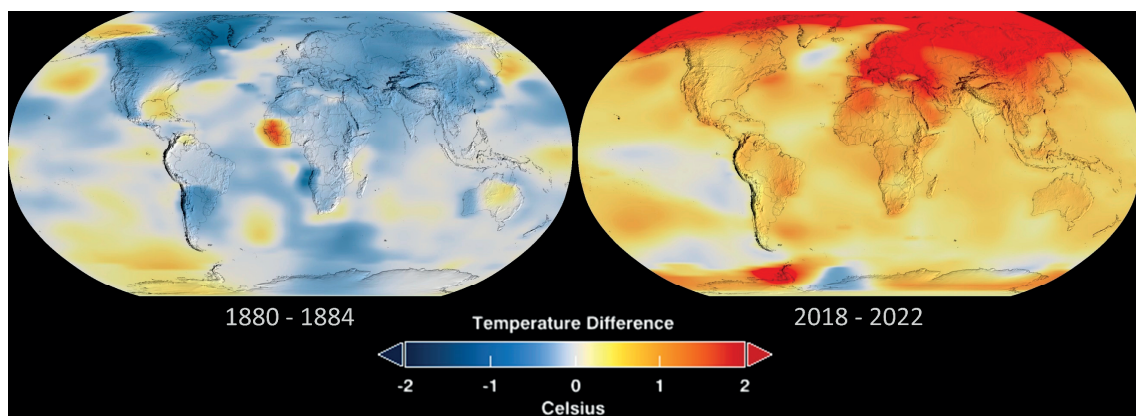


Figure 1.3. The change in global surface temperature (Celsius) for the periods 1880-1884 and 2018-2022 compared to the long-term average from 1951 to 1980. Dark blue color represents areas cooler than average and dark red color represents areas warmer than average. Figure source: NASA (2023b).

Climate change is not a new phenomenon, the Earth’s climate has been continuously changing throughout history. There have been several cycles of glacial advance and retreat within the past 800,000 years, which ended with the last ice age that occurred about 11,700 years ago and marked the start of the human civilization era and our modern climate (NASA, 2023c). Those major changes in climatic conditions are attributed to the change of solar energy received from the sun caused by very minor alterations in the Earth’s orbit that occurred throughout history. Also, Earth’s natural processes such as volcanic activities, plate tectonics, and biotic processes played an important role in historical climatic changes. Nowadays, records and observations show that climatic changes are still occurring. However, the current warming trend is of particular significance as this trend is mainly human-induced and occurs at an unprecedented rate that hadn’t occurred in the past millennium (e.g. IPCC, 2023; NASA, 2023c).

In this study, the terms “Climate change” and “Global warming” will be used interchangeably to refer to the recent and ongoing rise of the global average temperature due to, human-induced, increased greenhouse gas emissions in the atmosphere. Carbon dioxide (CO₂) is an important heat-trapping (greenhouse) gas. Since the onset of the industrialization era in the 18th century, CO₂ levels in the atmosphere have increased significantly (Figure 1.4) with current levels 50% higher compared to 1750. This increase was caused by deforestation and CO₂ release associated with the burning of carbon-based fossil fuels such as coal, oil, and gas. The correlation between the increasing carbon emissions and the percentage of atmospheric CO₂ is strong and confidently believed to be the main cause of the globally rising temperatures. Also, CO₂ emitted by burning fossil fuels has a unique chemical fingerprint that enables scientists to accurately identify. The rapidly rising atmospheric carbon dioxide percentage is increasing solar energy trapping within the Earth’s atmosphere and hence triggering global warming.

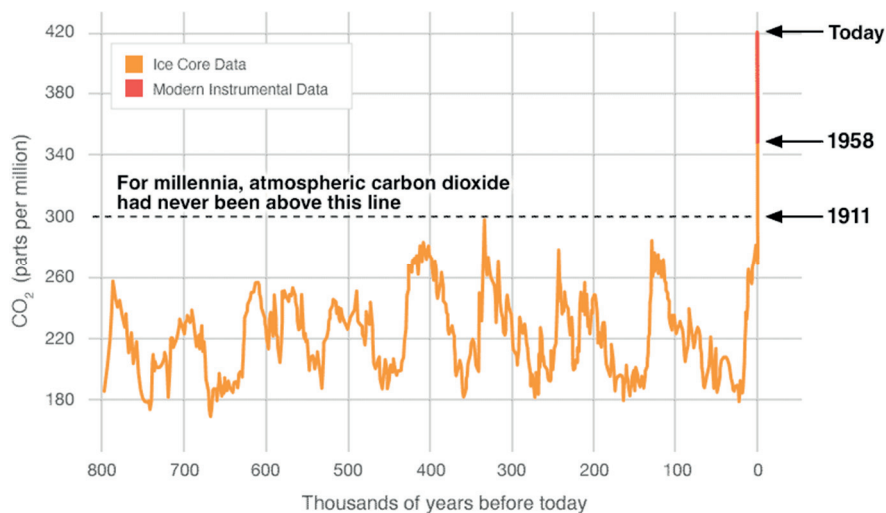


Figure 1.4. Historical atmospheric carbon dioxide concentrations (ppm). Figure source: NASA (2023d).

Global warming effects are worldwide and extend to different aspects of our life. When addressing global warming within the context of the estuarine environment and its morphological development, the effects that are of main concern are as follows:

- i. Accelerating the melting of ice sheets and glaciers and hence causing the sea level rise (e.g., Melillo et al., 2014).
- ii. Increasing the water temperature which contributes to sea level rise through thermal expansion.
- iii. Changing precipitation and weather (wind) patterns in different locations. Some areas are getting drier, resulting in droughts and other areas are experiencing more intense precipitation (IPCC, 2023; e.g., Melillo et al., 2014). These changes can have a significant effect on river discharges and their associated sediment load.
- iv. Changing the intensity, frequency, and duration of extreme weather events.

Global warming is expected to continue in the future. This research focuses on the global warming-induced sea level rise (SLR) impact on the long-term morphological development of estuaries.

1.3 SEA LEVEL CHANGES

Sea level has fluctuated throughout history following climatic changes and Earth's natural processes. Sea level changes can be classified according to cause and extent of effect into two main categories: global eustatic changes and local isostatic changes with the contribution of the former being much larger than that of the latter.

- i. Global effect (eustatic change)

The eustatic change of sea level occurs with the change of the amount and volume of the available water along with the shape and volume of the ocean basins and hence the amount of water that they can hold. Water volumes in oceans depend on water stored in reservoirs like aquifers, glaciers, lakes, rivers, ice sheets, polar ice caps, and sea ice. Also, water temperatures have a direct effect on water volumes as it changes its density. Increasing water temperature causes water to expand and hence greater water volumes, and vice versa.

Eustatic sea level changes occur during and after an ice age. During an ice age, water is frozen and it is stored in inland glaciers causing a drop in water levels. After an ice age ends, glaciers start melting and supplying oceans with water causing an increase in water volumes and hence a rise in sea level. Also, rising temperatures cause the melted water to expand hence increasing the water volume and enhancing the sea level rise. In addition, during this period ocean basin volumes can change due to the occurrence of tectonic movement which can either cause a drop or rise in sea level as it becomes larger or smaller, respectively.

ii. Local effect (isostatic change, tectonics & compaction)

An isostatic change of sea level occurs with the change of the land height. A change in land height can either cause a drop or rise in sea level as land height increases or decreases, respectively. For example, during ice ages water stored on inland glaciers increased the land weight causing land to sink slightly and the sea level to rise slightly. After the end of an ice age, the glaciers start melting and the load exerted on the land starts decreasing causing land elevations to increase slightly and hence the lowering of sea level slightly. Also, tectonic activity can result in the uplift or depression of the Earth's surface along the plate boundaries. In addition, soil compaction can cause land subsidence. Many deltas around the world have a considerable amount of peat, which is highly compressible (Van Asselen et al., 2011). This compaction can lead to considerable delta subsidence hence local SLR.

1.3.1 Historical sea level changes

Over geologic time scales, sea level fluctuations accounted for hundreds of meters (Figure 1.5a). Throughout history, it has been highly variable and periodic with high sea levels occurring during the warm eras and low sea levels occurring during the cold eras. Figure 1.5b shows a sharp drop in sea level from the last interglacial warm period (the warm interval between ice ages; 5e) which occurred about 125 k years ago. The sea level kept dropping until period 2 when it reached its lowest level. During the period from 5e till 2 which is about 110 k years, water levels dropped almost 120 meters at a rate of approximately 0.11 m/ century. Following that the sea level started to increase abruptly with a rate of approximately 0.66 m/century. Today's sea level is near the highest in history and it is about 120 meters above the lowest sea level reached during the Last Glacial Maximum roughly 20 k years ago (Figure 1.5b). During the last interglacial period, it is estimated that the sea level was about 3 to 6 m higher than its current level.

After the sea level reached its lowest levels near the Last Glacial Maximum, it started rising gradually again until about 15,000 years ago when a rapid deglaciation event (Meltwater Pulse 1A) occurred and resulted in a rapid rise in sea level (Figure 1.6a). The Meltwater Pulse 1A has been attributed in various studies to the rapid decay of the Eurasian and Laurentide Ice sheets which are believed to have covered North America and retreated now to the alpine sheets only. Some studies indicate other pulses following the Meltwater Pulse 1A. However, the existence of those pulses is still debatable.

A closer look at the sea level in the Holocene period (Figure 1.6b) shows that sea levels reached their modern levels from about 6,000 years ago. From that point onwards sea level rise has been slow and can be referred to as reached relative stability. The change of sea level during the past 6,000 was approximately 2.75 m accounting for an approximately 5 cm/century SLR.

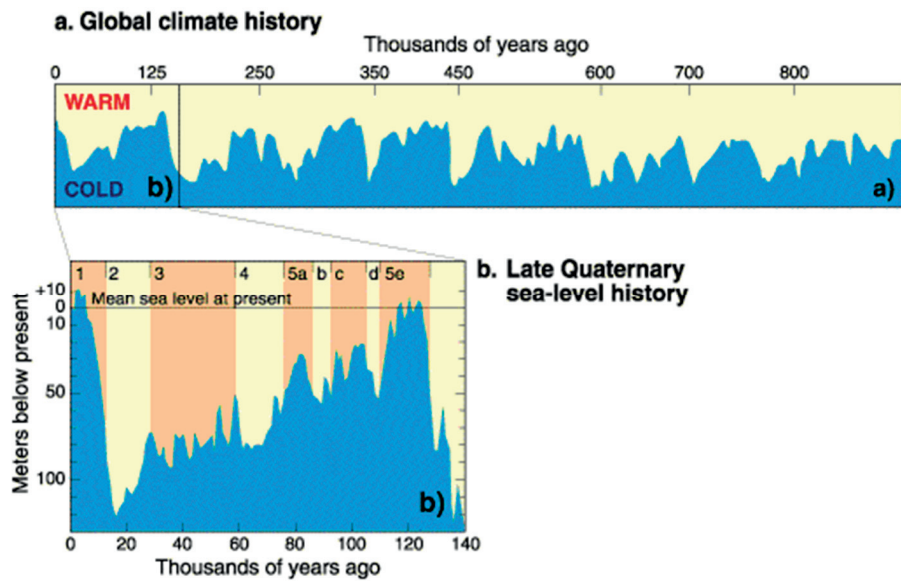


Figure 1.5. Eustatic sea level history along warm and cool periods during the (a) past 900 thousand years and (b) late Quaternary (past 140 years). Figure source: NOAA PaleoClimatology, <https://www.ncei.noaa.gov/products/paleoclimatology#sea>.

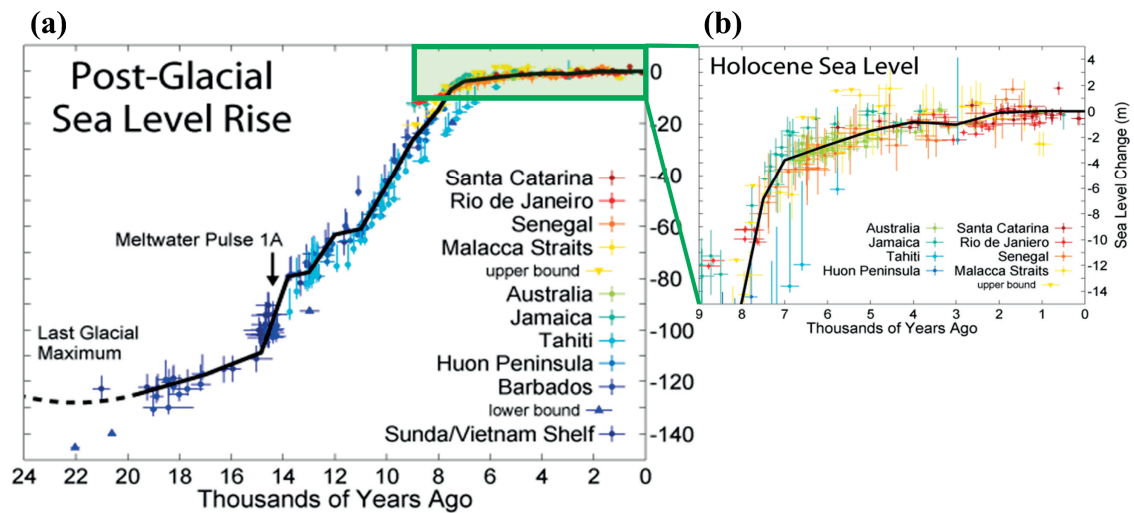


Figure 1.6. Reconstruction of the sea level curve showing the most recent period of rise and warming during the (A) Post-Glacial era and (B) Holocene era. Figures created by Robert A. Rohde based on data obtained from K. Fleming et al. (1998); K. Fleming (2000); and Milne et al. (2005).

Salt-marsh sedimentary sequences data obtained from North Carolina and global tidal gauge data (Figure 1.7) emphasize the occurrence of sea level rise within the past few centuries. There were relatively slight sea level changes between 1AD and 1800 AD. However, the sea level began to rapidly rise once more in the 19th century and accelerated again in the early 20th century. The recent SLR is much greater than at any time in the

past 200 years (Kemp et al., 2011). This recent rise in sea level coincides with the industrial era and the large carbon emissions that triggered global warming resulting in increased rates of glacial ice melting and hence accelerating SLR.

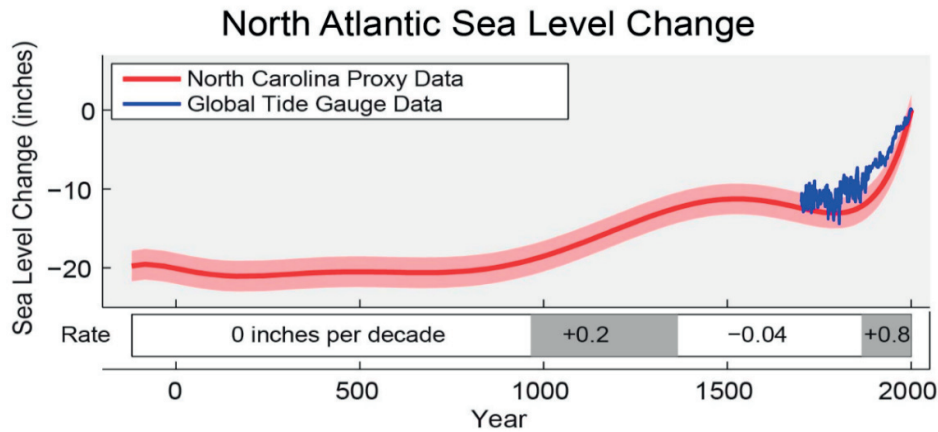


Figure 1.7. Sea level change in the North Atlantic Ocean based on data collected from North Carolina (red line, pink band shows the uncertainty range) compared with a reconstruction of global sea level rise based on tide gauge data (Blue line). Figure source: Adapted from Kemp et al. (2011).

1.3.2 Current sea level rise

Sea level rise (SLR) is still occurring, several observations within the past decades and centuries confirm that. Within the scale of the past few centuries, the eustatic sea level rise is of the most relevance as the current global warming-induced SLR has two main drivers: 1) The water expansion due to the increasing water temperature; and 2) The added water volume caused by the melting land ice as in the glaciers and ice sheets (Figure 1.8). Tidal gauge records (Figure 1.7) show that the sea level has risen about 20 cm during the past century (Kemp et al., 2011). As stated before, sea level rise is naturally occurring in this climatic era. However, the unprecedentedly high carbon emissions that started with the industrial era and are still occurring nowadays have accelerated its rate.

The NASA Goddard Space Flight Center provides live (from 1993 – present) global sea level changes (Figure 1.9) obtained from satellite observations. This data indicates a 103.3 mm sea level rise from 1993 till the present (2024). Also, NASA’s sea level change website provides live satellite estimates of the sea level-related parameters as provided in Table (1.1). Those recent satellite measurements indicate that, since 1993, the annual global SLR rate (2.2 mm/yr) has roughly doubled compared to the current (2024) rate of 4.4 mm/yr hence supporting evidence of SLR acceleration (e.g., Church, Gregory, et al., 2011).

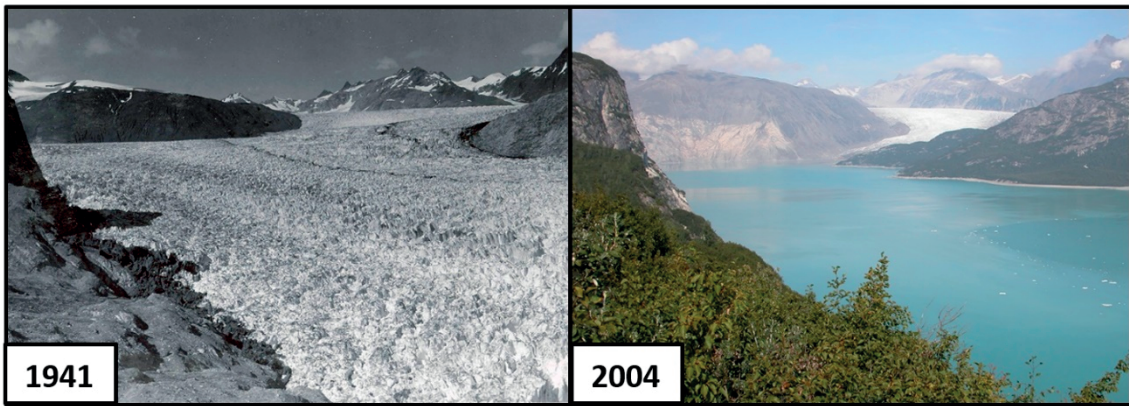


Figure 1.8. Muir Glacier in the Alaska Range. Photographed by William O. Field on 13/08/1941 (Left) and by Bruce F. Molnia on 31/08/2004 (Right). Image source: NSIDC Glacier Photograph Collection, https://nsidc.org/data/glacier_photo/.

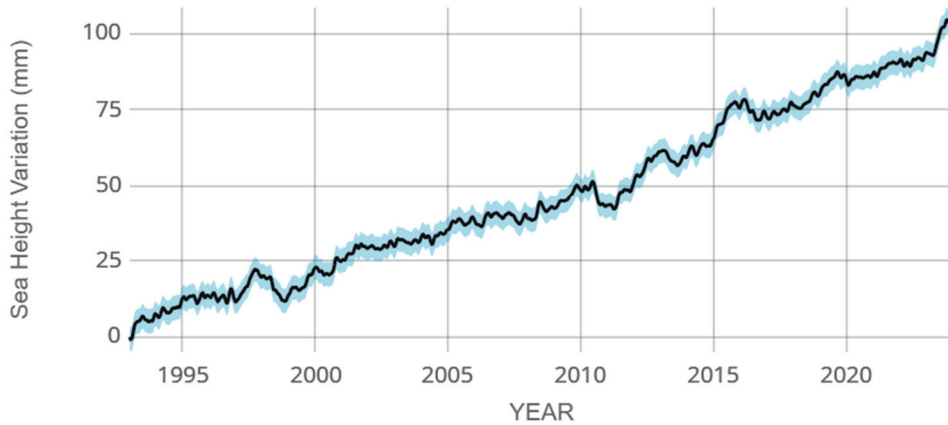


Figure 1.9. Sea level changes (mm) since 1993 as observed by satellite altimeters. The black line shows the measurements, while the blue shade indicates the uncertainty. Figure Source: NASA (2024).

Table 1.1. Sea level rise monitoring parameters on January 16, 2024. Source: NASA (2024)

Parameter	Unit	Trend	Magnitude	Error
Ocean Mass contribution	mm/yr	Increasing	2	± 0.3
Steric Height contribution	mm/yr	Increasing	1.3	± 0.2
Greenland Ice Mass Change	Gt/yr	Decreasing	267	± 21
Antarctica Ice Mass Change	Gt/yr	Decreasing	139	± 39

1.3.3 Sea level projections

The current SLR will continue in the future and is expected to accelerate. Oceans are absorbing about 90% of the increased atmospheric heat associated with human-induced global warming (Church, White, et al., 2011). Water's high latent heat capacity makes the ocean capable of absorbing and holding most of Earth's atmospheric heat, aiding climate regulation. However, ocean temperatures are rising, and hence water volumes. The current SLR is not expected to stop within the next century as oceans take a very long time to respond to Earth's surface temperature. Ocean water temperatures will continue to rise throughout the next centuries in response to the current increase in temperature. Recent studies suggest that current atmospheric CO₂ concentrations could be sufficient to melt Greenland completely over the next millennia (Philpott, 2015). SLR projections focus on the two main contributors: thermal expansion of oceans and melting ice glaciers.

Understanding the SLR is crucial due to its global effect on coastal areas worldwide. However, performing SLR projections is a challenging task. Even the most sophisticated climate models which explicitly simulate the Earth's natural processes can't simulate the rapid changes of the ice sheet dynamics and hence probably tend to underestimate the SLR (Melillo et al., 2014). Nowadays, most of the modeling efforts are focused on predictions for the end of the 21st century (2100). The current projections of global SLR in 2100 vary widely depending on the different modeling methods and assumptions which include the different greenhouse emission scenarios and the behavior of the ice sheets to the warming air and ocean water.

The IPCC Fifth Assessment Report (AR5) released in 2013 provided a range of projections for different greenhouse emissions scenarios and their associated radioactive forcing. Four Representative Concentrated Pathway scenarios (RCPs), ranging from low (RCP 2.6) to high (RCP 8.5) emissions, were considered and applied to process-based climate models to produce SLR scenarios. The RCP 2.6 scenario in which carbon dioxide levels stay less than 500 parts per million (ppm) and gas emissions declines after a peak, results in a projected rise of 0.28 m to 0.61 m with a median value of 0.44 m. The RCP 8.5 scenario in which CO₂ levels exceeded 700 ppm along with high concentrations of greenhouse gas emissions, results in a projected rise of 0.52 to 0.98 m with a median value of 0.74 m (Church, Monselesan, et al., 2013). Unlike previous reports, the IPCC Report (AR5) included the modeling of ice sheet dynamics; however, this modeling field is still new and comprises a lot of uncertainties (Church, Monselesan, et al., 2013).

Generally, current SLR projections during the 21st century range from 0.66 to 6 ft (\approx 0.2 to 2.0 m; Figure 1.10; Melillo et al., 2014; Parris et al., 2012). This range is not based on a specific modeling study, but it reflects the possible scenarios based on other scientific research. The large range of 0.2 to 2.0 m incorporates the uncertainties involved in modeling ice sheet dynamics. There is an ongoing scientific effort to narrow down this wide range. However, the uncertainty within the process makes it a challenging task.

Considering the lower end, most of the current studies agree that with the lowest possible emission scenarios, thermal water expansion and melting of ice glaciers will account for at least 11 inches (≈ 0.28 m) of SLR. This makes a lower end of 1 ft (≈ 0.3 m) a realistic value to use. Considering the higher end, a value of 4 ft (≈ 1.2 m) has been proposed in most studies. However, values higher than 2.0 m have been proposed up to 2.7 m (e.g., Le Bars et al., 2017; van de Wal et al., 2022) due to the uncertainty about the Antarctica ice sheet melting acceleration. Decision-makers prefer to use those high estimates to eliminate the risk. However, the probability of those values above the likely range can't be reliably evaluated. Regardless of the SLR magnitude in 2100, the rising levels are expected to continue as a result of both past and future human-induced greenhouse gas emissions.

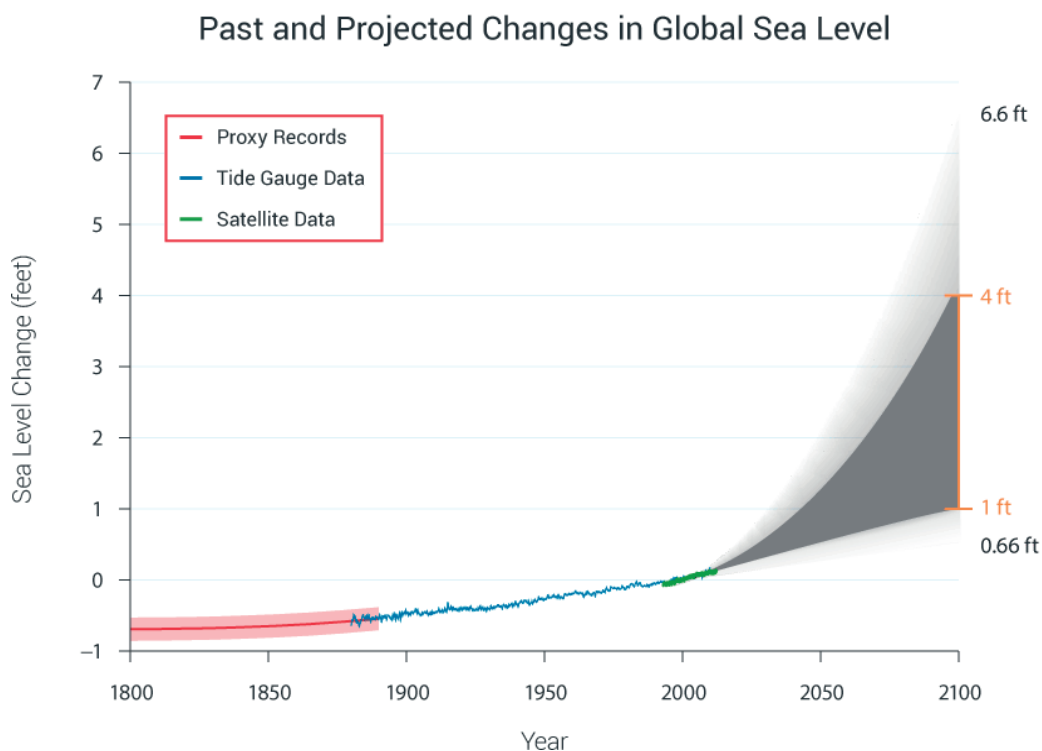


Figure 1.10. Past and projected SLR from 1800 till 2100, relative to year 2000. Estimates from proxy data (1800-1890) are shown in red, observed tidal gauge measurements (1880-2009) shown in blue, and satellite observations (1993-2012) shown in green. The orange line indicates the currently projected range of SLR in 2100 from 1 to 4ft (≈ 0.3 to 1.2 m). The larger range from 0.66 to 6.6 ft (≈ 0.2 to 2.0 m). represents the uncertainties involved in how glaciers and ice sheets will react to climate change. Figure source: Melillo et al. (2014), adapted from Parris et al. (2012) with input from NASA Jet Propulsion Laboratory.

Sea level rise is not uniform all over the world, some regional and local factors influence the relative SLR at the different coastlines around the world (e.g., Church, Clark, et al.,

2013; Karl et al., 2009). Over short time scales (hours to years), sea level variations occur mainly due to local variations in ocean currents, winds, tidal influence, storms, salinity, water temperatures, climatic processes such as El Niño, and location relative to the melting ice sheets. Over longer time scales (decades to centuries), changes in the land elevation either due to land subsidence or uplift result in significant changes in relative SLR (Church, Monselesan, et al., 2013). Karl et al. (2009) give an example of the deviation of sea level changes at particular locations from the global average. Based on the assumption that the historical geological forcing will not change, a 2 ft (≈ 0.6 m) rise in global sea level in 2100 would result in the following relative SLR: 1) 2.3 ft (≈ 0.7 m) at New York City; 2) 2.9 ft (≈ 0.9 m) at Hampton Roads, Virginia; 3) 3.5 ft (≈ 1.1 m) at Galveston, Texas; and 4) 1 ft (≈ 0.3 m) at Neah Bay in Washington State.

1.4 KNOWLEDGE GAPS AND OBJECTIVES

Estuaries have become part of our history, culture, and heritage, they are extremely valuable and we depend on them. They will certainly be part of our future so there is a need to find sustainable means of utilizing them while preserving their health for future generations. The growing threat of anthropogenic activities within estuaries along with global warming has raised the need for restoration projects and mitigation plans to maintain or restore the estuarine environment to its desirable status.

Estuarine restoration and management projects need to be based on a robust understanding of the historical development as well as the current, and future states of the estuaries. This need for better insight fueled a series of studies with the main aim of comprehending the fate of the estuarine environment under different threats with the main focus on global warming. This would help decision-makers realize the potential threat and develop management policies that ensure the estuarine environment sustainability.

This section highlights the existing problems and knowledge gaps considering the effect of SLR on the estuarine environment, with the main focus on the morphological development of estuaries. Also, the research goals and objectives are presented.

1.4.1 General Problem Identification

The concerning changes associated with global warming in an estuarine environment include sea level rise, alteration of riverine flows and sediment supply, change of wind conditions, extreme events, and changes in water temperature. SLR is occurring at an unprecedented rate and is expected to continue at an accelerating rate. Estuaries comprise delicate ecosystems that are vulnerable to SLR. At the same time, estuaries are amongst the most heavily populated areas around the world due to their high economic and environmental value. It's crucial to understand its SLR impact on estuaries to ensure the human welfare and sustainability of the estuarine environment. Forcing changes affect

different aspects within the estuarine environment, one of the most important aspects that is critical for the estuarine future is the morphological development of estuaries.

The estuarine morphology is controlled by infilling which depends on the fluvial and marine sediment supply along with the availability of accommodation space. As the infilling progresses, the tidal asymmetry starts diminishing and hence the infilling rate decreases. Eventually, the estuarine system reaches a state of dynamic equilibrium when sediment supplied to the system is balanced by sediment exported from the system (Dronkers, 1986). Estuarine environments subjected to constant forcing conditions tend to decrease energy dissipation levels over long time scales (longer than decades) due to bed resistance, which will eventually lead to morphodynamic equilibrium (Dam et al., 2016; van der Wegen & Roelvink, 2008). Any changes to the system's forcing conditions (e.g., sea level, tidal propagation, river discharge, or sediment supply) will result in a perturbation of this dynamic equilibrium causing the system to start shifting towards a new dynamic state of equilibrium (e.g., Pethick, 1994; van der Wegen, 2013; Z. Zhou et al., 2017). Achieving this new equilibrium state is a process that involves time as the system might seem to reach equilibrium at an annual or decadal timescale, while the system is still evolving when considering longer timescales (van der Wegen, 2013). This evolution is governed by the hydrodynamic, morphodynamic, and biological processes involved.

Throughout history, natural perturbations have continuously occurred and estuarine systems have continuously adapted. Nowadays, the main threat to the estuarine environment is human-induced. In most estuaries around the world, human interventions such as the lack of accommodation space and sediment supply decrease the system's ability to cope with major forcing changes such as the anticipated SLR. Also, the adaptation time scale can be centuries. This will create a conflict between the human settlements and interests and the system's tendency to evolve to a new desirable state.

The current concern is that the estuarine system will not be able to adapt to the SLR-induced perturbations and will start shifting toward an undesirable state. This shift will have a significant effect on human welfare represented in the loss of ecosystem services and the continuous threat to human settlements by flooding and inundation. The impact of global warming on the estuarine environment will be observed in estuaries worldwide. For example, SLR combined with decreased sediment supply will lead to considerable loss of valuable intertidal area and tidal marshes in various estuaries (Neil K. Ganju & Schoellhamer, 2010; van der Wegen, Jaffe, et al., 2017). Also, inundation and coastal squeeze caused by SLR have started threatening the existence of human settlements around estuaries (Pelling & Blackburn, 2013). In addition, alterations of riverine flows and extreme events are causing floods with devastating impacts on the ecosystem and human settlements as occurred during the 2017 California floods.

Understanding the SLR impact on the morphological development of estuaries is the crucial link for ensuring the sustainability of the ecological and environmentally valuable estuarine environment. Realizing this importance initiated a series of studies to model the long-term morphological development of estuaries under SLR and understand the underlying physical processes that govern the estuarine morphodynamics.

The long-term morphological development of estuaries underlies the future of estuaries. However, despite the importance involved in forecasting the long-term morphological development of estuaries under climate change, the complexity involved in the modeling process makes it one of the least understood and predicted aspects. This complexity mainly arises from the several challenges and uncertainties involved in the modeling process, which can be briefly summarized as follows:

i. Historical data sets:

A good understanding of the historical morphological development of estuaries is crucial for reliable SLR forecasts. This helps in understanding governing processes that shaped the historical morphological development along with validating the forecast models. However, historical relatively high-resolution, bathymetric, data sets are rarely available for most estuaries around the world. This issue raises the need to perform studies on well-monitored estuaries and relate those findings to other estuaries worldwide where data is scarce. Also, fundamental studies on idealized setups can help investigate governing processes.

ii. Sea level rise uncertainties:

There is a high uncertainty in SLR predictions resulting in a wide range. Different scenarios need to be taken into consideration during the modeling process by applying a worst and best-case scenario along with intermediate scenarios. Long-term morphological models generally require a high computational effort, and including multiple scenarios increases this effort and presents a challenge.

iii. Modeling uncertainties:

The modeling process comprises high uncertainty which arises from the large number of variables/parameters involved. This uncertainty exists in most modeling efforts and is not limited to long-term morphological modeling. However, in the case of long-term morphological modeling, quantifying this uncertainty represents a greater challenge mainly due to the longer time scales involved which could amplify the impact of those uncertainties. Also, the wide range of governing processes involved and its associated uncertainties contribute to the complexity of the forecast and put in question the trustworthiness of the models. Models are tools developed to simulate reality. Achieving an accurate representation of reality using models, even with the elimination of all sources of uncertainty, is a challenging task as most of the modeling methodologies have imperfections and shortcomings.

1.4.2 Specific Knowledge Gaps

The studies conducted in this research mainly focus on achieving a better understanding of the long-term morphological development of estuaries under different SLR scenarios. There are different modeling approaches to explore this aspect. As indicated later in the methodology (section 1.6), the process-based numerical modeling approach was chosen in this research. The following section gives a brief summary of the different specific knowledge gaps related to process-based modeling explored in this research.

1.4.2.1 Spatial Scales

Spatial scales within numerical modeling are mainly aspects related to grid resolution and model spatial coverage. One of the most important issues related to long-term modeling is the spatial resolution. A fine resolution can result in very high computational effort while a coarse resolution can result in a poor representation of the system along with the loss of important governing processes and hence provide poor predictions. Choosing an “adequate” resolution that achieves the balance between the two ends has always been a dilemma. Similarly, for the model spatial coverage, a large coverage decreases the impact of boundary conditions while increasing the computational effort.

1.4.2.2 Time Scales

Long-term morphological modeling under SLR comprises various governing processes. The main drivers of morphological development are riverine discharges, tidal forcing, sea level changes, salinity intrusion, wind, and waves. Those processes have different time scales that range from minutes to centuries. Main hydrodynamic forcing such as river discharges, waves, wind, and tides are typically short-term processes while morphodynamic development is usually examined on a longer time scale that extends from seasons up to thousands of years (de Vriend & Ribberink, 1996). The interaction between those processes with their different time scales is continuous. One of the challenges in long-term process-based morphological modeling is achieving an accurate representation of the interaction of those time scales (L. Guo et al., 2015).

Furthermore, all morphodynamic numerical modeling work requires a certain level of schematization and input reduction techniques. However, long-term morphodynamic process-based modeling always requires a much higher level of schematization mainly due to the high computational efforts required, lack of data, and the large number of uncertainties involved. The main aim of those schematizations and input reduction techniques is to simplify the modeling process along with achieving almost identical results as using the complete data set. Several schematizations and input reduction techniques have been developed for long-term morphological modeling such as:

- i. “Morphological tide” which involves a reduced tidal signal that can reproduce morphological developments as the full tidal spectrum (Hoitink, 2003; e.g., Latteux, 1995; Lesser, 2009).
- ii. Morphological factor (MF) to improve computational efficiency by accelerating the bed-level updates compared to hydrodynamics which operate on a much shorter time scale (e.g., Kuijper et al., 2004; Roelvink, 2006).
- iii. Wind and wave climate schematization to provide representative conditions that can be implemented in long-term morphological simulations (e.g., Hirschhäuser et al., 2000; Kuijper et al., 2004; van der Wegen, Jaffe, et al., 2011).
- iv. Representative discharge conditions that schematize the, for example seasonal, variations of riverine discharges (e.g., Neil K. Ganju et al., 2009; L. Guo et al., 2015; van der Wegen, Jaffe, et al., 2011)

The validity of those techniques is provided through previous studies. However, some of those schematizations involve changing the time scale of processes. When applying a set of schematizations and input reduction techniques to one model, the interaction between the new time scales of processes and between the schematizations can lead to a misrepresentation of reality or errors. SLR morphological forecasts using process-based models require a high level of schematizations, this arises the need for further testing if such a level of schematization can provide trustworthy morphological predictions and stable computations.

1.4.2.3 Processes

In addition to the spatial and time scales, some processes occurring within the short and long-term morphological development of estuaries under climate change are still not completely understood. Several studies attributed the poor performance of long-term morphological models to this gap. Many aspects related to the complex interaction between the flow, wave, sediment fluxes, and bottom changes haven't been investigated in a sophisticated manner for long-term applications. This understanding is especially important for practical applications, where solid morphological changes are required (X. Zhou, 2011). The processes and interactions that will be investigated with regard to SLR can be listed as follows:

- i. Wind Waves

Sea level rise causes a shift in sub-tidal areas, intertidal areas, and above-tidal areas. This shift in states implies an important influence on the estuarine morphodynamic development. SLR causes the inundation of intertidal areas. This inundation increases the landward extent of wind wave attack on intertidal areas, which enhances erosion. On the other hand, SLR causes the increase of water depth in subtidal areas and hence decreases the effect of wind waves, which enhances deposition (Neil K. Ganju & Schoellhamer, 2010).

Waves in previous long-term morphological studies were either neglected (Dam et al., 2016; L. Guo et al., 2015; van der Wegen, 2013; e.g., X. Zhou, 2011) or very simply schematized (Neil K. Ganju & Schoellhamer, 2010; Kuijper et al., 2004; van der Wegen, Jaffe, et al., 2011, 2017). Neglecting wind waves in sheltered environments can be justified but in most estuarine environments, wind waves can play an important role in shallow zones as intertidal areas, especially in muddy environments (Neil K. Ganju & Schoellhamer, 2009).

ii. Sediment properties

To reduce the complexity of morphological forecast models in sand-dominated systems (Dam et al., 2016; e.g., Dissanayake et al., 2009; Rübke et al., 2020; van der Wegen, 2013; van Maanen et al., 2013; Zheng et al., 2021), mud fractions are usually not considered. However, in most cases, mud flats also form a significant part of those sand-dominated systems and mud transport represents a secondary but important sediment transport contribution (e.g., Braat et al., 2017). The study of sand-mud mixtures is still one of the pioneering fields within sediment transport modeling (Toorman, 2000). This is due to the large amount of parameters and processes involved in simulating the behavior of the cohesive sediments. Including cohesive sediments will significantly increase the uncertainty involved in the modeling process. However, in order to forecast the fate of the intertidal areas under SLR the impact of cohesive sediments needs to be explored.

iii. Inundation and accretion

Sea level rise causes the inundation of intertidal areas and salt marshes. Landward migration will only occur in the case of no obstructions (Beets & van der Spek, 2000; e.g., Kraft et al., 1992). However, in constrained environments where vertical accretion is the only adaptation mechanism, the fate of intertidal areas under different SLR scenarios is still unknown and requires investigation. Such constrained systems with no room for lateral expansion or landward migration exist in several estuaries and tidal basins around the world (e.g., Wadden Sea, Western Scheldt, and San Francisco Bay) either due to urbanization (e.g., sea defenses) or geology.

1.4.3 Goals and Objectives

Sea level rise is a potential threat to the delicate estuarine environment. Understanding its impact on estuaries is crucial to ensuring the human welfare and sustainability of the estuarine environment. The morphological development of estuaries underlies the future of estuaries as it is the key aspect that ensures the sustainability of the ecological life, ecosystem services, and human welfare.

The main aim of this research is to assess SLR impact on the long-term (decades to centuries) morphological development of the estuarine environment, with a main focus on intertidal area.

- i. What are the processes required for morphodynamic predictions of sea level rise impact in estuarine environments?
- ii. What is the spatial resolution and time scale required for estuarine morphodynamic predictions of sea level rise impact?
- iii. Can we make trustworthy morphodynamic predictions in complex tidal environment case studies?
- iv. What is the fate of estuarine intertidal area under sea level rise?

1.5 DEVELOPMENT RELEVANCE

The team of researchers at IHE Delft and TU Delft believes in sustainable development and works towards achieving the Sustainable Development Goals defined by the United Nations (UN). Within the context of the estuarine environment sustainability, this research mainly contributes towards the Climate Action goal (Goal 13: Take urgent action to combat climate change and its impacts).

Estuaries are delicate environments which makes them one of the most vulnerable systems to climate change. This research contributes to this development goal by:

- i. Developing a better understanding of SLR impact on the estuarine environment.
- ii. Raising awareness about the potential threat of SLR to the general public and policymakers.

The knowledge obtained in this research eventually paves the way for understanding and combating SLR impact on estuaries not only in the investigated systems but also in developing countries where studies and data are scarce. Also, this research relates to other development goals such as Sustainable Cities and Communities (Goal 11) and Life Below Water (Goal 14).

Goal 11: Make cities inclusive, safe, resilient, and sustainable. Estuaries are one of the most heavily populated environments in the world. The conflict between the cities and the natural evolution of estuaries is threatening the sustainability and safety of cities. The models and knowledge developed in our research can help future studies assess the threat of SLR on human settlements around estuaries and plan mitigation/adaptation measures.

Goal 14: Conserve and sustainably use the oceans, seas, and marine resources. The estuarine environment is one of the most productive ecosystems in the world. In this research, we don't investigate the estuarine ecosystem. However, morphological modeling is the first step towards ecological modeling aimed toward sustainable use of estuarine resources.

The knowledge gained from this research will be a valuable advancement toward understanding the SLR impact and achieving a sustainable estuarine environment, as the “The damage that climate change is causing and that will get worse if we fail to act goes beyond the hundreds of thousands of lives, homes and businesses lost, ecosystems destroyed, species driven to extinction, infrastructure smashed and people inconvenienced” (David Suzuki).

1.6 LONG-TERM MORPHODYNAMIC MODELING APPROACHES

Morphodynamic models are useful tools for performing SLR impact investigations. Long-term morphodynamic modeling of coastal systems can be divided into two main approaches: 1) Behavior-based models; and 2) Process-based models (de Vriend et al., 1993). Also, other modeling approaches exist as a combination. The following section provides an overview of the two main modeling approaches based on the summary provided by Dastgheib (2012). Moreover, the limitations and advantages of each approach are presented. For more information about long-term morphological modeling approaches please refer to Dastgheib (2012) and de Vriend (1996).

1.6.1 Behavior-based models

Behavior-based models neglect the underlying physical processes and are based on a combination of expert analysis and empirical relationships developed from measurements and observations. These kinds of models can be divided into 1) data-based models; 2) empirical models; and 3) semi-empirical models (SEMs).

Data-based models are based on the assumption that the governing processes within the coastal system will not change over time. It is a direct form of extrapolation of historic morphological development to predict future morphological changes. This extrapolation can either be linear or non-linear. Also, data used can either be obtained from the same coastal system or another similar well-monitored system.

Empirical models can be divided into two main types: 1) equilibrium state models; and 2) transient empirical models. Equilibrium state models use relations developed from data obtained at similar well-monitored systems that are assumed to be in dynamic equilibrium. Transient empirical models describe morphological development between a specific actual condition and its equilibrium condition as an exponential decay process (de Vriend, 1996). They assume that the system’s elements behave independently.

Semi-empirical models, commonly referred to as “SEMs” in literature, are the combination of both data-based models and empirical models, where all the available data and relations are used.

A variety of behavior-based models have been successfully used to assess the effect of climate change on the morphological development of estuaries (Geselbracht et al., 2015;

Rossington & Spearman, 2009; Sampath et al., 2011; e.g., Van Goor et al., 2003). However, behavior-based models have several limitations which restrict their application:

- i. Behavior-based models don't provide an understanding of the underlying physical process, instead, they rely on extrapolating historical trends to predict future morphological development under the assumption that these relations are constant over time. However, this assumption might not be valid in some cases, especially when studying the effect of SLR on coastal systems. The current SLR is occurring at an unprecedented rate in the past millennia. The effect of such rise perturbations can exist in geological data tests, but not in historical bathymetric surveys. Using historical trends and modifying them to account for those unprecedented rates can result in unquantified errors.
- ii. In equilibrium state models, some relations used in current long-term morphological models were derived from data obtained at systems that are not in dynamic equilibrium (Dastgheib, 2012).
- iii. Most of the data analysis and empirical relationships used in behavior models are developed in similar well-monitored systems instead of the system under consideration. To which extent those well-monitored systems are similar to the studied system and whether the findings can be applied to the studied system is always a matter for discussion.
- iv. In transient empirical models, the assumption that each element in the system behaves independently is sometimes not valid in estuaries as there is continuous sediment exchange between the river network, estuarine body, and adjacent coastline. Also, within the estuarine body itself, different components (e.g., channels and shoals) interact and can behave differently in response to SLR.
- v. Anthropogenic interference is common in estuaries around the world. The historical data sets used for extrapolation or developing relations are commonly affected with this influence. Trying to isolate this influence is a challenging task. On the other hand, assuming that this interference will be constant can be an invalid assumption as it is continuously changing. In some estuaries, human influence is increasing, while in other estuaries restoration projects are limiting this influence.
- vi. Developing and accessing mitigation and prevention measures using behavior-based models is a challenging task.

On the other hand, behavior-based models can be advantageous since:

- i. They are less complex compared to process-based models. Simple empirical relationships and expert data analysis are the main tools to perform morphological predictions. Also, it does not involve a high level of input as the case for process-based models.

- ii. Computational times associated with behavior-based models are much lower than that for process-based models. This can be of great use in case quick analyses are required and for investigating multiple scenarios.

1.6.2 Process-based models

Process-based models are usually numerical models that describe the system by representing the governing physical processes. Those models comprise a series of modules that model the hydrodynamics (Current and waves) and sediment transport. These modules can either be used with a time loop or sequentially depending on whether bathymetric changes are taken into consideration or not, respectively. Ganju & Schoellhamer (2010), Dissanayake (2011), van der Wegen (2013), and van der Wegen et al. (2016) provide successful applications for the process-based modeling approach in investigating the SLR impact on the long-term morphological development of estuaries. However, as is the case for behavior-based models, process-based models have their limitations and challenges:

- i. Processes included in the model have to be selected carefully since each process has to be modeled adequately along with an adequate representation of the different module combinations (de Vriend, 1996). A solid understanding of the involved governing processes is required to achieve this adequate representation. However, some short and long-term governing processes within the estuarine environment are still not completely understood.
- ii. Numerical imperfections in the modeling software and formulations can result in errors and misrepresentations of the morphological development.
- iii. High computational effort is usually associated with process-based models. Combining that with long-term morphological modeling can result in very high computational times.
- iv. Unlike behavior-based models, in which relations from similar systems can be used, process-based models need historical data sets for the study area to calibrate and validate the model. Those data sets are usually rare.
- v. This modeling approach requires a higher level of input and its associated schematization techniques.
- vi. Process-based models claim to overcome the limitations of behavior-based models. However, within the field of modeling the long-term morphological development of estuaries under global warming, the capacity of process-based and behavior-based models has rarely been compared directly.

On the other hand, process-based models can be advantageous since:

- i. This modeling approach provides an understanding of the underlying physical processes, resulting in higher reliability and more confidence in model results.

- ii. Process-based models do not only try to simulate and predict reality but also can be used as a virtual lab to perform fundamental studies. Those studies can provide a better understanding of the effect of the different processes and identify the main processes that govern the morphodynamic development (Roelvink & Reniers, 2011). Also, the developed models can be used for developing and accessing different mitigation and prevention measures.

1.7 METHODOLOGY AND THESIS STRUCTURE

As indicated in section 1.6, there are several approaches for modeling the long-term morphodynamic evolution of coastal systems. Within the spectrum of other modeling techniques, in this research, a process-based numerical modeling approach is utilized, supported by field data and observations. Despite the complexity involved, the process-based modeling approach was mainly chosen as it provides a useful tool for exploring the processes governing the morphological development and the SLR impact. The process-based model implemented in this research is the Delft3D (D3D; Lesser *et al.*, 2004; Deltares, 2023). More information about D3D and the different modeling setups is provided in each chapter individually.

Fundamental studies (Chapters 2 and 3) are performed on idealized estuaries to isolate and investigate some knowledge gaps and processes using setups representing different spatial scales. Those studies also include relating the findings to real case studies from literature. The first study (Chapter 2) represents a small-scale, single channel-shoal, system that is inspired by fringing shoals found along the edges of estuaries. A 2DH high-resolution model is implemented to generate a shoal in a state of tidally averaged morphodynamic equilibrium. The intratidal dynamics, processes governing shoal formation, and small-scale tidal levees formation are investigated. Furthermore, the response of the equilibrium profile to both short-term (wave action) and long-term (SLR) forcing changes is explored. The second study (Chapter 3) utilizes a larger-scale 2DH modeling setup representing a constrained tidal basin. An initial, mildly sloping, bathymetry is subjected to constant forcing conditions which generates a channel-shoal system including mainly free shoals along with some small fringing shoals. The SLR impact on the morphological evolution of the channel-shoal system is explored with different forcing conditions such as SLR scenarios, wind-wave activity, tidal forcing, sediment supply, and mud inclusion.

Real case study applications (Chapters 4 and 5) are also investigated using 3D modeling setups. San Pablo Bay (San Francisco Estuary, USA; Chapter 4) represents a mud-dominated system, while the Western Scheldt Estuary (The Netherlands; Chapter 5) represents a sand-dominated system. Those case studies include a morphological hindcast compared to unique historical bathymetries followed by a forecast towards the end of the

21st century including SLR. The application of the findings is also examined in relation to other estuaries worldwide.

Finally, the concluding chapter (Chapter 6) summarizes the main study findings in the form of answers to the research questions and presents future research recommendations.

2

MORPHODYNAMIC EVOLUTION OF A FRINGING SANDY SHOAL FROM TIDAL LEVEES TO SEA LEVEL RISE¹

Abstract

Intertidal shoals are vital components of estuaries. Tides, waves, and sediment supply shape the profile of estuarine shoals. Ensuring their sustainability requires an understanding of how such systems will react to sea level rise (SLR). In contrast to mudflats, sandy shoals have drawn limited attention in research. Inspired by a channel-shoal system in the Western Scheldt Estuary (Netherlands), this research investigates governing processes of the long-term morphodynamic evolution of intertidal estuarine sandy shoals across different timescales. We apply a high-resolution process-based numerical model (Delft3D) to generate a channel-shoal system in equilibrium and expose the equilibrium profile to variations in wave forcing and SLR. Combined tidal action and wave forcing initiate ridge formation at the seaward shoal edge, which slowly propagates landward until a linear equilibrium profile develops within 200 years. Model simulations in which forcing conditions have been varied to reproduce observations show that the bed

¹ This chapter is based on:

Elmilady, H., van der Wegen, M., Roelvink, D., & van der Spek, A. (2020). Morphodynamic Evolution of a Fringing Sandy Shoal: From Tidal Levees to Sea Level Rise. *Journal of Geophysical Research: Earth Surface*, 125(6), e2019JF005397. doi:10.1029/2019JF005397

is most dynamic near the channel-shoal interface. A decrease/increase in wave forcing causes the formation/erosion of small tidal levees at the shoal edge, which shows good resemblance to observed features. The profile recovers when regular wave forcing applies again. Sandy shoals accrete in response to SLR with a long (decades) bed-level adaptation lag eventually leading to intertidal area loss. This lag depends on the forcing conditions and is lowest near the channel and gradually increases landward. Adding mud makes the shoal more resilient to SLR. Our study suggests that processes near the channel-shoal interface are crucial to understanding the long-term morphodynamic development of sandy shoals.

2.1 INTRODUCTION

Intertidal shoals are a major component of many estuaries worldwide. During the tidal cycle, they undergo a rhythm of wet-dry cycles which develops a unique ecosystem that supports a diverse array of species, especially at vegetated zones (Lipcius et al., 2013). The intertidal area provides ecosystem services and accommodates commercial fisheries. It also plays a major role in erosion control and flood protection by wave attenuation (Narayan et al., 2017; Shepard et al., 2011).

Being the buffer zone between sea and land, the intertidal zone is subject to continuous pressures like urbanization, changing river flow regime and sediment supply, subsidence, and sea level rise (SLR). Anthropogenic influence may notably impact the estuarine morphology (e.g., Jaffe et al., 2007; Luan et al., 2016; Ranasinghe et al., 2019) potentially leading to a notable degradation of the intertidal ecosystem and a continuous threat to associated ecosystem services.

Estuarine shoals may be considered as emergent features that evolve as a result of a fundamental instability of the morphodynamic system under tidal forcing. An initial bed-level perturbation triggers a positive morphodynamic feedback between currents and morphology leading to the emergence of large-scale channel-shoal patterns (Hibma et al., 2003; Schramkowski et al., 2002; Seminara & Tubino, 2001; Coeveld et al., 2003;). Over a long timescale (centuries to millennia), the residual sediment transport diminishes and leads to a relatively stable channel-shoal morphology where braiding ebb and flood channels circumvent sandy shoals (Ahnert, 1960; Hibma, 2004; van der Wegen et al., 2008; van der Wegen & Roelvink, 2008; Leuven et al., 2016; van Veen et al., 2005). Confined estuarine plan forms govern the location and evolution of particular channel-shoal patterns (Dam et al., 2016; Leuven et al., 2018; van der Wegen & Roelvink, 2012).

Although the previous section suggests that shoal formation is primarily associated with tidal currents, waves play an important role when shoals become shallow and intertidal (e.g., Kohsiek et al., 1988). Observations and modeling studies suggest that tidal flats tend to evolve towards a morphologically steady state maintained by a balance between

sediment supply, wave action, and tidal forcing (Friedrichs, 2011; Friedrichs & Aubrey, 1996; Hu et al., 2015; Maan et al., 2015, 2018; Roberts et al., 2000; van der Wegen et al., 2019; van der Wegen, Jaffe, et al., 2017). Tidal forcing is usually associated with deposition while erosion tends to be associated with wind-wave activity (e.g., Allen & Duffy, 1998; Christie et al., 1999; Janssen-Stelder, 2000; Yang et al., 2003). Spatial gradients in hydrodynamic energy and suspended sediment concentrations (SSC) across the tidal flat impact the direction of sediment flux. Tidal currents cause highest bed stresses at the deeper (subtidal) flat section, driving a landward transport, while wind-waves cause highest stresses on the shallower (intertidal) flat section, driving a seaward transport (Friedrichs, 2011; e.g., Kohsiek et al., 1988; H. Ridderinkhof et al., 2000; Yang et al., 2003). Janssen-Stelder (2000) shows a landward directed tidally-averaged suspended sediment flux across tidal flats in the Wadden Sea during calm wave conditions, which reverses to seaward as wave heights grow.

In addition to its erosional capacity, waves impact the sediment redistribution along the flat (Carniello et al., 2005; Houser & Hill, 2010; Z. Zhou et al., 2015). Intertidal shoals can be mudflats, sand flats, or a mixture depending on the sediment supply and hydrodynamic conditions. They can be found in a free (no landward constraints) or a fringing form. Sand fractions exist at locations where wave action and strong tidal currents prevent fine sediment deposition while mud fractions exist at more sheltered low-energy embayments and fringes.

2.1.1 Modeling intertidal flats

Several morphodynamic modeling studies explored tidal evolution and equilibrium profiles for a muddy environment including wave impact. This “morphological equilibrium” is loosely defined in literature as a state at which tide-residual transport diminishes and limited morphological development occurs within a characteristic forcing time span (Friedrichs, 2011; Z. Zhou et al., 2017). Friedrichs & Aubrey (1996) proposed a dynamic equilibrium theory with analytical solutions under the assumption of spatially constant maximum shear stress. Assuming a similar equilibrium concept, Hu et al. (2015) implemented the dynamic equilibrium theory while allowing for spatially and temporally varying bed shear stress.

Other studies implemented a process-based approach without underlying assumptions of equilibrium (e.g., Pritchard et al., 2002; Pritchard & Hogg, 2003). Roberts et al. (2000), and van der Wegen et al. (2016, 2019) showed modeled 1D profiles similar to observed mudflat profiles. 2D/3D process-based models provided skillful reproduction of observed morphodynamic developments in entire estuaries such as San Francisco Bay (Ganju 2009, van der Wegen 2011, Elmilady 2019), Western Scheldt (Maan et al., 2018), and Yangtze Estuary (Guo, 2014; Luan et al., 2016, 2017).

However, process-based modeling studies covering sandy shoals only applied relatively coarse grids and excluded wave dynamics (e.g., Dam et al., 2016; Guo, 2014; Hibma, 2004; van der Wegen & Roelvink, 2008, 2012; Van der Wegen 2013) to reduce computational effort and model complexity. Braat et al. (2017) modeled waves in a sand-mud estuarine environment, albeit with a sand transport formulation (Engelund & Hansen, 1967) which models a total transport and excludes sand stirring by waves. The inclusion of waves in sandy systems could be of high relevance, especially for the intertidal morphology. In addition, a relatively coarse grid could potentially disregard relevant sub-grid (wave) dynamics and features.

2.1.2 Tidal levees

An example of sub-grid features is a tidal levee. Levees are small ridges formed by deposits that build up along the sides of a channel. Their formation is commonly pronounced in riverine and deltaic systems during flood events (Adams et al., 2004; Brierley et al., 1997) or along submarine fan system channels during high flow turbid events (Normark et al., 2002; Straub & Mohrig, 2008). In tidal environments, they can be found along creeks in salt marshes and mudflats (Perillo & Iribarne, 2003; Temmerman et al., 2005) or on the edge of channels and shoals in tidal basins and estuaries (Cleveringa, 2013). They often fall dry near low water before the surrounding shoal area and usually consist of coarser material than that found on locations further away from the channel edge. Unlike riverine levees, tidal levees have drawn limited attention in research.

Based on field observations of sand transport and morphological changes in intertidal areas (Eastern Scheldt estuary; The Wash, U.K.; Wadden Sea), Wang et al., (2018, p. 194-197) developed a conceptual model for sandy tidal flat development over long timescales. They describe the flat evolution as the outcome of the opposing supply of suspended sand by the tide, predominantly at the shoal edge, and (re)suspension or erosion of the shoal surface sediments by waves. Formation of tidal levees has been observed during periods of mild wave conditions.

2.1.3 Sea level rise

Tide gauge records show that the sea level has risen about 20 cm during the past century (Kemp et al., 2011). Currently (2020), the SLR rate is 3.3 mm/year (NASA, 2024) with considerable global variations (Handleman, 2015). This rate is expected to accelerate towards the end of the 21st century (Church, Clark, et al., 2013; Parris et al., 2012). It is unclear how estuaries will morphodynamically react to SLR in particular with respect to the fate of intertidal area. The estuarine resilience to SLR may strongly depend on local conditions of tides, waves, sediment supply, and local SLR rate.

Process-based models provide useful tools to explore the possible impact of SLR on estuarine morphodynamics. SLR impact studies include validated modeling hindcasts (Elmilady et al., 2019; Neil K. Ganju & Schoellhamer, 2010; van der Wegen, Jaffe, et al., 2017; X. Zhou et al., 2013) or more schematized settings systematically exploring governing processes (Best et al., 2018; Dissanayake et al., 2009; van der Wegen, 2013; van Maanen et al., 2013; Z. Zhou et al., 2016). Rossington & Spearman (2009), and Van Goor et al. (2003) provide SLR studies applying an empirical approach (ASMITA), albeit that potential wave impact was not considered explicitly. A common finding of previous studies is that SLR leads to intertidal area accretion, however, the accretion rate is less than the SLR rate. A limited, linear rise in sea level may allow for an accretion rate equal to the SLR rate after an initial period of intertidal area loss (Van Goor et al., 2003).

2.1.4 Research Objective

This study aims to explore the mechanisms that drive the long-term morphodynamic evolution of sandy intertidal shoals across a range of timescales. This includes the mechanisms driving the formation of tidal levees and the impact of SLR. We hypothesize that a stable intertidal shoal morphology evolves from a balance between constant sediment supply, tidal action, and wave forcing and that changes in forcing lead to adaptation of this equilibrium profile that may recover when prevailing forcing is maintained again.

First, we focus on observed sandy shoal dynamics. We revisit field measurements carried out by Geomor team (1984) at the Galgeplaat shoal in the Eastern Scheldt Estuary (Figure 2.1). We then explore satellite imagery of sandy shoals in the Western Scheldt Estuary (WS, Figure 2.2), and LIDAR data at the Frisian Inlet in the Wadden Sea (Figure 2.3). Secondly, we apply a process-based model (Delft3D) that allows for a flexible application of processes across a range of scales. Using a schematized configuration inspired by conditions in the WS, we investigate sandy shoal evolution and perform a sensitivity analysis for different model parameters and varying forcing conditions including variations in wave forcing and SLR rate. Finally, we qualitatively compare model results with observations and literature in order to test the developed knowledge regarding shoal dynamics and tidal levees. SLR impact is compared to the findings of an empirical, more aggregated modeling approach (ASMITA).

2.2 SANDY SHOALS OBSERVATIONS

The Eastern and Western Scheldt estuaries (Figure 2.1a) are located in the southwest of the Netherlands, while the Wadden Sea tidal basin is located in the north of the Netherlands (Figure 2.3). The morphology of these systems comprises a sandy system of deep channels and intertidal shoals which generally become muddier in more landward

located regions. They are tide-dominated systems, the mean tidal range at the mouth of the WS (Vlissingen; Figure 2.1a) and the Frisian Inlet (Figure 2.3) is about 3.8 and 2 m, respectively. Shoals in the inner estuary are relatively sheltered from large offshore waves, wave attack is usually limited to small ($H_s < 0.25$ m) local wind-generated waves.

2.2.1 Eastern Scheldt

From 1982-1984, a unique pilot study was conducted with the aim of understanding the morphological evolution of the Eastern Scheldt shoals (Geomor team, 1984; van Vessem, 1984a, 1984b; Kohsiek et al., 1988). Since we managed to obtain only poor copies of these reports, we digitized the data and summarize their findings here. The study site is the Galgeplaat (Figure 2.1b) which is one of the largest ($\approx 2.3 \times 5.5$ km) sandy intertidal shoals in the estuary. It becomes completely inundated during high tide while most of it is exposed during low tide.

Geomor team (1984) monitored bed-level changes on a 400×700 m grid of the Galgeplaat (Figure 2.1b, black rectangle) with four lateral monitoring cross-sections (not shown on map) each with 11 monitoring points starting from the seaward shoal edge going landward. Geomor team (1984) and Kohsiek et al. (1988) noted that the seaward shoal edge experienced most bed-level fluctuations compared to areas on top of the shoal. Shoal edge erosion mainly occurred under the influence of powerful wave action (wind speed > 5 Bft, $H_s > 0.27$ m, $T_p \approx 3$ s). The increased wave action resulted in higher wave orbital velocities hence more resuspension. Combined with longshore and wind-driven currents, wave action increased the erosional transport capacity during stormy conditions. In contrast, during limited or no wave action (wind speed < 5 Bft, $H_s < 0.2$ m, $T_p \approx 2$ s), sedimentation processes dominated, especially during spring tides. Figure 2.1c shows that over the whole year (M1 monitoring period from 09/1982 to 08/1983), erosion and sedimentation were in the same order resulting in a relatively small net sedimentation/erosion.

From 1983 to 1984, bed levels were measured at 5 additional cross-sections (CRS1 to CRS5, Figure 2.1b) at different points in time for durations ranging from 1 to 3 weeks (van Vessem, 1984a, 1984b). In this research, we present 3 monitoring periods (Figures 2.1d to 2.1f), the two periods M2 and M3 represent intervals characterized with high wind-wave conditions while the period M4 represents an interval with mild wind-wave conditions. During M2 and M3, a clear erosional trend was observed, while during M4, the profile experienced net sedimentation. Similar to the one-year monitoring period (M1), bed-level fluctuations mainly occurred at the shoal edge and decreased when going landward.

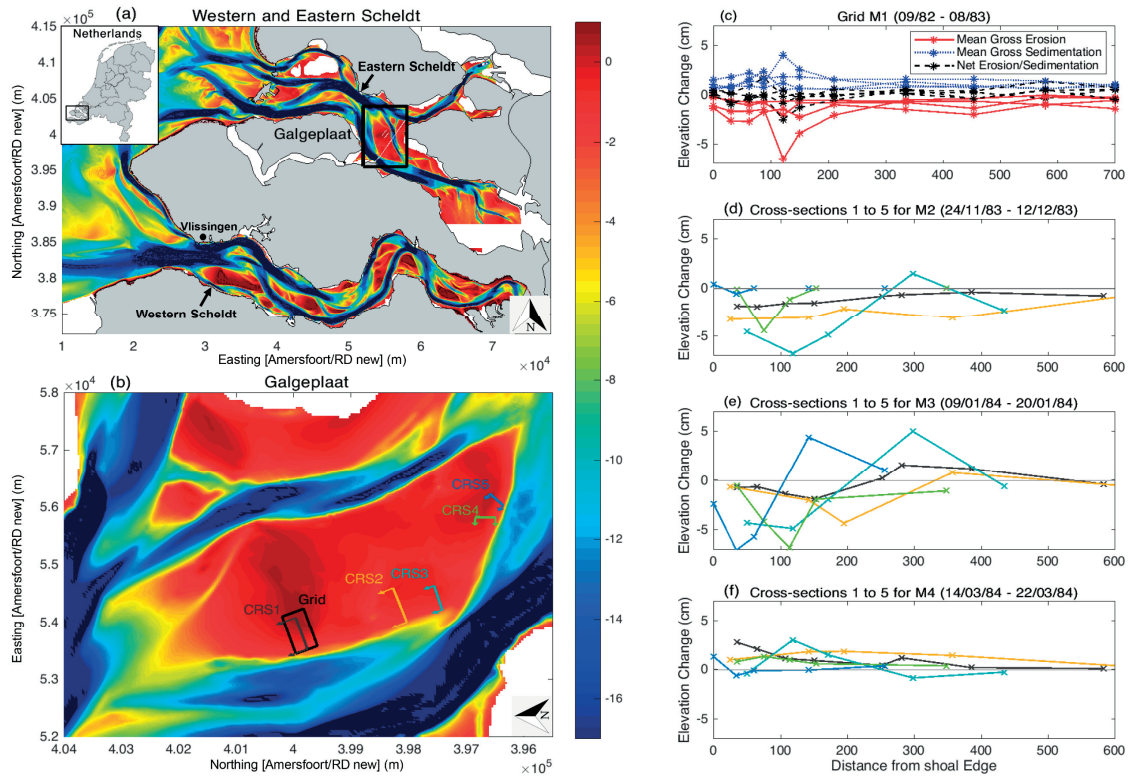


Figure 2.1. (a) Layout and bathymetry (m) of the Western and Eastern Scheldt estuaries with the location of the Galgeplaats indicated. (b) The 1993 Galgeplaats bathymetry (m; Reversed coordinates) showing the location of the 1982-1983 monitoring grid (black rectangle) along with the five cross-sections (CRS1 to CRS5) monitored during 1983-1984 period. (c) Bed-level changes (cm) at 4 cross-sections inside the monitoring grid during the one-year monitoring period (M1) divided into the mean annual gross erosion (Red) and sedimentation (Blue) along with the net annual erosion/sedimentation (Black). (d), (e), and (f) Bed-level changes (cm) at CRS1 to CRS5 (colors correspond to cross-sections in Figure 2.1b) during the monitoring periods of M2, M3, and M4, respectively. The figure was constructed by the digitization of Geomor team (1984), van Vessem (1984a), and (1984b). The bathymetric data (source: Rijkswaterstaat) are with respect to NAP (Dutch Ordnance Level).

2.2.2 Remote sensing at Western Scheldt and Wadden Sea

Relatively high elevation longitudinal ridge formations with dissecting drainage channels can be observed at the channel-shoal interface in sandy estuaries (e.g., Western Scheldt Estuary, Figure 2.2) and tidal basins (e.g., Wadden Sea, Figure 2.3). They can be visually identified as areas that emerge earlier during ebb tide than the surrounding shoal. Their width can be as small as 10 m which combined with their dynamic nature makes them hard to capture in large-scale bathymetric surveys. Figure 2.2 shows examples of levee formations spread along the WS. Cleveringa (2013) reports yearly measured high-

resolution bed-level cross-sections at several locations in the WS, some of which show levee formations at the channel-shoal interface.

LIDAR surveys during low tide are able to record the small-scale structures of the intertidal area. In this research, we present two LIDAR datasets (Figure 2.3) showing the Frisian Inlet of the Wadden Sea in 2012 and 2018 with 5 and 2 m spatial resolution, respectively.



Figure 2.2. Google Earth satellite images showing small-scale levee formations at the channel-shoal interface in the WS. Note: Large and small images scales (bottom right) are 6 km and 200 m, respectively.

Morphological ridge features resembling levees can be observed in a number of profiles at the shoal seaward edge. Their spatial scales can differ notably as their cross-sectional width ranged from 20 m (A6) up to 80 m (A1 2018). Tidal levees have a relatively dynamic nature, A4 and A6 show levees in both surveys, while A1, A3, and A5 show levees in just one survey. They can exist on a relatively flat profile (A1, A3, and A4) or on a sloping profile (A5, and A6). Also, in some cases (A2, A7, and A8), no visible levee formations were identified.

A7 and A8 are located on a sand-dominated shoal that resembles the schematized modeling configuration implemented in this study (section 2.3.1). The shoal is adjacent to a deep channel (15-20 m) on the north seaward side and its configuration is relatively fringed. The adjacent polder blocks the flow from the eastern and southern direction and

a groin blocks a portion of the flow from its open shallow western boundary. A7 experienced shoal edge erosion while the landward shoal side remained relatively constant. A8 shows an accreting profile with the highest accretion rates near the channel.

Within the presented map, there are several locations at which levees exist, but locations without levees are more common. The 8 presented cross-sections were selected from a large number of analyzed cross-sections in order to show different morphodynamic behavior.

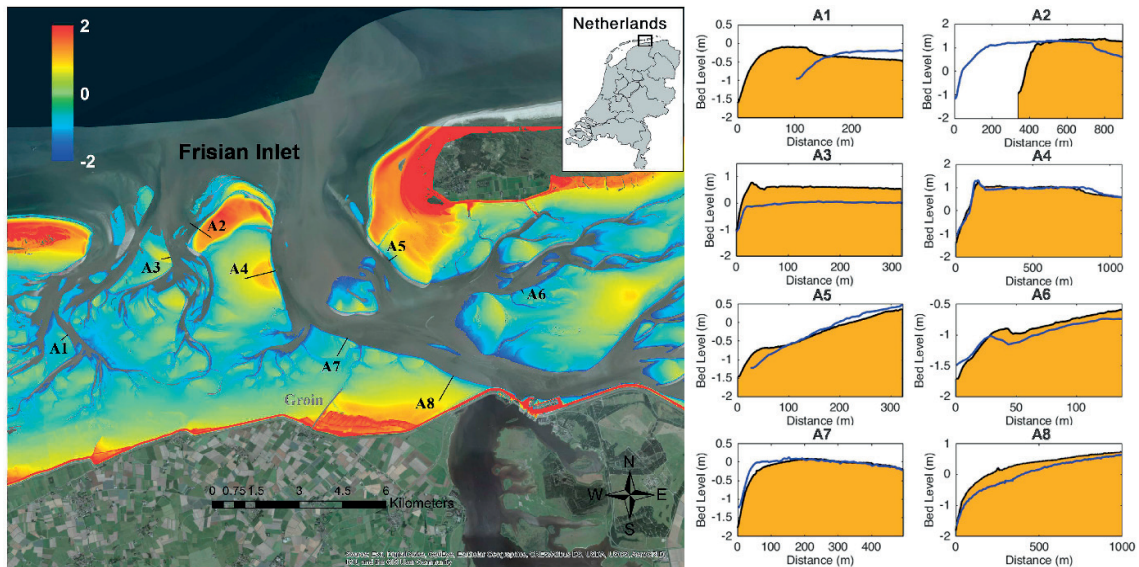


Figure 2.3. The left panel shows the 2018 bathymetry (m; reference NAP) of the intertidal zone at the Frisian Inlet of the Wadden Sea obtained from LIDAR imagery (source: Rijkswaterstaat) along with the locations of 8 cross-sections (A1-A8). The right panel shows bed-level profiles for 2018 (black line and solid hatch), and 2012 (blue line). The left and right sides of a cross-section are the seaward and landward sides, respectively.

2.3 NUMERICAL MODEL SETUP

2.3.1 Model setup and forcing

We implemented a small-scale idealized 2DH modeling configuration that represents a fringing shoal in an estuarine channel-shoal system (Figure 2.4). This idealized approach allows for reducing the system's complexity. The setup is inspired by fringing shoals found along the edges of the WS (e.g., Maan et al., 2018). The initial bathymetry comprises a flat submerged 850 m wide shoal (-3 m MSL) adjacent to a 150 m wide channel (-15 m MSL). The model domain is covered by a 2D horizontal fine resolution rectangular grid (20×30 m). We apply the Delft3D (D3D) process-based numerical model

(Deltares, 2017; Lesser et al., 2004). Delft3D-FLOW computes the flow by solving the two-dimensional shallow water equations at a high spatial (20×30 m) and temporal (12 s) resolution (Appendix A.1.1).

The only open model boundaries are at the channel, the Northern, Southern, and Seaward boundary (black lines; Figure 2.4a). The Seaward boundary is specified with a semi-diurnal, 1.75 m amplitude M_2 water level. The Northern and Southern boundaries are Neumann water level gradient boundaries specified with a phase difference based on the tidal wave propagation in the channel. Equilibrium sediment concentrations at the boundaries were applied. A Thatcher-Harleman relaxation time lag of 120 min was set at the boundaries to avoid SSC discontinuities during the turning of tides (Thatcher & Harleman, 1972). We applied the “coastal boundary” option to allow non-perpendicular flow across the boundaries (Deltares, 2017).

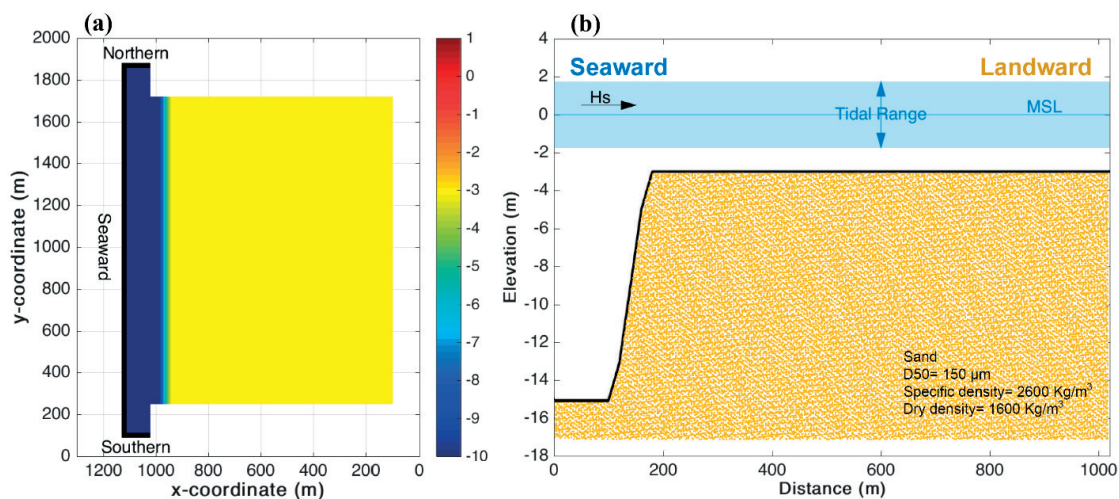


Figure 2.4. Model configuration and initial bathymetry (a) plan-view with the location of the three open model boundaries (black lines) and (b) cross-sectional profile indicating the seaward and landward side along with the MSL, tidal range, wave direction, and initial sediment thickness and properties.

2.3.2 Wave model

Wave heights (H_s) and orbital velocities are computed using the “roller model” (Deltares, 2017, appendix B.15; J. A. Roelvink, 1993) which is coupled with Delft3D-FLOW through online coupling that includes wave-current interactions (Wave-induced forcing included in the momentum equations). The roller model is used to simulate small ($H_s=0.2$ m), short waves ($T_p=3$ s) propagating from the seaward boundary towards the shoal (Perpendicular to the shoal; Figure 2.4b). It incorporates a short wave energy balance equation in which friction and wave breaking are the dissipation mechanisms. Short wave energy dissipation due to wave breaking acts as the source term for a roller energy balance

equation which delays the momentum release from wave breaking. Each time-step (12 s), the FLOW module computes (e.g. water level, velocities, and bed shear stress), and the roller model solves the wave energy propagation and dissipation across the shoal in order to evaluate the wave heights and its associated wave-induced shear stress. The Fredsoe wave-current interaction model (Fredsoe, 1984) is used to compute the maximum shear stress (τ_{max} , used for sediment computations) based on the combined flow (τ_c) and wave (τ_w) shear stress. A more detailed description of the roller model is provided in Appendix A.1.2.

2.3.3 Sediment transport and morphodynamics

Suspended sediment transport is calculated in D3D by an advection-diffusion solver which includes a sink and source term and is based on the local and time-varying velocities and water levels. The Van Rijn (1993) formulations are used to compute the sandy sediment transport for the combined effect of waves and currents for both bed- and suspended load transport (Appendix 1.3.1 provides more detailed information on the transport formulation).

We applied a non-cohesive sediment fraction with a D_{50} of 150 μm , a sediment density of 2650 kg/m^3 and a dry bed density of 1600 kg/m^3 . The minimum depth for sediment computations was set to 0.15 m. To account for bed slope effects, the transverse and streamwise bed gradient factors AlfaBn and AlfaBs were set as 20 and 1, respectively. The available sediment layer was set to -17 m MSL as initial runs showed a gradually continuous channel deepening. Instead of fixing the channel bed, this approach allows for the free development of the shoal along with limiting channel deepening.

Each time-step (12 s), the MOR module in Delft3D-FLOW uses the combined hydrodynamics (FLOW + WAVE) to compute the sediment transport rates. Bed-level changes are calculated based on the divergence of the sediment transport field. Following that, bed-level changes are multiplied by a morphological acceleration factor (MF) to enhance morphological developments (Roelvink, 2006). This loop is repeated for the next time-step using the updated bed levels. A MF of 100 was implemented for the base-case model based on a sensitivity analysis which showed minimal bed level differences compared to a MF of 25 (Figure 2.13; Appendix 1). Using this approach, modeling 4 years of hydrodynamics with a MF of 100 is equivalent to 400 years of morphodynamic development. This approach has been widely applied in various long-term morphological studies (Dam et al., 2016; Elmilady et al., 2019; Ganju & Schoellhamer, 2010; L. Guo et al., 2015). The presented model takes about 2 days to simulate 4 hydrodynamic years on a 4-core computer.

2.4 MODEL RESULTS

2.4.1 Development towards equilibrium

The initial bathymetry was subjected to constant tidal and wave forcing. The profile development starts first by a ridge formation near the channel which gradually grows horizontally landward and accretes vertically (Figure 2.5). The morphological development is rapid at the beginning but slows down over time. Morphological changes after a long time period (>200 years) are negligible. A 400 year simulation period was chosen to ensure equilibrium is achieved in all sensitivity simulations.

The initial bathymetry does not impact the equilibrium profile, but it affects the timescale at which equilibrium is achieved. The equilibrium bathymetry is slightly asymmetric along the y-axis due to a tide-residual, counter-clockwise wake flow on the shoal generated by the tide propagating from north to south. Also, higher flood velocities in the channel at the north lead to slightly higher SSC (sediment supply) during flood tide compared to southern locations. Since bed-level variations across the flat width are limited, all the cross-sectional plots and profiles presented throughout this research (e.g., Figure 2.5b) are a width-average of the 2D model. The small bed-level irregularity at the landward most location is due to the assumption of a closed boundary which blocks the wave energy propagation leading to an abrupt drop in the wave group velocity and a local, small increase in wave height at the last cell (see Figure 2.6).

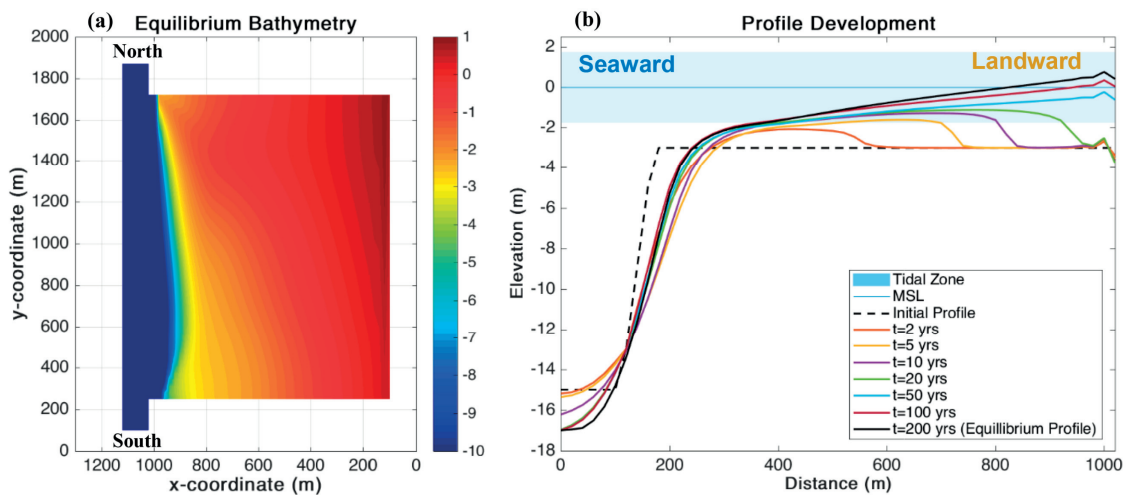


Figure 2.5. Modeled (a) equilibrium bathymetry after 200 years and (b) cross-sectionally averaged bed-level profile showing the profile evolution over time towards an equilibrium state.

2.4.2 Intratidal dynamics

We inspected the profile development during a tidal cycle (TCini) at an early stage of the simulation when the profile development is rapid. A MF of 200 is used to make bed-level changes more visible. TCini starts and ends at high water (Figure 2.6). The tidal wave is an almost standing wave. The phase lag between water levels and velocities is about 1 hour while the lag is about 0.5 hours longer on the shoal than in the channel.

The initial profile shows a ridge located at the shoal seaward side. In the vicinity of low water ($t = 6$ hr, Figures 2.6g and 2.6h), the shallow water depth over the ridge leads to high wave orbital velocities and wave energy dissipation due to bottom friction and breaking. The high wave-induced shear stress causes resuspension and creates a local SSC peak which combined with the flow drives suspended sediment transport. A landward directed suspended transport occurs at the landward section of the ridge which is slightly enhanced by a cross-shore wave-induced current. Whereas, a seaward directed transport occurs at the seaward shoal/ridge edge. In addition to the flow-induced transport, there is a wave-induced suspended transport component (included in Figure 2.6 within the bed load as described in Appendix 1.3.1) due to wave asymmetry effects. This component acts along the direction of the wave attack (landward). Both mechanisms cause erosion of the ridge top. A portion of this sediment is transported from the shoal towards the channel while the rest is redistributed landward resulting in the landward ridge growth.

As the water level rises and during maximum flood ($t = 10$ hr), the high flow velocities elevate the SSC in the channel which results in landward suspended sediment transport from the channel towards the ridge (Figures 2.6k and 2.6l). This mechanism causes deposition on top of the ridge which restores the previously eroded sediment and increases the ridge elevation slightly.

The sediment balance of the shoal can be simplified as tide-induced sediment input from the channel to the shoal edge counteracted by wave-induced erosion. During the initial stages of the profile development, tide-induced deposition is higher than wave-induced erosion due to the low shoal profile. The net sediment input to the shoal gets redistributed landward resulting in horizontal landward ridge growth along with slight vertical accretion as seen when comparing the initial bed-level profile (dotted black) to the profile at the end of the tidal cycle (solid black) in Figures 2.6m and 2.6n. This cycle repeats and the ridge continues to move landward and increase in height. The horizontal landward ridge motion is rapid at the beginning of the evolution and slows down notably with time (Figure 2.5b) because sediment supplied from the channel needs to be transported over a longer distance. After the ridge reaches the landward boundary, the net landward transport accretes the profile which continues until a linear tidally averaged steady-state profile develops. Similar to the horizontal ridge growth, the vertical accretion rate decreases with time.

2. Morphodynamic Evolution of a Fringing Sandy Shoal From Tidal Levees to Sea Level Rise

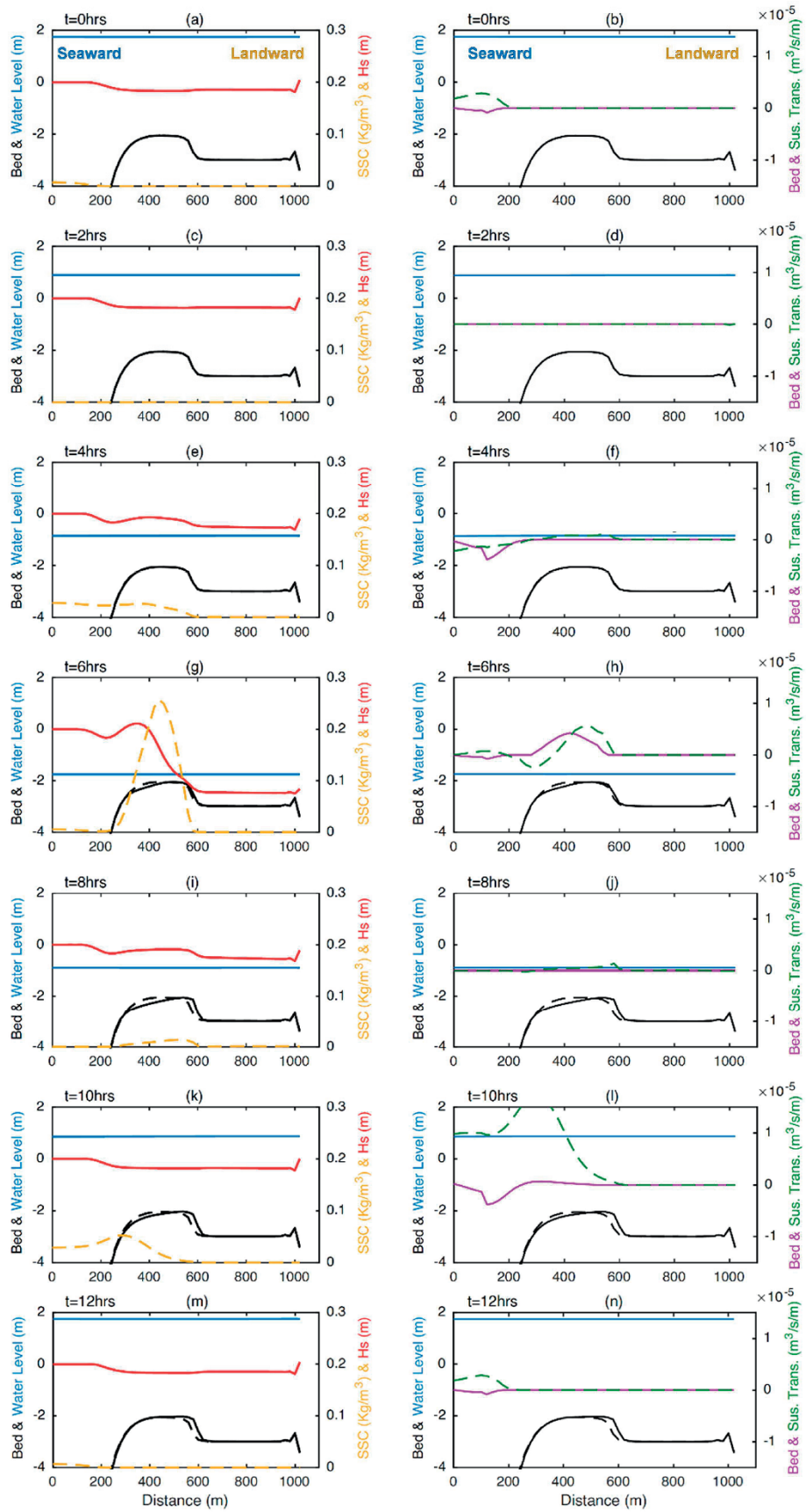


Figure 2.6. Cross-sectional profile showing the initial ($t = 0$ hr, dashed black) and time-varying (black) bed-level, water level (blue), H_s (red), SSC (yellow), bed (magenta) and suspended (green) transport during tidal cycle TCini. Positive and negative transport are landward and seaward directed, respectively.

With the increase in profile elevation, the wave-induced shear stress increases resulting in higher wave-induced erosion. An equilibrium shoal profile is achieved when the tide-induced sediment supply from the channel to the shoal edge is balanced by a seaward sediment transport by wave-induced erosion. Figure 2.7a shows the tidally averaged flow ($\bar{\tau}_c$), wave ($\bar{\tau}_w$), and maximum ($\bar{\tau}_{max}$) shear stresses for tidal cycle TCini (At an early development stage), and TCeq (At equilibrium). The shear stress distribution for TCeq shows good resemblance with observations and modeling results presented by Maan et al. (2018) for a similar fringed shoal setting in the WS.

There is a limited difference in $\bar{\tau}_c$ between TCini and TCeq, while $\bar{\tau}_w$ and $\bar{\tau}_{max}$ increase notably over the equilibrium profile (Figure 2.7a) due to a higher elevation profile. For TCeq, the high $\bar{\tau}_{max}$ at the seaward shoal edge ($x \approx 200-400$ m) is due to both high $\bar{\tau}_c$ and $\bar{\tau}_w$. Flow velocities are higher than landward locations, also it is subjected to wave attack for a long period within the tidal cycle. Figure 2.7b shows the time-varying τ_w during tidal cycle TCeq. Wave shoaling occurs across the shoal which creates a positive landward τ_w gradient with a peak near the landward extent of the wet section followed by a sudden drop if wave breaking occurs. At low water ($t = 6$ hr), wave influence is confined to the shoal edge causing a high narrow local peak.

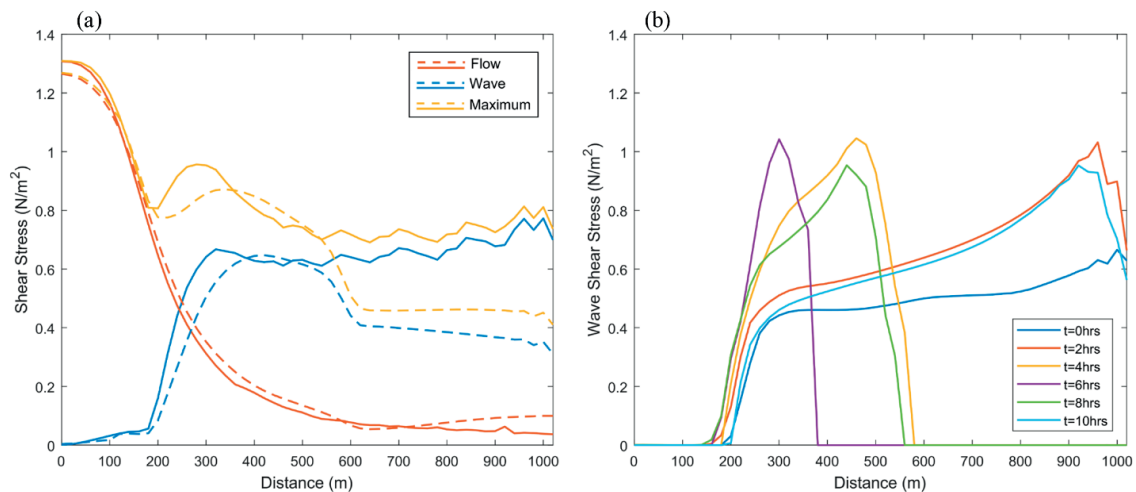


Figure 2.7. Modeled (a) flow ($\bar{\tau}_c$), wave ($\bar{\tau}_w$), and maximum ($\bar{\tau}_{max}$) tidally averaged shear stresses for tidal cycle TCini (dotted) and TCeq (Straight), and (b) wave-induced shear stress (τ_w) during tidal cycle TCeq. Note: For simplicity purposes, τ_w is roughly estimated by the difference between τ_{max} and τ_c .

2.4.3 Sensitivity analysis

A sensitivity analysis was performed using different forcing conditions (Figure 2.8) and model parameters (Figure 2.13; Appendix 1). Please refer to Table 2.1 in Appendix 1 for a full list of sensitivity runs. Exclusion of waves limits the suspension of sediments deposited at the shoal edge leading to the development of a pronounced high ridge (Figure 2.8a) and limited landward transport. A higher H_s steepens the profile with lower bed levels at the seaward shoal edge (Figure 2.8a). The H_s increase results in an increase in τ_w causing higher SSC over the developing ridge and more ridge top erosion along with higher transport rates. The landward section gets shallower due to larger landward sediment transport while higher τ_w at the shoal edge lowers its elevation. Also, the profile reaches equilibrium faster than that for milder wave conditions.

As the wave period (T_p) increases the profile gets steeper (Figure 2.8b). However, unlike the H_s increase, this increase is only due to higher bed levels at the landward edge while the seaward edge remains relatively constant. The reason is that the increase in T_p contributes to an enhanced wave asymmetry effect inducing landward suspended transport. However, it does not significantly impact τ_w on the developing ridge. Also, a larger T_p results in faster profile development.

The base-case applied a tidal range (dH) of 3.5 m to simulate a meso-tidal environment. Changing the tidal range alters the tidal velocities and the equilibrium concentrations at the boundary. Increasing dH shows a corresponding increase in the equilibrium profile elevation and a milder profile slope (Figure 2.8b). Larger dH results in higher channel flow velocities hence elevated channel SSC and a corresponding enhanced sediment supply towards the shoal.

Implementing finer ($125 \mu m$) and coarser ($175 \mu m$) sand fractions than the base-case ($D_{50}=150 \mu m$), showed that coarser fractions result in steeper equilibrium profiles with a shallower landward shoal edge (Figure 2.8c) which provides a good agreement with observed trends in beaches.

In most sandy estuaries, fine mud fractions are present along sand in sheltered low-energy areas (e.g., Houser & Hill, 2010). We thus also explored the impact of a sand-mud mixture by starting from an initial sandy bed ($D_{50}=150 \mu m$) and adding a relatively low mud concentration (25 mg/L) at the boundary. The Partheniades Krone formulations (Partheniades, 1965; see Appendix 1.3.2.) are used for mud transport, with a critical erosion shear stress ($\tau_{c,e}$) of 0.2 N/m^2 , an erosion parameter (M) of 2.5×10^{-4} , and a settling velocity (w_s) of 0.25 mm/s . For simplicity purposes, we do not account for sand-mud interactions. Figure 2.8c shows that the mixture equilibrium profile is steeper due to higher elevations at the landward edge. The relatively calm hydrodynamic conditions at the landward locations enhance mud deposition resulting in a muddier shoal than that at seaward locations. Also, the mixture profile reaches equilibrium faster than the base-case

sand profile. This trend provides good agreement with previous studies (Maan et al., 2018; van der Wegen et al., 2016, 2019). In our model, this is attributed to the combined effect of a larger sediment supply and, more importantly, to the ability of mud fractions to remain in suspension for a longer time than sand so that landward locations are reached faster.

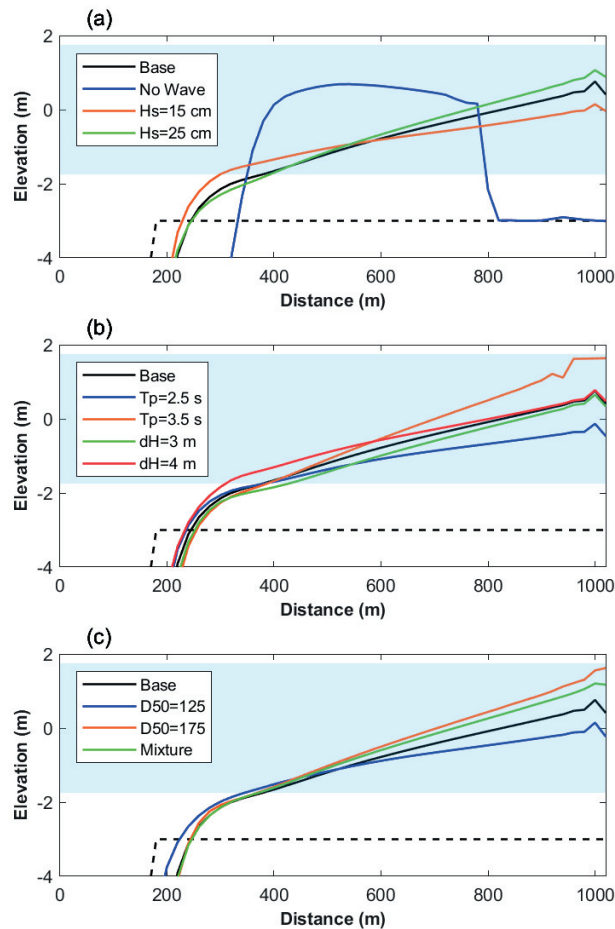


Figure 2.8. Sensitivity analysis showing the equilibrium profiles corresponding to different forcing conditions. The light blue shading indicates the base-case tidal difference, and the dashed black line indicates the initial profile.

2.5 FORCING VARIATIONS

The equilibrium profiles presented in section (2.4) develop under constant forcing. However, in nature, external forcing conditions can vary continuously on a short (e.g., wind-waves) or long-term basis (e.g., SLR) which leaves the morphology out of

equilibrium. In this section, we inspect the morphological response of the base-case equilibrium profile to forcing variations.

2.5.1 Wave conditions

The base-case equilibrium profile was subjected to an increase and a decrease in wave height for 6 morphological months. Figure 2.9 shows that an increase in H_s results in a steeper profile with erosion at the seaward edge along with slight deposition at the landward limit. In contrast, the profile at the shoal seaward edge accretes in response to a decreased wave height, forming a small tidal levee with negligible bed-level changes more landward. The profile is in the process of adjusting towards a new equilibrium state with a milder slope and higher bed levels at the seaward shoal edge. In case of high elevation levees, drainage channels dissecting the levee start forming. Profile recovery after restoring the original forcing took somewhat longer than the perturbation duration.

The profile response to 12 hr (MF=1) stormy wave conditions ($H_s \geq 1$ m, and $T_p=6$ s) was similar to the response to the increased wave action but with a higher magnitude. Notable erosion occurred at the seaward shoal edge. The largest portion of the eroded sediment was transported seaward out of the model domain while a smaller portion got deposited landward on the shoal. Following the storm, the profile starts recovering rapidly. The largest part recovers within ≈ 2 years after the storm, although some small differences from the original equilibrium profile remain after 10 years. Please refer to Figure 2.14 (Appendix 1) for the impact of stormy conditions and recovery.

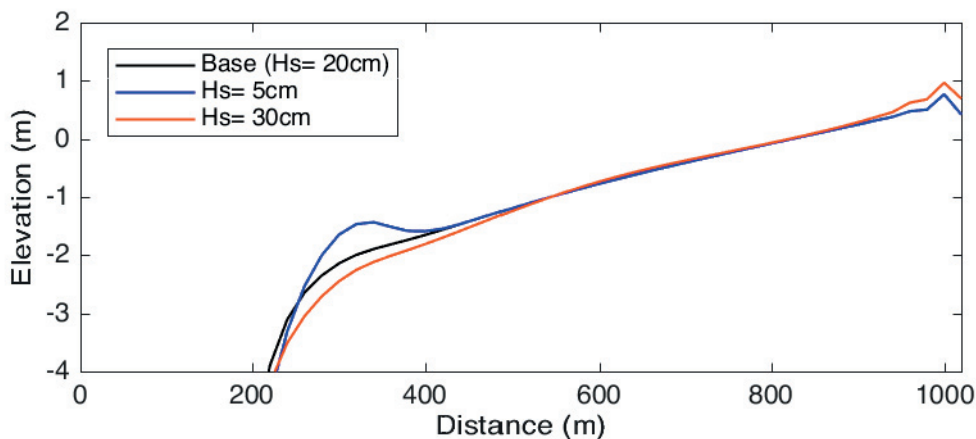


Figure 2.9. Cross-sectional bed-level profile after 6 morphological month wave forcing change.

2.5.2 Sea level rise

We imposed SLR on the equilibrium profile for 100 years with Year 2000 as a starting point. The rise was prescribed as an increase in the mean sea level (MSL) based on a sinusoidal function and as a linear rise. Following that, we assume an abrupt stop of SLR for the following 200 years (2100-2300). This assumption allows for investigating the recovery from SLR.

When the sea level rises based on a sinusoidal function (rising from the minimum to the intercept) during the first 100 years, the profile accretes in response (Figure 2.10). The larger water depth decreases the wave-induced shear stress allowing the profile to heighten. The accretion is largest near the channel and gradually extends landward. Due to inertial effects, a phase lag (decades) exists between SLR and the bed-level response. This lag increases over time with the increasing SLR rate. The lag is smallest near the channel and increases landward leading to a milder profile slope. Similar to tidal levee formation (section 2.5.1), the disturbance propagates from the shoal edge towards the landward limit.

Extending the simulations for 200 years with constant MSL showed a continued profile accretion till the profile reaches a new equilibrium state approximately equal to the old equilibrium profile plus the SLR magnitude. The recovery can range from decades to centuries based on the system's forcing conditions and the shoal dimensions. Seaward locations recover faster than landward locations. By 2300, the accretion was spatially uniform and the profile restored its initial 2000 slope. However, the profile remained about 3 cm deeper compared to MSL. A probable explanation is that the channel was maintained at the original depth so that tidal velocities decreased in a deeper channel leading to lower prevailing SSC at the channel edge.

Figures 2.11a and 2.11b show that for all simulations, by 2100, SLR resulted in a loss of intertidal area along with increased inundation (ratio between inundation duration and tidal period). Depending on the wave forcing, the intertidal area decline ranged from about 7 to 60%, and the inundation increased by about 8 to 15%. The initial profile at Year 2000 played an important role in determining the intertidal area resilience. The higher the initial elevation and the lower initial inundation, the less the intertidal area decrease was. A 14% increase to the initially high inundation ($\approx 74\%$) of $H_s=0.1$ m resulted in a notably larger intertidal area loss compared to a 10% increase to the initially lower inundation ($\approx 57.5\%$) of the base-case ($H_s=0.2$ m). Simulations with higher wave action experienced less intertidal area loss. The higher wave energy leads to an increase in sediment resuspension and transport rates which accelerates SLR adaptation.

Increased SLR rate results in an increased inundation and intertidal area decline (Figures 2.11c and 2.11d). This impact is non-linear, the loss created by the 1.5 m scenario is not triple that for the 0.5 m. In reality, this non-linearity is expected to be more pronounced

due to large-scale changes such as sediment supply, salinity, tidal prism, and tidal asymmetry.

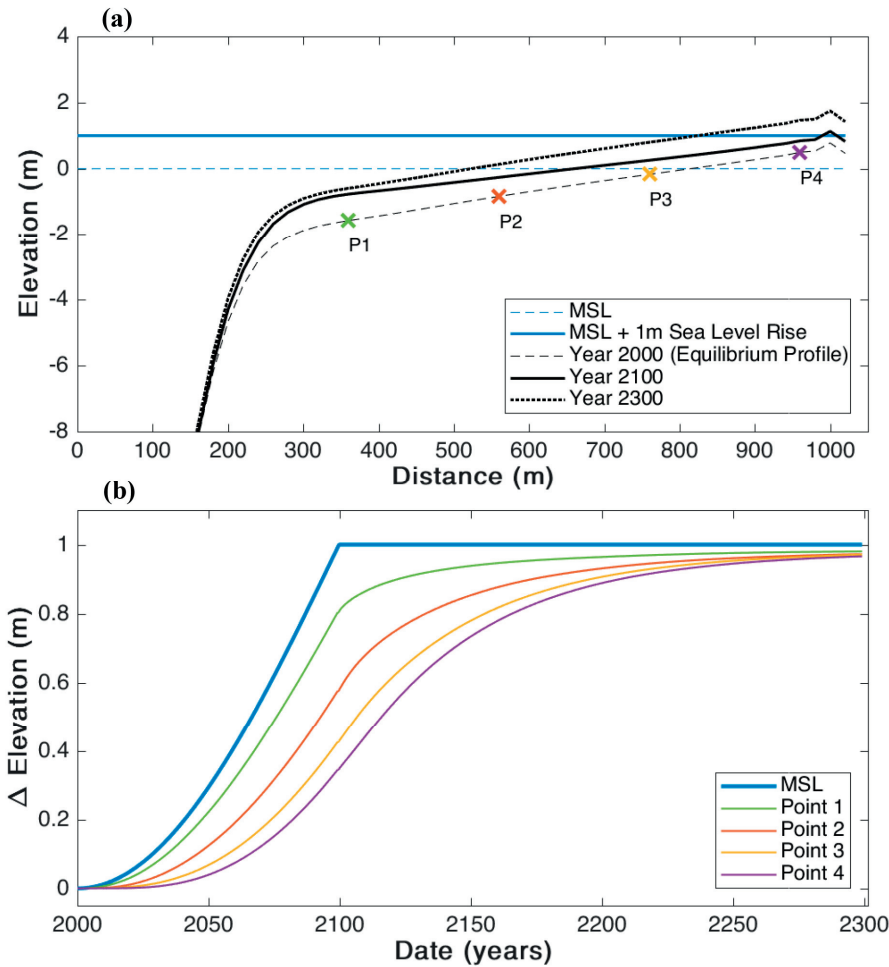


Figure 2.10. Top panel shows the forecasted bed levels at Years 2100 and 2300 under 1m SLR scenario starting from the 2000 equilibrium profile and 0 m MSL. The bottom panel tracks the SLR and bed-level changes over time at 4 points on the shoal.

We implemented a linear rise of a constant 10 mm/year (Figures 2.12a and 2.12b) leading to a rise in MSL after 100 years equal to the sinusoidal SLR. The reason to explore this is that SLR at the Dutch coast has been linear to date and no SLR rate increase has been observed (Vermeersen et al., 2018). This may be an exceptional but temporal trend due to specific local (North-Western Europe) conditions of SLR dynamics.

The linear 2100 profile experienced larger accretion at all points compared to the sinusoidal rise, with the difference increasing going landward. This resulted in a steeper profile along with a slight decrease in intertidal area loss and inundation. The accretion is also largest near the channel edge and follows, with increasing lag, the SLR. Fastest adaptation was at locations closer to the channel edge. After 100 years, the accretion rates

at all locations are approximately similar, suggesting that the profile shape developed by then does not notably change. However, the 2100 rate (about 8.5 mm/year) is somewhat smaller than the SLR rate (10 mm/year). Extending the linear SLR towards 2200 (see Figure 2.15; Appendix 1), showed that by 2200, the rates at all points approximately match the SLR rate. This suggests that the profile reached a new deeper, milder slope, equilibrium state that follows SLR at the same rate with a constant “overdepth”.

We also imposed a sinusoidal SLR to the sand-mud mixture equilibrium profile presented in Figure 2.8c. The mixture simulation showed larger accretion in response to SLR, especially at landward locations (Figures 2.12c and 2.12d). The seaward most point (P1) experienced negligible differences as high shear stresses at seaward locations limit mud deposition. Mud fractions are able to remain in suspension for a longer period and reach calm landward locations faster than sand. This suggests that sandy-mud shoals are more resilient against SLR but will become muddier in case of SLR.

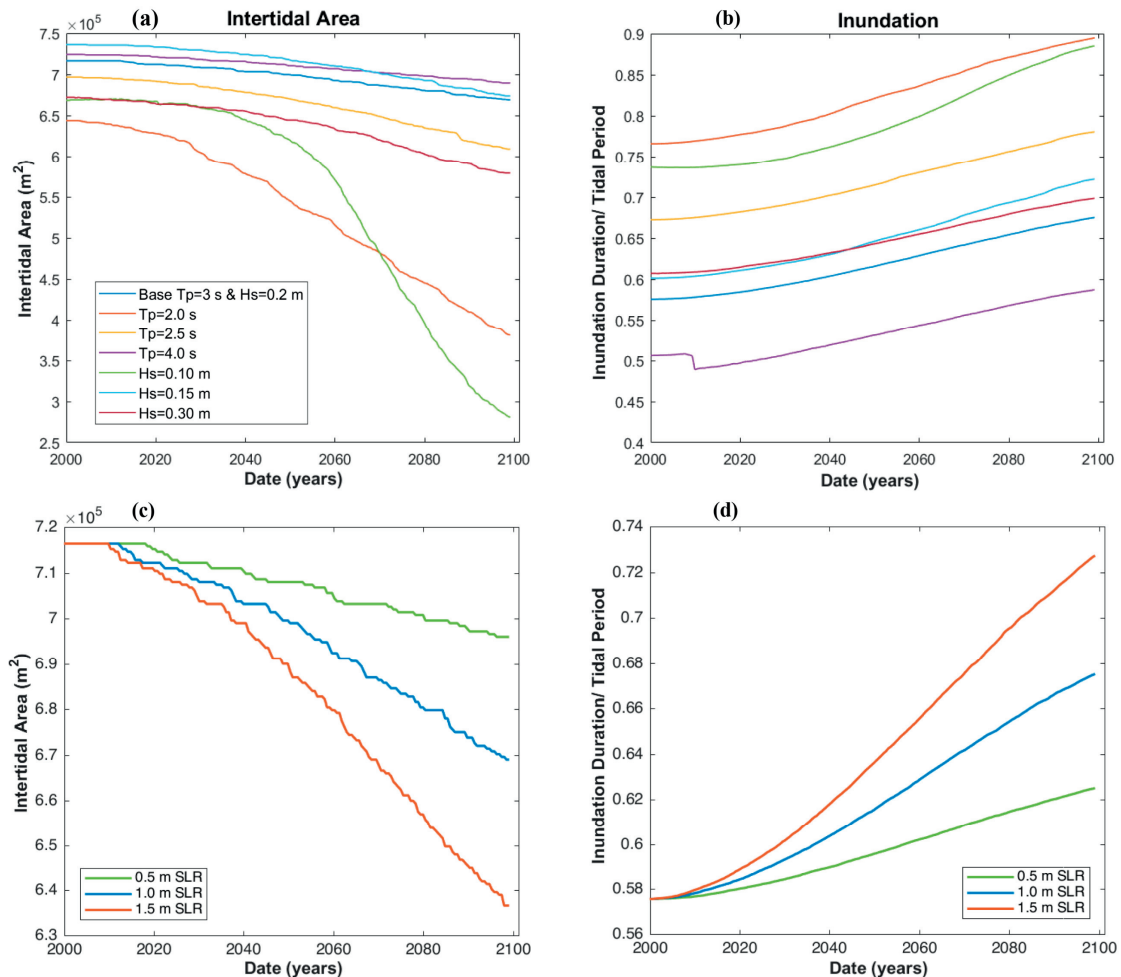


Figure 2.11. Modeled development of intertidal area (m^2) and its inundation over time for (a, and b) different forcing conditions, and (c, and d) different SLR scenarios.

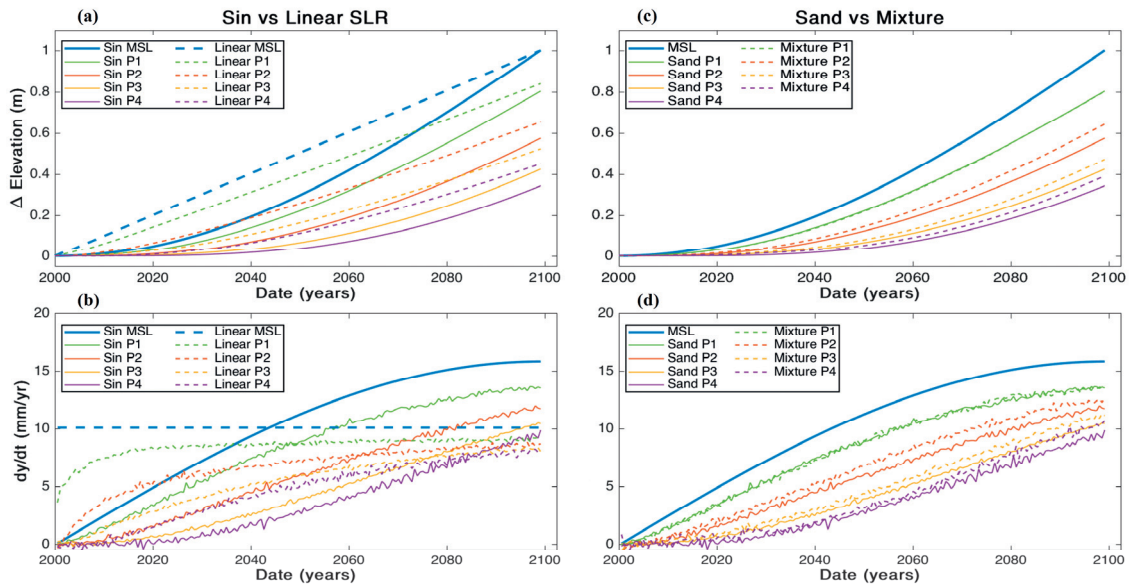


Figure 2.12. The top panels show SLR and bed-level changes at 4 points on the shoal (see Figure 2.10). The bottom panels show the rates.

2.6 DISCUSSION

2.6.1 Observed and Modeled trends

Monitoring techniques of intertidal shoals have notably improved in recent years. However, it is still hard to find a long-term data set of bed-level changes, waves, and currents with a high spatial and temporal resolution. This limits the possibility of performing a quantitative comparison between long-term model results and observations. In this section, we discuss our modeling approach and results in relation to the literature (section 2.1) and limited observations (section 2.2).

2.6.1.1 Shoal dynamics

Shoals evolve over time towards a state of decreased morphological activity (e.g., Friedrichs, 2011; Maan et al., 2015, 2018). However, they tend to maintain a short-term, dynamic nature which can be mainly correlated to wind-wave activity. During calm conditions, shoals experience a net landward transport leading to shoal accretion while during high wave conditions, a net seaward transport exists leading to shoal erosion (e.g., Allen & Duffy, 1998; Janssen-Stelder, 2000; H. Ridderinkhof et al., 2000; Wang et al., 2018). The seaward shoal section experiences more bed dynamics than landward locations (de Vet, 2020; e.g., Geomor team, 1984; Houser & Hill, 2010; Kohsiek et al., 1988).

Our modeling approach is based on the morphological equilibrium concept. Similar to previous modeling studies (Maan et al., 2018; Roberts et al., 2000; van der Wegen et al., 2019; van der Wegen, Jaffe, et al., 2017), the shoal evolves over time towards a state of reduced tide-residual sediment transport maintained by a balance between sediment supply, tidal forcing, and wave action. This state might imply the loss of shoal dynamics. However, the system dynamics are still maintained on the intratidal timescale. Despite being in an equilibrium state, the profile experiences intratidal bed-level changes which are largest at the shoal seaward edge ($x \approx 200\text{-}400$ m; Figure 2.6). The higher maximum shear stresses at this area (Figure 2.7a) enhance resuspension and make it more dynamic compared to landward locations.

The shoal dynamics are also reflected in the modeled morphological response to forcing variations. Changes in equilibrium forcing impact the sediment balance leading to shoal evolution. A morphological disturbance starts at the shoal edge and propagates landward with time. Over the short timescale (days to month), the disturbance is somehow limited to the shoal seaward section. A long-term (century) forcing change such as SLR has a larger spatial-scale (whole shoal) impact with higher accretion again at seaward locations. Restoration of original forcing showed the profile recovery with associated timescales. Shoals are thus quite resilient systems that are able to adapt to and are not fundamentally changed by forcing variations.

Observations confirm this resilient nature, Geomor team (1984; Figure 2.1) shows that during a monitoring year, the Galgeplaat experienced both periods of erosion and deposition with a relatively small net effect. Variations in the wind-wave climate were the main driver for the bed-level changes which were highest at the shoal seaward section. De Vet (2020) and Zhu et al. (2017) show that, in most instances, intertidal flats were able to recover from storm events. Van der Wegen et al. (2019) highlight that this resilience also holds for mudflats in response to seasonal forcing changes. Similar to the Galgeplaat, the largest morphological activity occurred at the mudflat edge and channel slope while it notably decreased towards the landward section.

2.6.1.2 Tidal Levees

In nature, shoals usually appear to be quite stable in the sense that, over some characteristic period of natural forcing, they do not experience notable morphological changes that fundamentally alter their structure. However, we do not expect that shoals reach an equilibrium state in the strict sense due to the continuous forcing changes which operate at multiple timescales and the inertia involved in the profile adaptation (Z. Zhou et al., 2017).

A close investigation of measured intertidal shoal profiles and satellite imagery over the short timescale (years) in the WS (e.g., Figure 2.2; Cleveringa, 2013) and Wadden Sea (e.g., Figure 2.3) showed tidal levee formations at the shoal seaward edge (channel-shoal

interface). Such features have different spatial scales (dimensions) and relatively dynamic nature (short-lived features). They exist on different profile shapes, while some profiles do not show such formations.

We hypothesized that their evolution is an essential part of the shoal evolution. Model results show that sustained durations of forcing conditions favoring deposition (e.g. drop of wave action) resulted in a net landward transport causing levee formation at the profile seaward edge. On the other hand, an increase in wave action resulted in a net seaward transport causing the destruction of such features along with shoal edge erosion.

Clear examples of tidal levees have been observed in the Dutch Wadden Sea during spring tides under extremely calm wave conditions. Observations show that they usually exist on a small scale (width <50 m). Our work suggests that their spatial scale is related to the duration and magnitude of the forcing enhancing shoal edge deposition. Their evolution occurs over multiple tidal cycles and only in extreme situations (limited wave action for days), they grow to extents which can be visually identified. In reality, the regular alternation between forcing inducing deposition and erosion (e.g., Geomor team, 1984) could limit their growth to visible extents. A continuously varying wave climate in nature could be the reason for levees being short-lived dynamic features and that we do not see them in most profiles. Cross-sections A7 and A8 (Figure 2.3) are located on a shoal that resembles our modeling configuration. Despite no visible levees being identified at the two survey moments, both cross-sections showed bed-level changes with the highest changes being at the shoal seaward section.

More long-term high-resolution data is needed to further validate the co-relation between levees and wind-wave activity. The existence of such features could also be due to other forcing variations such as sediment supply or tidal range (e.g., spring/neap tides). Our work suggests that tidal levees are essential for explaining the shoal evolution since the processes leading to their formation/destruction represent the sediment balance at the shoal seaward edge. The reproduction of such features can be a good indication of the model's ability to capture the channel-shoal dynamics. These relatively short timescale dynamics are highly relevant for investigating the morphological impact of long-term forcing changes such as SLR.

2.6.2 Sea level rise

We assumed equilibrium concentrations at the model boundaries which are maintained during SLR. However, in real scenarios, this may not be the case. Sediment needs to be available for import at the offshore boundary. The morphological response of other estuarine elements (e.g., channels or ebb-tidal delta) to SLR may lead to a change in prevailing SSC and sediment redistribution within the system which would eventually impact the sediment supply towards the shoals and limit the shoal accretion.

ASMITA is an example of a model that explicitly addresses these dynamics in an aggregated manner. The grid resolution covers entire entities such as the ebb-tidal delta, the basin's channel, and the basin's intertidal flats represented as volumes. An important assumption of this model is that equilibrium occurs when uniform concentrations exist within the system. Morphodynamic adaptation due to a forcing change (e.g., SLR) follows empirical equations that describe the sediment demand and availability along with the transport capacity for the different morphological elements. A new dynamic equilibrium state is reached when uniform concentrations are restored.

Our approach explicitly defines detailed processes while ASMITA is based on empirical equilibrium concepts, which makes it more straightforward and faster to use. Wave impact and intra-tidal dynamics are implicitly reflected by calibration coefficients. Both approaches aim to reduce tide-residual sediment transport gradients by morphodynamic adaptations. In that sense, they should lead to the same results. Here we qualitatively compare our approach and model results to ASMITA.

Van Goor et al. (2003) explored SLR adaptation of tidal basins including intertidal area. Their work suggests that a linear SLR will lead to a deeper profile that follows SLR at the same rate. Our model reproduces this “overdepth” (see Figures 2.12b and 2.15) as well. We found that the adaptation timescale required to create the constant “overdepth” profile is long (about 200 years for a 800 m profile when an abrupt linear SLR of 100 cm/century is imposed). Also, we show that the “overdepth” value varies across the profile because the profile slope becomes milder under SLR. ASMITA confirms these results showing the inertia of entire estuarine systems adapting to a change in linear SLR rate from 11 to 56 cm/century within 200-400 years depending on the system's size and the element under consideration. Both approaches show that SLR adaptation timescale may be long (~ centuries). It is plausible that the “overdepth” has been reached for the Dutch conditions of more than a millennia of relatively constant linear SLR (Vermeersen et al., 2018). However, a future increase in the SLR rate can still pose a notable threat to the intertidal area.

Both our work and Van Goor et al. (2003) suggest the existence of a state at which SLR is too fast to have a stable “overdepth”. In our model, this state occurs when the SLR-induced disturbances at the shoal edge (“levees”) don't reach the landward shoal section and the flat disintegrates. Van Goor et al. (2003) highlights that this drowning state comprises high uncertainties as it highly depends on parameters defining the adaptation timescale. ASMITA describes the detailed transport and adaptation processes described in this paper (intratidally varying wave action and sediment concentration along the profile, changing profile shape) by tuning parameters such as a diffusion coefficient and fall velocity. These parameters do not represent actual physical values but merely reflect representative processes. There is insufficient long-term field data to improve the

parameters estimates. Future studies may focus on quantifying these parameters by our process-based approach.

2.6.3 Future Research

There is value in gradually increasing the model complexity by incorporating more processes such as 3D processes, multiple sand fractions, and more detailed implementation of cohesive fractions including sand-mud interactions. A real case study implementation can provide validation of the research findings and a better connection to reality. This requires the acquisition of high temporal and spatial resolution long-term data with the focus on the channel-shoal dynamics.

Extending the study towards a large scale incorporating a part of or a whole estuary configuration is the next step. This extension would allow for investigating SLR impact on the different estuarine morphological elements along with their interactions and the impact of sediment supply. Also, it would enable exploring a variety of geometric shoal configurations such as a free shoal.

2.7 CONCLUSIONS

This study explores the mechanisms that drive the long-term morphological evolution of estuarine intertidal sandy shoals across a range of timescales. We developed a Delft3D, 2DH high-resolution, process-based model to simulate the morphological evolution of a channel-fringing shoal system inspired by conditions in the WS.

Observations and modeling studies in literature suggest that shoals aim to evolve towards a stable morphodynamic state maintained by a balance between sediment supply, wave action, and tidal forcing. Short-term morphological variations around the equilibrium occur in response to natural forcing variations such as wind-wave activity.

We investigated a shoal in morphodynamic equilibrium and its response to both short-term (wave action) and long-term (SLR) forcing changes. These disturbances result in a morphological adaptation that first impacts the shoal edge and gradually propagates landward. The area near the channel-shoal interface experiences the largest morphological adaptation. Tidal levees develop/erode at the shoal edge when wave action decreases/increases. The levees resemble observed features in estuaries (e.g., Western Scheldt) and tidal basins (e.g., Wadden Sea). A continuously varying wind-wave climate in nature can be the reason why they are dynamic and often short-lived features that are hard to capture in bathymetric surveys. Our work suggests that tidal levees are an essential part of the shoal evolution since their governing processes represent the sediment balance at the shoal edge. Such features should be taken into account when exploring the morphological response of shoals to long-term forcing variations such as SLR.

SLR has a long-term (~ centuries), and a larger spatial-scale impact. The whole shoal accretes in response to SLR mainly due to the drop of wave-induced shear stress. However, accretion rates are less than the SLR rate due to inertia-induced phase lag (decades) between the bed-level response and SLR which is at its highest at the landward edge and at its lowest near the channel. Natural recovery from 100 years of SLR can range from decades to centuries depending on estuarine forcing conditions. Assuming the continuation of the current observed linear SLR showed larger accretion rates and a decreased lag compared to a sinusoidal rise, especially at landward locations. Accretion rates increased with time and reached the SLR rate after ≈ 200 years, suggesting that the profile reached a new deeper, milder slope, equilibrium state that follows SLR at the same rate with a temporally constant “overdepth”. Incorporating mud fractions, showed that shoals in a muddy environment could be more resilient against SLR. The mixture profile exhibited larger profile accretion due to increased mud deposition which made the shoal slightly muddier.

Shoals are quite resilient features in the sense that they are able to adapt to forcing changes without fundamentally changing their structure. However, a long (decades) lag is involved in the profile adaptation to SLR. In all SLR simulations, shoals experience a drop in intertidal area and increased inundation. In real scenarios, a possible shortage of sediment supply to shoals could amplify this effect. This raises questions about possible mitigation and adaptation measures to ensure the sustainability of the valuable intertidal environment.

APPENDIX 1

The appendix aims to provide a brief description of the numerical model used in this study including formulations and relevant parameters. Also, we present supplementary figures.

A.1.1 Hydrodynamics

We apply the Delft3D (D3D) process-based numerical model (Deltares, 2017; Lesser et al., 2004). Delft3D-FLOW computes the flow by solving the unsteady two-dimensional shallow water equations (Continuity and Momentum) at a high spatial (20×30 m) and temporal (12 sec) resolution. The continuity equation (Eq. A.1.1) and the horizontal momentum equations (Eq. A.1.2, and A.1.3), neglecting the influence of density differences, Coriolis force, and wind are as follows:

$$\frac{\partial \eta}{\partial t} + \frac{\partial hu}{\partial x} + \frac{\partial hv}{\partial y} = 0 \quad (\text{A.1.1})$$

$$\frac{\partial u}{\partial t} + u \frac{\partial u}{\partial x} + v \frac{\partial u}{\partial y} + g \frac{\partial \eta}{\partial x} + c_f \frac{u\sqrt{u^2 + v^2}}{h} - \nu_e \left(\frac{\partial^2 u}{\partial x^2} + \frac{\partial^2 u}{\partial y^2} \right) - F_x = 0 \quad (\text{A.1.2})$$

$$\frac{\partial v}{\partial t} + v \frac{\partial v}{\partial y} + u \frac{\partial v}{\partial x} + g \frac{\partial \eta}{\partial y} + c_f \frac{v\sqrt{u^2 + v^2}}{h} - \nu_e \left(\frac{\partial^2 v}{\partial x^2} + \frac{\partial^2 v}{\partial y^2} \right) - F_y = 0 \quad (\text{A.1.3})$$

With,

$$c_f = \frac{g}{c^2} \quad (\text{A.1.4})$$

Where, η is the water level with respect to datum, h is the water depth, u and v are the horizontal depth-averaged velocities in the x and y directions, respectively, g is the gravitational acceleration, c_f is the friction coefficient, c is the Chezy coefficient (60 m^{1/2}/s), ν_e is the eddy viscosity (1 m²/s), and F_x and F_y are the depth-averaged wave-induced forcing.

A.1.2 Roller Model

Modeled waves propagate from the seaward channel boundary towards the shoal. Wave action across the model domain is simulated by the “roller model” (Deltares, 2017, appendix B.15; D. Roelvink et al., 2009; J. A. Roelvink, 1993) which is coupled with Delft3D-FLOW through online coupling that includes wave-current interactions. Application of the roller model is possible in case the wave spectrum is narrow-banded with respect to frequency and direction (Deltares, 2017; van der Wegen, Jaffe, et al., 2017). The roller model computes the wave-energy propagation and dissipation, from which the wave height (H_s) can be derived. It incorporates a balance equation for the short wave energy and another for the roller energy. The short wave energy (E_w) is defined as:

$$E_w = \frac{1}{8} \rho_w g H_{rms}^2 \quad (\text{A.1.5})$$

Where, ρ_w is the water density, and H_{rms} is the root-mean-square wave height. Wave friction and breaking are the two dissipation mechanisms in the short wave energy balance equation which can be written in the stationary form as follows:

$$\frac{\partial}{\partial x}(E_w C_g \cos(\theta)) + \frac{\partial}{\partial y}(E_w C_g \sin(\theta)) = -D_w - D_f \quad (\text{A.1.6})$$

Where, C_g is the group wave velocity, and θ is the shore normal wave angle. D_f and D_w are the wave energy dissipation due to bottom friction (Eq. A.1.7) and wave breaking (Eq. A.1.8), respectively.

$$D_f = f_w \frac{\rho_w}{\sqrt{\pi}} u_{orb}^3 \quad (\text{A.1.7})$$

$$D_w = \frac{1}{4} \alpha_{rol} \rho_w g f_p \exp\left(-\frac{H_{max}^2}{H_{rms}^2}\right) (H_{max}^2 + H_{rms}^2) \quad (\text{A.1.8})$$

$$H_{max} = \frac{0.88}{k} \tanh\left(\frac{\gamma_w}{0.88} k h_{ref}\right) \quad (\text{A.1.9})$$

Where, f_w is a user defined bottom friction factor (0.01), u_{orb} is the orbital velocity based on the linear wave theory, α_{rol} is a user-defined constant (1), H_{max} is the maximum wave height, k is the wave number, γ_w is the wave breaking index (0.75), and h_{ref} is a reference water depth. The short wave energy dissipation due to wave breaking (D_w) is the source term for the stationary balance equation of the roller energy (Eq. A.1.10) which delays the momentum release from wave breaking and results in a landward shift of wave forcing.

$$\frac{\partial}{\partial x}(2E_r C \cos(\theta)) + \frac{\partial}{\partial y}(2E_r C \sin(\theta)) = D_w - D_r \quad (\text{A.1.10})$$

$$D_r = 2\beta_{rol} g \frac{E_r}{C} \quad (\text{A.1.11})$$

Where, E_r is the roller energy, C is the wave celerity, D_r is the roller energy dissipation, and β_{rol} is the slope of the wave front (0.1). The spatially and temporary varying wave energy (E_w) and roller energy (E_r) cause a variation in the depth-averaged radiation stresses, through the following equations:

$$S_{xx} = \left(\frac{C_g}{C}(1 + \cos^2(\theta)) - \frac{1}{2}\right) E_w + 2\cos^2(\theta) E_r \quad (\text{A.1.12})$$

$$S_{xy} = S_{yx} = \sin(\theta)\cos(\theta) \left(\frac{C_g}{C} E_w + 2E_r\right) \quad (\text{A.1.13})$$

$$S_{yy} = \left(\frac{C_g}{C}(1 + \sin^2(\theta)) - \frac{1}{2}\right) E_w + 2\sin^2(\theta) E_r \quad (\text{A.1.14})$$

The depth-averaged wave-induced forcing (F_x , and F_y) are given by the gradients of the radiation stress tensor (S) as follows:

$$F_x = -\frac{\partial S_{xx}}{\partial x} - \frac{\partial S_{yx}}{\partial y} \quad (\text{A.1.15})$$

$$F_y = -\frac{\partial S_{xy}}{\partial x} - \frac{\partial S_{yy}}{\partial y} \quad (\text{A.1.16})$$

A.1.3 Sediment transport

A.1.3.1 Sand transport

Suspended sediment transport is calculated in the D3D by an advection-diffusion solver (Eq A.1.17) which includes a sink and source term and is based on the local and time-varying velocities and water levels.

$$\frac{\partial hc}{\partial t} + \frac{\partial huc}{\partial x} + \frac{\partial hvc}{\partial y} = \frac{\partial}{\partial x} (h\varepsilon_h \frac{\partial c}{\partial x}) + \frac{\partial}{\partial y} (h\varepsilon_h \frac{\partial c}{\partial y}) + S \quad (\text{A.1.17})$$

Where c is the sediment mass concentration (kg/m^3), ε_h is the prescribed horizontal diffusivity ($5 \text{ m}^2/\text{s}$), S is the source/sink term which represents the exchange of sediment between the bed and flow (water column). The Van Rijn (1993) formulations are used to compute the sandy sediment transport for the combined effect of waves and currents for both bed load and suspended load transport. A reference height a is defined to distinguish between the bed and suspended transport as follows:

$$a = \min \left[\max \left(AKSFaC k_s, \frac{\Delta r}{2}, 0.01h \right), 0.20h \right] \quad (\text{A.1.18})$$

Where $AKSFaC$ is a user-defined proportionality factor, k_s is a user-defined effective roughness height, Δr is the wave-induced ripple height (0.025 m). The critical bed shear stress is computed mainly based on the median sediment diameter (D_{50}) and according to the classical Shields curves. A reference concentration is calculated based on the sediment availability in the top bed layer (Van Rijn et al., 2000). This concentration is imposed at the reference height in order to entrain bed sediment to the water column. The settling velocity (w_s) of sand fractions in suspension is calculated based on (Van Rijn, 1993) as follows:

$$w_s = \frac{10\nu}{D_{50}} \left(\sqrt{1 + \frac{0.01(s-1)gD_{50}}{\nu^2}} - 1 \right) \text{ for } 100\mu\text{m} < D_s \leq 1000\mu\text{m} \quad (\text{A.1.19})$$

Where s is the relative density (ρ_s / ρ_w), and ν is the water kinematic viscosity coefficient. For more details on suspended sediment entrainment and deposition computation please refer to (Deltares, 2017). The bed load is calculated according to (Van Rijn, 1993) based on the combined flow and wave as follows:

$$|S_b| = 0.006 \rho_s w_s D_{50} \frac{u_{eff} (u_{eff} - u_{cr})^{1.4}}{[(s-1)gD_{50}]^{1.2}} \quad (\text{A.1.20})$$

$$u_{eff} = \sqrt{u_R^2 + U_{on}^2} \quad (\text{A.1.21})$$

Where S_b is the bed load transport (kg/m/s), u_{eff} is the combined velocity magnitude (m/s) of the flow depth-averaged velocity and the near-bottom peak orbital velocity in onshore direction based on the significant wave height (Hs), u_{cr} is the critical depth-averaged velocity for motion initiation based on Shields curve (m/s), u_R is the magnitude of an equivalent depth-averaged velocity (m/s), and U_{on} & U_{off} are the high frequency near bed orbital velocities due to short waves in the on and offshore directions, respectively. The direction of the bed load transport is computed based on a division into current induced transport ($S_{b,c}$) which acts in the flow direction and wave-induced transport ($S_{b,w}$) which acts in the wave direction.

$$S_{b,c} = \frac{S_b}{\sqrt{1 + r^2 + 2|r|\cos\varphi}} \quad (\text{A.1.22})$$

$$|S_{b,w}| = r |S_{b,c}| \quad (\text{A.1.23})$$

$$r = \frac{(|U_{on}| - u_{cr})^3}{(|u_R| - u_{cr})^3} \quad (\text{A.1.24})$$

In the Delft3D, an additional component ($S_{s,w}$) is added to the bed load. $S_{s,w}$ represents the wave-induced suspended transport due to wave-asymmetry. This component acts in the direction of the wave propagation and is calculated according to Van Rijn 2001 as follows:

$$S_{s,w} = f_{susw} \gamma U_A L_T \quad (\text{A.1.25})$$

$$U_A = \frac{U_{on}^4 - U_{off}^4}{U_{on}^3 + U_{off}^3} \quad (\text{A.1.26})$$

$$L_T = 0.007 \rho_s D_{50} \frac{(u_{eff} - u_{cr})^2}{(s-1)gD_{50}} \quad (\text{A.1.27})$$

Where f_{susw} is a user-defined wave-related suspended transport calibration parameter (0.5), γ is a phase lag coefficient, U_A is the velocity asymmetry value (m/s), L_T is the suspended sediment load (kg/m²).

A.1.3.2 Mud Transport

We apply the Partheniades-Krone formulations (Partheniades, 1965) for cohesive sediment transport as follows:

$$E = MS_e(\tau_{cw}, \tau_{cr,e}), \quad (\text{A.1.28})$$

2. Morphodynamic Evolution of a Fringing Sandy Shoal From Tidal Levees to Sea Level Rise

$$D = w_s c_b S_d(\tau_{cw}, \tau_{cr,d}), \quad (\text{A.1.29})$$

Where,

E erosion flux ($\text{kg m}^{-2} \text{s}^{-1}$)
 M erosion parameter ($\text{kg m}^{-2} \text{s}^{-1}$)
 $S_e(\tau_{cw}, \tau_{cr,e})$ erosion step function:

$$S_e(\tau_{cw}, \tau_{cr,e}) = \left(\frac{\tau_{cw}}{\tau_{cr,e}} - 1 \right), \text{ when } \tau_{cw} > \tau_{cr,e}$$

$$= 0, \text{ when } \tau_{cw} \leq \tau_{cr,e}$$

D depositional flux ($\text{kg m}^{-2} \text{s}^{-1}$)
 w_s sediment fall velocity (m/sec),
 C_b average near bottom sediment concentration,
 $S_d(\tau_{cw}, \tau_{cr,d})$ deposition step function:

$$S_d(\tau_{cw}, \tau_{cr,d}) = \left(1 - \frac{\tau_{cw}}{\tau_{cr,d}} \right), \text{ when } \tau_{cw} < \tau_{cr,d}$$

$$= 0, \text{ when } \tau_{cw} \geq \tau_{cr,d}$$

τ_{cw} maximum bed shear stress due to current and waves (N m^{-2})
 $\tau_{cr,e}$ critical erosion shear stress (N m^{-2})
 $\tau_{cr,d}$ critical deposition shear stress (N m^{-2})

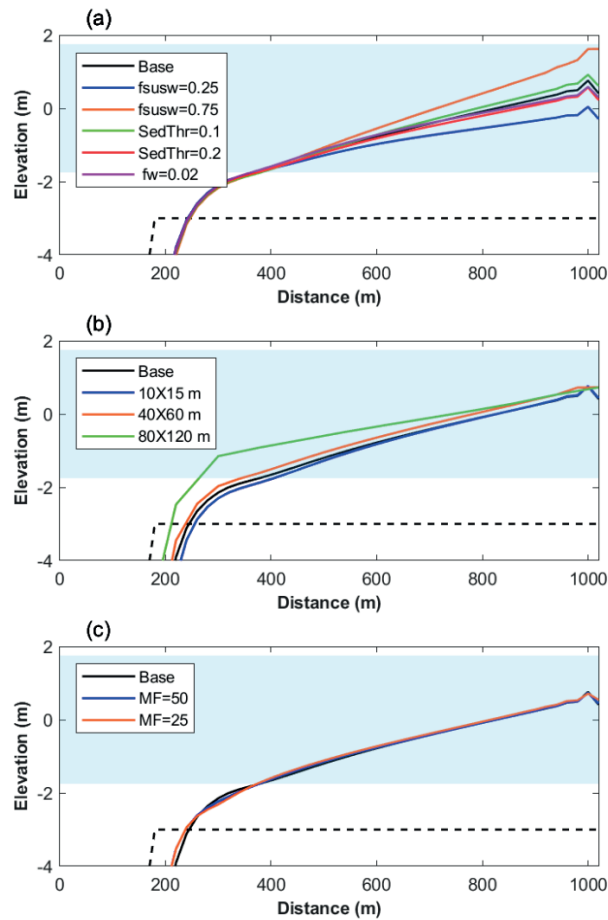


Figure 2.13. Sensitivity analysis showing the equilibrium profiles corresponding to different parameter values of the (a) wave-induced suspended transport parameter ($fsusw$), minimum depth for sediment computation ($SedThr$), and wave friction factor (fw), (b) grid resolution, and (c) morphological factor (MF). The light blue shading indicates the tidal difference, and the dashed black line indicates the initial profile.

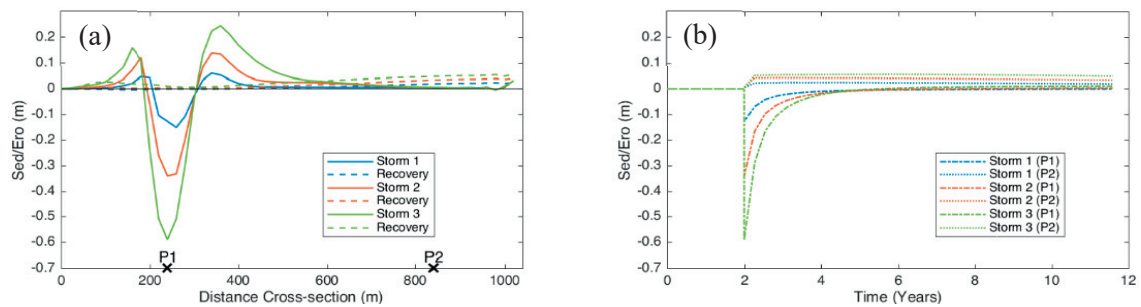


Figure 2.14. Modeled (a) cross-sectional profile of the sedimentation/erosion (m) due to three storm conditions of $T_p=6$ sec and $H_s=1, 1.5$ and 2 m for Storm 1, 2, and 3, respectively. (b) Sedimentation/erosion overtime at two selected points (P1, and P2; see Figure 2.14a x-axis) showing the storm event at $t = 2$ yr and the recovery till $t \approx 12$ yr.

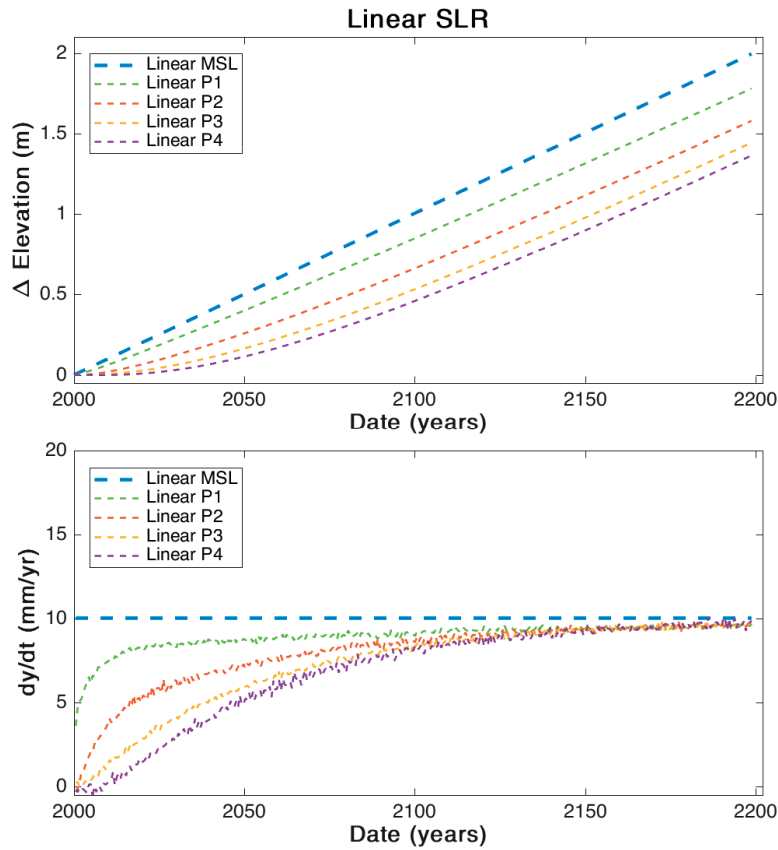


Figure 2.15. The top panel shows SLR and bed level changes at 4 points on the shoal (see Figure 2.10). The bottom panel shows the rates.

Table 2.1. The forcing conditions and model parameters investigated in the sensitivity analysis.

Forcing/ Parameter	Base case value	Sensitivity values
Wave height (H_s)	20 cm	No waves, 15, 25 cm
Wave period (T_p)	3 s	2.5, 3.5 s
Tidal range (dH)	3.5 m	3, 4 m
Sediment diameter (D_{50})	150 μ m	125, 175 μ m
Mud fraction	No	Included
Wave-induced suspended transport parameter (f_{susw}) *	0.5	0.25, 0.75
Minimum depth for sediment computation (SedThr) *	0.15 m	0.1, 0.2 m
Wave friction factor (f_w) *	0.01	0.02
Grid resolution *	20×30 m	10×15, 40×60, 80×120 m
Morphological Factor (MF)*	100	25, 50

* Sensitivity run result presented in the appendix Figure 2.13.

3

MODELING THE MORPHODYNAMIC RESPONSE OF ESTUARINE INTERTIDAL SHOALS TO SEA- LEVEL RISE²

Abstract

Intertidal shoals are key features of estuarine environments worldwide. Climate change poses questions regarding the sustainability of intertidal areas under sea level rise (SLR). Our work investigates the SLR impact on the long-term morphological evolution of unvegetated intertidal sandy shoals in a constrained channel-shoal system. Utilizing a process-based model (Delft3D), we schematize a short tidal system in a rectangular (2.5 × 20 km) basin with a high-resolution grid. An initial, mildly sloping, bathymetry is subjected to constant semidiurnal tidal forcing, sediment supply, and small wind-generated waves modeled by SWAN. A positive morphodynamic feedback between hydrodynamics, sediment transport, and morphology causes the emergence of large-scale channel-shoal patterns. Over centuries, tide-residual sediment transport gradually decreases leading to a state of low morphological activity balanced by tides, waves, and

² This chapter is based on:

Elmilady, H., van der Wegen, M., Roelvink, D., & van der Spek, A. (2022). Modeling the Morphodynamic Response of Estuarine Intertidal Shoals to Sea-Level Rise. *Journal of Geophysical Research: Earth Surface*, 127(1), e2021JF006152. doi:10.1029/2021JF006152

sediment supply. Tidal currents are the main driver of the SLR morphodynamic adaptation. Wave action leads to wider and lower shoals but does not fundamentally change the long-term morphological evolution. SLR causes increased flood dominance which triggers sediment import into the system. Shoals accrete in response to SLR with a lag that increases as SLR accelerates, eventually causing intertidal shoals to drown. Seaward shoals near the open boundary sediment source have higher accretion rates compared to landward shoals. Similarly, on a shoal-scale, the highest accretion rates occur at the shoal edges bounding the sediment-supplying channels. A larger sediment supply enhances the SLR adaptation. Waves help distribute sediment supplied from channels across shoals. Adding mud fractions leads to faster, more uniform, accretion and muddier shoals under SLR.

3.1 INTRODUCTION

The intertidal zone is a key component of many estuaries and tidal basins. It provides flood protection, erosion control (Narayan et al., 2017; Reed et al., 2018), has significant recreational and cultural value (Wilson et al., 2005), and includes valuable habitats for fish, benthic species, and birds (e.g., Galbraith et al., 2002; Lipcius et al., 2013).

Worldwide, intertidal areas are experiencing a notable decline due to anthropogenic impact and climate change (Airoidi & Beck, 2007; N. J. Murray et al., 2014, 2019; Song et al., 2020). Pressure sources include urbanization (Lai et al., 2015; MacKinnon et al., 2012), changes in riverine flows and sediment supply (Blum & Roberts, 2009; Jaffe et al., 2007), and sea level rise (SLR; Lovelock et al., 2017; Passeri et al., 2015).

Ensuring the sustainability of soft-sediment intertidal environments (e.g., unvegetated intertidal shoals) requires an understanding of the processes governing their capacity for SLR adaptation. The current (2020) global mean sea level (MSL) has increased by about 20-25 cm since 1880, with about 9.5 cm since 1993 (NASA, 2024; Sweet et al., 2017). The current global SLR rate is about 3.3 mm/yr (NASA, 2024) which is unprecedented over the past 2 millennia (Kemp et al., 2011; Kopp et al., 2016). This rate is predicted to accelerate, although exact rates remain uncertain. SLR projections for the 21st-century range from about 0.3 m to 2.7 m, depending on the potential rapid loss of the Antarctic ice sheet mass (Church, Clark, et al., 2013; Le Bars et al., 2017; Miller et al., 2013; Sweet et al., 2017).

Channel-shoal systems form as a result of an instability of the morphodynamic system under tidal currents. This triggers a positive morphological feedback leading to the emergence of large-scale channel-shoal patterns when tide-residual transports converge over shoals enhancing their growth and diverge in the channels leading to their deepening (Coeveld et al., 2003; Schramkowski et al., 2002; Seminara & Tubino, 2001). Over decades to centuries, the residual transport gradients gradually diminish resulting in

decreased morphological activity and stable patterns (e.g., Hibma, 2004; van der Wegen & Roelvink, 2008). Shoals can exist in a free form surrounded by deeper channels or in a fringing form connected to the land.

In addition to tidal currents, fine sediment (mud, $4 < D_{50} < 62.5 \mu\text{m}$, or very fine and fine sand, $62.5 < D_{50} < 250 \mu\text{m}$; Wentworth, 1922) supply is a key factor for tidal flat formation (Friedrichs, 2011; e.g., Reineck & Singh, 1980). Fine fractions are more effectively transported by tidal currents towards calmer shoal locations than coarser fractions which can resist the higher flow velocities in deeper channels. For example, sand dominates the Western Scheldt estuary and Wadden Sea (The Netherlands) with coarser sandy material present in channels than on the shoals, while mud dominates the low energy locations (Kuijper et al., 2004; Postma, 1957).

Relatively high wave impact at open coasts causes the formation of steep sandy beaches. Calmer wave conditions around sheltered locations in estuaries or tidal basins allow for the formation of intertidal shoals. However, relatively small waves can still play an important role in shaping the intertidal morphology (Allen & Duffy, 1998; Christie et al., 1999; Elmilady et al., 2020; e.g., Friedrichs & Aubrey, 1996; Janssen-Stelder, 2000; Roberts et al., 2000; van der Wegen, Jaffe, et al., 2017). Measurements show that subsequent periods of lower and higher wave action cause cycles of shoal erosion and deposition, respectively (Fan et al., 2002; Houser & Hill, 2010; Janssen-Stelder, 2000; e.g., Kohsiek et al., 1988).

Observations and modeling studies suggest that, over decades to centuries, shoals evolve towards a state of decreased morphological activity (Elmilady et al., 2020; Friedrichs, 2011; Maan et al., 2018; Roberts et al., 2000; van der Wegen, Jaffe, et al., 2017). Short-term forcing variations such as storm activity (de Vet, 2020; Elmilady et al., 2020; Q. Zhu et al., 2017) or seasonal changes (van der Wegen et al., 2019) result in morphological adaptation which, in most instances, recovers when normal forcing is restored. On the other hand, longer-term forcing variations can notably impact the intertidal morphology (de Vet et al., 2017; e.g., Jaffe et al., 2007).

SLR will impact the hydrodynamics of tidal systems including tidal current velocities, tidal asymmetry, and tidal range (Friedrichs et al., 1990; Jiang et al., 2020; Seiffert et al., 2014; Wachler et al., 2020). The anticipated impact depends on the basin geometry and bathymetry (Du et al., 2018; Friedrichs et al., 1990; Leuven et al., 2019). Changes in the tidal regime will influence residual sediment transports and the associated import/export trends and it will trigger a long-term morphological adaptation process (e.g., Dissanayake et al., 2009; van der Wegen, 2013).

Different modeling strategies are available to assess SLR impact on the morphodynamics of estuarine systems. Lodder et al. (2019), Rossington & Spearman (2009), Van Goor et al. (2003), and Wang et al. (2018) show the ability of low-resolution models based on

empirical equilibrium relationships to reproduce historic decadal morphological development and predict SLR impact. Process-based, high-resolution modeling studies include real case studies with validated hindcasts followed by SLR forecasts (Elmilady et al., 2019; Neil K. Ganju & Schoellhamer, 2010; van der Wegen, Jaffe, et al., 2017; X. Zhou et al., 2013), and schematized modeling which systematically investigates governing processes (Best et al., 2018; Dissanayake et al., 2009; Elmilady et al., 2020; van der Wegen, 2013; van Maanen et al., 2013; Z. Zhou et al., 2016).

A common finding of these studies is that the intertidal areas accrete under SLR albeit with a time lag. The projected 21st century accelerating SLR rate increases the risk of intertidal areas drowning especially in systems with low sediment supply and systems constrained by sea defenses or geological outcrops, with no room for lateral expansion or landward migration. In natural unconstrained systems, the intertidal areas (vegetated or unvegetated) could be maintained if SLR causes marine transgression which depends on the available accommodation space and sediment supply (Allen, 1990; Beets & van der Spek, 2000; Townend et al., 2021).

Thus far, most modeling studies have focused on muddy environments, whereas limited attention was paid to sandy shoals. Also, sandy studies (e.g., Dissanayake et al., 2009; van der Wegen, 2013, Lodder et al. 2019) implemented coarse resolution grids and neglected wave impact as they mainly focused on the large-scale SLR impact such as basin-scale import/export trends. Elmilady et al. (2020) applied a high-resolution (≈ 20 m grid) model of a single, fringed, sandy shoal showing the importance of detailed wave attenuation processes and tidal levee formation.

This research aims to investigate SLR impact on the long-term morphodynamic evolution of a sandy channel-shoal system in a short tidal basin (15-25 km) dominated by intertidal sandy shoals. Our main focus is on the intertidal shoal morphodynamics including the impact of wind waves and the potential presence of mud. The “intertidal shoals” investigated in this study are mainly free shoals along with some small fringing shoals in a constrained system. Although some shoals in nature may eventually develop into vegetated environments (e.g., mangrove belts, seagrasses beds, and salt marshes), our research investigates unvegetated shoals. We implement a schematized high-resolution large-scale process-based numerical modeling approach driven by main forcing conditions (tidal action, waves, and sediment supply).

3.2 MODEL DESCRIPTION

We schematize the system as an enclosed, non-convergent, rectangular (2.5×20 km) tidal basin with an open seaward boundary, see Figure 3.1. The model grid has an outer coarse grid (100×200 m) for both the seaward and landward sides and an inner fine grid ($\approx 33\times 66$ m) for the middle section. The high-resolution middle section allows for a detailed study

of the shoal structure and for exploring the impact of processes related to wave attenuation and tidal levee formation that would be sub-grid in a lower resolution grid.

We apply the Delft3D (D3D) process-based numerical model in 2D mode (Deltares, 2017; Lesser et al., 2004), which solves the unsteady two-dimensional shallow water equations (momentum and continuity; Appendix A.2.1). The domain decomposition option was applied (3 domains) to allow for parallel computation and to link coarse and high-resolution domains.

The initial bathymetry is a mildly sloping bathymetry from -6 to -2 m with an initial random meandering 10 cm bed level perturbation to mimic the morphology of a natural landscape that drowns due to tidal invasion. We apply an initial evenly distributed sediment mixture of two sandy sediment fractions of 100 and 250 μm representing fine and coarse fractions, with a sediment density of 2650 kg/m^3 and a dry bed density of 1600 kg/m^3 . The implementation of multiple fractions serves to represent the variation of sediment sizes found in nature, with coarse material mainly existing in deep channels and finer fractions at shallow locations (see Figures 3.15, and 3.18 in Appendix 2 for an example showing the Wadden Sea basins' bathymetry and mean grain size). The available sediment depth was set to 20 m to allow for the evolving channels to deepen.

The seaward open model boundary was prescribed by a semidiurnal (12 hr) tidal component with an amplitude of 1.5 m mimicking a meso-tidal environment. The use of a 12 hr instead of 12 hr 25 min tidal period is for simplifying the analysis of the results and is commonly used in idealized morphodynamics modeling work (e.g., W. Ridderinkhof et al., 2016). The remaining boundaries are closed boundaries. This schematization represents a constrained system, with no room for lateral expansion or landward migration, which is the case in several estuaries and tidal basins around the world (e.g., Wadden Sea, Western Scheldt, and San Francisco Bay) either due to urbanization (e.g., sea defenses) or geology.

Constant suspended sediment concentrations (SSC) of 0.05 and 0.01 kg/m^3 were set at the boundary for the coarse and fine sand fractions, respectively, based on typical concentrations observed at the Wadden Sea Inlets (Postma, 1961, 1967, 1981). To avoid SSC discontinuities at the boundary during turning tides, we applied a Thatcher-Harleman relaxation time lag of 120 min (Thatcher & Harleman, 1972). The coastal boundaries option in Delft3D was applied to prevent the advection terms at the boundary from generating an artificial boundary layer (Deltares, 2017). To prevent instabilities by intertidal areas at the open boundary, the water depth, only at the boundary, was not allowed to drop less than 0.5 m.

The spectral wave model SWAN (Booij et al., 1999; <http://swanmodel.sourceforge.net/>; Appendix A.2.2) is used in stationary mode to simulate small wind-generated waves (10 - 20 cm) by a constant landward directed wind field of 4 m/s. The wave model covers the

whole flow domain with a constant grid resolution of 100×200 m. No waves are prescribed at the seaward boundary, so that wave action is limited to locally generated wind waves. SWAN is coupled to Delft3D-FLOW through online coupling at a 30-minute interval implying constant wave conditions during that interval. Each hydrodynamic time step (15 s), Delft3D-FLOW computes the flow including wave generated forces (F_x and F_y) as a source in the momentum equations. The Fredsoe formulations (Fredsoe, 1984) are used to compute the maximum shear stress (τ_{max}) based on the combined current (τ_c) and wave (τ_w) shear stress.

The default Van Rijn (1993) formulations are used to compute the sand transport (suspended load and bedload) for the combined effect of waves and currents. Based on the locally- and time-varying velocities and water levels, the suspended sediment transport is calculated every timestep by an advection-diffusion solver which includes a sink and source term describing sediment exchange with the bed (Appendix A.2.3). Bed level changes are computed based on the divergence of the sediment transport field. Using the MORFAC approach, bed-level changes are multiplied by a morphological acceleration factor (MF) to enhance the morphological evolution. Extensive modeling studies for similar tidal systems show good results up to a MF of 400 (Braat et al., 2017; Dissanayake, 2011; e.g., Roelvink, 2006; van der Wegen & Roelvink, 2008), while wave action usually requires a lower MF.

In this research, we simulate 2 hydrodynamic years with a MF of 100 resulting in 200 years of morphological development. This MF provides stable morphodynamics with a reasonable computational effort. We perform our investigations using a configuration without (referred to as Flow simulations) and with wave action (referred to as Wave simulations). Both simulations incorporate wind forcing. The model takes about 2.5 and 4 days to simulate 1 hydrodynamic year on a 4-core (2.6 GHz) computer for the Flow and Wave simulations, respectively.

To account for bed slope effects, the streamwise and transverse bed gradient factors AlfaBs (α_{bs}), and AlfaBn (α_{bn}) were set as 1 (default) and 25, respectively, based on initial sensitivity runs within the reported range in literature. The α_{bn} is a very important parameter for the channel-shoal morphology and is often used as a calibration parameter, while model results are practically insensitive to α_{bs} . In estuarine and tidal basin models, especially when using the Van Rijn transport formulations, the α_{bn} is often set much (an order of magnitude) larger than the experimental and default values (1.5; Ikeda, 1982) to prevent the formation of unrealistically steep banks, and narrow deep channels with sharp bends (e.g., Dissanayake, 2011; van der Wegen & Roelvink, 2012).

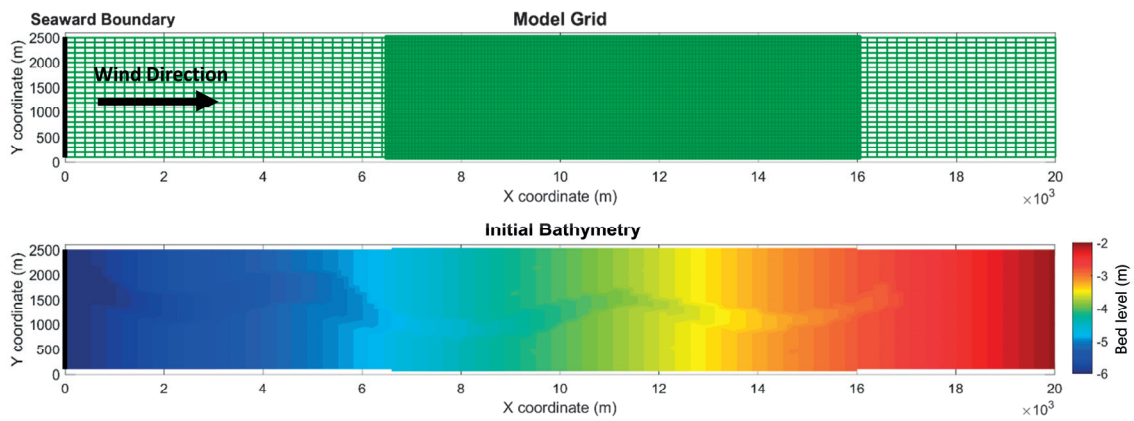


Figure 3.1. Model domain and the initial model bathymetry (m).

3.3 MODEL RESULTS

In this section, we present model results without SLR which serve as validation for our modeled morphological evolution.

3.3.1 Morphology

We simulate the morphological evolution of the initial bathymetry for 200 years towards a stable channel-shoal system (Figure 3.2). Over time, channel-shoal patterns emerge eventually creating intertidal areas. The morphological development is rapid in the beginning but gradually decreases over time leading to a state of low morphological activity.

For both Flow and Wave simulations, shoals develop at roughly the same locations. The end morphologies ($T = 200$ years) show that the Wave simulation leads to more coherent, lower elevation shoals with fewer intersecting channels and a smoother surface than in the Flow simulations. The Wave simulation also shows wider and shallower channels.

Previous studies (e.g., Allen & Duffy, 1998; Carniello et al., 2005; Elmilady et al., 2020; S Fagherazzi et al., 2007) provide an explanation for this. Flood tides supply sediments to the shoals that deposit near the channel-shoal edge as tidal levees. These sediments are re-suspended by wave-induced shear stresses at lower water levels. Subsequent flood flows then transport the re-suspended sediments further on to the shoal.

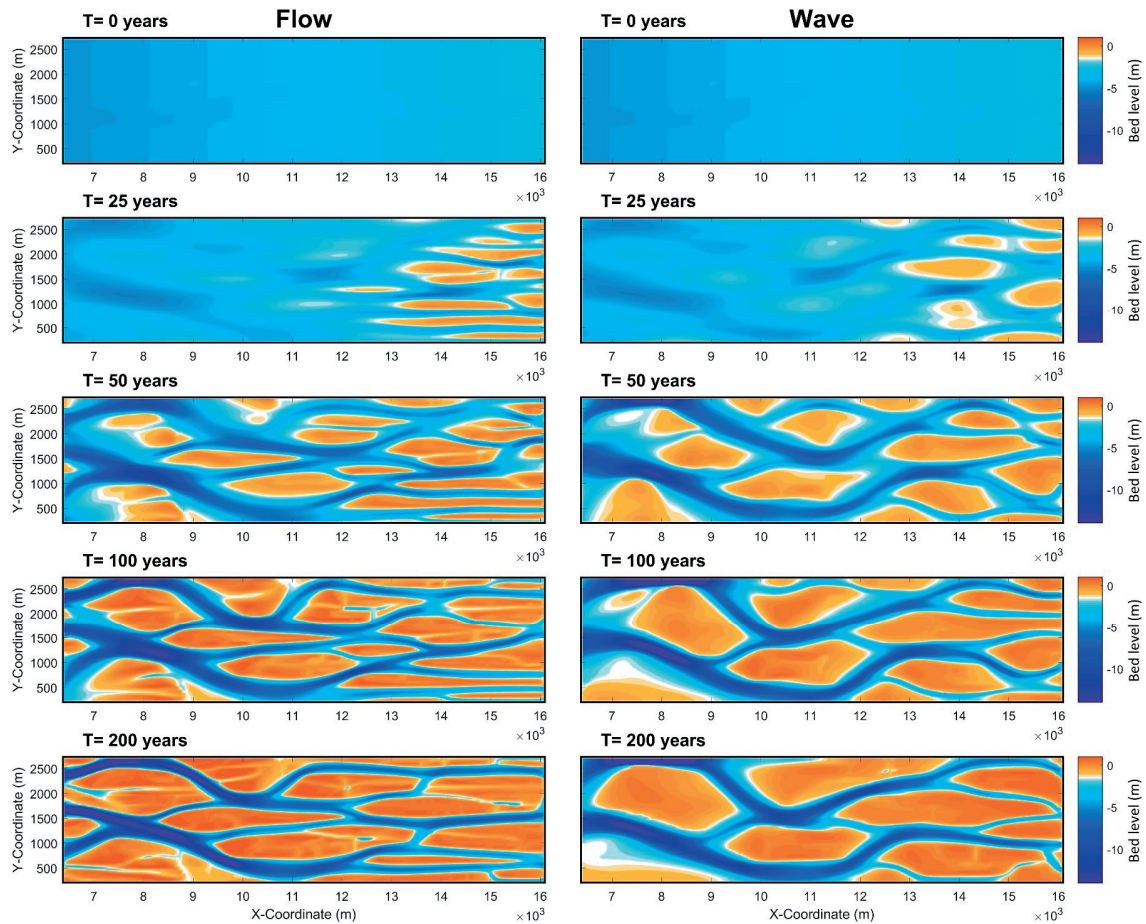


Figure 3.2. Modeled bathymetry (m) of the high-resolution domain over time for the Flow (left panel) and Wave (right panel) simulations. The white color band is the average low water level ($LW \approx -1.6$ m) which indicates the approximate border between the intertidal (shoal) and subtidal (channels) areas.

3.3.2 Shear stresses

For both simulations, the tidally averaged maximum shear stresses ($\bar{\tau}_{max}$) is highest at the beginning as the initial shallow bathymetry causes high flow resistance (Figure 3.3a). As shoals start emerging and gain elevation, the flow gets redirected into the deepening channel. The $\bar{\tau}_{max}$ over the shallow sections gradually decreases with time towards a relatively stable state.

Waves increase the maximum shear stresses over the shoals. The wave impact (the difference between the solid and dashed identical color lines in Figure 3.3a) on the $\bar{\tau}_{max}$ is highest at the shallow intertidal areas and gradually decreases with depth. On the other hand, the highest $\bar{\tau}_{max}$ occurs at the deep subtidal channels and decreases towards the shallow intertidal areas (Figures 3.3b and 3.3c).

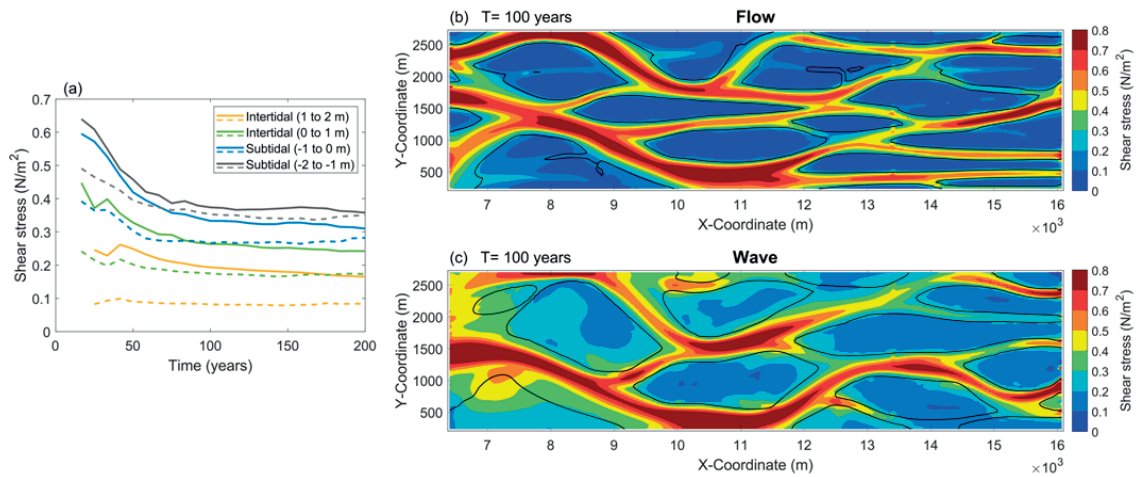


Figure 3.3. (a) Temporal development of $\bar{\tau}_{max}$ (N/m^2) spatially averaged over the whole model domain and over 1m vertical elevation bins. The bin range is with respect to LW and is divided into subtidal bins (-2 to -1 m; grey, and -1 to 0 m; blue), and intertidal bins (0 to 1 m; green, and 1 to 2 m; yellow). Solid and dotted lines correspond to Wave, and Flow simulations, respectively. (b, and c) $\bar{\tau}_{max}$ map of the high-resolution domain at $T = 100$ years for the Wave, and Flow simulations, respectively. The black contour lines indicate the border (LW) between intertidal and subtidal areas.

3.3.3 Sediment transport

The initial bed level perturbation creates variations in the currents and sediment transport. This triggers a morphological feedback in which tide-residual sediment transport convergence accretes the shoals and sediment transport divergence deepens the channels. The emergence of intertidal areas decreases the tidal prism and the tidal asymmetry which favors flood dominance and landward-directed tide-residual sediment transport. Also, the channel deepening decreases the depth-averaged SSC levels. Over time, the residual transport gradually diminishes resulting in a stable channel-shoal system. As an example, Figure 3.4 shows the residual sediment transport magnitude and direction for the Wave simulation at a state of low morphological activity after 150 years. The presented sediment transport throughout this paper is the total transport (bed and suspended). The bed transport is highest at the initial stages of the channel-shoal formation. Over time, the bed transport decreases and becomes an order of magnitude smaller than the suspended transport.

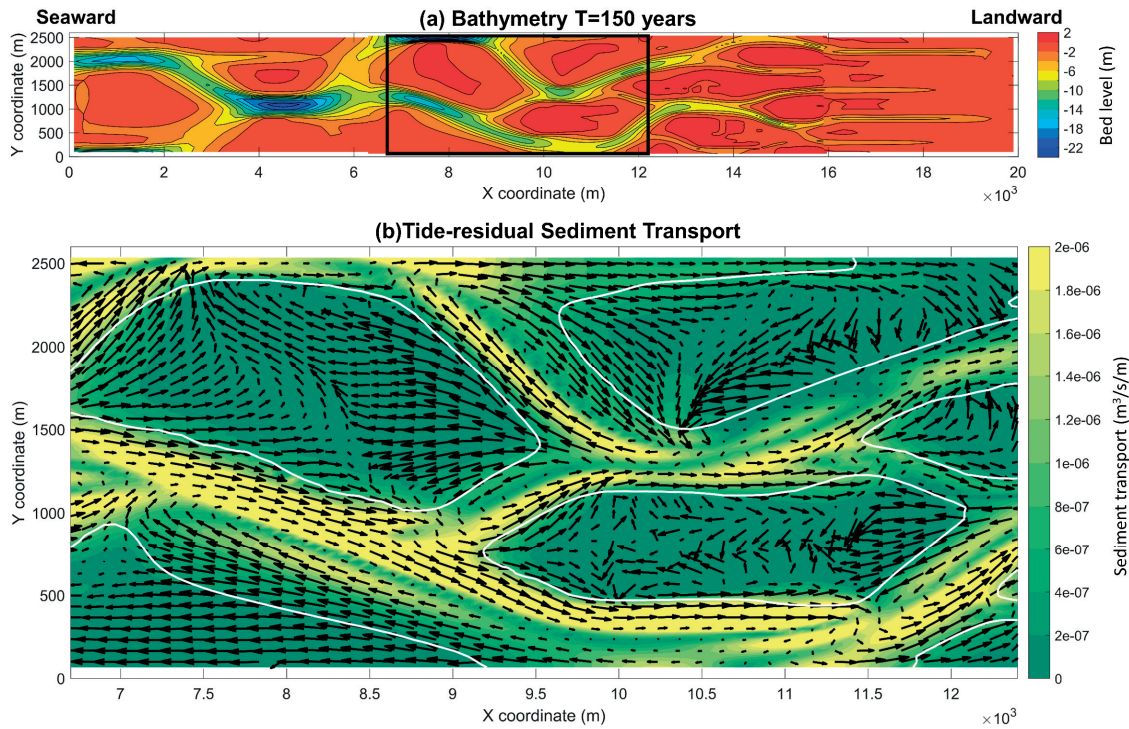


Figure 3.4. (a) The modeled bathymetry (m) at $T = 150$ years for the whole model domain. The black box indicates the location of the bottom plot. (b) The tide-residual sediment transport magnitude ($m^3/s/m$) and direction. Arrows are RMS normalized and plotted on a grid with half the model grid resolution to make them more visible. The white contour lines indicate the border (LW) between the intertidal and subtidal areas.

3.3.4 Wave impact

Tide-residual sediment transports generate channel-shoal patterns, while wave action only becomes important when shoals emerge. To explore the long-term impact of waves on the shoal morphology, we subjected the 150-year modeled Wave morphology to a 50-year variation in the wave forcing (Figure 3.5). Three wave conditions were investigated: 1) no waves; 2) 10-20 cm waves (continuation of Wave Base-case normal forcing); 3) 15-25 cm waves (increased wave action).

The variation of wave conditions only had an impact on the shoal area and elevation. Excluding waves (Figures 3.5b, 3.5e, and 3.5h) resulted in the largest area and highest elevation shoals with high elevation ridges at the shoal edges and drainage channels on top of the shoal. The highest accretion occurs at the shoal edge and decreases going landward. This can be explained as the profile accretes over time, the cross-shore velocities over the shoal start gradually dropping until they are not strong enough to resuspend the sediment supplied by the channels and distribute it across the shoal. In the absence of wave-induced resuspension, the sediment accumulates at the shoal edge causing the formation of high elevation ridges (tidal levees) and a seaward extension of

the shoal (widening). Wang et al. (2018) show that tidal levee features are indeed found on sandy shoals in Dutch estuaries, although they may be short-lived due to strong variations in wave action. On the other hand, for the increased wave action case (Figures 3.5d, 3.5g, and 3.5j), the higher wave shear stresses resulted in the smallest area and lowest elevation shoals with the smoothest surface and limited drainage channels. For all forcing conditions, the morphodynamic activity decreases over time which suggests that it is approaching an equilibrium state.

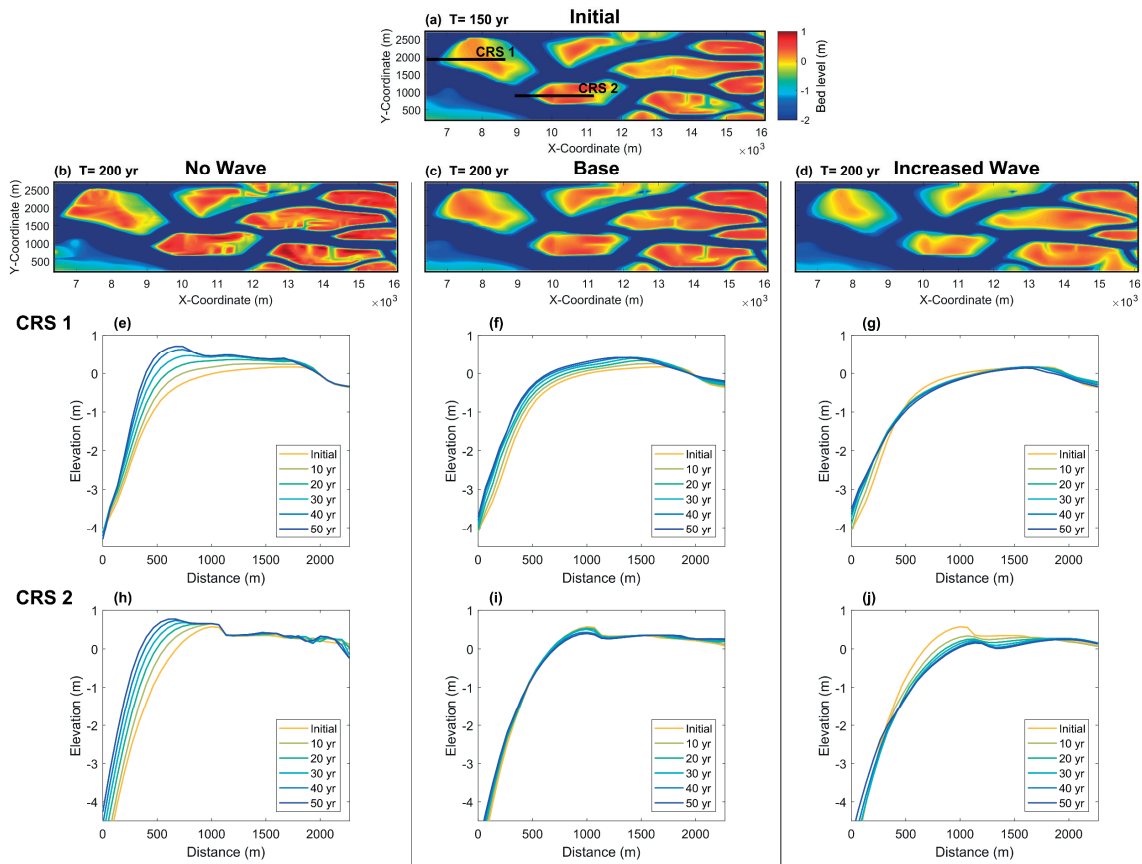


Figure 3.5. (a) The initial bathymetry (m) (Wave simulation; $T = 150$ years) along with the location of the two cross-sections (CRS 1, and CRS 2). The modeled bathymetry after 50 years of (b) no waves, (c) Base-case waves, and (d) increased waves. The cross-sectional profile development over time for CRS 1 (e, f, and g), and CRS2 (h, i, and j) for the three wave scenarios. The profiles were chosen parallel to the wind field direction and on the upwind side of the shoals which is subjected to the highest wave attack.

3.4 SEA LEVEL RISE

SLR is imposed as a rise of the mean sea level (MSL) over 100 years, starting from the modeled morphology at $T = 100$ years to $T = 200$ years (Figure 3.6). At this stage ($T =$

100 years), the system has reached a relatively stable state with limited morphological activity which allows for investigating and isolating the SLR impact. We explore 4 SLR scenarios; the rise is imposed either as a non-linear rise (0.96, 1.67, and 2.63 m/century) based on a sinusoidal function rising from the minimum to the intercept or as a linear rise with a constant rate (0.96 cm/yr). The SLR magnitude is based on high-end global SLR probabilistic projections by Le Bars et al. (2017) which includes the potential rapid loss of the Antarctic ice sheet mass. The 0.96 m is maybe the most likely scenario and corresponds to the 50th percentile of the representative concentration pathway scenario RCP4.5, while the 1.67 and 2.63 m correspond to the 50th and 95th percentile of the RCP8.5 scenario.

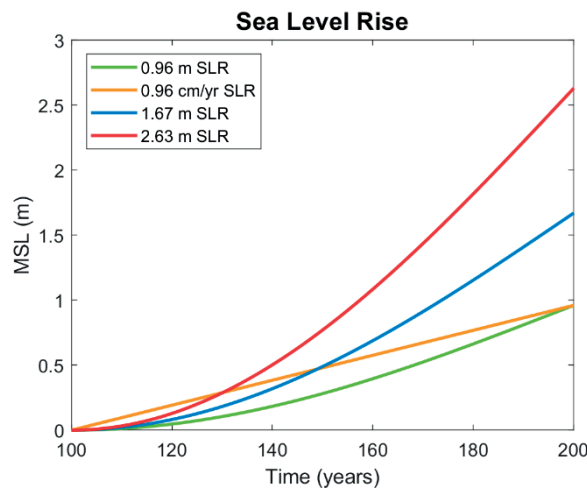


Figure 3.6. The mean sea level (MSL; m) for the implemented SLR scenarios.

3.4.1 Morphology

SLR notably impacts the shoal morphology. Figure 3.7 shows the 0.96 m non-linear SLR impact on the shoal morphology for the Base Wave (BW; a, b, c, d, and e), and the Base Flow (BF; f) simulations. The initial bathymetry of the BF run (not shown) is the 100-year bathymetry of the no SLR run with Flow. Comparing Figure 3.7a with 3.7b shows that limited morphological change occurs during the 100 years with no SLR, while shoals accrete significantly in case of SLR (Figure 3.7c). Figure 3.7d shows that shoals remain at approximately the same locations while experiencing more accretion (red color) under SLR. Spatial variations exist in the accretion magnitude. Shoal accretion is highest near the seaward boundary (basin sediment source). On the shoal scale, accretion is highest at the shoal edges near the channels (shoal sediment source). This causes the formation of high elevation ridges (tidal levees) at the shoal edges.

In most locations, the accretion magnitude is less than the SLR magnitude. Correcting the shoal elevation with the SLR magnitude (Figure 3.7e) and comparing it with the No SLR

elevation (Figure 3.7b) shows that the intertidal shoal areas experienced a notable decrease in their relative elevation and a slight decline in their areal extent.

In general, we see the same response from the Flow simulation under SLR. A major difference is that much shoal accretion occurs near the channel-shoal interface leading to more pronounced levee formation at shoal edges (Figure 3.7f and Appendix 2 Figure 3.19), while waves lead to smoother intertidal flats.

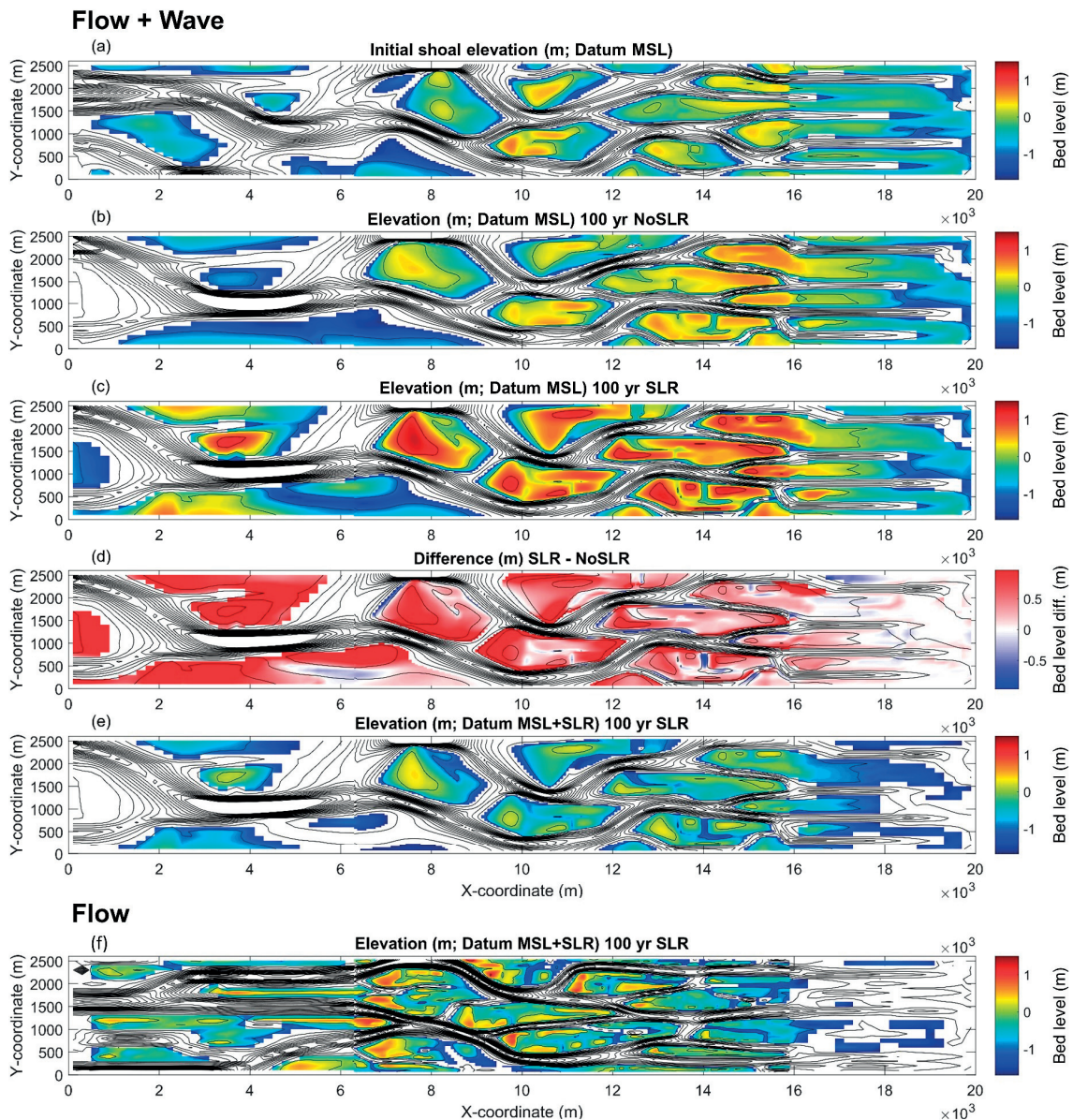


Figure 3.7. SLR impact on the shoal morphology for the simulation including wind-wave impact (a, b, c, d, and e; Base Wave; BW). (a) The initial shoal elevation (m; with respect to MSL), (b) the shoal elevation (m; w.r.t MSL) after 100 years with no SLR, (c) the shoal elevation (m; w.r.t MSL) after 100 years with a non-linear 0.96 m/century SLR, (d) the

difference between the shoal elevation for the SLR and No SLR scenarios (color bar from -0.96 to 0.96 m), and (e) the shoal elevation (m; w.r.t MSL + SLR) corrected with the SLR magnitude. (f) The shoal elevation (m; w.r.t MSL + SLR) corrected with the SLR magnitude (0.96 m) but for the simulation excluding wind-wave impact (Base Flow; BF). The black lines are the elevation contours with 1 m intervals.

3.4.2 Hydrodynamics and Sediment transport

Figure 3.8 shows the SLR impact on the hydrodynamics and sediment transport, the presented SLR results are for the 0.96 m non-linear scenario as it is the most likely scenario. Other SLR scenarios have the same impact, albeit with different magnitudes (see Figure 3.20; Appendix 2). We present the maximum flood and ebb velocities in the plots because their difference shows a good correlation with the tide-residual transport magnitude and direction since the majority of sediment transport occurs during or in the vicinity of peak flow.

Both flood and ebb velocities increase due to an increase in the tidal prism under SLR (Figures 3.8c to 3.8f). The increase in the tidal prism is mainly due to the inundation of intertidal areas along with a slight increase in the tidal range. For example, for the 0.96 m SLR, at the seaward border of the presented domain (e.g., Figure 3.8c), the tidal prism increased by 18% and the tidal amplitude increased by approximately 1.5%, while the tidally-averaged cross-sectional volume increased only by 9%. In addition to the increase of flow velocities, SLR enhances the tidal asymmetry favoring flood dominance. The increase in flood velocities is larger than that for the ebb velocities (Figures 3.8g to 3.8h). Also, the flood duration is shortened while the ebb duration is elongated (Figure 3.21; Appendix 2). This increased asymmetry is caused by the inundation of the intertidal areas.

Changes in the system's hydrodynamics under SLR notably impact the tide-residual sediment transports (Figures 3.8i and 3.8j). Without SLR, the residual sediment transport gradually diminishes over time leading to a state of low morphological activity (Figure 3.8i). The SLR-induced increase in flow velocities elevates the SSC levels in the system (Figure 3.22; Appendix 2). This combined with the increased flood dominance with SLR results in a notable landward tide-residual sediment transport and sediment import to the system (Figure 3.8j). The majority of the sediment import to the system is composed of the fine sand fraction.

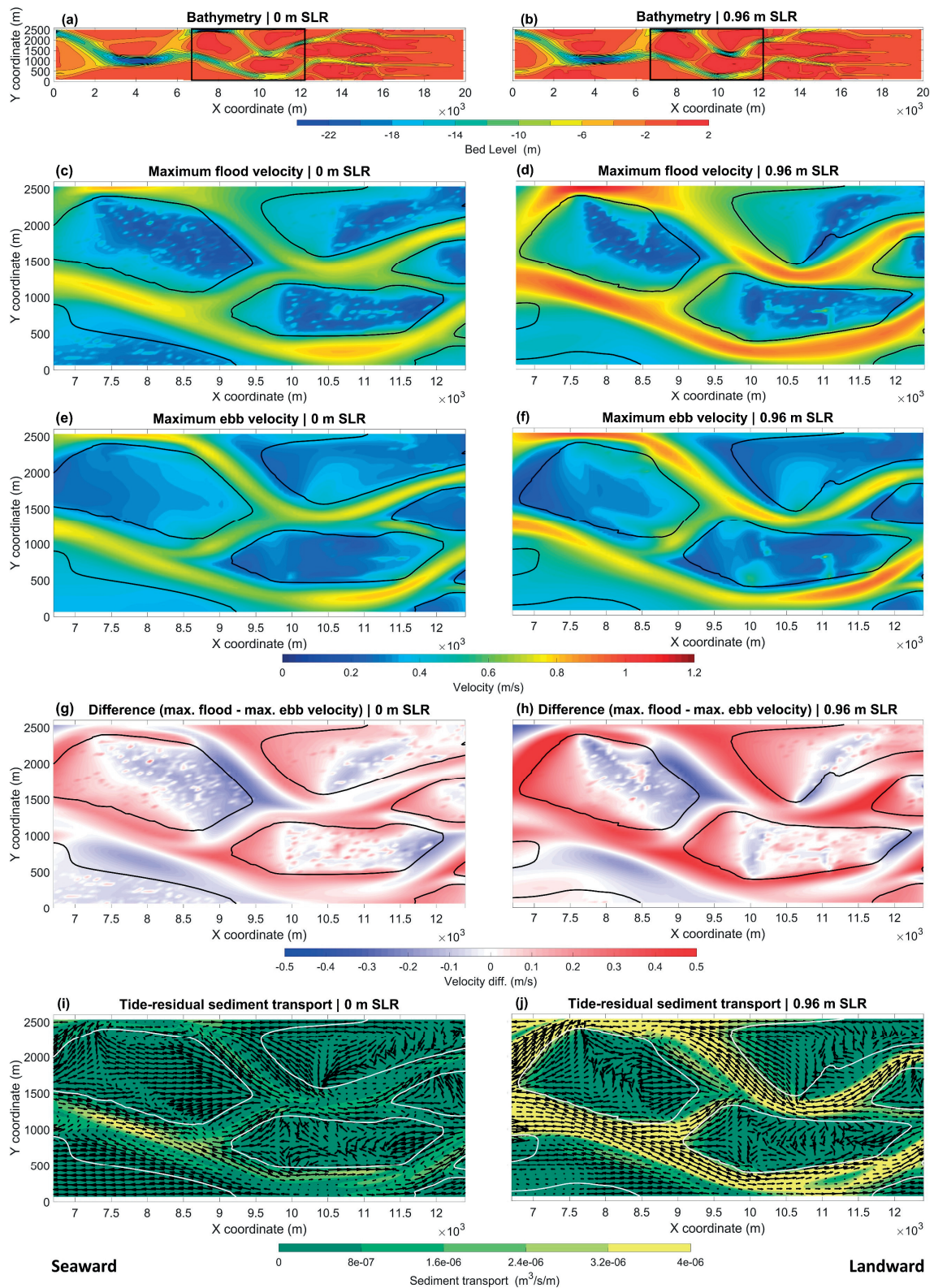


Figure 3.8. The modeled bathymetry (m) for the Wave Base-case simulation after 100 years with (a) no SLR, and (b) 0.96 m SLR. The black box indicates the location of the

below plots. (c, and d) maximum flood velocities, (e, and f) maximum ebb velocities, (g, and h) difference between maximum flood and ebb velocities, and (i, and j) the tide-residual sediment transport magnitude ($m^3/s/m$) and direction. Arrows are RMS normalized and plotted on a grid with half the model grid resolution to make them more visible. The black/white contour lines indicate the border (LW) between the intertidal and subtidal areas.

3.4.3 Sensitivity analysis

We performed a sensitivity analysis to explore the SLR impact with different forcing conditions such as SLR scenarios (set 1, and 2), wind-wave activity (set 3), tidal forcing (set 4), sand supply (set 5), and the inclusion of mud fractions (set 6), Figure 3.9. The sensitivity analysis was carried out based on the two Base-case simulations discussed in section 3.4.1; Base Flow (BF; set 1), and Base Wave (BW; set 2 to 6). The shoal and channel volumes are calculated based on a fixed datum (LW) of the No SLR case. This allows for visualizing the impact of SLR on the morphology while excluding the state changes between shoals and channels which are caused by the SLR-induced increase in the water level. The shoal volume (m^3) is defined as the sediment volume above LW, while the channel volume (m^3) is defined as the water volume below LW. For example, an increase in shoal volume indicates depositional shoals, while a decrease in channel volume indicates channel infilling.



Figure 3.9. Summary of the sensitivity analysis for different forcing conditions showing (a) the shoal volume (m^3 ; w.r.t LW), and (b) the channel volume (m^3 ; w.r.t LW) for the whole model domain for the initial state (blue), after 100 years without SLR (Orange), and after 100 years with SLR (Green). The legend presents the abbreviations used for the different simulations and the description of the varying forcing condition. BF and BW refer to the Base Flow and Base Wave simulations, respectively.

3.4.3.1 Sea level rise scenarios

The SLR-induced sediment import to the system results in notable deposition on the shoals and in the channels. The shoal volume increases while the channel volume decreases (Figure 3.9; set 1, and 2). The increase/decrease magnitude depends on the SLR magnitude and rate. Higher SLR results in more sediment import. Also, a linear SLR causes more deposition compared to a non-linear rise. For the linear SLR, during the entire simulation period, the SLR magnitude is higher than that for the non-linear SLR which only reaches the same magnitude at the end (see Figure 3.6). This allows the system with the linear rise more time to adapt to the imposed SLR thus resulting in higher accretion. Elmilady et al. (2020) note this behavior and highlight a faster adaptation to the linear rise.

Figure 3.10 shows the temporal development of the shoal and channel volume and area for the Wave simulations under the different SLR scenarios. The dashed lines are based on a fixed reference (LW), while the solid lines are based on a moving datum with the SLR (LW + SLR). In this section, parameters (e.g., shoal volume) based on the moving datum are referred to as “relative” parameters as being relative to the SLR.

SLR induces shoal deposition with higher magnitudes with the increasing SLR leading (Figure 3.10a; dashed lines). However, accounting for the SLR-induced rise in the water levels, the relative shoal volume (Figure 3.10a; solid lines) decreases for all scenarios. The morphodynamic adaptation lags behind SLR as accretion rates do not match the SLR rate. For all the non-linear SLR scenarios, this lag continues to increase with the accelerating SLR which leads to continuous shoal drowning. Remarkably, the linear constant SLR rate (0.96 cm/yr), experienced the least shoal volume decline. There is an initial loss of the relative shoal volume in the first ≈ 50 years which gradually flattens and follows the No SLR signal when the SLR-induced accretion rates start approaching the constant SLR rate. This behavior has been noted in previous modeling studies with ASMITA (Van Goor et al., 2003; Wang & Roelfzema, 2001) and Delft3D (Elmilady et al., 2020). It represents the system’s adjustment to the “initial” perturbation due to the introduction of SLR and a need to establish an “overdepth” to generate a new dynamic equilibrium that follows the SLR at the same rate.

SLR also favors channel deposition with higher magnitudes under increasing SLR (Figure 3.10b; dashed lines). However, the SLR-induced rise in the water levels causes an

increase in the relative channel volume (Figure 3.10b; solid lines). Similar to the shoal volume, the non-linear SLR resulted in the least relative channel volume increase.

SLR causes a drop in the relative shoal area and an equivalent increase in the relative channel area (Figure 3.10c, and 3.10d; solid lines). For instance, by the end of the simulation, the relative shoal area became 12.5 % (0.96 m linear SLR) to 51.5 % (2.63 m non-linear SLR) smaller than that for the No SLR scenario.

For all SLR scenarios, the percentage of the relative shoal volume decrease (Figure 3.10a; solid lines) is higher than that for the relative shoal area decrease (Figure 3.10c; solid lines) thus resulting in lower elevation surviving shoals. For example, with the 2.63 m SLR scenario, SLR caused a decrease in the relative shoal volume and area of 77% and 51.5%, respectively, leading to a drop in the average relative shoal elevation (w.r.t LW + SLR) from 1.22 m with No SLR to 0.57 m with SLR. On the other hand, SLR caused an increase in the relative channel volume and area of 31% and 67%, respectively, leading to a drop in the average relative channel depth (w.r.t LW + SLR) from 4.3 m with No SLR to 3.4 m with SLR. The main reason behind this relative depth decrease is that the SLR-induced increase in water level changes a large portion of the intertidal areas to shallow channels. However, the whole domain is becoming deeper with SLR, especially the deepest subtidal sections.

Flow simulations (Figure 3.23; Appendix 2) show a trend of morphological evolution under SLR that is similar to the Wave Simulations (Figure 3.10). A difference is that, for all SLR scenarios, Flow simulations experience larger channel deposition. For the Flow linear SLR, the relative channel volume even turns from increasing to decreasing. The reason behind this is that shoal accretion in the flow simulations mainly occurs at the channel-shoal interface (see section 3.4.1). The SLR turns a portion of this area into shallow channels thus this deposition is considered as channel accretion. Also, since most of the SLR-induced accretion is composed of the fine fraction (section 3.4.2), this makes channels in Flow simulations more likely to experience sediment fining which impacts the equilibrium channel volume (decreases).

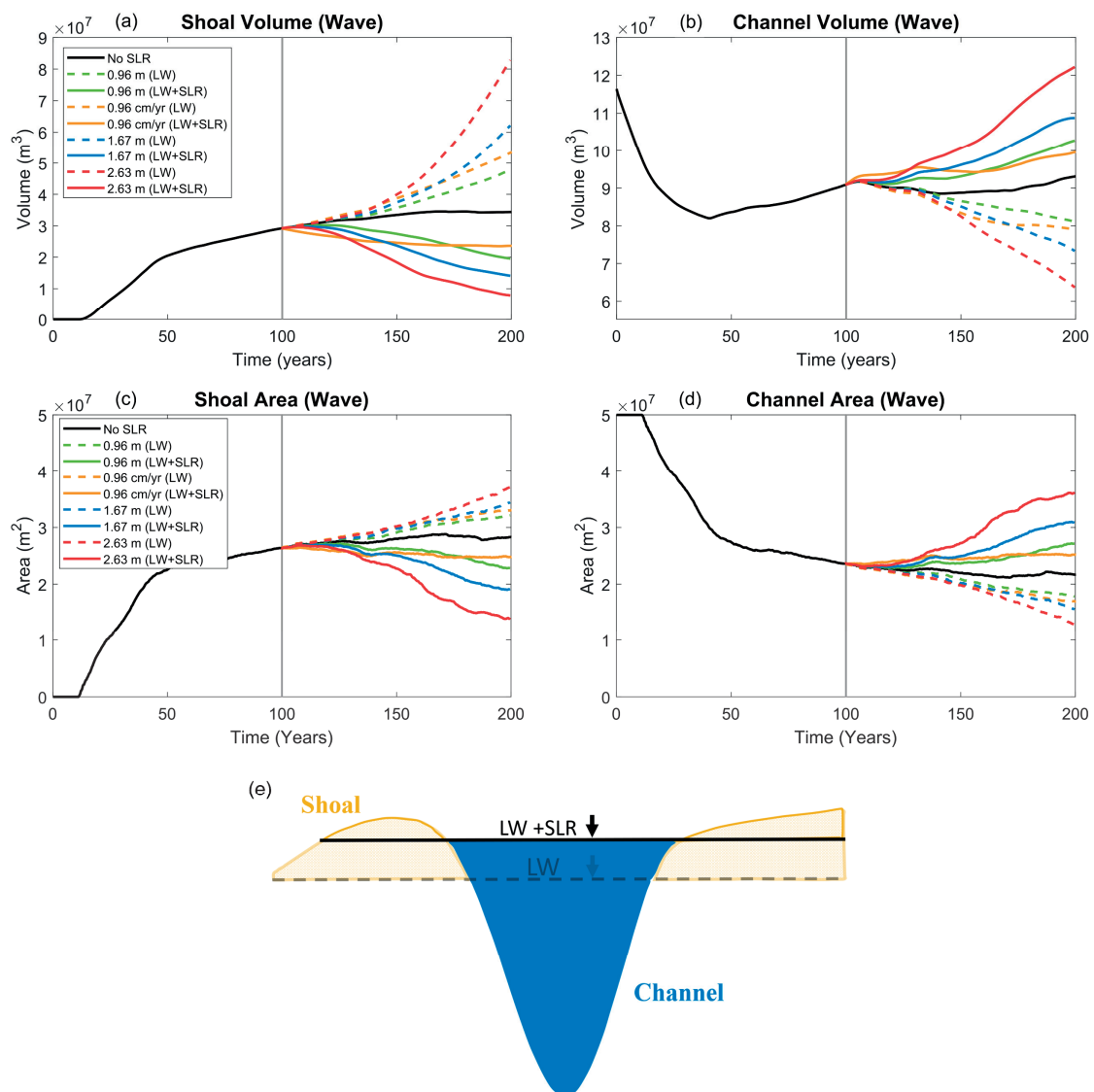


Figure 3.10. The temporal development of the shoal (a) and channel (b) volume (m^3) and the shoal (c) and channel (d) area (m^2) for the whole model domain and for the Wave simulations. The solid black line is the No SLR scenario, while the color lines are for the different SLR scenarios. (e) Schematic showing the shoal and channel definition along with the datums used for the dashed lines (fixed datum; LW), and the solid lines (moving datum; LW+SLR).

SLR can impact the large-scale channel-shoal patterns. As shown before in Figure 3.7, this impact is minimal for the 0.96 m non-linear SLR. Shoals remained in approximately the same location while experiencing accretion and slightly losing intertidal area from their edges. The SLR impact on the spatial patterns becomes more pronounced with the higher SLR scenarios (e.g., Figure 3.11 including wave action). The secondary shallow channels (black arrows in Figure 3.11a) connecting the two main deep channels

experience notable deposition which results in shoals merging. Figures 3.11a, and 3.11b show the morphology not corrected with the SLR magnitude. A large section of the merged shoal is not intertidal since only specific locations can keep pace with the SLR and do not drown.

The hypsometry curves and the shoal slopes for the Flow and Wave simulations are presented in Appendix 2 (Figures 3.24, and 3.25; Section A.2.5).

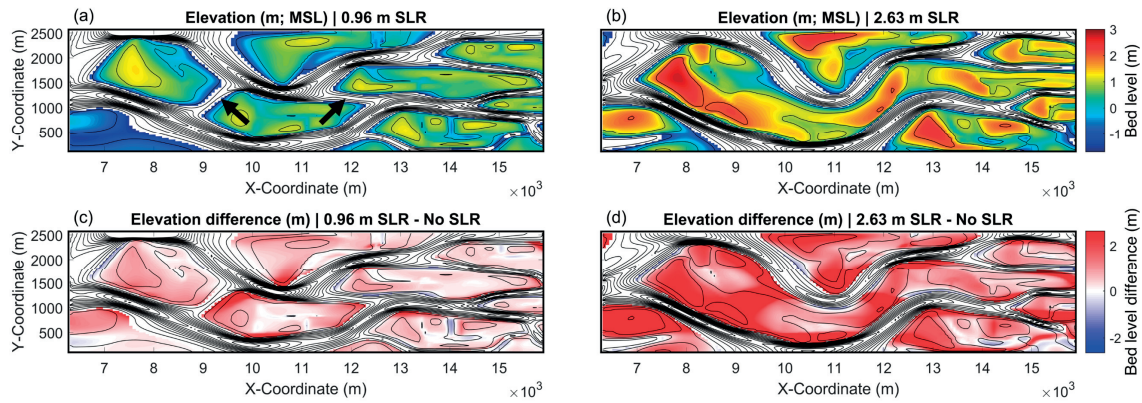


Figure 3.11. (a, and b) The shoal elevation (m; w.r.t MSL) for the 0.96, and 2.63 m non-linear SLR, respectively. The black arrows in (a) point to the location of the secondary channels. (c, and d) The shoal elevation difference (m) between the SLR and No SLR scenario. The plots are for simulations including wave action.

3.4.3.2 Wave action

In the Base-case Wave simulation (BW) we implement a constant (4 m/s) wind field, while in nature the wind field varies continuously. Also, in the Wadden Sea region, the average wind speed ranges from 6 to 7 m/s (Brinkman et al., 2001; KNMI, 2014). Modeling a high wind speed (> 6 m/s) requires decreasing the morphological factor (MF), especially during the initial period (≈ 100 years) with high morphological activity. The Base-case value of 4 m/s allows for performing a sensitivity analysis without extensive simulation times and with equal morphological factors. In this section, starting from the BW initial ($T = 100$ yr) morphology, we investigate different wind conditions including lower, higher, and time-varying wind speeds. The spatially (over the model domain) and temporally averaged wave-orbital velocity squared (u_{orb}^2) was used as a metric to compare the wave action between the different simulations. For the No W simulation, there is no wave action. The constant base wind speed of 4 m/s (BW) creates approximately equivalent wave action to a varying wind speed from 2 to 5.35 m/s (W1). Section A.2.4 and Figure 3.26 in Appendix 2 provide more information regarding the variable wind speed implementation and the wave orbital velocities.

Model results suggest that the largest wave action leads to the highest SLR shoal adaptation capacity, albeit the resulting morphology is different. Figure 3.9; set 3 shows the shoal and channel volume for the different wind-wave conditions. Variations in wind-wave activity mainly impact the shoal volume, while the impact on the channel volume is relatively low. Compared to the BW simulation, excluding waves (No W) resulted in larger shoal deposition without SLR which is further enhanced by SLR. Time-varying conditions (W1) with an approximately equivalent wave action resulted in similar shoal deposition magnitudes to that of the BW both with and without SLR. The increased wave action (W2) resulted in slight shoal erosion with No SLR, however, similar to the other conditions, SLR induces shoal deposition. The SLR-induced shoal deposition magnitudes for the No W, BW, and W2 are 1.23 , 1.35 , and $1.18 \times 10^7 \text{ m}^3$ which represent a 29, 39, and 50% increase to their No SLR shoal volume of 4.25 , 3.43 , and $2.38 \times 10^7 \text{ m}^3$, respectively.

Similar to the noted behavior when starting from different initial bathymetries (section 4.1), wave action exclusion (Figures 3.12a, and 3.12c) resulted in spatial variations in the SLR-induced shoal accretion with the highest accretion occurring at the shoal edges. On the other hand, the highest wave action (Figures 3.12b, and 3.12d) resulted in the most uniform accretion and the smoothest shoal morphology under SLR. This is caused by the added wave shear stresses which enhance sediment resuspension and distribution over the shoal (see section 3.3.4). In addition to the shoal-scale impact, waves also enhance the sediment distribution along the basin's longitudinal axis. This leads to larger accretion and faster adaptation of landward shoals to SLR.

Despite the differences between the two opposite end situations (without waves and with high wave action), the system reacts to the SLR in the same manner. Also, a constant wind speed showed similar results to an approximately equivalent wave action generated by a time-varying signal.

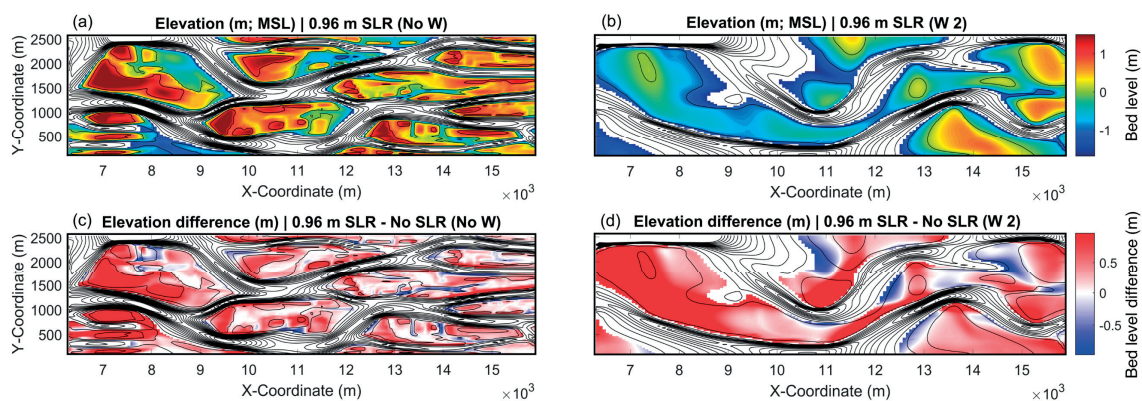


Figure 3.12. (a, and b) The shoal elevation (m; w.r.t MSL) for the No W and W2 wind-wave conditions, respectively. (c, and d) The shoal elevation difference (m) between the SLR and No SLR scenario for each wind-wave condition.

3.4.3.3 Tidal forcing

We investigated the impact of the tidal range (dH) on the morphological response to SLR by comparing the Base-case wave simulation (BW; dH= 3.0 m) to other simulations with lower (dH= 2.5 m) and higher (dH= 3.5 m) tidal range (Figure 3.9; set 4). Unlike the waves, the change in the tidal range notably impacts the channel volume. Without SLR, a drop in the tidal range (dH=2.5 m) resulted in a notable channel volume decrease due to deposition, while an increase in the tidal range resulted in a notable channel volume increase due to erosion. This response represents the system's adaptation to the newly imposed forcing conditions that deviate from the original forcing. The increase in tidal range causes higher channel flow velocities which leads to channel deepening. This is the only simulation in which the system shifted from a slightly importing system to being an exporting system. The opposite happens with the drop in tidal range leading to an increase in the sediment import and to shallower channels.

Despite the different morphodynamic evolution of the channel, in all simulations, the system responds to SLR in the same manner. SLR induces sediment import in the system resulting in channel deposition thus leading to shallower channels compared to the No SLR case. For the dH 2.5 case, the SLR-induced channel deposition ($1.78 \times 10^7 \text{ m}^3$) is notably higher than the dH 3.5 case ($1.07 \times 10^7 \text{ m}^3$). The reason is that for the dH 2.5 case there are two forcing changes that are enhancing sediment import to the system, the SLR and the drop in tidal range. While for the dH 3.5, the SLR-induced import is opposing the export trend caused by the increase in dH. With regard to the shoal volume, SLR causes an increase in shoal volume due to deposition, again this increase is more pronounced in the case of dH 2.5 for the same above-indicated reason.

In addition to the tidal range, we also investigated the impact of a lunar spring-neap tidal cycle (LUN) and a schematized mixed semi-diurnal tidal cycle (MS) by implementing the tidal constituents M_2 with S_2 , and M_2 with C_1 (artificial constituent combining K_1 and O_1 ; lesser et al. 2009), respectively. The amplitudes for the M_2 , S_2 , and C_1 are 1.5, 0.4, and 0.2 m, respectively. The ratios between the tidal amplitudes are based on Wadden Sea conditions (Herrling & Winter, 2015). We assume no phase differences between the constituents.

Results show a similar SLR adaptation as the base case (BW) simulation, albeit with different magnitudes. For the LUN case, without SLR, the increased tidal range/flow velocities during the spring tides resulted in deeper channels (lower channel volume). However, the SLR adaptation remained the same with channels and shoals experiencing accretion. For the MS case, the small amplitude of the diurnal signal (0.2 m) resulted in limited differences compared to the BW simulation with the semi-diurnal signal.

It is important to note that the values presented in Figure 3.9 (set 4) are not corrected for the change in LW (border between shoals and channels) due to the change in the tidal

range between the simulations. The only difference is the volume magnitude based on what is considered shoals and channels. However, the SLR impact on the morphological development and the noted differences between the simulations do not change when implementing the corrections.

3.4.3.4 Sand supply

We investigated the impact of the sandy sediment supply on the morphological adaptation to SLR (Figure 3.9; set 5). We implemented lower (LS) and higher (HS) sand supply scenarios compared to the BW simulation by increasing and decreasing the open boundary SSC of the fine sand fraction by 50%, respectively. Without SLR, the decrease and increase in sediment supply mainly impacted the channel volume causing larger, and smaller volumes compared to the BW, respectively. For all sand supply scenarios, shoals and channels accrete in response to the SLR. However, the SLR-induced accretion is notably higher for the HS case than that for the LS. The shoal and channel accretion for the HS ($1.68 \times 10^7 \text{ m}^3$ and $1.67 \times 10^7 \text{ m}^3$) is more than 2 and 3.5 times than that for the LS ($0.77 \times 10^7 \text{ m}^3$ and $0.45 \times 10^7 \text{ m}^3$), respectively.

3.4.3.5 Mixture sand and mud fractions

In most sand-dominated estuarine environments and tidal basins, fine mud fractions are present as well in sheltered low-energy locations (e.g., Colombia River Estuary; Sherwood & Creager (1990), Western Scheldt Estuary; Kuijper et al. (2004), and Wadden Sea; Postma (1957)). We thus explored the impact of mud presence on the morphological response to SLR. Starting from an initial sandy bed (BW), we impose a mud fraction as a small constant concentration (20 mg/l) at the model seaward boundary. For these mixture runs, we simulate two situations of 100 years without and with 0.96 m/century nonlinear SLR. The mud transport is modeled using the Partheniades Krone formulations (Partheniades, 1965; Appendix A.1.3.2). This implementation accounts for the mud impact on the sand erodibility but not vice versa. The applied mud fractions have a critical erosion shear stress ($\tau_{c,e}$) of 0.25 N/m^2 , an erosion parameter (M) of 2.0×10^{-4} , and a settling velocity (w_s) of 0.5 mm/s for simulation Mix1 and 1 mm/s for simulation Mix2.

Figure (3.9; set 6) shows that, without SLR, the inclusion of mud results in more deposition in the model domain reflected by a larger shoal volume and less channel volume. This increase in sediment import to the system is due to the higher and finer SSC (sediment supply) imposed at the seaward boundary in the case of the mixture.

Sediment supplied at the seaward boundary needs time to reach landward locations (Figures 3.13b, and 3.13d). With the sand fractions, the landward-directed sediment transport is slower than with the finer mud fractions that can remain in suspension for a longer duration. This results in a larger deposition gradient along the basin axis for the sandy case. Mud inclusion resulted in a notably larger deposition at the landward section

(10 – 20 km) along with lower deposition at the more energetic seaward section. For the mixture cases, shoals experienced more SLR-induced deposition than the sandy case due to mud deposition. On the other hand, the channel deposition is lower as mud fractions are less likely to settle in the deep channels.

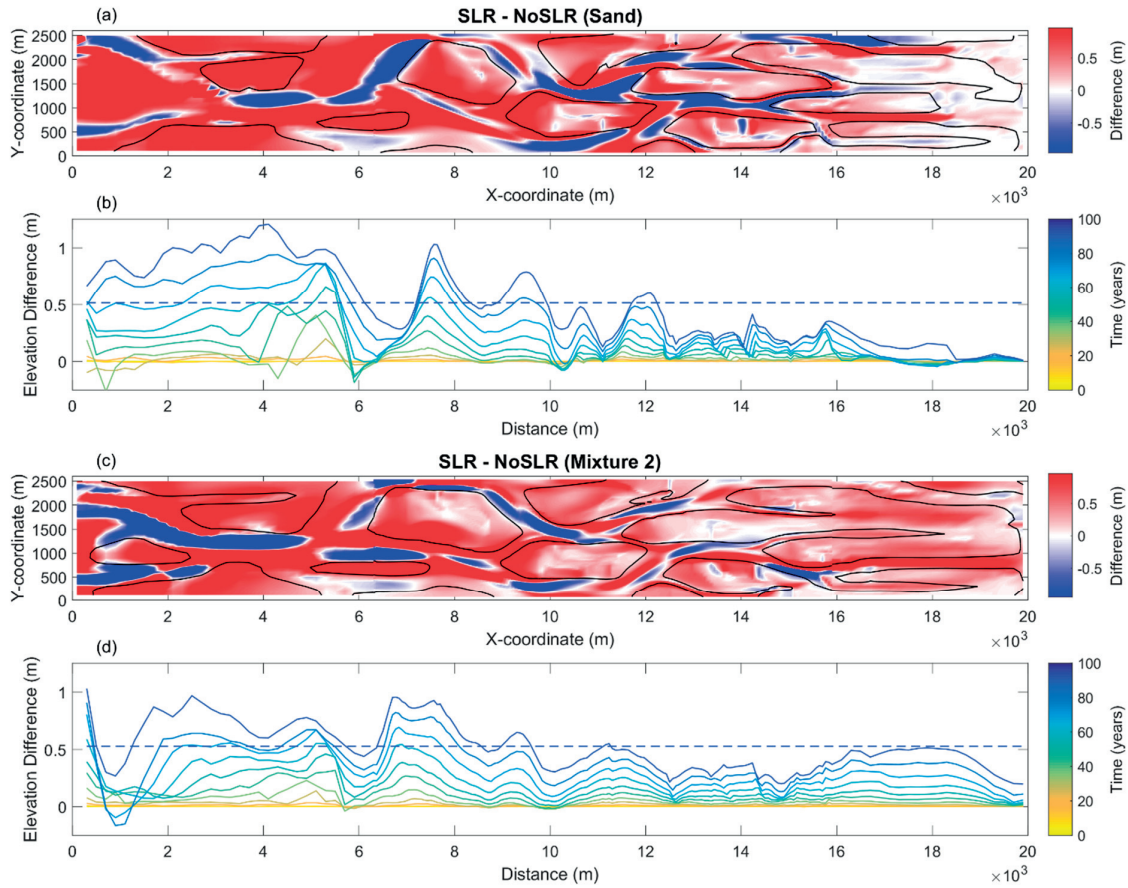


Figure 3.13. (a, and c) The elevation difference (m) between the SLR and No SLR scenarios for the sand (BW) and mixture 2 (Mix2) simulations, respectively. The black contour line indicates the border (LW) between the intertidal shoals and channels. (b, and d) The colored solid lines show the temporal development of the width-averaged elevation difference. The dotted line shows the end elevation difference averaged over the whole domain.

Figure 3.14 shows the mud percentage in the top sediment layer (0.25 m) for Mix1 and Mix2 with and without SLR. Mud fractions mainly settle on the shoals while the channels with larger flow velocities remain relatively mud-free. Without SLR, the mud presence in the system remains comparatively low. SLR results in muddier shoals with landward locations mainly experiencing the largest differences, while the mud content in the channels does not change much. A difference in the mud settling velocity (w_s) has an impact on the mud availability in the system. With the w_s of 1 mm/s (Mix2), mud is more

easily deposited on the shoals which results in muddier shoals than the lower w_s of 0.5 mm/s (Mix1). However, the deposition locations are similar for both cases. Mud fractions favor deposition in locations subjected to low flow velocities and wave attack such as downwind shoal locations and landward shoals.

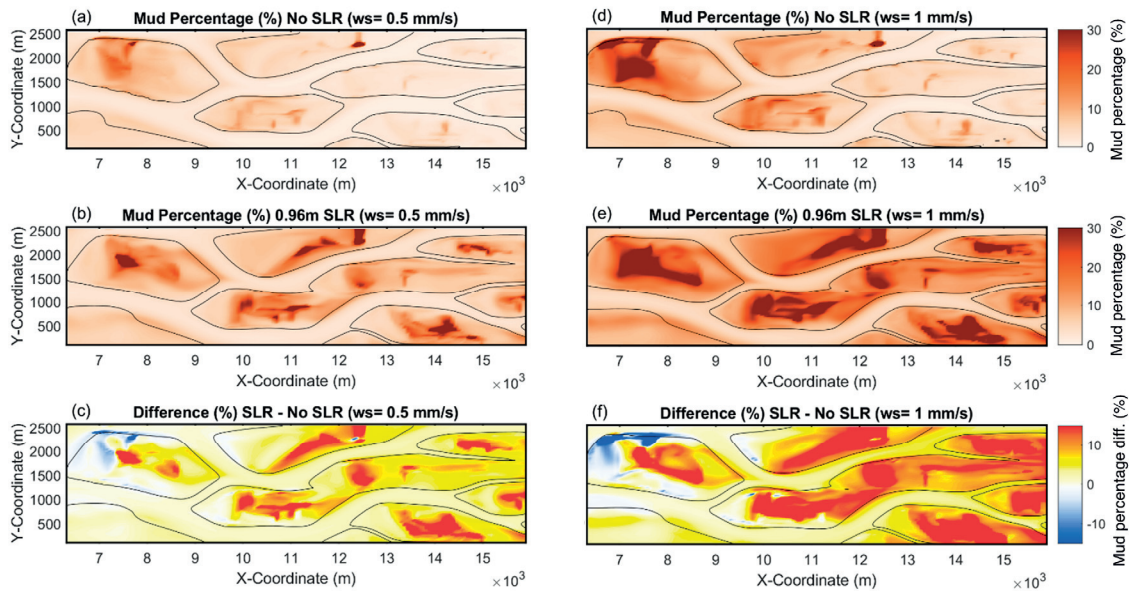


Figure 3.14. The mud percentage (%) in the top 0.25 m sediment layer for the simulation with a settling velocity of (a, and b) $w_s = 0.5$ mm/s, and (d, and e) $w_s = 1$ mm/s each without and with SLR, respectively. The difference between the mud percentage (%) for the No SLR and the 0.96 m non-linear SLR scenario for the different settling velocities. The black contour lines indicate the border (LW) between intertidal shoals and channels.

3.5 DISCUSSION

In accordance with previous studies (e.g., Coeveld et al., 2003; Hibma, 2004; van der Wegen & Roelvink, 2008), this study shows that tide-residual sediment transports are the main driver of the morphological development of channel-shoal systems in a tidal embayment. Our work highlights that changes in the tidal currents combined with the sediment availability drive the SLR morphodynamic adaptation of intertidal sandy shoals by accretion. Wave action is a secondary but important process which impacts the shoal morphology but not the basin's SLR response. The presence of fine sediment supply (mud) enhances the morphological adaptation.

3.5.1 Implications for real case studies

Forcing conditions vary in nature between the different systems depending on the local environment and hydraulic conditions. We expect the relevance of the mechanisms

underlying SLR adaptation (e.g., tidal action, sediment supply, and wave action) to vary between the different systems as well. Mudflats in San Francisco Bay are projected to accrete with SLR mainly due to a drop in the wave-induced shear stresses at larger water depths which allow for mud deposition (Elmilady et al., 2019; Neil K. Ganju & Schoellhamer, 2010; van der Wegen, Jaffe, et al., 2017). A lack of sediment supply constrains shoal accretion causing a notable decline of the intertidal areas due to the morphodynamic adaptation time lag.

Forcing conditions at the Wadden Sea basins are closer to those described in this study. The Wadden Sea sandy shoals accrete under current SLR mainly due to a tide-driven sediment import to the system caused by the creation of accommodation space under SLR, while waves play a secondary role by inducing sediment resuspension over the shoals (Dissanayake et al., 2009; Elmilady et al., 2020; Wang et al., 2018). During the Holocene, over the past 7000 years, the Wadden Sea tidal basins reacted to SLR by shifting landward. SLR not only caused a vertical increase in accommodation space but also a landward expansion of the basin boundary. An apparently insufficient external sediment sand supply could not fill this increase, leading to substantial erosion and recession of the coastline of the bounding barrier islands. Hence, the whole system migrated landward. With the deceleration of the Holocene SLR, the basin partly filled in and coastal recession declined (see Beets & van der Spek, 2000 for details). The construction of dykes and partial reclamation of the tidal basins prevent a landward translation of the Wadden Sea under future accelerating SLR. The predicted accelerating SLR is expected to increase the flood dominance of the system and the associated sediment import (Dissanayake et al., 2009; Seiffert et al., 2014; Wachler et al., 2020). Lodder et al., (2019), Wang et al. (2018) and Van Goor et al., (2003) predict a lag in the morphological adaptation to SLR leading to loss of intertidal areas. Their work highlights a critical SLR rate at which sediment import can become insufficient for the basin bed levels to follow the SLR causing the system to drown. Even with ample sediment availability, this drowning can occur due to insufficient transport capacity through the inlet.

The following sub-sections discuss some of our main modeling approach assumptions and their potential implications for our understanding of the SLR impact.

3.5.1.1 Marine transgression

We simulate a constrained system and the active build-up of existing intertidal shoals under SLR. Figures 3.15, 3.16, and 3.17 in Appendix 2 show examples of constrained systems in the Netherlands (Wadden Sea basins), Australia (Venus Bay), and New Zealand (Otago Harbour). In natural unconstrained systems, marine transgression (lateral expansion or landward migration) may also occur as a SLR adaptation mechanism (Allen, 1990; Beets & van der Spek, 2000; L. Guo et al., 2021; Townend et al., 2021). In addition

to the active shoal build-up, marine transgression will lead to “passive shoal formation” due to the drowning of the coastal plain causing dry land to shift from the supratidal realm into the intertidal realm. Guo et al. (2021) show the lateral expansion of a convergent system forming new tidal flats along its margins while existing inner intertidal shoals experience accretion in response to SLR.

3.5.1.2 Interacting time scales

We follow an approach that is based on isolating a century-scale SLR impact signal in a system with low morphological activity. In reality, the modeled morphological development could occur over a much longer time scale. Also, in real case studies, there could be other simultaneous and ongoing morphological adaptations with different time scales (decadal to geological) that could influence the SLR adaptation. Around the world, estuaries and tidal basins are subjected to dredging activities (Depreiter et al., 2013), land reclamation (MacKinnon et al., 2012), subsidence (Fokker et al., 2018), and changes in the tidal regime (Eelkema et al., 2013), varying riverine discharges, and sediment supply (Jaffe et al., 2007; Portela, 2006; B. Zhu et al., 2020). Also, other systems are still infilling and not in equilibrium (de Haas et al., 2018; e.g., van der Spek, 1994). This includes systems that were formed by the Holocene SLR and are still adapting to the decreasing SLR rates to their current levels (van der Spek & Beets, 1992). The past century's relatively low global SLR (≈ 0.2 m/century) makes it difficult to discriminate the SLR impact from other adaptations. Calibrating and validating long-term morphological models using observed historical evolution (e.g., bathymetries) is a challenging task that comprises notable uncertainties and does not necessarily guarantee the ability to capture the SLR contribution to the morphological evolution. Also, such historical data sets with sufficient frequency are extremely scarce. This makes the schematized approach presented by this study necessary for understanding the fundamental processes.

3.5.1.3 Sediment fractions and supply

In nature, tidal flats/shoals form in sediment-rich environments with sufficient fine-grained sediment supply (e.g., Friedrichs, 2011; Gao, 2019). Channel-shoal systems usually comprise a wide range of sediment fractions including coarse material which mainly exists in energetic deep sections (e.g., Wadden Sea; Postma (1957), and Figure 3.18 in Appendix 2). In this research, we implement two sand fractions. The coarse fraction mainly exists in channels and plays an important role in stabilizing the channel-shoal patterns such as by controlling the channel deepening, while shoals are mainly composed of the finer fraction. The existence of the finer sand fraction played an important role in the shoal SLR adaptation as it constituted the majority of the SLR-induced sediment import to the system causing the shoal accretion. They were more easily suspended and transported to fill the accommodation space created by the SLR. On the

other hand, simulations with a single coarse sand fraction (not presented) showed limited shoal adaptation due to low SSC levels and associated transports.

The imposed Base case SSC levels are based on typical conditions in the Wadden Sea (Postma, 1961, 1967, 1981). We assumed a constant sediment source at the boundary, while this might not be the case in reality if the morphological response of other elements (e.g., ebb-tidal delta) leads to a change in prevailing SSC. Some systems are predicted to face sediment supply shortages, while other systems could experience an increase in sediment supply (e.g., due to the erosion of other morphological elements). Our sand supply sensitivity showed that a sediment supply shortage/increase could limit/enhance the morphological adaptation, respectively. Adding a finer mud fraction also enhanced the morphological adaptation.

3.5.2 Future work

Gradually increasing the complexity of schematized models is of great value to better understand the potential SLR impact. Our research contributes by adding waves, mud, and high-resolution modeling along with focusing on the intertidal shoals. Several subjects remain for future exploration.

In our research, we mainly focus on a meso-tidal environment with a semi-diurnal tidal signal. Sensitivity analysis with tidal ranges, a lunar spring-neap tidal cycle, and a schematized mixed semi-diurnal tidal cycle showed the same trend of SLR morphological adaptation. We recommend performing a more detailed investigation of the impact of lunar and mixed semi-diurnal tidal cycles by testing different amplitudes and relative phasing. Also, overtides (e.g., M4, and M6) and their relative phasing could be highly relevant for the morphodynamics of tidal systems (e.g., Lesser, 2009). In addition, the impact of the SLR-induced changes of the tidal dynamics at the seaward boundary of tidal systems requires exploration.

We investigated non-convergent, short tidal basins which are dominated by intertidal shoals. Future work should investigate different geometries and bathymetries along with larger-scale basins and the availability of accommodation space. The dimensions (length, width, depth, and convergence) of tidal systems can impact their SLR adaptation (Leuven et al., 2019). Including riverine discharges and sediment supply makes findings more relevant to estuarine systems with notable riverine influence. Finally, implementing a more complex sand-mud interaction scheme would further increase the value of the results.

3.6 CONCLUSIONS

Our work investigates the SLR impact on the long-term morphological development of intertidal sandy shoals. This includes exploring the importance of small wind-generated waves along with the mud presence to the intertidal morphodynamics. We implemented a 2DH process-based numerical model (Delft3D) which simulates the morphological evolution and the SLR adaptation of a channel-shoal system in a constrained short tidal basin dominated by intertidal shoals.

Tidal currents are the main driver of the channel-shoal system's morphological evolution. Shoals evolve as a result of the tide-residual sediment transport convergence. Over time, the morphological activity gradually slows down as the residual transports diminish. Our work highlights that wave action is a secondary but important process which impacts the shoal morphology but does not fundamentally change the morphological evolution of the system. Wave-induced shear stresses enhance the sediment transport and distribution over shoals leading to lower and smoother intertidal flats.

Shoals accrete in response to SLR due to tide-residual sediment transports. Wave action, again, plays a secondary role in the sense that it impacts the intertidal shoal morphology but not the basin's response to SLR in general terms. The morphodynamic adaptation lags behind SLR eventually leading to the drowning of intertidal shoal areas under SLR. Loss of shoal area favors flood dominance which, combined with the availability of sediment supply, triggers sediment import to the system. Locations near the sediment source experience more accretion both on a basin-scale and on a shoal-scale. A larger sediment supply enhances the SLR morphodynamic adaptation. Waves help distribute sediment supplied from channels across shoals. The presence of mud enhances the morphodynamic adaptation leading to faster, more uniform, accretion and muddier shoals under SLR.

The knowledge developed in this study serves as a fundamental step towards assessing the potential impact of SLR on the sustainability of valuable, intertidal environments. Future studies should focus on including other processes and forcing conditions.

APPENDIX 2

A.2.1 Hydrodynamics

We apply the Delft3D (D3D) process-based numerical model (Deltares, 2017; Lesser et al., 2004). Delft3D-FLOW computes the flow by solving the unsteady two-dimensional shallow water equations (continuity and momentum). The continuity equation (Eq. A.2.1) and the horizontal momentum equations (Eq. A.2.2, and A.2.3), neglecting the influence of density differences, and Coriolis force are as follows:

$$\frac{\partial \eta}{\partial t} + \frac{\partial hu}{\partial x} + \frac{\partial hv}{\partial y} = 0 \quad (\text{A.2.1})$$

$$\frac{\partial u}{\partial t} + u \frac{\partial u}{\partial x} + v \frac{\partial u}{\partial y} + g \frac{\partial \eta}{\partial x} + c_f \frac{u\sqrt{u^2+v^2}}{h} - v_e \left(\frac{\partial^2 u}{\partial x^2} + \frac{\partial^2 u}{\partial y^2} \right) - \frac{\tau_{sx}}{\rho h} - F_x = 0 \quad (\text{A.2.2})$$

$$\frac{\partial v}{\partial t} + v \frac{\partial v}{\partial y} + u \frac{\partial v}{\partial x} + g \frac{\partial \eta}{\partial y} + c_f \frac{v\sqrt{u^2+v^2}}{h} - v_e \left(\frac{\partial^2 v}{\partial x^2} + \frac{\partial^2 v}{\partial y^2} \right) - \frac{\tau_{sy}}{\rho h} - F_y = 0 \quad (\text{A.2.3})$$

With,

$$c_f = \frac{g}{c^2} \quad (\text{A.2.4})$$

Where, η is the water level with respect to the datum, h is the water depth, u and v are the horizontal depth-averaged velocities in the x and y directions, respectively, g is the gravitational acceleration, ρ is the water density, c_f is the friction coefficient, c is the Chezy coefficient (60 m^{1/2}/s), v_e is the eddy viscosity (1 m²/s), τ_s is the wind shear stress, and F_x and F_y are the depth-averaged wave-induced forcing.

A.2.2 Wave model

The spectral wave model SWAN (Booij et al., 1999; <http://swanmodel.sourceforge.net/>) is used in stationary mode to simulate the wind-generated waves. The SWAN model is based on the action density spectrum $N(\sigma, \theta)$, where σ is the relative frequency, and θ is the wave direction. The spectral action balance equation in Cartesian coordinates is:

$$\frac{\partial}{\partial t} N + \frac{\partial}{\partial x} c_x N + \frac{\partial}{\partial y} c_y N + \frac{\partial}{\partial \sigma} c_\sigma N + \frac{\partial}{\partial \theta} c_\theta N = \frac{S}{\sigma} \quad (\text{A.2.5})$$

Where, c_x , c_y , c_σ , and c_θ are the propagation velocities in the x, y, σ , and θ -space, respectively. The first term on the left-hand side describes the local rate of change of the action density in time. The second and third terms describe the propagation of the action density in space. The fourth term describes the shift of the relative frequency due to depth and current variations. The fifth term describes the depth- and current-induced refraction. The right-hand side term denotes the source term for the action density which includes generation by wind, dissipation by bottom friction, and depth-induced breaking. The Delft3D-Flow uses the gradients of the radiation stress tensor (S) to compute the depth-

averaged wave-induced forcing (F_x and F_y ; Eq. A.2.6 and A.2.7) which is a source term in the momentum equations. Also, the hydrodynamic equations are solved in Generalised Lagrangian Mean (GLM; Andrews and McIntyre 1978) formulation in order to account for the Stokes drift caused by the wave oscillating motion. Furthermore, the Fredsoe formulations (Fredsoe, 1984) are used to compute the maximum shear stress (τ_{max}) based on the combined current (τ_c) and wave (τ_w) shear stress.

$$F_x = -\frac{\partial S_{xx}}{\partial x} - \frac{\partial S_{yx}}{\partial y} \quad (\text{A.2.6})$$

$$F_y = -\frac{\partial S_{xy}}{\partial x} - \frac{\partial S_{yy}}{\partial y} \quad (\text{A.2.7})$$

A.2.3 Sediment transport

Suspended sediment transport is calculated in the D3D by an advection-diffusion solver (Eq A.2.8) which includes a sink and source term and is based on the local and time-varying velocities and water levels.

$$\frac{\partial hc}{\partial t} + \frac{\partial huc}{\partial x} + \frac{\partial hvc}{\partial y} = \frac{\partial}{\partial x} (h\varepsilon_h \frac{\partial c}{\partial x}) + \frac{\partial}{\partial y} (h\varepsilon_h \frac{\partial c}{\partial y}) + S \quad (\text{A.2.8})$$

Where c is the sediment mass concentration (kg/m^3), ε_h is the prescribed horizontal diffusivity ($7 \text{ m}^2/\text{s}$), S is the source/sink term which represents the exchange of sediment between the bed and flow (water column). The Van Rijn (1993) formulations are used to compute the sandy sediment transport for the combined effect of waves and currents for both bedload and suspended load transport. A reference height a is defined to distinguish between the bed and suspended transport as follows:

$$a = \min \left[\max \left(AKSFaC k_s, \frac{\Delta r}{2}, 0.01h \right), 0.20h \right] \quad (\text{A.2.9})$$

Where $AKSFaC$ is a user-defined proportionality factor, k_s is a user-defined effective roughness height, Δr is the wave-induced ripple height (0.025 m). The critical bed shear stress is computed mainly based on the median sediment diameter (D_{50}) and according to the classical Shields curves. A reference concentration is calculated based on the sediment availability in the top bed layer (Van Rijn et al., 2000). This concentration is imposed at the reference height in order to entrain bed sediment to the water column. The settling velocity (w_s) of sand fractions in suspension is calculated based on (Van Rijn, 1993) as follows:

$$w_s = \frac{10v}{D_{50}} \left(\sqrt{1 + \frac{0.01(s-1)gD_{50}}{v^2}} - 1 \right) \quad \text{for } 100 \mu\text{m} < D_{50} \leq 1000 \quad (\text{A.2.10})$$

Where, s is the relative density (ρ_s / ρ_w), and v is the water kinematic viscosity coefficient. For more details on suspended sediment entrainment and deposition computation please

refer to (Deltares, 2017). The bedload is calculated according to (Van Rijn, 1993) based on the combined flow and wave as follows:

$$|S_b| = 0.006 \rho_s w_s D_{s0} \frac{u_{eff} (u_{eff} - u_{cr})^{1.4}}{[(s-1)gD_{s0}]^{1.2}} \quad (\text{A.2.11})$$

$$u_{eff} = \sqrt{u_R^2 + U_{on}^2} \quad (\text{A.2.12})$$

Where, S_b is the bedload transport (kg/m/s), u_{eff} is the combined velocity magnitude (m/s) of the flow depth-averaged velocity and the near-bottom peak orbital velocity in the onshore direction based on the significant wave height (H_s), u_{cr} is the critical depth-averaged velocity for motion initiation based on Shields curve (m/s), u_R is the magnitude of an equivalent depth-averaged velocity (m/s), and U_{on} & U_{off} are the high frequency near-bed orbital velocities due to short waves in the on and offshore directions, respectively. The direction of the bedload transport is computed based on a division into current-induced transport ($S_{b,c}$) which acts in the flow direction and wave-induced transport ($S_{b,w}$) which acts in the wave direction.

$$S_{b,c} = \frac{S_b}{\sqrt{1 + r^2 + 2|r|\cos\varphi}} \quad (\text{A.2.13})$$

$$|S_{b,w}| = r |S_{b,c}| \quad (\text{A.2.14})$$

$$r = \frac{(|U_{on}| - u_{cr})^3}{(|u_R| - u_{cr})^3} \quad (\text{A.2.15})$$

We apply the Partheniades-Krone formulations (Partheniades, 1965) for cohesive sediment transport, please refer to Appendix A.1.3.2 for the formulations.

A.2.4 Wind conditions

In addition to a constant wind speed of 4 and 6 m/s, we implement a temporary varying wind speed from a minimum value of 2 m/s to a maximum value of 5.35 m/s. The wind cycle is imposed over 4 tidal cycles in order not to associate a specific wind speed with a specific time during the tidal cycle (see Figure 3.26a). During the first and third tidal cycles, the wind speed is constant with the minimum and maximum values, respectively. While, during the second and fourth tidal cycles, the wind speed is either linearly increasing from the minimum or decreasing from the maximum, respectively.

The magnitude of the wave-averaged bed shear-stress ($\bar{\tau}_w$) due to waves is a function of the wave orbital velocity near the bottom (u_{orb}), water density (ρ), and the friction coefficient (f_w) as follows:

$$|\bar{\tau}_w| = \frac{1}{2} \rho f_w u_{orb}^2$$

Based on that, the spatially and temporally averaged magnitude of u_{orb}^2 is used as a metric to compare the wave action between the different scenarios (see Figure 3.26b). For example, the constant base wind speed of 4 m/s creates a wave field approximately equivalent to a varying wind speed from 2 to 5.35 m/s (W1).

A.2.5 Shoal slope computation

Figure 3.25 shows the bed level slope over the shoal elevation range. The slopes are calculated based on the contour lines. The slope of each contour belt with a mean contour (z) and bound by a lower ($z-\Delta z/2$) and upper ($z+\Delta z/2$) contour is calculated as follows:

$$\frac{dz}{ds} = \frac{\Delta z}{\Delta \bar{s}}$$

Where, Δz is the elevation difference between the two bounding contour lines (0.15 m), and $\Delta \bar{s}$ is the average horizontal distance between the two contours which is calculated as follows:

$$\Delta \bar{s} = \frac{\Delta A}{l(z)} = \frac{A_{z+\Delta z/2} - A_{z-\Delta z/2}}{l(z)}$$

Where, ΔA is the area between the lower and upper contours, and $l(z)$ is the length of the mean contour line at elevation (z). For more information, regarding the shoal slope calculation, please refer to de Vet et al. (2017).

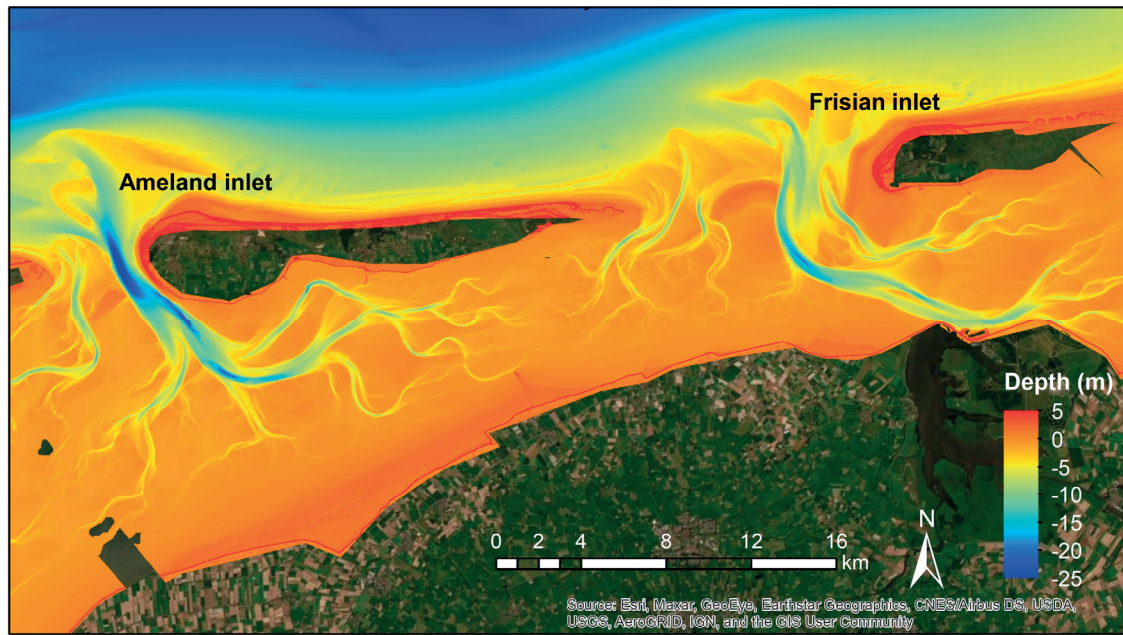


Figure 3.15. Satellite image of the Ameland and Frisian Inlet (Wadden Sea, The Netherlands) with the 2011/2012 bathymetry (m; source: Rijkswaterstaat) plotted. (<https://publicwiki.deltares.nl/display/OET/Dataset+documentation+Vaklodingen>)

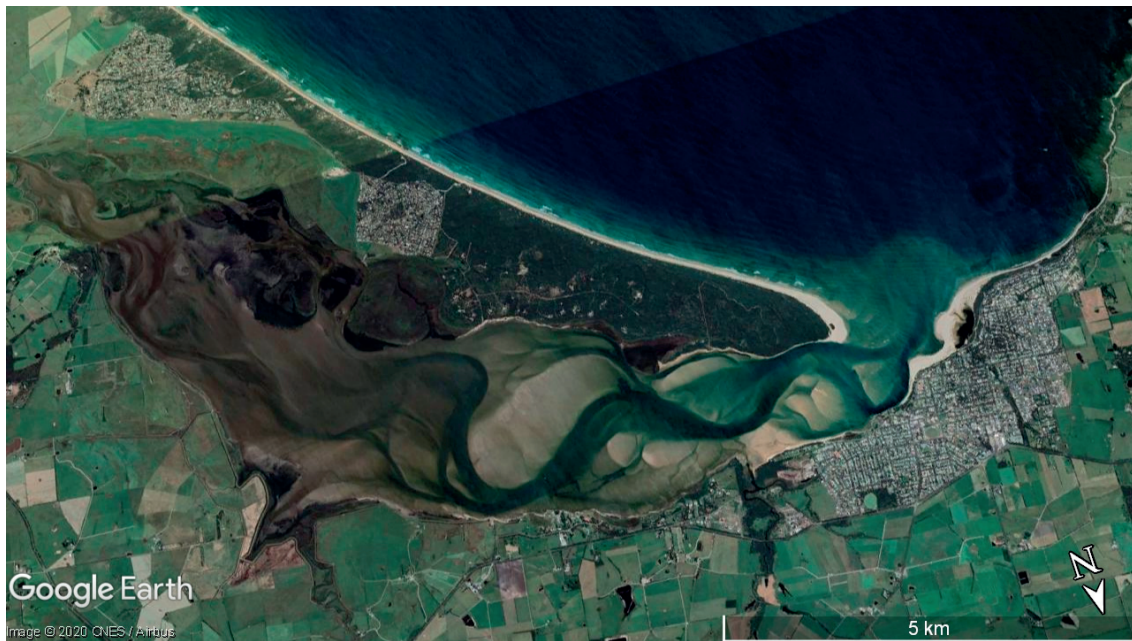


Figure 3.16. Google Earth image of Anderson Inlet and Venus Bay (Victoria, Australia).

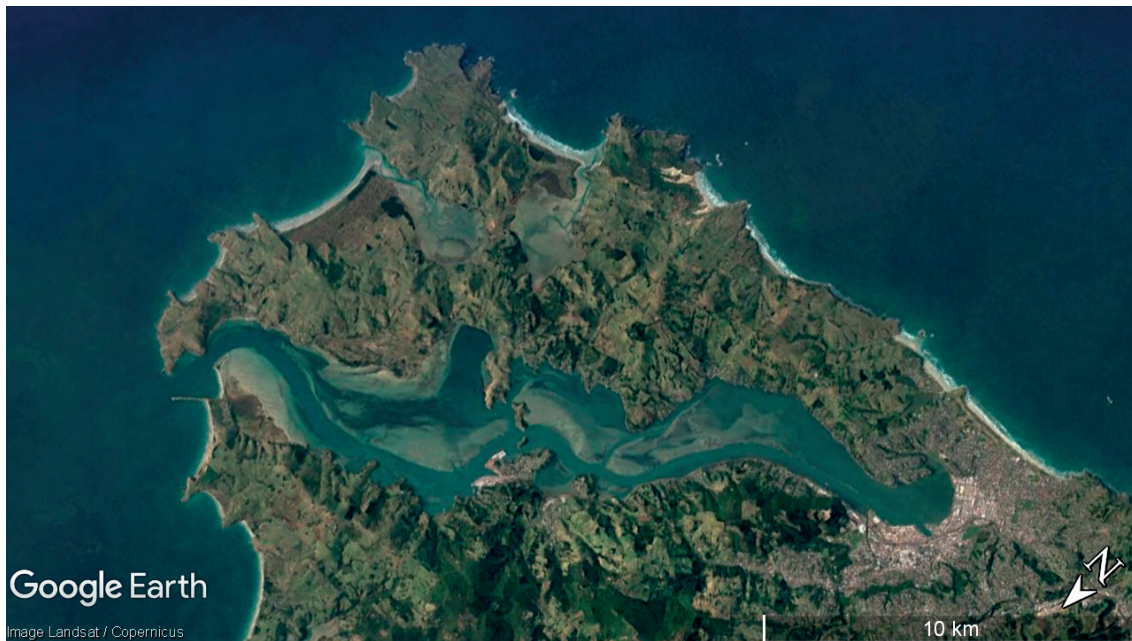


Figure 3.17. Google Earth image of Otago Harbour (Dunedin, New Zealand).

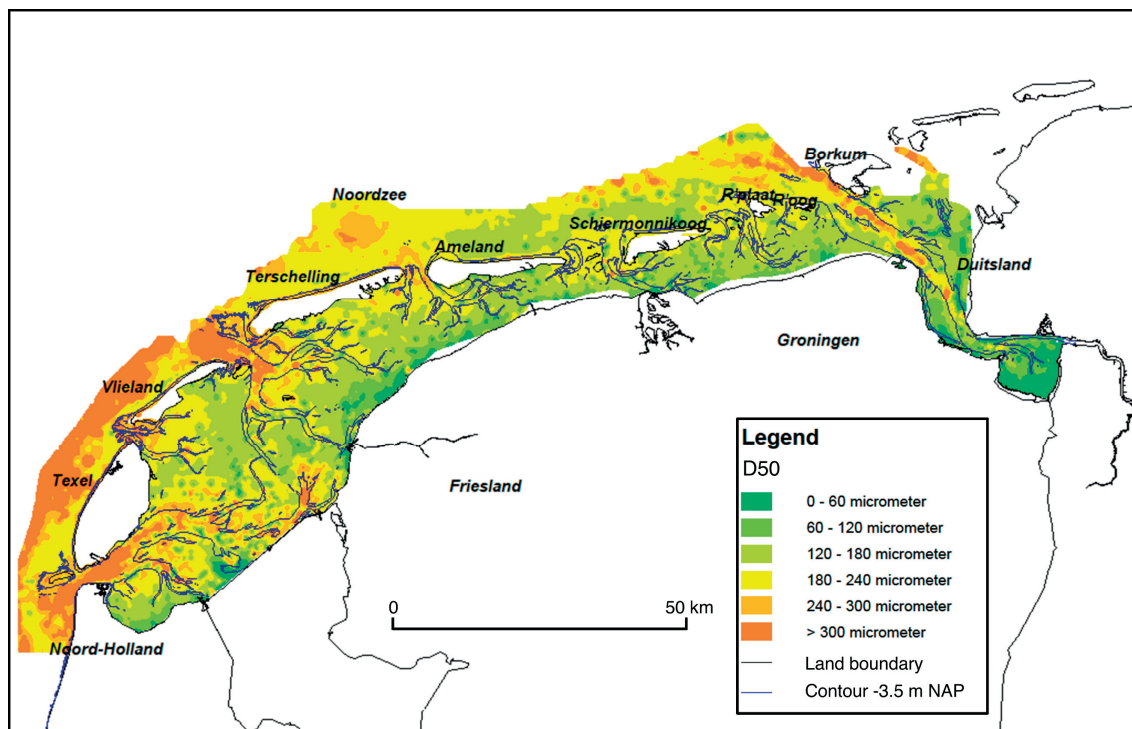


Figure 3.18. Median grain size in the Wadden Sea (The Netherlands). The figure is generated using the Sediment Atlas Wadden Sea.
(<https://publicwiki.deltares.nl/display/OET/Dataset+documentation+Sediment+atlas+wadden+sea>)

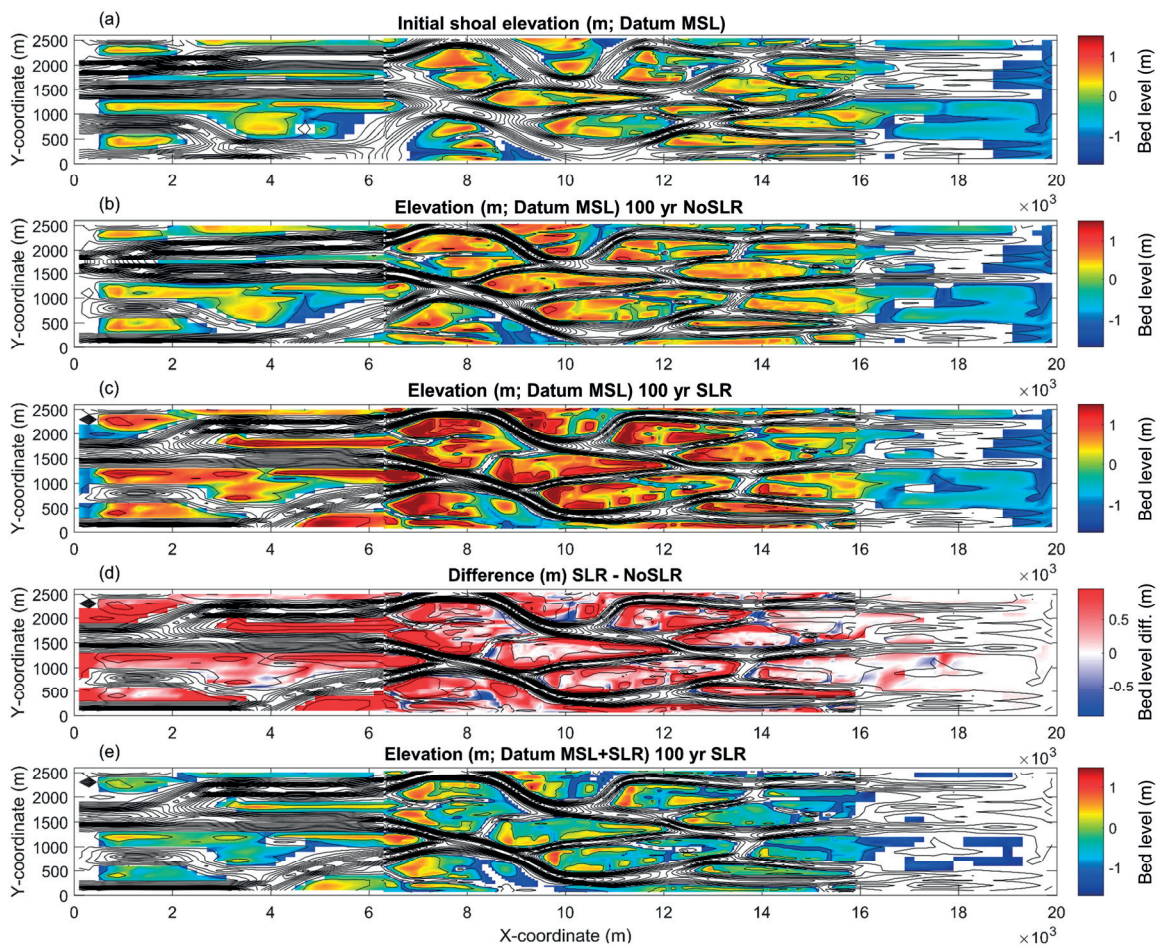


Figure 3.19. SLR impact on the shoal morphology for the simulation excluding wind-wave impact (Base Flow; BF). (a) The initial shoal elevation (m; with respect to MSL), (b) the shoal elevation (m; w.r.t MSL) after 100 years with no SLR, (c) the shoal elevation (m; w.r.t MSL) after 100 years with a non-linear 0.96 m/century SLR, (d) the difference between the shoal elevation for the SLR and No SLR scenarios (color bar from -0.96 to 0.96 m), and (e) the shoal elevation (m; w.r.t MSL + SLR) corrected with the SLR magnitude. The black lines are the elevation contours with 1 m intervals.

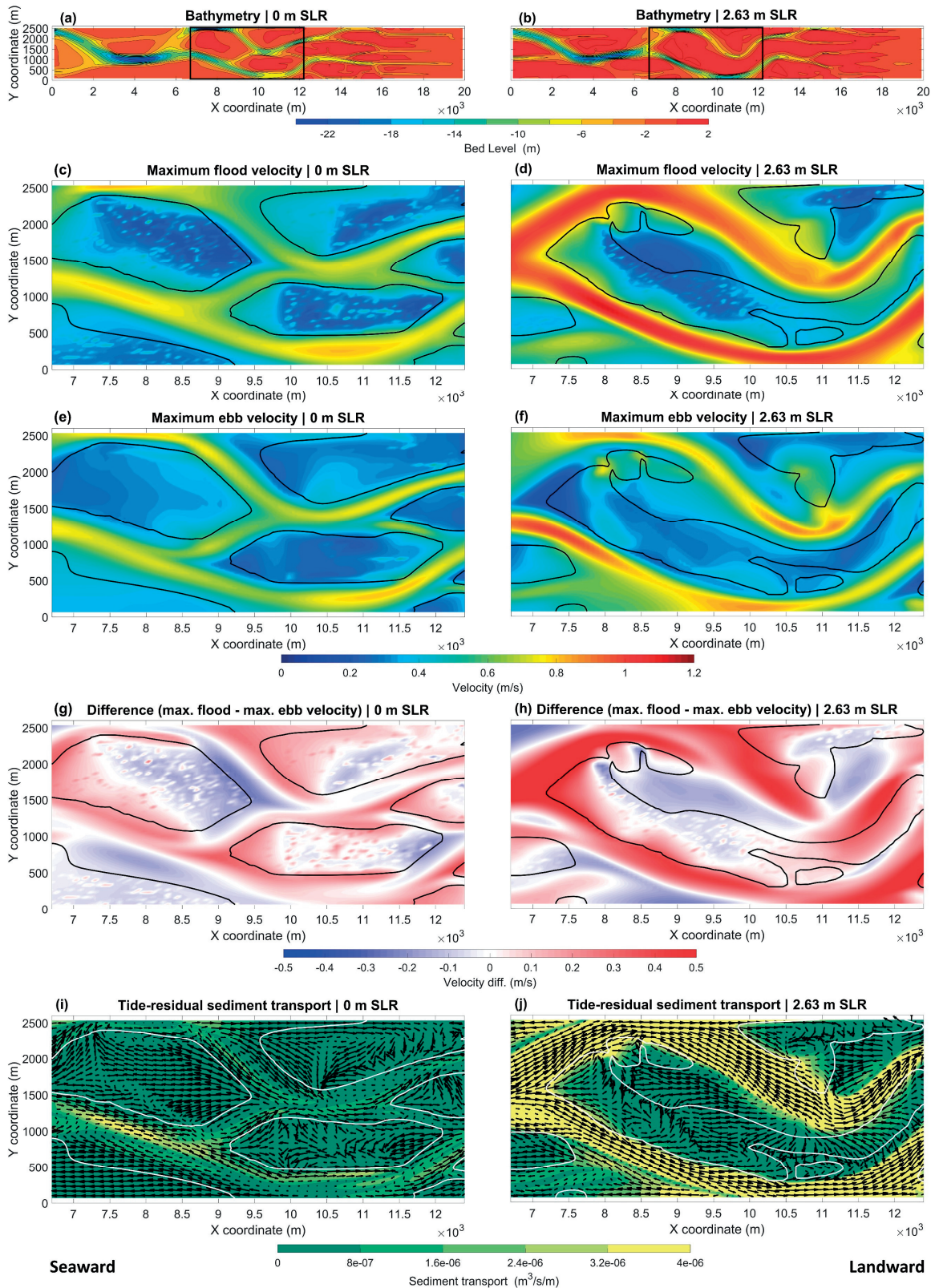


Figure 3.20. The modeled bathymetry (m) for the Wave Base-case simulation after 100 years with (a) no SLR, and (b) 2.63 m SLR. The black box indicates the location of the

below plots. (c, and d) Maximum flood velocities, (e, and f) Maximum ebb velocities, (g, and h) difference between maximum flood and ebb velocities, and (i, and j) the tide-residual sediment transport magnitude ($m^3/s/m$) and direction. Arrows are RMS normalized and plotted on a grid with half the model grid resolution to make them more visible. The black/white contour lines indicate the border (LW) between the intertidal and subtidal areas.

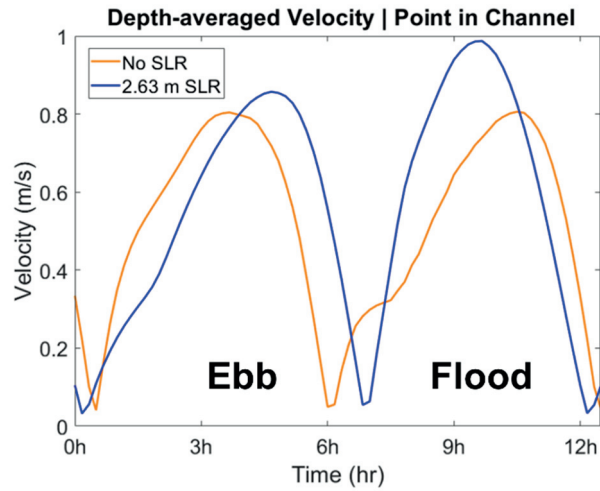


Figure 3.21. Depth-averaged velocities during a tidal cycle at a point in the channel for the No SLR (orange) and 2.63 m SLR (blue) scenarios.

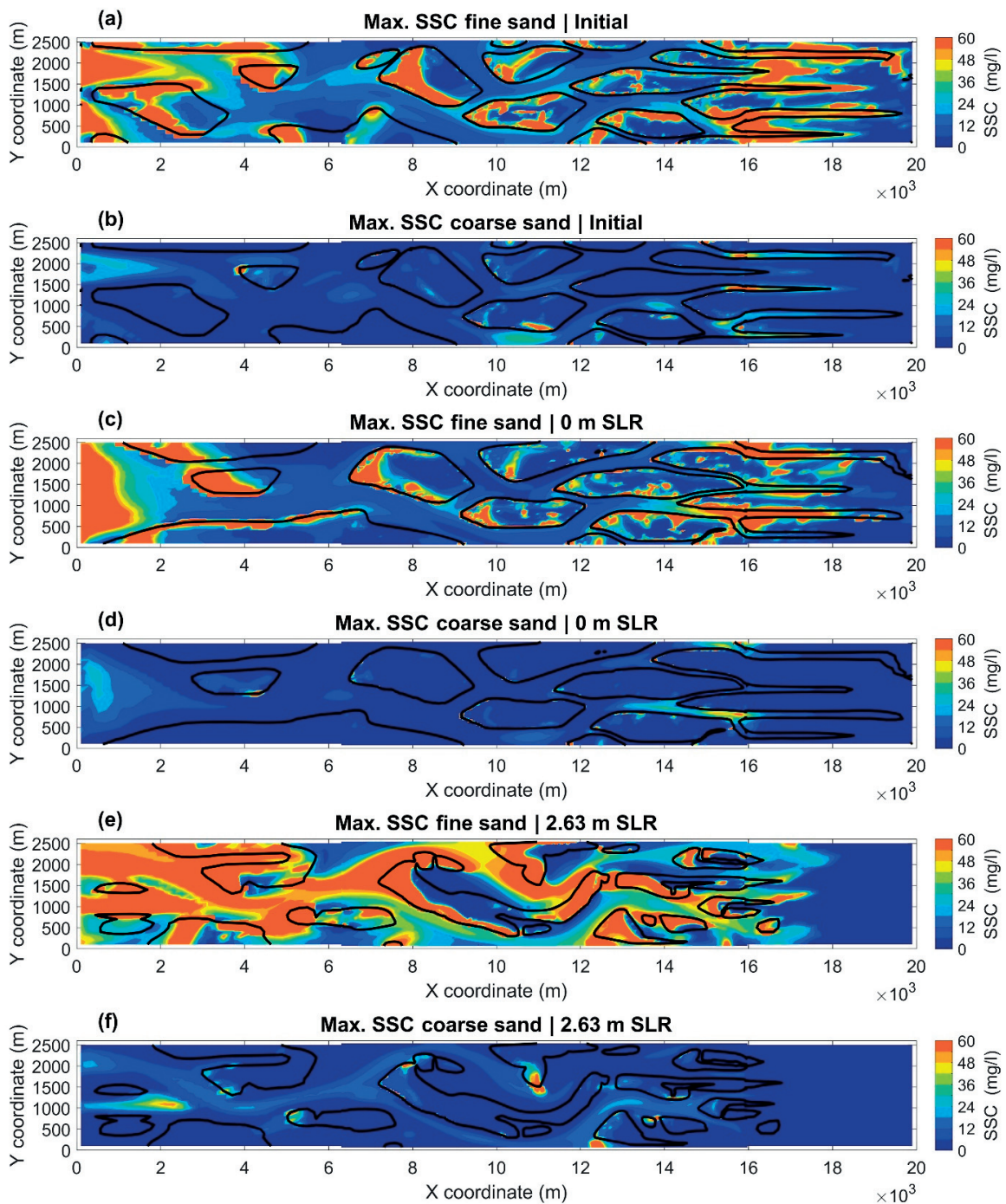


Figure 3.22. Maximum depth-averaged suspended sediment concentration (SSC; mg/l) for the fine (100 μm) and coarse (250 μm) sand fractions; (a, and b) Initial, (c, and d) after 100 years with no SLR, and (e, and f) after 100 years with a 2.63 m/century SLR.

3. Modeling the Morphodynamic Response of Estuarine Intertidal Shoals to Sea-Level Rise

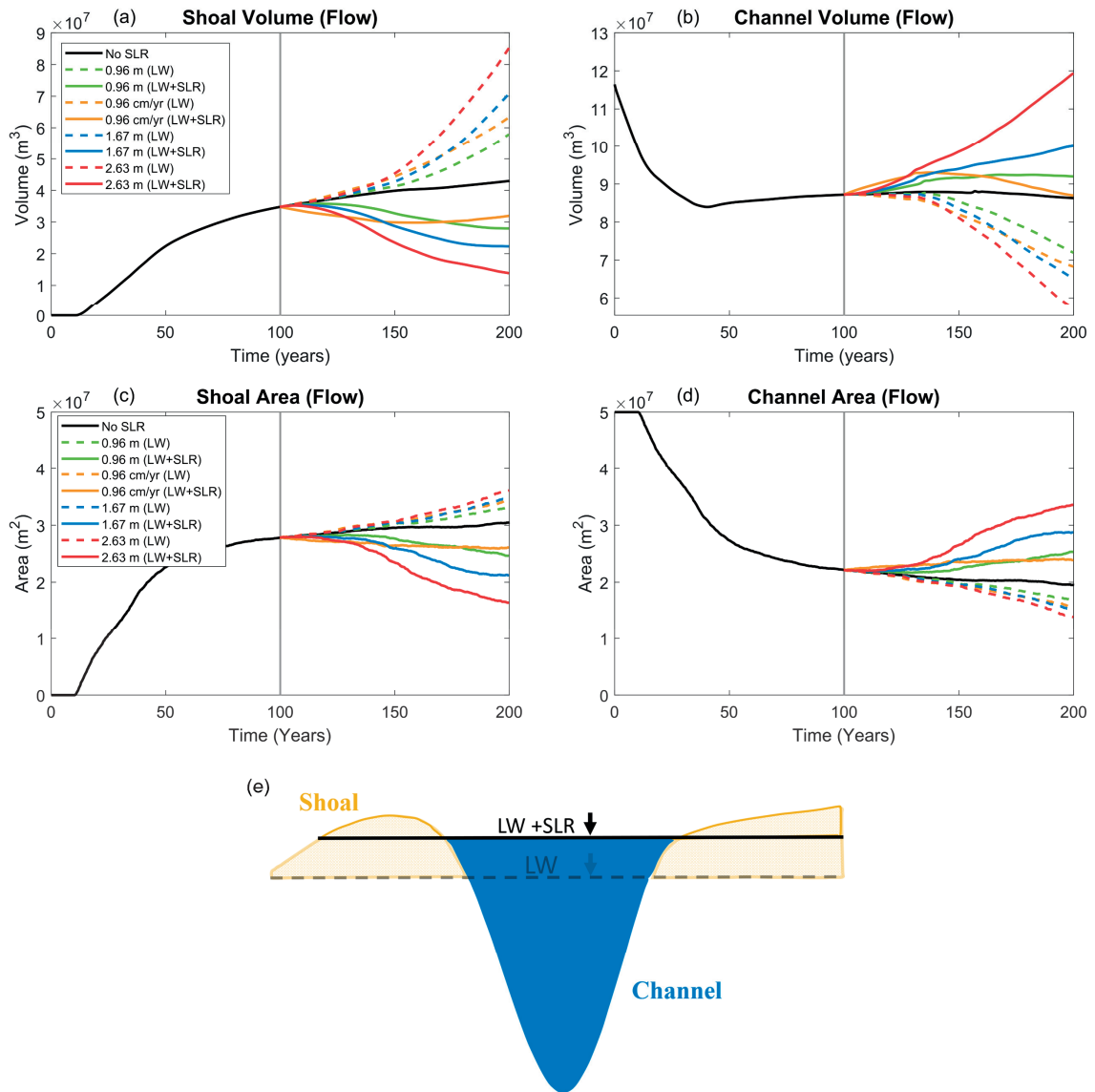


Figure 3.23. The temporal development of the shoal (a) and channel (b) volume (m³) and the shoal (c) and channel (d) area (m²) for the whole model domain and for the Flow simulations. The solid black line is the No SLR scenario, while the color lines are for the different SLR scenarios. (e) Schematic showing the shoal and channel definition along with the datums used for the dashed lines (fixed datum; LW), and the solid lines (moving datum; LW+SLR).

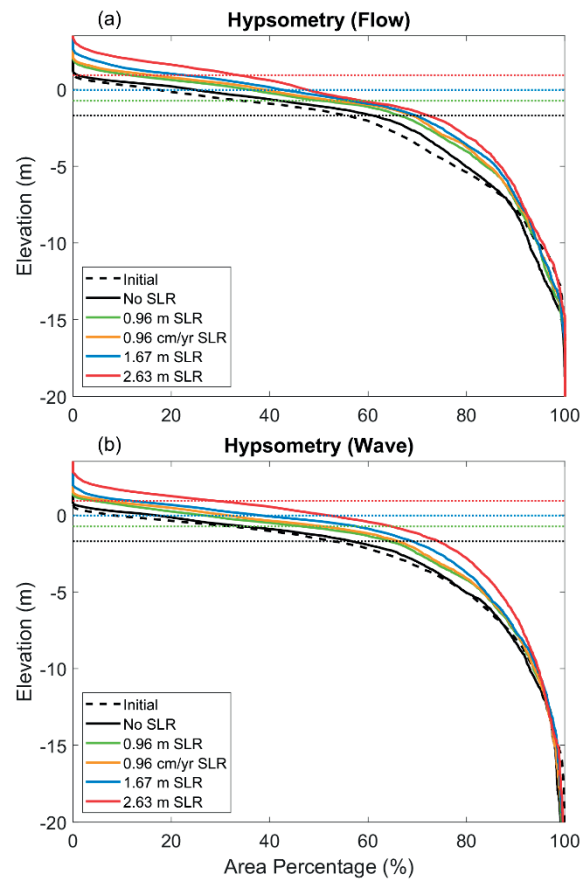


Figure 3.24. Hypsometry curves of the (a) Flow, and (b) Waves simulations for the different SLR scenarios. The horizontal dotted lines indicate the border ($LW + SLR$) between the intertidal and subtidal sections of the hypsometry for the different scenarios.

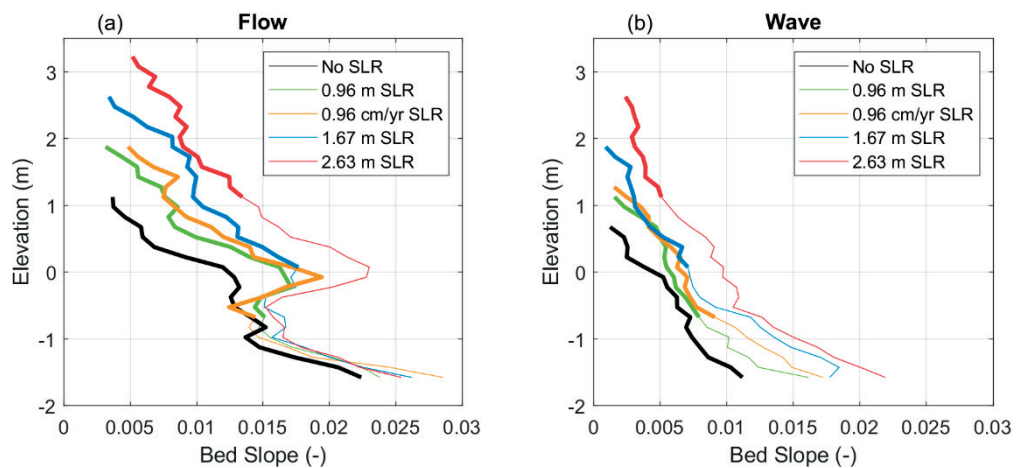


Figure 3.25. The bed level slopes vs elevation (m; w.r.t MSL) in the whole model domain for the simulations without (a) and with (b) wave action and for the different SLR scenarios. The thick solid line indicates the elevation range corresponding to the intertidal section of the shoal.

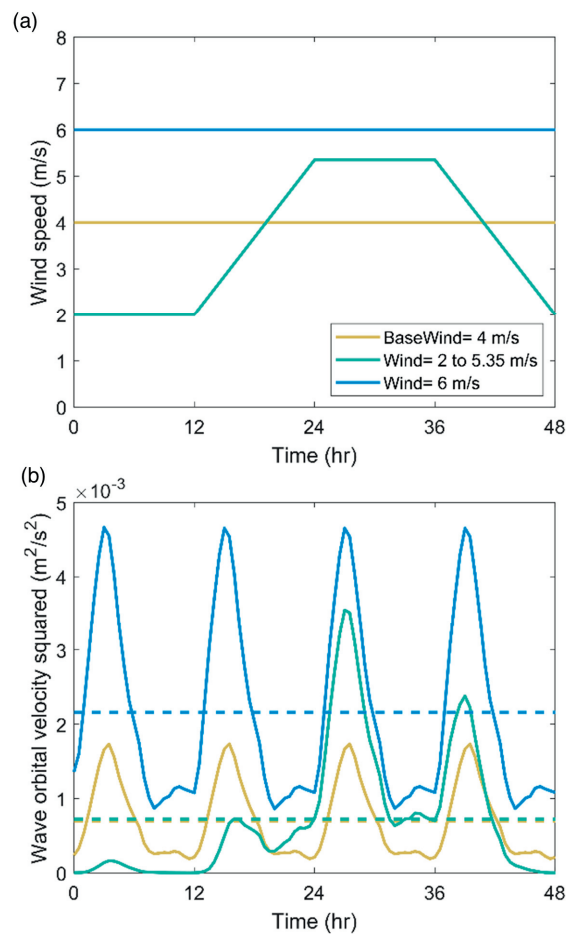


Figure 3.26. (a) Wind speed (m/s) during a wind cycle (48 hours). (b) The spatially averaged wave orbital velocity squared (m^2/s^2) across the whole model domain during a wind cycle (solid lines). The dashed lines indicate the time average.

4

INTERTIDAL AREA DISAPPEARS UNDER SEA LEVEL RISE 250 YEARS OF MORPHODYNAMIC MODELING³

Abstract

Anticipated sea level rise (SLR) threatens intertidal areas and associated ecosystems in estuaries worldwide. There is a need to develop validated modeling tools to assess the impact of SLR on estuarine morphodynamics. This study explores the morphological impact of SLR on a channel-shoal system in San Pablo Bay, a sub-embayment of San Francisco Bay, California, using a 3D, process-based modeling approach (Delft3D) including density currents and wave action. The Bay underwent considerable morphologic development in response to variations in fluvial sediment load and discharge associated with a period of hydraulic mining for gold and later damming in the watershed. The availability of a unique 150-year, 30-year sequenced, bathymetric data set provided a rare opportunity for model validation. We investigate a 250-year period of morphodynamic evolution including a 150-year hindcast and a 100-year forecast with different SLR scenarios. The model shows significant skill in hindcasting volumes and

³ This chapter is based on:

Elmilady, H., van der Wegen, M., Roelvink, D., & Jaffe, B. E. (2019). Intertidal Area Disappears Under Sea Level Rise: 250 Years of Morphodynamic Modeling in San Pablo Bay, California. *Journal of Geophysical Research: Earth Surface*, 124(1), 38–59. doi:10.1029/2018JF004857

patterns of bathymetric development during both net depositional (1856-1951) and erosional (1951-onwards) periods. Forecasts show that sea level rise alters the Bay's erosional trend to a depositional trend again. Despite increased sediment trapping rates the intertidal mudflats drown under all modeled SLR scenarios (42, 84, and 167 cm by end of the 21st century). Our work highlights the potential of using process-based models to assess the morphodynamic impact of SLR. The study also suggests that SLR can greatly increase the loss of intertidal area when landward migration is not possible. Sustainable management strategies are required to safeguard these valuable intertidal habitats.

4.1 INTRODUCTION

Estuaries are the transition zones between land and sea where the interaction between freshwater and tidally varying saline water makes it one of the most productive ecosystems in the world (Harvey et al., 1998). The estuarine bed has a dynamic nature and is subject to marine (e.g., waves, tides, salinity, and sea level) and fluvial (e.g., discharges and sediment load) forcing. Sediments may have local, fluvial, or marine origin and shape the estuarine morphology into channels, shoals, and intertidal area. This morphology forms the basis for valuable estuarine habitat and ecosystems (Harvey et al., 1998). Maintaining this diverse nature is crucial for ensuring the estuarine sustainability. Constant hydrodynamic and sedimentological forcing leads to morphological equilibrium over a timescale longer than decades (Dam et al., 2016; van der Wegen & Roelvink, 2008). However, changes in forcing conditions lead to continuous morphological adaptations ranging from seasons to millennia (e.g., Pethick, 1994; van der Wegen et al., 2016).

Throughout history, natural forcing perturbations occurred and the estuarine morphology adapted accordingly. Sea level fluctuated in accordance with Earth's climate and reached its modern levels from about 6,000 years ago (Fleming et al., 1998). Between 1 and 1800 AD, there were relatively slight sea level changes. However, sea level began to rapidly rise in the 19th century and further accelerated in the early 20th century. Currently, the sea level rise (SLR) rate is much greater than any time in the past 200 years (Kemp et al., 2011) and global SLR projections range from 0.2 m to approximately 2.0 m by the end of the 21st century (Parris et al., 2012).

Estuaries must accrete by trapping sediment in order to keep up with the rising sea level (Castagno et al., 2018; Sergio Fagherazzi et al., 2013; Leonardi et al., 2018). The current accelerated SLR is expected to have a slow, potentially governing impact on the future state of estuarine systems. Examples are shoreline erosion (Passeri et al., 2015), loss of salt marshes and coastal wetlands along with their associated habitats (Nicholls & Cazenave, 2010; Sampath et al., 2011; Thorne et al., 2018), coastal squeeze and increased inundation and flooding (Pelling & Blackburn, 2013), decline of intertidal area

(Rossington & Spearman, 2009; van der Wegen, Jaffe, et al., 2017), and economic losses due to disruption of economic activities or land loss (Asuncion & Lee, 2017; Peri & Šverko, 2015).

Estuaries provide the economic livelihood for several communities (Mitsch & Gosselink, 2000). Human-induced pressure can be seen in estuaries through several aspects such as lack of accommodation space, flow-regulating structures, land reclamations, dredging operations, and ecosystem manipulation (Cooper, 2003). A solid understanding of SLR impact on the morphological state of estuaries is critical for identifying potential threats and associated adaptation measures. Predicting SLR impact on the long-term morphological evolution is challenging as anticipated SLR rates are historically unprecedented and are associated with high uncertainties which require a solid comprehension of the estuarine system dynamics (Sampath et al., 2011).

4.1.1 Previous Studies

Roughly, behavior-based and process-based models are the two main approaches used in long-term morphodynamic modeling (de Vriend et al., 1993; A. B. Murray, 2003; Werner, 2003). Behavior-based models are based on empirical relationships developed from measurements and observations which are extrapolated to address conditions under SLR. Sampath et al. (2011, Guadiana Estuary), Rossington and Spearman (2009, Thames Estuary) and Van Goor et al. (2003) provide examples of behavior-oriented modeling to study SLR impact on estuarine morphodynamics. Their work showed that SLR potentially affects the estuarine morphology more than any other developments in recent history, including for example the drowning of intertidal area despite local accretion. This modeling approach doesn't provide an understanding of the underlying physical mechanisms instead it is based on a combination of expert analysis and empirical relationships developed from observations.

Process-based models take detailed description of physical processes as a starting point. Zhou et al., (2015) implemented a 1D fundamental approach to investigate the morphological evolution of intertidal flats and sediment sorting dynamics. Van der Wegen and Roelvink (2008) showed millennial time scale 2D morphodynamic developments using highly schematized conditions in a rectangular embayment. Other implementations of 2D or 3D process-based modeling efforts with considerable skill in hindcasting observed bathymetric developments are Dam et al. (2016) for the Western Scheldt (110 years), Ganju et al. (2009) for Suisun Bay (30 years) and van der Wegen et al. (2011a, 2013b) for San Pablo Bay (30 years). In addition to reproducing the morphological evolution, models can be used as virtual labs to perform various investigations of interest. Zhou et al. (2013) implemented this approach to investigate the impact of SLR on the long-term morphological development of the Yangtze Estuary. Van der Wegen et al. (2016) used a 1D model to reproduce a mudflat profile in South San

Francisco Bay and quantify the impact of a 100-year SLR. Van der Wegen (2013) evaluated the morphodynamic impact of SLR on a schematic 2D rectangular tidal basin. Ganju and Schoellhamer (2010) performed a decadal timescale (30 years) morphological forecast for Suisun Bay under different SLR, sediment supply and river flow scenarios. In all of the above SLR studies, the estuarine morphology experienced notable development and the intertidal area gradually declines.

Previous research provides a solid understanding of the morphological development of the period under consideration and the system's governing processes. However, most previous case studies investigated periods with a timescale that ranges from years to decades. Also, usually the different periods (e.g., Depositional/Erosional) were treated in a relatively separate way such as the use of different parameters. In this study, we use the 3D process-based model applied by van der Wegen et al. (2011a) to investigate the morphological development of San Pablo Bay over a 250-year period incorporating both a validated hindcast from 1856 to 1983 (Last available survey) and a SLR forecast from 1983 to 2103. Studying the system on a longer time scale allows for achieving a wider perspective on the morphodynamic evolution and the potential impact of SLR. Our research combines the findings of shorter time-scale previous studies into one model in order to produce the first morphological forecast for San Pablo Bay.

4.1.2 Research Objective

The aim of this study is to assess the impact of SLR on the long-term morphological development of an estuarine channel-shoal system. San Pablo Bay, a sub-embayment of San Francisco Estuary, was chosen as a case study due to the availability of a unique historic bathymetric data set that captures the considerable morphological changes over the past 150 years (Jaffe et al., 2007). The dataset is used to validate a morphodynamic model hindcast over the past 150 years and to forecast 100 years under SLR scenarios. Our aim is to provide a reliable morphological forecast for the system which will help identify and understand the potential threat of SLR. We apply the process-based, numerical model Delft3D (D3D) to compute detailed hydrodynamics, sediment dynamics, and associated morphodynamic development. This research tests the ability of process-based models to predict representable morphological development and provides a methodology for performing such forecasts on a centennial timescale.

4.2 CASE STUDY

4.2.1 Setting

San Francisco Estuary is the largest estuary on the west coast of the USA. Its watershed covers more than 195,000 km² (US EPA, 2018) and drains about 40% of California State

(Kimmerer, 2004). The present-day estuarine configuration with its complex topographical and geological features is a tectonically reshaped river valley which started gradually drowning with sea level rise since the last ice age (Atwater et al., 1977).

The San Francisco estuarine system is commonly referred to as the Bay-Delta system which comprises both San Francisco Bay and Sacramento-San Joaquin Delta (Figure 4.1). This system starts inland with two main river branches, the Sacramento and San Joaquin Rivers that drain the enormous watershed through a complex network of tributaries. Following that water flows to the Sacramento-San Joaquin Delta, the only inland Delta in the world (US EPA, 2018), which is located at the confluence zone between both major rivers. Eventually, fresh water gets discharged into San Francisco Bay where it passes through a series of sub-embayments heading towards the mouth of the estuary at the Golden Gate Bridge. Starting landwards from the Delta there is Suisun Bay followed by San Pablo Bay to the west, then Central Bay to the south in front of Golden Gate, and finally there is South Bay located more to the south of Central Bay. In this research, we model North San Francisco Bay (Figure 4.9; Appendix 3) which comprises both Suisun Bay and San Pablo Bay along with their only connection through Carquinez Strait.

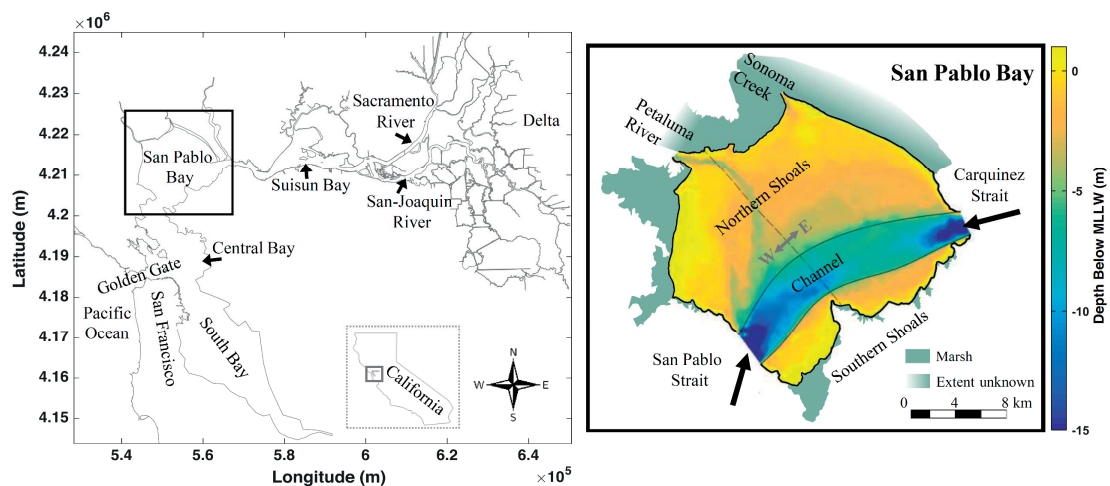


Figure 4.1. Left panel shows San Francisco Estuary land-boundary. Right panel shows a zoom on San Pablo Bay with its 1856 bathymetry and marsh extent plotted, the thin black line indicates the main channel while the grey dotted line in the middle donates the division used in this study between the eastern and western side of San Pablo Bay.

4.2.2 Morphology

San Pablo Bay (Figure 4.1), a sub-embayment of North San Francisco Bay, is bound by San Pablo Strait to the west and Carquinez Strait to the east. It covers an area of approximately 300 km² comprising a channel-shoal system which consists of shoals (<5 m MLLW) dissected by a deep main channel with a depth larger than 12 m MLLW

(Schoellhamer et al., 2008). This channel serves as the main shipping channel as it provides the connection between the deep San Pablo Strait and Carquinez Strait. The surrounding Northern and Southern shoals occupy most of the Bay area accounting for about 190 and 43 km², respectively (Bever & MacWilliams, 2013). A small secondary navigation channel bisects the northern shoals and joins to the Petaluma River (Schoellhamer et al., 2008). Throughout this paper, the terms “channel” and “secondary channel” refer to the main and secondary channel, respectively. The Petaluma River and Sonoma Creek are the two main tributaries that flow into San Pablo Bay. San Pablo Bay margins comprise large intertidal mudflats which are in some locations bound by salt marshes.

Carquinez Strait extends about 11 km from Carquinez Bridge at the eastern boundary of San Pablo Bay till Benicia Bridge at the western boundary of Suisun Bay. Its morphology is characterized by a deep channel (max. depth 35 m), steep bed level slopes, a narrow cross-section (\approx 1000 m wide), multiple bends, and rocky banks. When entering Suisun Bay, Carquinez Strait splits into two navigational channels the Northern Channel that extends northeast towards Grizzly Bay and the Southern Channel that extends east-northeast towards the Delta (Ganju & Schoellhamer, 2008). Shoals cover more than 50% of Suisun Bay and can be found in-between and surrounding the two channels and in Honker and Grizzly Bays (Ganju & Schoellhamer, 2006). Similar to San Pablo Bay, a large portion of Suisun Bay shoals are intertidal mudflats bound by salt marshes.

4.2.3 Tides

San Francisco Bay has a mixed semidiurnal tidal signal, with a median tidal range of approximately 1.8 m (Kimmerer, 2004). In San Pablo Bay, the tidal range can reach about 2.5 m during spring tides and about 1 m during neap tides (Bever & MacWilliams, 2013). The tidal wave propagates from the Pacific Ocean through the Golden Gate into Central Bay then toward San Pablo Bay. Within North Bay, which includes San Pablo Bay, Carquinez Strait, and Suisun Bay, the tidal wave is a progressive wave. Going upstream, the tidal amplitude starts gradually diminishing due to frictional effects, shoreline interaction, and river discharge attenuation. During periods of low discharge, the tide can propagate far upstream, while during high discharges the tide is dampened out at Sacramento (Kimmerer, 2004). Simulations of Achete et al. (2017) showed that SLR will impact the tidal prism and tidal wave penetration. The decreased effect of the bottom friction resulted in further tidal wave penetration in the Delta. The tidal prism increased (\approx 5%) due to higher flow velocities and slight changes in the net discharge.

4.2.4 Salinity

Analysis of water quality samples (USGS, 2018) showed that salinity levels within San Pablo Bay channel can be as high as 30 psu during extreme dry conditions such as the

2012-2015 period and as low as about 10 psu during extreme wet conditions such as in years 1997 and 2017. Furthermore, the deep nature of the main channel enhances the formation of salinity stratification during high river flow conditions reaching about 15 psu within the vertical water column during a 2017 peak flow event. During dry conditions, a vertically well-mixed, longitudinal salinity gradient exists between San Pablo and Suisun Bay. This gradient drives gravitational circulation and associated exchange processes between the two sub-embayments through Carquinez Strait (e.g., Elmilady, 2016).

4.2.5 River Inflow

San Francisco Bay is fed by both the Sacramento and San Joaquin rivers which account for about 80% and 10-15% of the total annual discharge, respectively (Barnard et al., 2013; Kimmerer, 2004), the remaining discharge is supplied from minor tributaries. The freshwater flow is highest during the winter-spring period (Wet season) and lowest during the summer-fall period (Dry season). There is a high seasonal and annual variability with peak flows during the wet season reaching as high as 16000 m³/sec and as low as 300 m³/sec during the dry season (Kimmerer, 2004).

River discharges changed considerably during the past century due to anthropogenic influence. From 1910 to 1975, the Delta and watershed were modified by enhanced channel conveyance, land reclamation, construction of several flow regulation structures, export facilities, and dikes (Barnard et al., 2013). During this period, freshwater discharges were affected significantly, especially during the wet season. Currently, the values and timing of discharges are artificially controlled with a series of flow regulating structures so that the location of the 2 psu isohaline does not retreat landward further than the Sacramento and San Joaquin rivers convergence zone (Kimmerer, 2004). Water is stored in Delta reservoirs during the wet season and released during the dry season to satisfy the fresh water demand and control the salinity levels in the Delta for ecological and agricultural purposes.

Climatic changes are expected to affect riverine flows (IPCC, 2013). Knowles and Cayan (2002) show that in San Francisco Bay watershed, river discharges at the end of the 21st century are expected to increase slightly during the wet seasons with higher run-off peaks and decrease during the dry season compared to the present-day situation. Annual flow volume is expected to remain steady or slightly decline due to a decrease in snowmelt contribution and unimpaired runoff (Cloern et al., 2011).

4.2.6 Waves and Wind

Locally generated wind waves play a significant role in shaping the morphology of San Francisco Bay, especially at the muddy shoals (e.g., Ganju et al., 2009; van der Wegen et

al., 2016; van der Wegen & Jaffe, 2014). Bever & MacWilliams (2013) show the significant role that wind-generated waves play in the resuspension of sediment and elevating the SSC in both the relatively deep and shallow portions of San Pablo Bay. Schoellhamer et al., (2008) observed up to 0.6 m (4 s period) wind waves in San Pablo Bay with 700 mg/l SSC while 0.2 m waves resulted in a SSC of 200 mg/l. In addition to causing sediment resuspension, wave-induced bed shear stress can lead to high SSC vertical gradients and formation of sediment-induced stratification (MacVean & Lacy, 2014).

The complex topography surrounding North Bay is a strong control on meteorological conditions. The seasonal variability of wind directions in San Pablo Bay can be represented by a western and south-western dominant wind direction (Wet/dry season) along with an eastern and south-eastern secondary wind direction (Dry season) (Hayes et al., 1984; NOAA, 2018; Windfinder, 2018). The average wind speed (2011-2018) is about 4.5 m/sec with higher speeds associated with the dominant wind direction (Windfinder, 2018). Maximum sustained wind speed can reach up to 24 m/sec (Weather2, 2018). Typically there is little to no wind during the night.

4.2.7 Sediment Characteristics

Within North Bay, the sediment size distribution has a high correlation with the local geometry and topography. Fine cohesive sediment (mud) persists at the shoals, while sandy sediment is usually found in and around deep channels (e.g., Conomos & Peterson, 1977; Kimmerer, 2004). This is attributed to the high tidal currents in the channels that cause tidal scouring, while relatively low flow velocities at the shallow zones allow for mud deposition. Locke (1971) reported that more than 90% of the shallow tidal flats in San Pablo Bay are covered with mud, and dynamic patches of mud partly cover the sandy channel.

4.2.8 Sediment load

The Sacramento-San Joaquin Delta has supplied most sediment to North Bay (Krone, 1979; B. J. Smith, 1965; Wright & Schoellhamer, 2004), although in recent years the impact of local tributaries increased (Lewicki & McKee, 2010; McKee et al., 2013; Moftakhari et al., 2015). Sediment supplied from the Delta partly deposits on the mudflats in Suisun Bay and San Pablo Bay, while wind-wave-driven resuspension events may further enhance seaward transport (Krone, 1979, 1996). During high river flow events, sediment can be directly transported to the ocean resulting in turbid plumes seaward of the Golden Gate (Ruhl & Schoellhamer, 2004). Studies that investigated the sediment fluxes through Golden Gate show an ebb-dominated system with a clear net seaward sediment transport (Elias & Hansen, 2013; Erikson et al., 2013; Teeter et al., 1997).

Sediment load to the Bay has changed significantly over the past centuries (Ganju et al., 2008; Gilbert, 1917). Natural variations in precipitation patterns played a role (Goman and Wells 2000), but human interventions dominated the sediment supply variations. Moftakhari et al., (2015) estimate that about 55% of the 1500 ± 400 million tons delivered to the estuary from 1849 to 2015 was caused by anthropogenic influence within the watershed. The most important impact was caused by hydraulic mining for gold between 1852 and 1884 (Jaffe et al., 2007; Krone, 1979) resulting in an excessive and mercury-contaminated supply of sediments to the Bay. When hydraulic mining came to a halt, there was a considerable decline of sediment loads which was later enhanced during a period of Delta and watershed modifications from 1910 to 1975 (Barnard et al., 2013). This period included reservoir construction and Delta land reclamation projects, declining tidal marsh area and increasing flow conveyance through the Delta. The Bay's sediment trapping efficiency decreased with the decline of tidal marsh area, which had a considerable effect on the sediment balance (Atwater et al., 1979). Flow-regulating structures trapped sediment in their upstream and freshwater export facilities extracted sediment from the system (Oltmann 1996; Oltmann et al. 1999; Kimmerer 2004). This decrease in sediment load continued towards the end of the 20th century while gradually leveling off and resulting in the current low SSC levels (Ganju et al., 2008; Wright & Schoellhamer, 2004).

During the hydraulic mining period, San Pablo Bay received a high sediment load which resulted in a net accretion of $256\pm 14\times 10^6$ m³ from 1856 to 1887 and mudflats area increased (Jaffe et al., 2007). During the following period of decreasing sediment supply and Delta and watershed modifications, the mudflats became lower although they expanded laterally and narrowed the channel at the same time. In the mid-20th century, San Pablo Bay became net erosional (Jaffe et al., 2007; Kimmerer, 2004) and the sediment supply from local tributaries (Petaluma River and Sonoma Creek) became more important relative to the supply from the Sacramento and San Joaquin Rivers (Lewicki & McKee, 2010; McKee et al., 2013). Ganju et al. (2004) studied the sediment exchange between San Pablo Bay and its tributaries. Their analysis showed a tidally oscillating sediment mass which is effectively trapped within their confluence region except during the high flow conditions when a net seaward transport occurs.

SLR combined with the decreased fluvial sediment supply are posing new challenges to the system. Shallow mudflats might not be receiving the required sediment to cope with SLR causing their area to decline. If not for restoration projects, the sustainability of mudflats and adjacent tidal marshes will potentially be at stake (Barnard et al., 2013; Kimmerer, 2004). Because of their wave attenuating effect, drowning of marshes and mudflats will increase wave attack on existing levee systems. Thus, SLR poses a threat to the critical infrastructure around the Bay (Knowles, 2010). SLR also increases the risk

of dike breaching within the Delta, which would alter hydrodynamics and sediment transport in the system.

It is unclear what SSC levels will be in the coming century. A better understanding of the physical mechanisms is needed in order to project the future sediment load (Wright & Schoellhamer, 2004). Also, climate change increases the uncertainty as it is expected to affect the future sediment yield. When performing a morphological forecast for Suisun Bay, Ganju et al. (2010) applied a decreasing sediment supply by extending the declining trend identified by Wright & Schoellhamer (2004). This method yielded a 34% decrease in sediment supply for their 30-year modeling period. Modeling performed by Achete et al., (2017) showed that SLR is expected to increase the Delta's suspended sediment discharge due to an increased tidal action and its induced suspension. The combined effects of SLR and a drop in the sediment load resulted in a considerable decline of SSC levels in the Delta.

4.2.9 Regional Sea Level Rise

Tidal gauge records from a location near the Golden Gate Bridge showed that during the period from 1855 to 1999, mean sea level (MSL) rose with a rate of approximately 1.5 mm/year (Flick et al., 2003; Smith, 2002). However, this rate has increased considerably over the past decades to more than 3 mm/year (Smith, 2002). NRC (2012) projections for the San Francisco area range from 43 to 167 cm with a median value of 91.9 cm by the end of the 21st century. They forecast a rise of 4-30 cm by 2030, 12-61 cm by 2050, and 43-167 cm by 2100 compared to 2000. In this research, we implement 3 SLR scenarios by 2100 to cover the wide range of uncertainties: 1) an optimistic scenario (42 cm); 2) an intermediate scenario (84 cm); and 3) a worst-case scenario (167 cm).

4.3 MODELING

Van der Wegen et al. (2011a) and van der Wegen & Jaffe (2013b) developed a model setup for hindcasting the 1856-1887 depositional period and the 1951-1983 erosional period in San Pablo Bay, respectively. They applied different river flow forcing and sediment supply to reflect decreasing sediment supply by the cease in hydraulic mining and dam construction as well as more regulated stream flows by increased conveyance and reservoir operations. In addition, van der Wegen & Jaffe, (2013b) applied a slightly modified wind field and sediment erosion to optimize model skill.

We implemented the same model setup and generally the same parameter settings as previous studies along with some minor modifications. The average grid size is about 550×550 m. The hydrodynamic time step is 2 minutes indicating that we include short time scale processes covering intratidal dynamics. The model is 3D with 15 vertical sigma layers and includes saline-fresh water interaction while wind fields generate wave heights

up to 0.3 m. In the sigma layer approach, number of layers is spatially constant and the top and bottom layers follow the water surface and bottom topography, respectively. Higher vertical grid resolution was implemented near the bed and water surface to provide adequate representation of the near-bed velocity shear and wind-wave action, respectively. To save computational time we use the morphological acceleration factor (MF) to model a representative single high-low river cycle instead of modeling 30 consecutive years each with a wet and dry season. We start with a 1 month of wet season with a MF of 30 followed by 4 months of dry season with a MF 82.5 which adds up to 30 morphological years. The wet season is assigned a lower MF to provide a better representation of the higher morphological activity that occurs during the wet season compared to the dry season. Van der Wegen et al. (2011a) and van der Wegen & Jaffe (2013b) extensively tested this approach of separate scaling and the MF values implemented. With the use of the MF and the parallel computations option in D3D, the resulting model simulates 250 morphological years (≈ 3.5 hydrodynamic years) in about 8 days on a 4 core (2.6 GHz) computer. Appendix 3 provides a more detailed description of the model setup.

Our starting point is to model an entire ~ 250 -year period with constant wind forcing conditions and sediment characteristics, while adapting only the river flow forcing and SSC at the landward boundaries and implementing a sea level rise at the seaward boundary. A single run consists of a 127-year hindcast period from 1856 to 1983 (used for validation while 1983 was the last bathymetric survey for the area) and a 120 years forecast from 1983 to 2103. We break down the modeling period into eight 30 to 34-year periods (Figure 4.2). The 4 periods during the hindcast period correspond with available bathymetric surveys (i.e., 1856-1887, 1887-1921, 1921-1951, and 1951-1983). The remaining 4 forecast periods are set to 30-year intervals (i.e., 1983-2013, 2013-2043, 2043-2073, and 2073-2103).

Figure 4.2 shows the modeling timeline while indicating the imposed boundary conditions for each period. For example, the river discharge imposed during the wet and dry seasons of the 1856-1887 period is 5000 and 350 m^3/sec , respectively. Van der Wegen (2011a, 2013b) used the wet season river discharge as a calibration parameter leading to lower discharge during the erosional period (2100 m^3/sec in 1951-1983) than during the depositional period (5000 m^3/sec in 1856-1887). Although we could not find clear indications of decreasing discharges over the past 150 years in literature, the different values may reflect somehow the change in river flow regime as the result of dam construction and conveyance measures in the catchment. In addition to the discharge decreasing trend, we imposed decreasing SSC at the boundary leading to an 1856-1983 decay in sediment load similar to values suggested by Ganju et al. (2008) and presented by Wright & Schoellhamer (2004).

The forecast from 1983 to 2103 is performed using the 1983 modeled bathymetry as an initial condition. During the forecast, the SSC is kept constant while the sea level starts

rising starting from 2013 to 2103. This SLR is imposed at the seaward boundary of a large Delft3D FM model (see Appendix A.3.3) that covers the entire San Francisco Bay-Delta system and is used to derive the hydrodynamic boundary conditions for the smaller D3D North Bay model used in this study. Implementing this approach enables us to account for the SLR-induced variations in the tidal signal and river flow at the D3D North Bay model boundaries. SLR is imposed incrementally for each 30-year period with the magnitude of the rise calculated using a sine curve and the value at the end of each period. For example, a 167 cm sea level rise is imposed as 22, 84, and 167 cm for the 2013-2043, 2043-2073, and 2073-2103 periods, respectively.

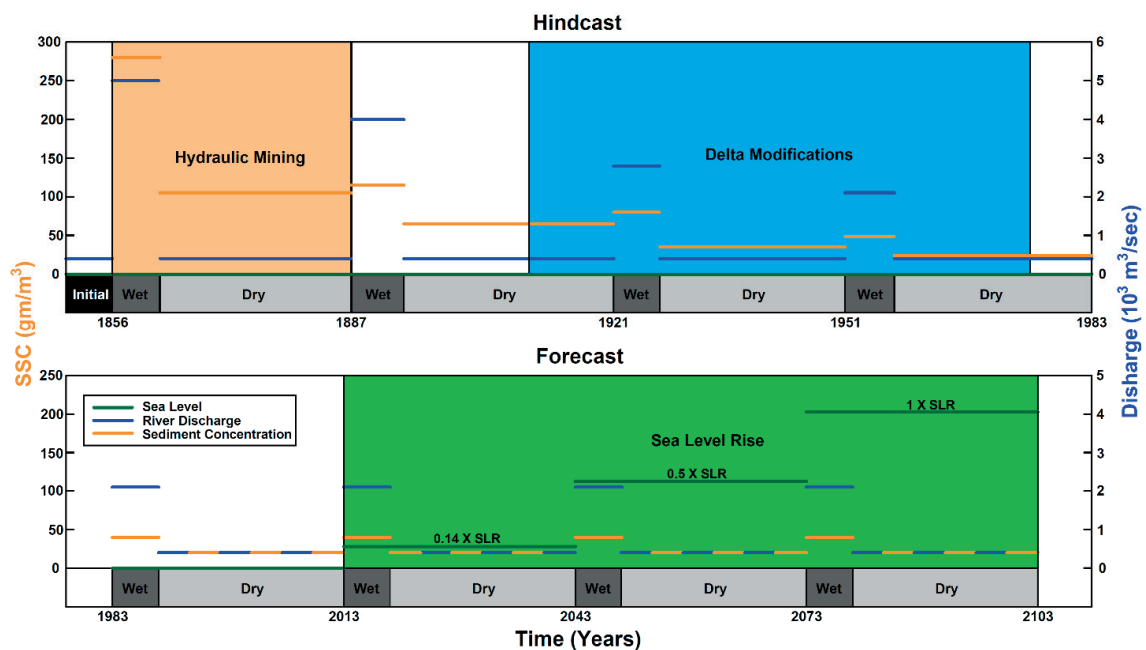


Figure 4.2. Schematization of the modeling timeline showing the hindcast (1856-1983) and forecast (1983-2103) along with the associated boundary conditions. The orange, blue, and green lines represent the SSC, river discharge, and sea level, respectively. Sea level is increased for the forecast scenarios with 14%, 50%, and 100% of the total SLR imposed for 2013-2043, 2043-2073, and 2073-2103 periods, respectively.

4.4 RESULTS

4.4.1 Hindcast

Comparing the 1856 initial bathymetry (Figure 4.3a) to the measured and modeled 1983 bathymetries (Figures 4.3b, and 4.3c) shows that the model provides a good representation of the 127-year morphological development of the intertidal area (< 0 MLLW), shoals (0-5 m MLLW), and channel (> 5 m MLLW) during the hindcast period.

This is also reflected by the good correspondence of observed and modeled cumulative sedimentation/erosion patterns (Figures 4.3e, and 4.3f) and by a high Brier Skill Score of 0.54 (Excellent Category, see Table 4.3 in Appendix 3).

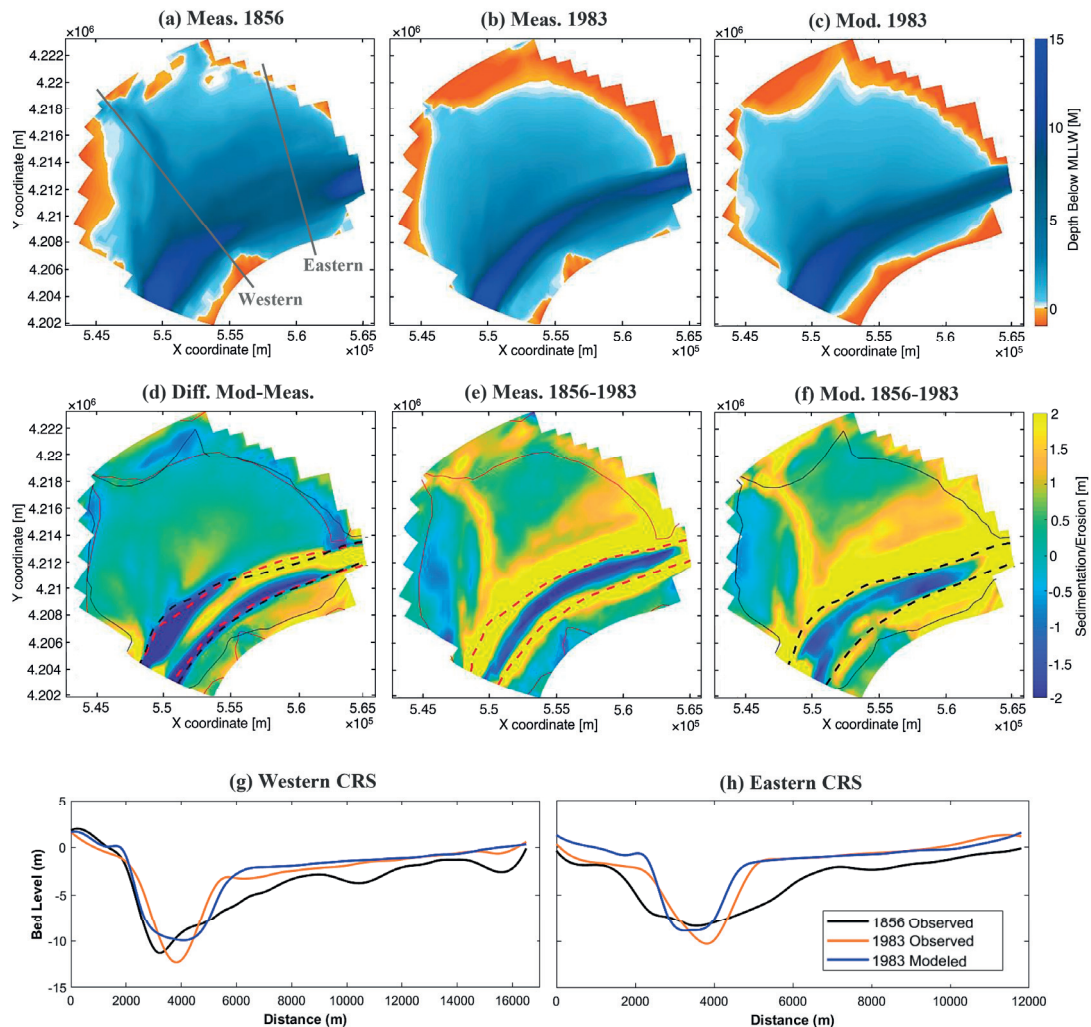


Figure 4.3. The top panel shows San Pablo Bay bathymetry (a) 1856 measured, (b) 1983 measured, and (c) 1983 modeled. The middle panel shows (d) difference between 1983 measured and modeled bathymetries, (e) measured, and (f) modeled cumulative sedimentation/erosion from 1856 to 1983. Continuous and dashed lines represent the 0 and 5 m MLLW contour lines, respectively. The observed 1983 contours are shown in red in both (d) and (e). The bottom panels are (g) western and (h) eastern bed level cross-sections shown in (a).

Both measurements and hindcasts show a significant increase in intertidal area caused by deposition at the Bay's margins. The model captures the considerable deposition volumes over the shoals near the main channel margin which resulted in a narrower main channel.

The secondary channel fills in fully. Model results reflect the observed slightly erosional shoals to the west and the east of the secondary channel.

Figure (4.3d) shows that the largest discrepancy exists near the main channel margin. The model hindcasts a total cumulative deposition of $3.48 \times 10^8 \text{ m}^3$ which is about 20% larger than the observed $2.85 \times 10^8 \text{ m}^3$. Compared to the 1983 measurements, the modeled channel is generally shallower along the model domain, wider in the west (Figure 4.3g), and narrower in the east (Figure 4.3h). A possible explanation is that the applied sand fraction in the deep section of the channel is coarser than in reality. Also, in the model, we don't simulate (limited) dredging activities in the channel (Jaffe et al., 2007).

The model reflects the observed depositional trend in periods from 1856 to 1951 and a slightly erosional trend from 1951 to 1983 (Figure 4.4). Both measurements and hindcasts show erosion in the deepest channel section during all periods. The model slightly underestimates this erosion, especially during the 1887-1951 period. Hindcasts show deposition at the northern channel bank which starts from the eastern end and propagates gradually with time towards the western end. This behavior is observed in measurements, however, the deposition at the eastern end starts earlier in hindcasts (1887-1921) than that in observations (1921-1951). For the southern channel bank, hindcasts match the measured trend of considerable deposition during the 1856-1887 period.

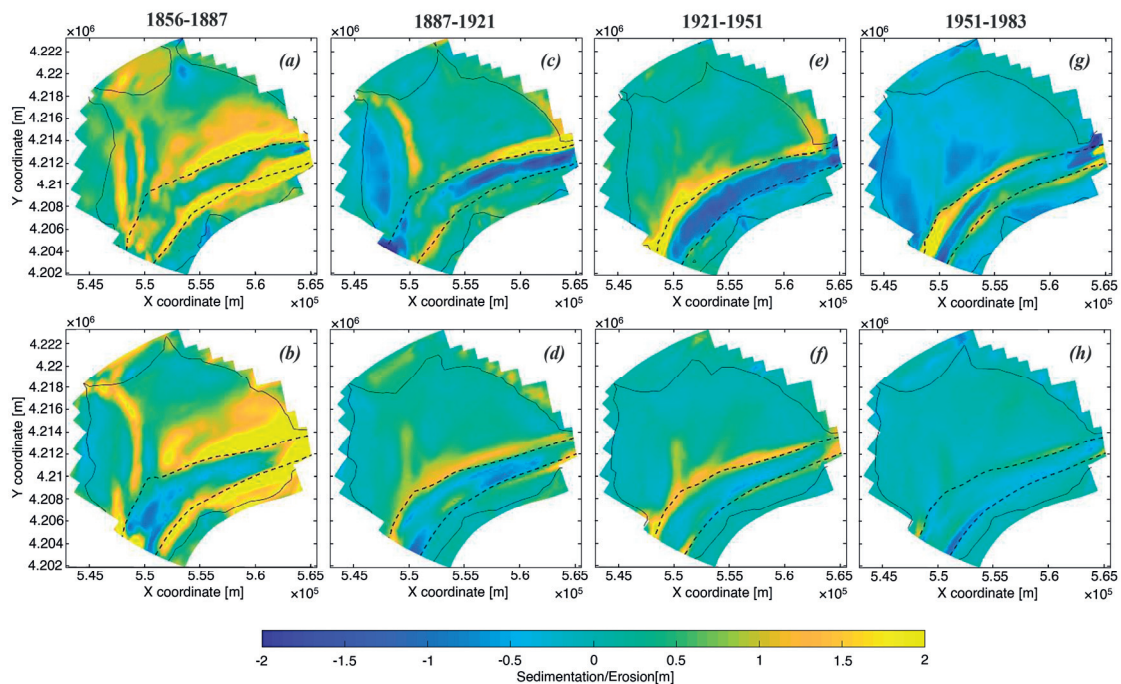


Figure 4.4. Measured (top panel) and modeled (bottom panel) sedimentation/erosion maps for each period.

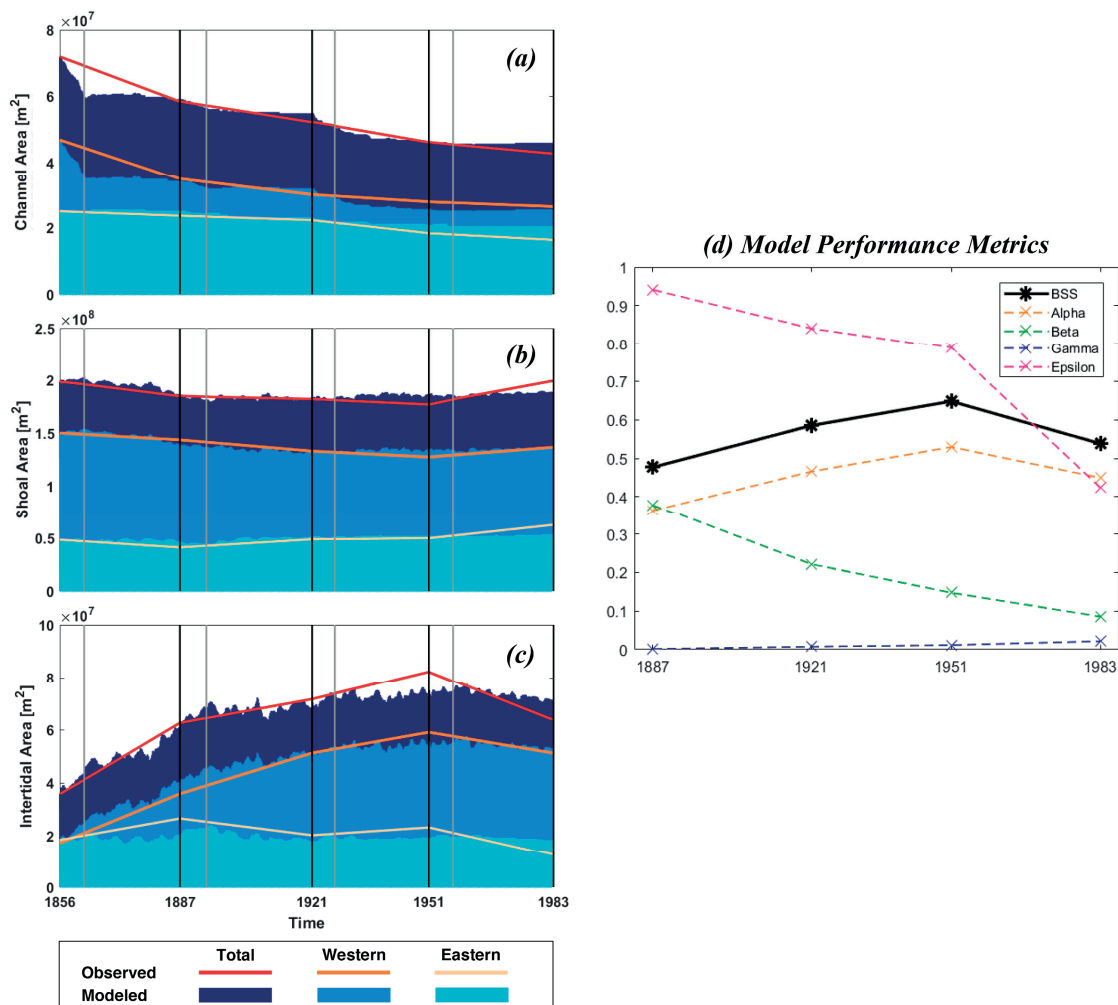


Figure 4.5. Modeled (color shaded) and observed (lines) spatial coverage of the model domain and its changes over time divided between (a) channel (< -5 m MLLW), (b) shoals (0 to -5 m MLLW), and (c) intertidal area (>0 m MLLW) for both the eastern and western sides of San Pablo Bay. Vertical gray lines indicate the end of the wet season runs. Right panel (d) shows the development of the BSS score and its Murphy and Epstein (1989) decomposition throughout the hindcast period compared to the 1856 initial bathymetry.

Figures 4.5a, 4.5b, and 4.5c show that the model reproduces changes in channel, shoal, and intertidal area. Channel narrowing occurs throughout the entire hindcast with a gradually decreasing rate over time (Figure 4.5a). The model provides a good representation of this trend showing higher rates in the wet season than that for the dry season which implies that its main driver is bank deposition associated with the wet season sediment pulse. This is especially evident for the eastern side during the 1856-1887 wet season. Shoal area remains fairly constant over time (Figure 4.5b) due to the fact that it lies between a narrowing channel and widening intertidal flats. Channel banks

experienced sedimentation and shifted to shoals at the same time deposition landward transformed shoals into intertidal flats.

Hindcasts successfully capture the large increase in intertidal area that occurred during the depositional period from 1856 to 1951 (Figure 4.5c). Unlike the channel narrowing, this intertidal area growth occurs during both the wet and dry seasons with the latter having the higher contribution. A possible explanation is that a portion of the sediment deposits during the wet season sediment pulse while a larger portion is supplied by wave-induced resuspension during the dry season from either newly deposited wet-season sediment or older sediment being eroded from the shoals. Intertidal flats accretion is highest during the 1856-1887 period and continues with a gradually decreasing rate towards the end of the depositional period (1951), while model results underestimate the drop in intertidal areas after 1951.

Investigating the development of the BSS (Sutherland et al., 2004; Appendix A.3.7) and its Murphy and Epstein (1989) decomposition over time (Figure 4.5d) provides a more objective insight into model performance. For the depositional period from 1856 to 1887, the model shows good performance (BSS of 0.47). The low mean error ($\gamma = 1.8 \times 10^{-3}$) indicates good skill in hindcasting the total depositional volume. The model hindcasts a total depositional volume of $2.46 \times 10^8 \text{ m}^3$ which is about 3% higher than the $2.39 \times 10^8 \text{ m}^3$ observed during this period.

The model performance gradually increases to a BSS of 0.63 in 1951, 1) α increased (0.36 to 0.52) indicating a phase error decrease; 2) β decreased (0.38 to 0.15) illustrating a better performance in hindcasting the sedimentation/erosion amplitudes/phases; 3) γ increased (1.8×10^{-3} to 1.1×10^{-2}) showing a decreased performance in mean level; and 4) ϵ decreased (0.96 to 0.80). The small decrease in BSS after 1951 is attributed to the small net erosion being more difficult to model than the large depositional signal (van der Wegen & Jaffe, 2013b). The shoal erosion is underestimated during the 1951-1983 period. Another reason is that the ϵ value dropped sharply from 0.80 to 0.43. However, it is important to note that a decreasing epsilon value doesn't directly indicate a decreased model performance instead it indicates that the difference between the 1856 initial reference bathymetry and the compared bathymetry have dropped hence errors are more severely penalized. A sensitivity analysis was carried out for the hindcast period and the results for some selected sensitivity runs are presented in section (4.5.2).

4.4.2 Forecast

We performed a morphological forecast that extends 120 years from 1983 till 2103 for a No SLR scenario along with 3 SLR scenarios of a 42 cm (optimistic), 84 cm (intermediate), and 167 cm (worst-case) rise during the final approximately 100 years (Figure 4.6). Forecasts show that for the No SLR scenario, the Bay's erosional trend continues till the end of the 21st century (Figures 4.6a, and 4.7a). By 2103, the spatially

averaged intertidal area height decreases by 12.8 cm while an average shoal erosion of 4.1 cm occurs (Table 4.1). The main drivers of this erosion are the lack of sediment supply from the Delta and the wind-wave attack. Also, channel slope deposition continues resulting in a narrower and deeper main channel. However, the average channel depth remains relatively constant (+2.0 cm) as the deposition and erosional volumes are in the same order of magnitude.

During the hindcast period, our simulations slightly overestimate the cumulative deposition volumes (Figure 4.7a). However, simulations are still able to capture the shift from a depositional Bay (1856-1951) to an erosional Bay (1951-1983). The forecast shows the continuation of this erosion from 1983 to 2103 and, for the No SLR scenario, a net erosion of about $20 \times 10^6 \text{ m}^3$ from 2013 to 2103. In contrast, for the 42 cm SLR scenario, the Bay is neither strongly erosional nor depositional. However, for the 84 and 167 cm scenarios, the Bay turns from erosional to depositional with net deposition of 16×10^6 and $58 \times 10^6 \text{ m}^3$, respectively. The patterns of deposition and erosion are similar for all 3 scenarios, the deposition magnitude increases with higher SLR (Figures 4.6e, 4.6f, and 4.6g).

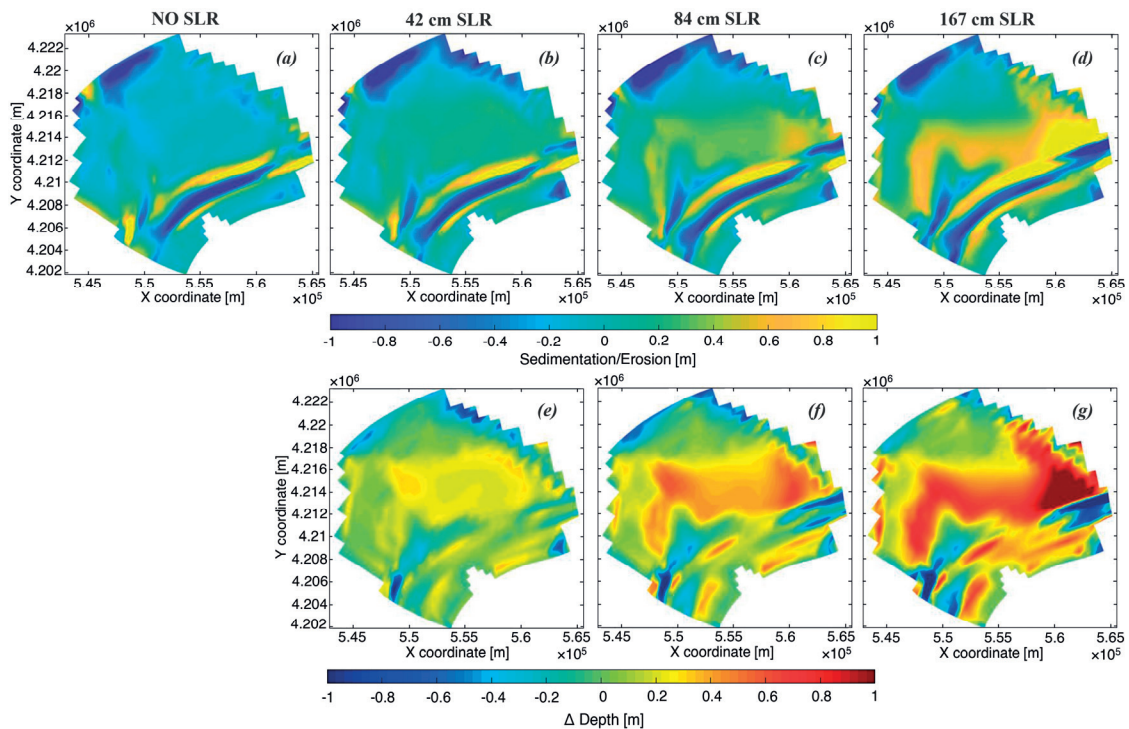


Figure 4.6. Top panel shows the cumulative sedimentation/erosion maps from 1983 to 2103 for the (a) No SLR and (b, c, and d) SLR scenarios. Bottom panel shows SLR-induced bed level changes for the (e) 42 cm, (f) 84 cm, and (g) 167 cm SLR scenarios. For example, (f) is the difference between (c) and (a) with the red and blue colors indicating higher and lower bed levels, respectively.

Shoals experience a net depositional trend for the 3 SLR scenarios. This trend is due to an increased sediment trapping efficiency, deposition is mainly driven by the SLR-induced increase in water depth which decreases the effect of waves on the bottom and creates calmer flow conditions that enhance mud deposition. This deposition is highest near the channel and decreases gradually towards the landward margins. In response to SLR, the average shoal depth increased by 12.3, 23.7, and 40.4 cm for the 42, 84, and 167 cm SLR scenarios, respectively. However, this accretion rate is only 25-30% of the SLR rate which means that it can't keep up with the rising sea levels and the relative shoal depth will increase leading to the drowning of San Pablo Bay shoals.

Model results (Figure 4.7b) show an increase in intertidal area during the depositional period (1856-1953). Following that, they begin decreasing gradually towards the present day resulting in an intertidal area of $6.91 \times 10^7 \text{ m}^2$ in 2013. For the No SLR scenario, this gradually decreasing trend is predicted to continue at a relatively constant rate which would lead to the loss of approximately 13% of the current (2013) intertidal area by the end of the 21st century. Implementing the different SLR scenarios, showed a sharp drop in intertidal area and a considerable loss of about 43%, 66%, and 91% of intertidal area by 2103 for the 42, 84, and 167 cm SLR scenarios, respectively.

In addition to the inundation-induced loss of intertidal area, SLR increases the landward extent of wind wave attack which enhances erosion along the landward margins. For the optimistic 42 cm SLR scenario, this effect results in a spatially averaged intertidal area erosion of 15.2 cm. While, for the worst-case 167 cm SLR scenario, this erosion is observed at the early stages but as the inundation height increases, the wave-induced bottom shear stress starts dropping causing the erosional trend to shift to depositional. However, the average depositional magnitude (+7.1 cm) is much less than the rising sea level (167 cm) eventually leading to inundation-induced loss of intertidal area.

Table 4.1. Spatially averaged bed level changes between 1983-2103 for the No SLR and for the 3 SLR scenarios relative to the No SLR case.

Depth Range (MLLW)	Coverage Area (%)	Δ depth relative to No SLR (cm)			
		No SLR (cm)	+42 cm SLR	+84 cm SLR	+167 cm SLR
> 0 m (Intertidal)	24.2	-12.8	-15.2	-13.1	+7.1
0 to -5 m (Shoals)	60.7	-4.1	+12.3	+23.7	+40.4
< -5 m (Channel)	15.1	+2.0	+1.1	-4.1	-6.6

Channel bank deposition and erosion in the channel observed for the different SLR scenarios (Figures 4.6b, 4.6c, and 4.6d) are similar to the No SLR scenario (Figure 4.6a). However, Figures 4.6e, 4.6f, and 4.6g show that SLR caused slightly higher bed levels in the middle section and lower bed levels towards the eastern and western end of the main

channel. This trend is most clear for the 167 cm scenario (Figure 4.6 g), especially at the eastern channel end where the elevation difference is more pronounced, even reaching more than 1 m compared to the No SLR scenario. The eastern channel erosion starts from Carquinez Strait (not shown) which experienced considerable deepening due to SLR. This eroded sandy sediment is carried seaward and settles in the shallower and calmer middle section of San Pablo Bay channel eventually resulting in higher bed levels. This behavior also occurs in the western end at San Pablo Bay Strait; however, the sediment eroded there gets carried seaward out of the model domain.

Throughout the hindcast period, the channel volume decreased significantly (Figure 4.7c). Forecasts show that, without SLR, the channel volume will experience a slight drop towards the end of the 21st century and imposing SLR results in a notable increase in channel volume. This increase occurs during the dry season, while during the wet season, it is either constant or there is a slight drop. This is caused by the wet season sediment pulse that enhances channel bank deposition which is in the same order as the SLR-induced added water volume.

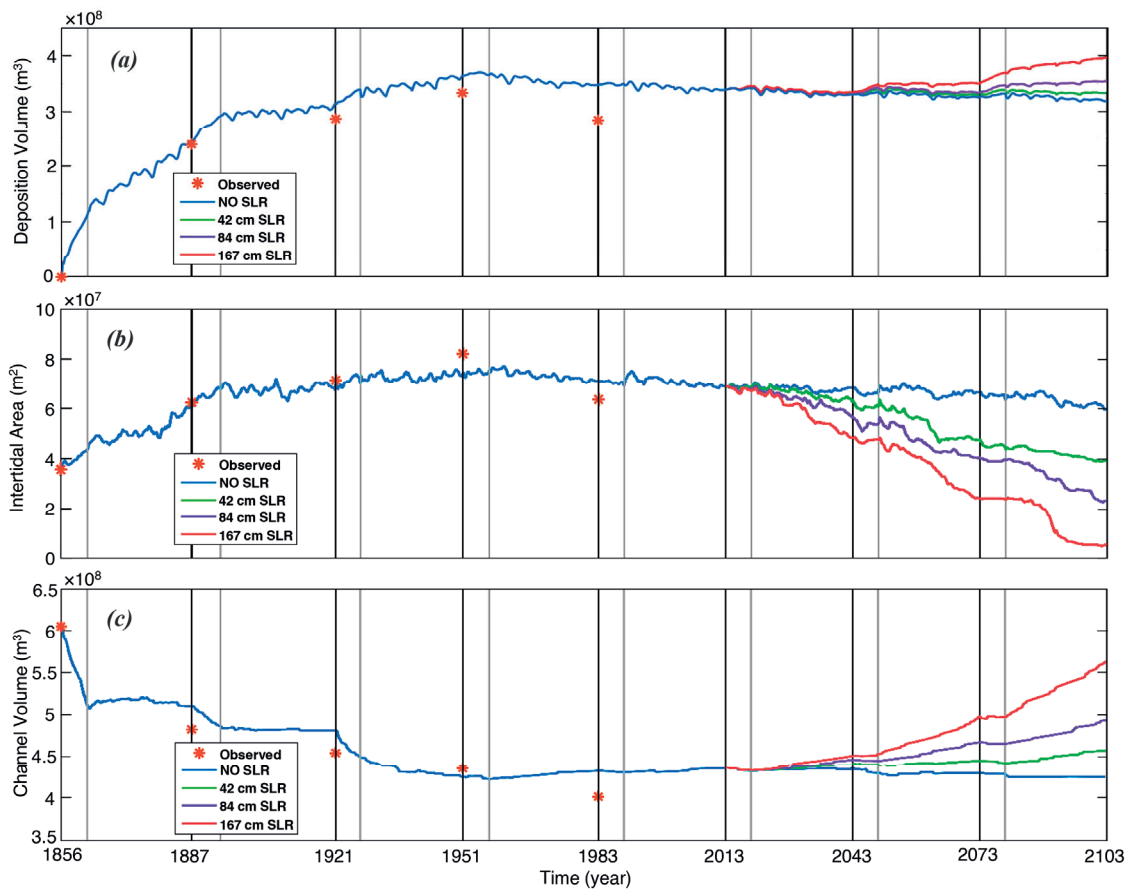


Figure 4.7. Quarter millennium development of (a) depositional volumes, (b) intertidal area, and (c) channel volume for the No SLR (blue) and the 42 cm (green), 84 cm (purple), 167 cm (red) SLR scenarios.

4.5 DISCUSSION

4.5.1 General Model Performance

The high model skill obtained in this work is in line with model skill reported by Dam et al. (2016) when performing a 110-year morphological hindcast (1860-1970) for the Western Scheldt Estuary in the Netherlands with a similar process-based model. They observed a decreasing skill in the first decades and an increasing skill to a value of 0.52 after 110 years. A possible explanation for this behavior is a decadal morphological spin-up time in which the bathymetry adjusts to its roughly schematized model parameters, imposed constant forcing conditions, and process descriptions (Dam et al., 2016). Afterward, the model captures the morphological development that is governed on the long-term by the interaction of the major tide with the estuary's plan form. We think that the interaction between major tidal and fluvial forcing and the estuary's plan form also plays a major role in San Pablo Bay morphodynamic development. Another explanation

is that the sediment supply signal is very strong in the first decades and dominates more subtle processes such as wave action. Van der Wegen & Jaffe (2013b) showed that net volume changes during the erosional period are an order of magnitude smaller than the depositional period. The wave-driven erosion is subtle compared to the sediment supply signal during the preceding decades and leads to lower skill scores than during the depositional period.

4.5.2 Hindcast Sensitivity

We performed a sensitivity analysis for the base case hindcast presented in section (4.4.1) to achieve optimal skill and a better understanding of the processes that govern the morphological development of San Pablo Bay. In this section, we present a selected set of sensitivity runs; 1) Excluding salinity effect (No Salinity); 2) Excluding 3D processes (2DH-Model); 3) Excluding wind-wave generation (No Waves); and 4) Imposing SLR in the hindcast (Hindcast SLR).

4.5.2.1 No Salinity

Salinity exclusion affects several aspects, most importantly it eliminates salinity stratification and density currents. Two-layer flow and gravitational circulation associated with salinity gradients have been noted in previous studies to have a considerable effect on North Bay sediment dynamics (e.g., Elmilady, 2016; Ganju & Schoellhamer, 2008). Our model results (Figures 4.8a, and 4.8e) confirm the importance of salinity-driven processes on the long-term morphological development of San Pablo Bay. Excluding salinity results in considerably lower bed levels at the estuarine margins, shoals, and channel banks. Channel narrowing and shoal accretion are very poorly represented. This can be explained by shoal accretion first starting with channel bank deposition that gradually propagates landward towards the estuarine margins (van der Wegen, Jaffe, et al., 2017).

Despite a slight increase in sediment import from its landward boundary, San Pablo Bay's net depositional volume for the No Salinity scenario ($1.44 \times 10^8 \text{ m}^3$) was significantly lower than that for the base case simulation ($3.48 \times 10^8 \text{ m}^3$) and measurements ($2.85 \times 10^8 \text{ m}^3$). This was caused by a simultaneous significant increase in the seaward sediment export from San Pablo Bay, resulting in a decrease of the Bay's sediment trapping efficiency (Import/Export). This can be explained by salinity stratification, landward directed density currents, and gravitational circulation increasing sediment retention in the system. This occurs primarily because of the resulting calmer conditions near the bottom that enhance sediment settling and drives landward directed sediment transport (Elmilady, 2016).

4.5.2.2 2DH-Model

Running the model in a 2DH form instead of the 15 sigma layers (Figure 4.8b) showed a high resemblance with the No Salinity sensitivity run (Figure 4.8a). This suggests that salinity-driven 3D processes have considerable influence relative to other 3D processes.

Similar to the No-Salinity case, there was a slight increase in sediment import from the Delta along with a considerable simultaneous increase in the seaward sediment export from the Bay. This resulted in a net depositional volume for 2DH-Model ($2.03 \times 10^8 \text{ m}^3$) that is considerably lower than the base case ($3.48 \times 10^8 \text{ m}^3$). However, the sediment trapping efficiency for the 2DH model was slightly higher than that for the No Salinity case that is reflected in a 41% increase in deposition volumes. A possible explanation for this increase is that despite neglecting the effect of the salinity stratification and gravitational circulation, the 2DH model still simulates the landward directed density currents driven by the longitudinal salinity gradient between San Pablo Bay and Suisun Bay.

4.5.2.3 No Waves

The sediment input from the Delta is almost the same as the base case, however, the seaward sediment export decreased hence resulting in a more depositional San Pablo Bay. This increase in sediment trapping efficiency was caused by a 26% drop in bed shear stresses over the shoals. This drop resulted in a net deposition of $4.46 \times 10^8 \text{ m}^3$ which is about 35% higher than that for the base case. Most of this difference occurred during the dry season when wind waves play an important role in sediment resuspension and redistribution. Also, by inspecting Figure (4.8e) and comparing the No Waves run with other simulations, we found that wind waves are responsible for the –erosive– signal fluctuations that mainly occur during the dry season throughout the hindcast.

Compared to the base case (Figure 4.8c), significantly higher depositional volumes occur on the landward margins and their adjacent shoals resulting in a significant increase of intertidal area and higher elevation shoals. The decreased flow over the accreting shoals resulted in larger flow volumes through the main channel which enhanced its erosion and caused the formation of a secondary channel that bisects the north-eastern shoals.

The No Wave simulation clearly illustrates that wind waves play a very important role in maintaining the channel-shoal structure in San Pablo Bay by limiting shoal elevation and ensuring a gradual transition in elevation based on wave energy.

4.5.2.4 Hindcast SLR

Between 1855 to 1999, the MSL at the Golden Gate rose at a rate of approximately 1.5 mm/year (Flick et al., 2003; Smith, 2002). This rate equates to approximately 19 cm SLR during the modeled hindcast period. Our model results (Figure 4.8d) show that implementing this gradual SLR during the hindcast has a minor impact on the

morphological development. Less deposition occurred on the main channel northern bank that resulted in a slight decrease in overall depositional volumes to $3.28 \times 10^8 \text{ m}^3$, which is closer to observed volumes than the base case (Figure 4.8c). The end BSS decreased slightly to 0.52, but still remained on the same order as that for the base case (0.54). Also, when modeling the morphological development of San Pablo Bay during the erosional period, van der Wegen & Jaffe (2014) applied a 20 cm rise/drop in MSL and their results showed that it had a minimal effect on the erosional/deposition patterns and volumes, eventually concluding that it is only when sea level rise accelerates that larger influences are expected. Furthermore, Rossington & Spearman (2009) showed that the 2 mm/year SLR observed over the past 100 years in the Thames Estuary (UK) had a limited effect on the morphological development of the estuary compared to the anthropogenic influence and the predicted future SLR.

Based on the above, the effect of this 1.5 mm/year rise was excluded in our base case. This exclusion enables us to create a hypothetical base case NO SLR scenario that extends into the forecast that allows us to isolate the effect of future SLR by acting as a comparison point for the other three SLR scenarios. Errors resulting from this assumption are small compared to implementing SLR in the hindcast and then abruptly stopping it in the forecast. Van der Wegen et al. (2016) showed that the adaptation timescales of mudflats for abruptly changing boundary conditions can be on the order of decades. Also, our simulations following 2103 (not shown) indicated that when SLR is abruptly stopped, the system will still be adapting for decades. The exclusion of SLR in hindcasts serves the main aim of this study, which is to understand the effect of the predicted accelerated SLR on the morphological development.

4.5.3 Forecast Analysis

SLR increases San Pablo Bay's sediment trapping efficiency and shifts the system's erosional trend to a depositional one for the intermediate and worst-case SLR scenarios. This increase in deposition is mainly driven by the increase in mean water depth which under similar wind-wave conditions results in a decreased effect of waves on the bottom and creates conditions that enhance mud deposition, especially on the shoals. As a result, the shoals capture more sediment and start accreting in response to SLR. However, due to the low sediment supply from the Delta, the accretion rate is only between 25-30% of the SLR rate and San Pablo Bay shoals are drowning. For a similar depth range, Ganju & Schoellhamer (2010) indicated that Suisun Bay shoals are expected to accrete at a rate between 35-40% of the SLR. This higher value can be explained by Suisun Bay being located closer to the inland source of sediment supply.

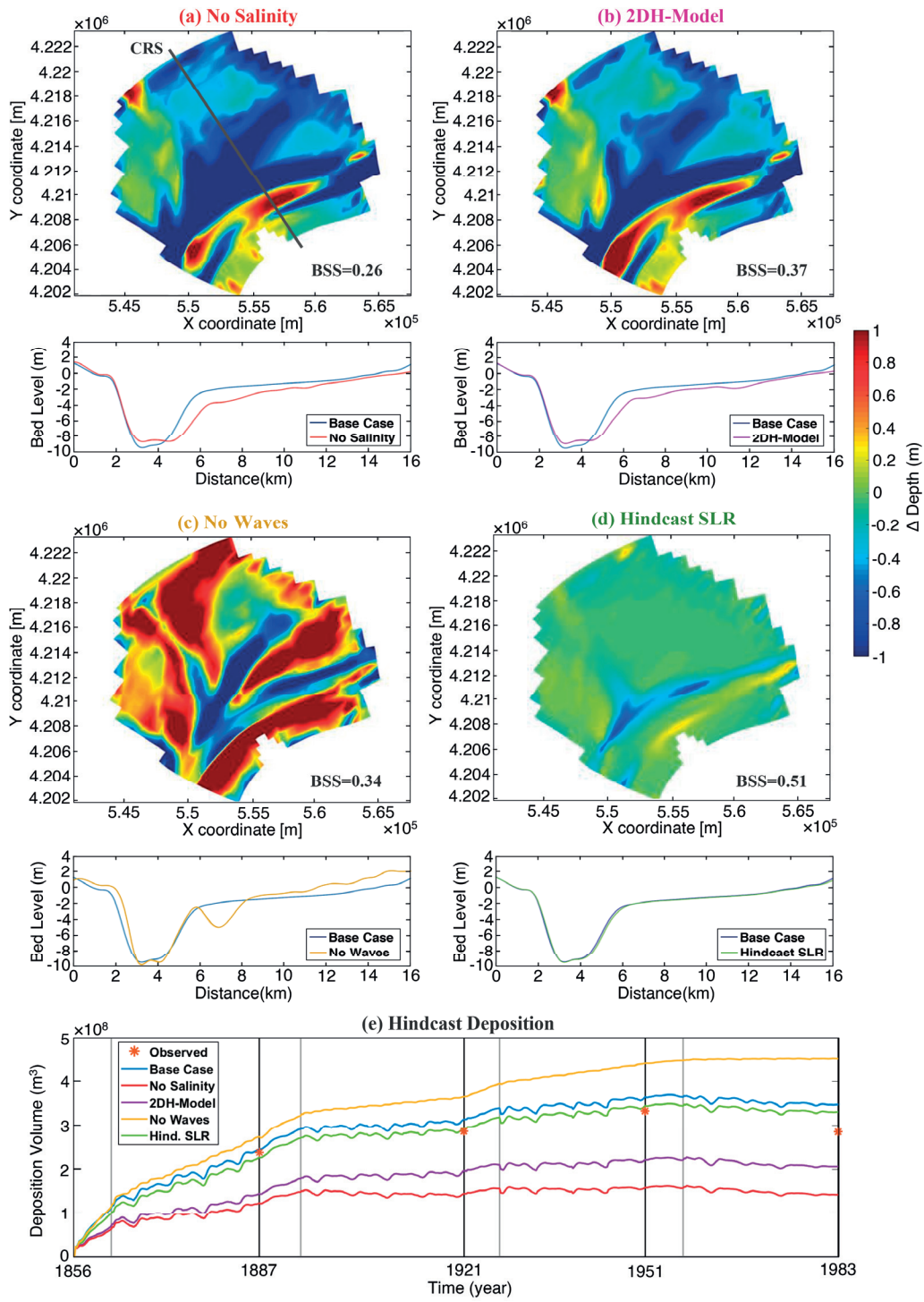


Figure 4.8. Hindcast sensitivity results for (a) No Salinity, (b) 2DH-Model, (c) No Waves, and (d) Hindcast SLR. Maps indicate bed level difference between sensitivity run and base case, red and blue color donates higher and lower than base case bed level, respectively. Transects below each map are bed-level cross-sections along CRS shown in (a) for base case (blue) and sensitivity run. Bottom panel (e) shows deposition volumes for the hindcast period.

In San Pablo Bay, the rate of shoal accretion is about 29, 28, and 25% of the SLR rate for the 42, 84, and 167 cm SLR scenarios, respectively. This relatively small variation between the different scenarios suggests the relative independence of accretion rates on the magnitude of SLR. Sediment supply sensitivity runs (not shown) illustrated that this rate is mainly dependent on the sediment load from the Delta. The current sediment supply is too low for the shoals to keep up with SLR. In addition, Figure 4.7a shows that the effect of SLR on the deposition volumes is small compared to the effect of the hydraulic mining period that delivered a huge sediment pulse to San Pablo Bay. This suggests that sediment supply from the Delta plays an important role in determining whether there is net erosion/accretion of the Bay.

Our forecasts showed that the current trend of channel narrowing and deepening will continue in the future at a gradually decreasing rate, regardless of SLR. However, we found that SLR enhances channel slope deposition leading to a narrower main channel at the eastern side of the Bay. In addition, forecasts showed considerable SLR-induced erosion starting in Carquinez Strait and propagating seawards towards the San Pablo Bay channel. We attribute this to the larger tidal prism conveyed to Carquinez Strait. For the worst-case 167 cm SLR scenario, this erosional trend can be clearly observed at the eastern side of the Bay. Additional simulations beyond 2103 showed that this erosion progresses gradually seaward leading to a deeper San Pablo Bay channel. This illustrates that at the end of the 21st century the system is still reacting to the imposed SLR and that the channel is expected to get deeper over time with a seaward residual transport. It might take decades, or even longer, for the full effect of this imposed SLR to change the morphology. The deeper channel sections like Carquinez and San Pablo Straits react faster to SLR than the shallower channel sections. A similar trend was forecasted by Ganju & Schoellhamer (2010) who showed that SLR results in deeper Suisun Bay channels. They found that the highest erosion occurred in the deepest sections of the channel from 18-20 m and decreases gradually and shifted towards being depositional for the 10-12 m depth range.

We identified a considerable threat to the intertidal area. Model results showed that the 2013 intertidal area will experience a drop of 13%, 43%, 66%, and 91% by the end of the 21st century for the No SLR, 42, 84, and 167 cm SLR scenarios, respectively. The forecasted decrease for the No SLR scenario is mainly driven by the lack of sediment supply and the wind wave attack which extended the Bay's erosive trend observed in the hindcast. Imposing SLR increased the intertidal area decline due to inundation and the increase of the landward extent of wind-wave attack, with the former having a higher contribution. When modeling the evolution of the South Bay mudflats to the end of the 21st century van der Wegen et al. (2016) reported a decline of about 40% of intertidal area for the 167 cm scenario and a complete loss of intertidal area when combined with a 50% decrease in sediment supply.

Rising sea level will increase the inundation frequency of the intertidal mudflats hence subjecting them to an increased wind-wave attack. For the 42 and 84 cm SLR scenarios, this resulted in erosive estuarine margins due to the lack of sediment supply to compensate for the increased wave attack. Ganju & Schoellhamer (2010) reported a similar trend of SLR-induced erosional estuarine margins in Suisun Bay. For the 167 cm SLR scenario, the large inundation height leads to a drop in the wave-induced bottom shear stresses and shifts this erosional trend to a depositional trend. However, the deposition rate was minimal compared to the SLR rate resulting in a considerable loss of intertidal area due to inundation.

Erosion, or accretion with a rate less than the SLR, resulted in inundation due to an increased relative water depth. This increase caused a transition in states where shoals turned to channel and intertidal mudflats turned to shoals. Consequently, salt marshes are expected to give way to the migration of their adjacent intertidal area. However, in this research, no accommodation space was implemented thus intertidal area migration is not possible as the Bay's boundary was imposed as a fixed boundary. Migration will only occur in the case of no obstructions and accommodation space available (Kraft et al., 1992). In reality, there are no obstructions and accommodation space is available at some locations in northern San Pablo Bay. At most locations in San Pablo Bay, however, migration is not possible due to obstructions.

The fate of San Pablo Bay salt marshes under SLR has been assessed in previous studies (e.g., Takekawa et al., 2013). At some locations, salt marshes are expected to be able to trap sediment eroded from mud flats and accrete at a rate that matches the SLR rate. At other locations, especially the young salt marshes, the SLR-induced increased inundation frequency is expected to drown salt marshes and give away for intertidal mud flat migration. The fate of San Pablo Bay intertidal mudflats heavily depends on whether or not salt marshes will give way for migration. The results presented in this research assume that migration is not possible, thus it can be argued it is a worst-case scenario. Indeed, we anticipate that the significant forecasted loss of intertidal mudflats would have been much lower if migration was possible. However, in this case, migration means the loss of valuable salt marshes.

4.5.4 Modeling Approach

There were some challenges associated with the forcing schematization. We imposed SLR in steps instead of a gradual rise. A gradual SLR would have resulted in a lower rise during the wet season than that for the dry season while a sudden rise overestimates the SLR impact. However, comparing the results of both methodologies showed similar morphological behavior with a negligible difference in the magnitude of the deposition/erosion volumes that would not affect the conclusions. The reason is that a model spin-up exists when a new sea level is imposed.

We start the modeling with a wet season followed by a dry season. The order of seasons is of significance when considering a single 30-year period, especially for the hydraulic mining period. However, on the longer run the effect gradually becomes insignificant since it is overruled by the long-term morphological development.

4.5.5 Application to Other Estuaries

In this research, San Pablo Bay is presented as a case study. The value of this research extends beyond achieving a better understanding of SLR impact on the long-term morphological development of a particular system. Findings and the process-based methodology can be applied to estuaries with similar forcing conditions. In this estuary with low sediment supply and artificially regulated flows, we show that SLR poses a considerable threat to the estuarine environment. This situation is common in estuaries worldwide where the construction of flow-regulating structures upstream resulted in a considerable decline in the sediment supply and controlled discharges during the wet season significantly reduced the system dynamics. Not being able to accrete at a rate equal to or greater than the SLR rate will lead to the system drowning and the potential loss of valuable habitat. Landward migration is critical for the sustainability of those ecosystems. However, as is the case in San Pablo Bay, several estuaries around the world lack accommodation space due to urbanization pressure.

We illustrate the potential of applying the process-based modeling approach to identify governing processes and to simulate the morphological development over a centennial time scale. Such models can be a useful tool to assess the impact of climate change-induced perturbations on the morphological development of estuaries worldwide. In addition, we present and test a framework for performing such long-term morphological forecasts.

4.5.6 Future Research and Recommendations

We recommend further developments to this research such as using the developed model to assess the impact of SLR combined with other climate change-induced changes in sediment supply, river flow, and meteorological conditions. Moreover, there is value in including more processes (e.g., flocculation), specifying more detailed forcing description (e.g., wind conditions including extreme events), and incorporating the available accommodation space and surrounding salt marshes in the model. In addition, obtaining a more recent bathymetry would allow further evaluation of the model and investigation of Bay's erosional trend continuity. Also, investigating the impact of possible Delta polders breach on the upstream boundaries. Finally, studying the system on a longer timescale beyond the end of the 21st century could improve understanding of the evolution of estuaries.

4.6 CONCLUSIONS

San Pablo Bay historical bathymetric surveys showed considerable morphological development from 1856 to 1983 due to variations in fluvial sediment load and discharges associated with a period of hydraulic mining for gold, modification of the Delta, and damming in the watershed.

Our 3D processes-based modeling effort resulted in a reasonable reproduction of the morphological development that occurred during this period. Further extending our model simulations in a forecast to the end of the 21st century allowed us to study the effect of SLR on the Bay's morphological evolution. We identified that SLR poses a considerable threat to intertidal area when landward migration is not possible. SLR enhances the recent erosional trend due to the inability of the low sediment supply to compensate for the increased landward extent of wind-waves attack and inundation frequency.

Forecasts showed that SLR increases the Bay's trapping efficiency which for the intermediate and worst-case SLR scenarios caused the system to shift from being erosional to depositional. Despite that, San Pablo Bay drowns under all SLR scenarios. The decreased effect of waves on the bottom allows shoals to accrete in response to SLR. However, due to the low fluvial sediment supply, accretion is only 25-30% of the SLR and results in an increase in relative water depth.

Model results indicated that the behavior of main channel narrowing and deepening observed during the hindcast will continue to the end of the 21st century at a decreased rate and that it is not primarily SLR-induced. SLR enhances channel erosion which starts in the deepest channel sections with a seaward residual transport. By the end of the forecast, the system was still reacting to the imposed SLR.

The performed hindcast sensitivity analysis highlighted the considerable influence of the salinity-driven and 3D processes on the long-term morphological evolution of the Bay. They decrease the seaward sediment export from the system resulting in a higher trapping efficiency. Wind-generated waves also play a very important role in sediment redistribution, limiting shoal elevation, and maintaining the channel-shoal structure.

Finally, our modeling exercise shows that process-based models can be a useful tool to achieve a better understanding of the morphodynamic response of estuaries to climate change-induced forcing conditions perturbations. Similar to the findings of Dam et al. (2016), we conclude that even with a large number of schematizations implemented, such models can perform well in estuarine environments, especially when considering centennial time scales.

APPENDIX 3

The appendix aims to provide a brief description of the numerical model used in this study including the modeling software, model domain & forcing conditions. Also, we briefly introduce some of the parameters implemented, the formulation used for mud transport, and model performance metrics. The model setup used in this study was first developed by (van der Wegen, Jaffe, et al., 2011a). We implemented this modeling configuration while performing some minor modifications to better suit our objective.

A.3.1 Numerical model

We apply the 3D Delft3D (D3D) numerical, process-based software (Deltares, 2017; Lesser et al., 2004) to simulate the long-term morphological development of San Pablo Bay. The D3D solves the Reynolds-averaged Navier-Stokes equations at a high horizontal spatial and temporal resolution. It includes the k- ϵ turbulence closure model and allows for density (salt-fresh water) driven flows. Sediment transport is calculated by a 3D advection-diffusion solver based on the local and time-varying velocities and water levels for both cohesive and non-cohesive sediments. Bed level changes are calculated every time step based on the divergence of the sediment transport field and include variations in the bed composition (such as combining different percentages of both sand and mud fractions). Delft3D is coupled with the SWAN wave model (<http://swanmodel.sourceforge.net/>) to simulate the effect of the wind-waves such as the increased bed shear stress in shallow waters.

Each time step (2 minutes) the FLOW module computes the hydrodynamics (e.g., water level, velocities, and bed shear stress). The SWAN wave model uses the generated hydrodynamics and wind field to compute the wave field. The computationally expensive wave field is updated every hour. The effect of this wave field (e.g. wave-induced shear stress and wind setup) is then added to the previously computed hydrodynamics. The MOR module uses the combined hydrodynamics (FLOW + SWAN) to compute the sediment transport rate for each of the sediment fractions and the associated bed level changes. Following that, the bed level changes are multiplied by a morphological acceleration factor (MF) to enhance morphological developments (Roelvink, 2006). This loop is repeated for the next time step using the updated bed levels.

A.3.2 Model Domain

The model domain (Figure 4.9) covers the entire North Bay comprising San Pablo Bay, Carquinez Strait, and Suisun Bay, while two small branches at the landward side represent the Sacramento and San Joaquin rivers. The seaward model boundary is located at Richmond and the 4 riverine boundaries are located at Sacramento River, San-Joaquin River, Petaluma River, and Sonoma Creek.

The 3D model comprises a horizontal curvilinear grid (650 km²) with a spatially varying resolution and an average grid size of 550×550 m. The vertical grid consists of 15 sigma layers with higher resolution near the surface and bottom in order to provide a better representation of wind-driven flows near the surface and sediment transport near the bottom (Deltares, 2017).

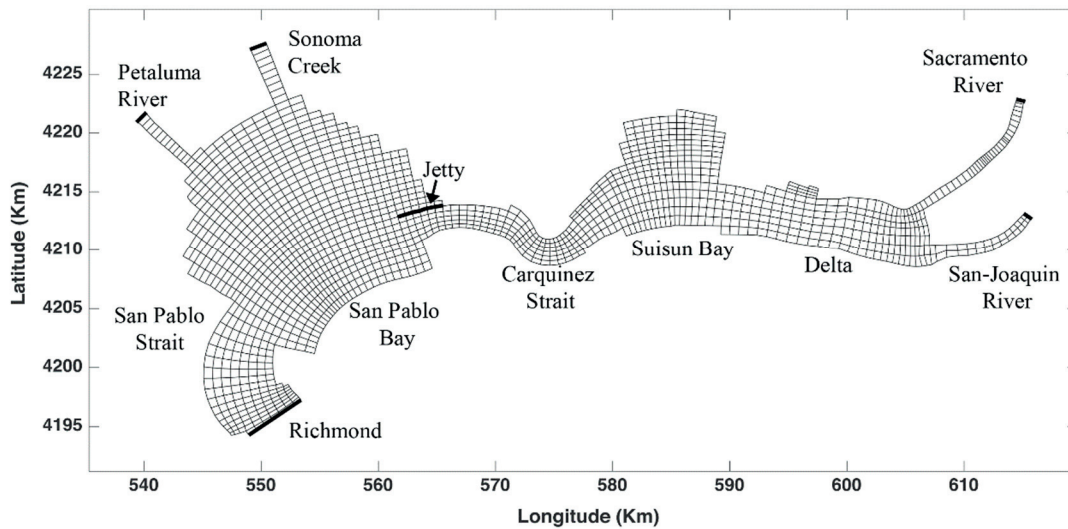


Figure 4.9. The Northern San Francisco Bay D3D structured model grid based on the work of van der Wegen et al. (2011a).

A.3.3 Boundary Forcing

The model domain has one seaward water level and 28 ppt salinity forced boundary, near Richmond, and four, freshwater flow forced riverine boundaries, i.e. the Sacramento River, the San Joaquin River, and two local tributaries, the Petaluma River and the Sonoma Creek. The main reason for adding the local tributary boundaries is that including these resulted in a better representation of the shape of the tidal flats.

All boundaries are tidally influenced; however, no data is available covering the entire 250-year period. We used a larger Delft3D Flexible Mesh (D3D FM) community model (Achete et al., 2015; Martyr-Koller et al., 2017; Vroom et al., 2017; www.D3D-Baydelta.org) that covers the entire San Francisco Bay-Delta system and a section of the Pacific Ocean in order to derive the hydrodynamic boundary conditions for the smaller North Bay D3D model of the current study. This larger model is able to simulate the tidal propagation throughout the estuary and has been validated in previous studies. The D3D FM model is forced at its seaward boundary by astronomic component water levels and at its landward non-tidal boundaries with discharges at the Sacramento (80%) and San Joaquin (20%) Rivers based on Ganju et al. (2008).

We implemented the concept of representative tides (Latteux, 1995) by simplifying the tidal boundary conditions into three main components (i.e. M_2 , O_1 , and K_1). To have a regular daily signal instead of a spring-neap cycle, we merged O_1 and K_1 into a single artificial C_1 based on similar tide residual sediment transports (Hoitink et al., 2003; Lesser, 2009).

The values of the river flow used to force the D3D FM model and the SSC for the North Bay D3D model are presented in section (4.3). To avoid SSC and salinity discontinuities at the turning of the tide we implemented a Thatcher-Harleman time relaxation lag of 120 minutes which gradually adapted outflow concentration at ebb to boundary defined concentration at flood.

A.3.4 Sea Level Rise

We impose 3 different sea level rise scenarios of a 42, 84, and 167 cm rise by the end of the 21st century, based on NRC, (2012). The wide range of those scenarios aims to cover the high uncertainty involved in SLR projections through optimistic, intermediate, and worst-case scenarios.

A.3.5 Wind

Wave action in San Pablo Bay is assumed to be limited to locally generated wind waves since limited offshore waves are able to penetrate through Golden Gate and reach North Bay. This raises the need for implementing a schematized wind signal that results in similar morphological development as the actual conditions (Ganju & Schoellhamer, 2010; Kuijper et al., 2004; van der Wegen et al., 2011a). We applied a diurnal sinusoidal wind signal with a constant amplitude of 6 m/sec but seasonally varying direction. A wind direction of 245° was imposed during 60% of the time (including high river flow conditions), while during the other 40% the wind direction was set to 90° .

A.3.6 Sediment Characteristics

We apply 5 different sediment fractions, i.e, 2 cohesive mud fractions and 3 non-cohesive sand fractions (fine sand to coarse sand). The mud fractions are mainly located on the shoals while the sand fractions are mainly located within the deep channel. The Partheniades-Krone formulations (Partheniades, 1965) are used for cohesive sediment transport, and the Van Rijn et al. (2004) formulations for non-cohesive sediment transport. In North Bay, mud transport dominates sand transport. The Partheniades-Krone formulations used in this study for mud transport are presented as follows, please refer to Appendix A.1.3.2 for the formulations.

Due to the scarcity of data on bed composition for the 19th century, we first start by generating an initial bed composition using the methodology defined by van der Wegen et al. (2011). We assume a simple uniform sediment distribution across the model domain.

This distribution is subjected to a 1-month period of low river flow conditions and sediment is allowed to redistribute according to the hydrodynamics and without bed level changes. The resulting sediment distribution is then used as the bed composition input for the model simulation starting in 1856. For more information about the initial bed composition generation please refer to van der Wegen et al. (2011) and van der Wegen et al. (2011a). Table (4.2) shows the applied sediment parameters derived based on sensitivity analysis. The $\tau_{cr,d}$ was set to 1000 N/m² following the recommendation of (Winterwerp and Van Kesteren, 2004). This approach suggests that sedimentation is not limited by a critical shear stress but instead by the settling velocity and concentration. The flocculation processes are not included in the model in an effort to reduce the complexity of the model description.

Table 4.2. *Implemented sediment parameters.*

	Sand	Mud
Median Sediment Diameter (D ₅₀) (μm)	200,400,800	
Fall Velocity (w _s) (mm/sec)		0.1, 0.2
Critical shear stress (τ _{cr,e}) (N/m ²)		0.25,1
Erosion parameter		2×10 ⁻⁴

A.3.7 Model Performance Evaluation

The model calibration and validation performed in this study are based on comparing modeled and measured bathymetries during the hindcast period. Following the recommendation of Sutherland et al. (2004), the Brier Skill Score (BSS) metric is used for evaluating model performance. The BSS measures the relative accuracy of model forecasts over a defined baseline by comparing model results (Modeled Bathymetry) with a reference case (1856 Initial Bathymetry) using the mean-squared error (MSE) as follows:

$$BSS = 1 - \frac{MSE}{MSE_r} = 1 - \frac{\langle (z_{mod} - z_{meas})^2 \rangle}{\langle (z_i - z_{meas})^2 \rangle} \quad (A.3.1)$$

Where the letter “z” denotes the bed level and the subscripts “mod”, “meas”, and “i” indicates the modeled, measured, and initial bed levels, respectively. The angle brackets indicate an arithmetic mean (Spatially weighted average). The BSS scale has no lower boundary (-∞ to 1; Table 4.3) which can result in negative scores indicating that predicted bathymetry is worse than reference bathymetry while a BSS value of 1 implies perfect agreement between modeled and measured bed levels.

Table 4.3. *Brier Skill Score proposed classification (Sutherland et al., 2004).*

	BSS
Excellent	0.5-1.0

Good	0.2-0.5
Reasonable/fair	0.1-0.2
Poor	0-0.1
Bad	<0.0

Findings of previous research illustrate the capability of the BSS single-number metric for judging the accuracy of morphodynamic forecasts for both 1D cross-shore models (e.g., de Alegria-Arzaburu et al., 2011) and for 2D/3D area models (e.g., Dam et al., 2016; van der Wegen et al., 2011a). However, caution must be taken when using the BSS because: 1) BSS values are extremely sensitive to small changes when the denominator is low (small morphological changes); 2) The BSS only looks at the cumulative change and not the transport mechanisms, models with seasonal transport are not rewarded for successful representation of seasonal variations. Also, the modeled bathymetry season (Wet or Dry) should match that of the compared reference bathymetry (Bosboom et al., 2014); and 3) It has a tendency to reward underestimations, especially when there is low correlation, forecasts with misplaced morphological features are likely to get lower scores than forecasts without those morphological features which counteract expert judgment (Bosboom et al., 2014; Bosboom & M. Reniers, 2014). This means that the correlation and standard deviation of both model results and measurements that make up the score must be checked. Also, visual inspection by experts is required, relying on automated calibration and validation can result in a misrepresentation of the system.

The BSS score is a useful metric to objectively determine the overall model performance which comprises amplitude, phase and mean errors. Identifying the source of model errors can be either done by visual inspection or by applying the BSS decomposition provided by Murphy and Epstein (1989) which allows for separate evaluation of those errors as follows:

$$BSS = \frac{\alpha - \beta - \gamma + \varepsilon}{1 + \varepsilon} \quad (\text{A.3.2})$$

Where,

$$\alpha = r_{Y'X'}^2$$

$$\beta = \left(r_{Y'X'} - \frac{\sigma_{Y'}}{\sigma_{X'}} \right)^2$$

$$\gamma = \left(\frac{\langle Y' \rangle - \langle X' \rangle}{\sigma_{X'}} \right)^2$$

$$\varepsilon = \left(\frac{\langle X' \rangle}{\sigma_{X'}} \right)^2$$

And,

σ is the standard deviation

r is the correlation coefficient

$$X' = z_{\text{mod}} - z_i$$

$$Y' = z_{\text{meas}} - z_i$$

Sutherland et al. (2004) describe the errors as follows: 1) α is a measure of the phase error, an α value of 1 indicates a perfect match in the sedimentation/erosion spatial patterns; 2) β is the combined measure of amplitude and phase error, a β value of 0 indicates perfect model forecasts for both the height and location of the morphological features; and 3) γ is a measure of the map-mean error, a zero value for γ indicates equal modeled and measured sedimentation/erosion volumes. The γ parameter indicates the reduction of skill due to sediment budget error. ε is a normalization term for the measured bed level changes, it donates the difference between the mean of initial and measured bed levels.

5

THE IMPACT OF MUD DYNAMICS ON LONG-TERM MORPHODYNAMIC EVOLUTION OF THE WESTERN SCHELDT ESTUARY UNDER SEA LEVEL RISE⁴

Abstract

Morphodynamic adaptation timescales of estuaries under sea level rise (SLR) will depend on local conditions such as sediment supply, sediment composition, and hydrodynamic forcing by tides, waves, and river flow. Important uncertainties relate to the evolution of intertidal area not only providing a natural barrier against wave attack but also serving unique ecological values. The objective of this study is to gain insight into the potential SLR morphodynamic impact on the channel-shoal system of the Western Scheldt (WS) Estuary in the Netherlands, with a focus on the role of mud and intertidal shoal adaptation.

We apply a process-based modeling approach (Delft3D) to model the long-term morphodynamic evolution of the WS estuary including a hindcast (1964-2012), and a forecast (2020-2100) under different SLR scenarios. The model domain covers the WS system in 3D and includes saltwater tidal forcing, fresh water river flow, waves as well

⁴ This chapter is based on:

Elmilady, H., et al. (in prep.): The impact of mud dynamics on long-term morphodynamic evolution of the Western Scheldt estuary under sea level rise.

as both sand and mud transport. Dredging operations are implemented to simulate the maintenance dredging of the navigation channel.

The model hindcast shows a good match to observed cumulative sedimentation/erosion trends and sediment budget. Forecast simulations till the end of the 21st century show that SLR impacts the system's hydrodynamics favoring ebb dominance which leads to a decrease in sediment import or an increase in the export for both sand and mud fractions. Sand transport experienced a larger SLR impact than that for mud. Mud transport constitutes a secondary, but still important contribution to sediment transport and the sediment budget of the system. The intertidal area accretes in response to SLR, however, accretion rates remain less than the SLR rate leading to lower intertidal area bed levels and less intertidal area. Mud favors intertidal shoals accretion under SLR only at fringed low-energy locations such as Land van Saeftinghe. At other intertidal areas, shear stresses on the intertidal area increase preventing further accretion. This is due to higher prevailing flow velocities under enhanced intertidal water depth. SLR poses a threat to the sustainability of the intertidal environment and may change intertidal flat sediment composition by creating unfavorable conditions for mud deposition.

Our work shows the potential of using process-based models to assess the complexity of climate change impact in estuaries. These models may help to explore the possibility of generalizing morphodynamic SLR impact in various types of estuaries under a variety of local forcing conditions.

5.1 INTRODUCTION

Channel-shoal systems are dynamic and complex geomorphological features of the estuarine environment. This network of channels and shoals sustains both ecological and economic aspects of the ecosystem. It serves as an important habitat for diverse marine species and supports fisheries, while also functioning as a natural buffer zone for coastal protection along with sheltering harbors and their navigational channels.

The interaction between the tidal currents, wave action, sediment transport, and bathymetric changes governs the formation and evolution of these channel-shoal systems (Coeveld et al., 2003; Elmilady et al., 2022; Hibma, 2004; e.g., Schramkowski et al., 2002; van der Wegen, 2013). Sea level rise (SLR) will impact the hydrodynamics of tidal systems which in turn will influence the residual sediment transports and trigger a long-term morphological adaptation process (e.g., Dissanayake et al., 2009; Elmilady et al., 2022; Neil K. Ganju & Schoellhamer, 2010; Jiang et al., 2020; van der Wegen, Jaffe, et al., 2017). Low-lying intertidal area face a threat of drowning if they are not able to morphologically adapt and keep up with the SLR (e.g., Best et al., 2018; Elmilady et al., 2019; van der Wegen et al., 2019).

Observations show that the global sea level has increased by about 103 mm over the past 3 decades (1993-2023; NASA, 2024) which is unprecedented over the past 2 millennia (Kemp et al., 2011; Kopp et al., 2016). The current rise is expected to accelerate, although there is a wide variation (0.3 to 2.7 m) in SLR forecasts (e.g., Church, Clark, et al., 2013; Le Bars et al., 2017; van de Wal et al., 2022) during the 21st century due to the uncertainty about the acceleration of the Antarctica ice sheet melting.

There is a need for a better understanding of processes governing the SLR-induced morphological response of estuarine systems. Process-based numerical models provide a useful tool to perform such explorations. To reduce the complexity of morphological forecast models in sand-dominated systems (Dam et al., 2016; e.g., Dissanayake et al., 2009; R bke et al., 2020; van der Wegen, 2013; van Maanen et al., 2013; Zheng et al., 2021), mud fractions are usually not considered. However, in most cases, mud flats also form a significant part of those sand-dominated systems and mud transport represents a secondary but important sediment transport contribution. Studies that include mud fractions (e.g., Braat et al., 2017; Dam et al., 2022; Elmilady et al., 2022) show that fine-grained sediments such as mud fractions play an important role in governing the sediment transport and morphological evolution of estuarine systems. Compared to the coarser sand fractions, mud is easily suspended, in turn, impacting the bed shear stresses and sediment deposition patterns which contributes to the formation and adaptation of channel-shoal systems within estuaries. Furthermore, the presence of mud fractions in the bed causes a more cohesive behavior, thus causing a harder erodibility of the sand fractions (e.g., Groenenboom, 2015). The SLR-induced increase in water level is expected to create sediment demand in tidal systems (L. Guo et al., 2021; Townend et al., 2021; e.g., Wang et al., 2018). The existence of mud could enhance the morphodynamic adaptation leading to faster, more uniform, accretion and muddier shoals under SLR (Elmilady et al., 2022).

The Western Scheldt (WS) Estuary, in the Netherlands, is a sand-dominated channel-shoal system with both marine and fluvial mud supply. This system has been the subject of various numerical modeling morphological studies due to its high ecological and economic value. It is also subjected to various human interventions such as dredging operations to maintain the navigational channel of Antwerp Port. Van der Wegen and Roelvink (2012) and Dam et al., (2016) showed that the interaction between the tidal forcing and the basin plan form (dykes and the non-erodible bed substrate) is the main driver of the morphological evolution and the formation of the channel shoal system. Using a 2D, high-resolution, process-based model, Dam et al., (2016) performed a long-term (110-year) hindcast, which showed significant skill in reproducing the observed morphological evolution. Both measured and modeled bathymetries show a trend of decreasing morphological activity over time, albeit with an adaptation time scale of approximately centuries. It is unclear how the anticipated SLR will impact the

morphological evolution of the WS estuary. Röbbke et al., (2020) investigated the long-term hydro- and morphodynamic response of the WS estuary to SLR and the different sediment strategies utilizing a 2D high-resolution Delft3D model including wave impact. Their work shows SLR-induced changes in the hydrodynamics causing the system to be less flood-dominant and even ebb-dominant at some locations which leads to a reduction of the net sediment input. Using a similar modeling approach, Zheng et al. (2021) highlight the relevance of the wind-generated waves for the long-term morphological evolution of the shoals and show shoal elevation increasing with SLR while experiencing a notable decline of intertidal area due to the increased inundation. The aforementioned studies simulate the WS bed composition with one characteristic grain size representative of a sand fraction. Various studies concerning the mud balance of the WS estuary (Baeyens et al., 1997; Dam & Cleveringa, 2013; e.g., Van Alphen, 1990; Van Maldegem et al., 1993) show that mud transport is a major contributor to the sediment balance of the estuary where marine mud is imported from the North Sea as well as by riverine mud input from the Scheldt river. Dam et al., (2022) performed a sediment (sand and mud) budget for the WS system using historic (1860 to 1955) bathymetric surveys combined with a subsurface model which showed a net exporting system with a contrasting behavior between sand (net export) and mud fractions (net import). Using a unique series of historic bathymetric surveys and human-sediment interaction (dredging, disposal, and sand mining) data, Elias et al. (2023) present a comprehensive sediment budget for the follow-up period from 1955 to 2020 with estimates of the contributions of sand and mud based on the analysis of a bed-composition map. Long-term data-based sediment balances (e.g., Dam et al., 2022; Elias et al., 2023) provide trustworthy historical sediment budgets. However, there is a need for process-based morphological models since observations do not reveal the underlying mechanisms, still rely on estimates of sediment input at the boundaries, and do not assess possible future developments.

This study aims towards a better understanding of the impact of mud dynamics on the long-term (century-scale) morphological evolution of sand-dominated estuarine channel-shoal systems under SLR, with the main focus on the role of mud fractions in the intertidal shoals' adaptation. We investigate the Western Scheldt (WS) estuary case study utilizing a coarse-resolution, 3D, process-based modeling approach (Delft 3D) to assess the long-term morphodynamic evolution of the WS Estuary including a hindcast (1964-2012), and a forecast (2020-2100) under different SLR scenarios. Our approach includes the main forcing conditions of tidal forcing, riverine discharges, sediment (sand and mud) supply, dredging operations, salinity, and wave impact. We compare our findings to the Röbbke et al. (2020) 2D, high-resolution, sand-only modeling study and the data-based sediment budgets by Dam et al., (2022) and Elias et al. (2023), and examine the possible relevance to other systems.

5.2 WESTERN SCHELDT ESTUARY

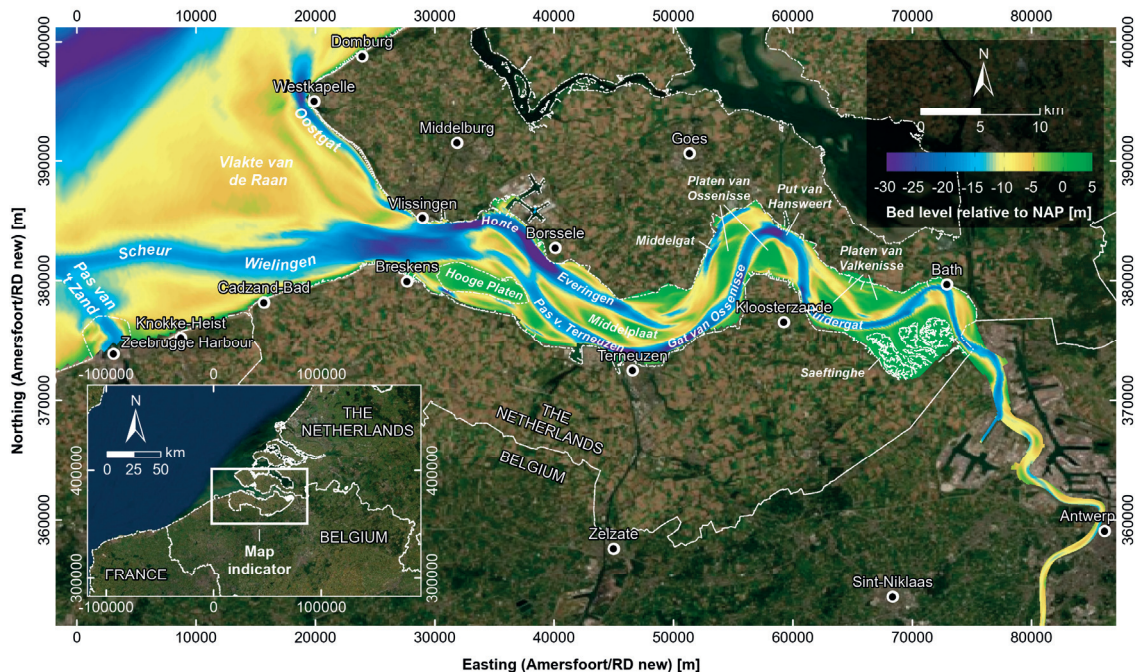


Figure 5.1. Satellite image and the 2012 Bathymetry of the Western Scheldt Estuary (The Netherlands) with labels of the main morphological features. Figure source: Rbke et al. (2020).

The following section gives a brief introduction to the Western Scheldt Estuary which is mainly based on the work of Kuijper et al. 2004 unless indicated otherwise.

5.2.1 Geometric Configuration

The Scheldt Estuary is a funnel-shaped estuary that connects the North Sea with the Scheldt River (Figure 5.1). It extends from the North Sea to Ghent, which is the section of the river basin that is influenced by tides. The segment between Ghent and the Belgian-Dutch border (≈ 130 km) is referred to as the Sea Scheldt, while the section from the border to Vlissingen (≈ 60 km) is referred to as the Western Scheldt. The Western Scheldt is located in the southwest of the Netherlands and covers an area of approximately 370 Km². It has a funnel-shaped geometry with a width ranging from about 6 km at the mouth to approximately 1.5 km near the border. Its cross-sectional area decreases exponentially from the estuary mouth at Vlissingen and going landwards.

5.2.2 Morphological characteristics

The Western Scheldt comprises a well-developed system of channels and shoals, while the mouth of the estuary is a shallow ebb-tidal delta. The geometrical scale of the meandering channel system increases as we go seaward. The channel system comprises a repetitive pattern of meandering main ebb channels and relatively straight main flood channels which are laterally constricted by man-made dikes and bank protection measures. The main transport takes place within those recent main channels. In main flood channels, more water and sediment are transported during flood tide than ebb tide, and vice versa for the ebb channels. Those main channels are separated by intertidal shoals and linked by stable or migrating secondary connecting channels, present in the estuarine cross-section. Currently, the morphodynamics is governed by the quasi-cyclic morphologic behaviour of those secondary channels with a timescale ranging from years to decades.

Shallow areas in the channels are formed at the transition between channel bends due to the channel meandering. At these locations, intensive dredging operations are continuously carried out to keep the navigation channel at a minimal depth of 15 m, which secures safe navigation to Antwerpen Harbor, one of Europe's largest ports. The dredged material is dumped on the shoals and the channel's outer bends (Fokkink et al., 1998).

The morphological features within the Western Scheldt can be divided according to their elevation into subtidal areas, intertidal areas, and salt marshes. The subtidal zone exists roughly between -5 and -2 m NAP, while intertidal shoals lie roughly between -2 m NAP and high water during neap tide (Van Rijn, 2013). Salt marshes exist above the intertidal zone and have an upper boundary defined as the bed level with a flooding frequency of five times per year.

Winterwerp et al. 2001 schematized the channel system into a chain of so-called macro-cells and meso-cells, based on morphological features and patterns of tide-averaged sand transports. Each macro-cell comprises a main flood and ebb channel, while meso cells comprise connecting channels. The intertidal and subtidal areas in the western part of the estuary have decreased significantly by about 20% to 30 % during the period between 1950 to 2000 (Van Rijn, 2013).

5.2.3 Hydrodynamics

The Scheldt River annually averaged river discharge amounts to about 110 m³/s with approximately equal contributions from both tributaries, the Rupel and the Scheldt (Kuijper et al., 2004; Wang et al., 2002). Annual variations exist, with discharges ranging from 50 m³ to 200 m³/sec. Also, seasonal variations may be substantial, with minimum and maximum discharges between 20 and 600 m³/sec (van der Werf & Briere, 2013) with the highest discharges recorded during winter.

The tidal wave in the Western Scheldt is meso- to macro-tidal and semi-diurnal, it is amplified as it propagates upstream due to the funnel-shaped geometry of the inner estuary. The mean tidal range varies from about 3.8 m at Vlissingen to about 5.2 m at Antwerpen. The asymmetry of the horizontal and vertical tide is stronger during the spring tide than that for the neap tide, which suggests that the asymmetry increases with the tidal amplitude (Wang et al., 1999). Maximum flow velocities in main channels range from 1 to 1.5 m/sec and can increase locally to reach 2 m/sec during spring tides.

The river discharge is of minor importance as it accounts for only about 0.6 % of the tidal prism at the estuary mouth (van der Spek, 1997). Based on that, the Scheldt estuary can be classified as a tide-dominated estuary.

Salinity at the estuary mouth typically ranges from 30 to 34 psu with tidal (semi-diurnal and spring-neap) and seasonal (e.g., river discharge) variability (e.g., van Maren et al., 2020). Salinity intrusion reaches up to Rupelmonde (92 km inland), while depending on the fresh water discharge this zero salinity point can shift over about 40 km (van Kessel et al., 2023). The longitudinal salinity gradient generates a horizontal pressure gradient which drives a landward-directed near-bed residual flow. The Western Scheldt system is generally well-mixed with limited vertical salinity differences over the water column due to the relatively large tidal range.

The average wind speed in the Scheldt estuary varies from 5 to 7 m/sec while the dominant wind direction is south to southwest. North Sea waves propagate from the north or southwest into the estuary, the significant wave height at the mouth of the estuary ranges from 1 to 2 m (Groenenboom, 2015). The increasing bottom friction attenuates the waves as they intrude further within the estuary. Within the estuary, friction between the air and water surface causes the generation of relatively small wind waves. However, wind set-up has a significant importance and could result in a sustainable rise of water levels during storms.

5.2.4 Sediment Characteristics

Sediment in the Western Scheldt is segregated due to the varying hydrodynamic conditions in the deep channels and shoals. The Scheldt estuary sediment is mainly composed of medium fine sand in the channels and fine sand on the shoals. Mud percentage in the main channels is rather small (< 10%). However, alongside the estuarine margins (intertidal areas and salt marshes), the mud percentage is much higher. Characteristic values for the median grain size (D_{50}) are given by Kuijper et al. (2004), based on Van Eck (1999) as channels $D_{50} > 150 \mu\text{m}$, shoals $50 \mu\text{m} < D_{50} < 150 \mu\text{m}$, and along the banks (Intertidal areas and salt marshes) $D_{50} < 125 \mu\text{m}$.

The North Sea and Scheldt River are the main sources of fine sediment (mud) fractions input to the Western Scheldt with a wide range of values reported in the literature (Table 5.1). Residual currents along the French, Belgian, and Dutch coasts line transport suspended sediments (mud) from the Straits of Dover northward resulting in an alongshore north-east-directed sediment flux. The residual suspended sediment transport through Dover Strait values widely varies (2.5 to 57.8 Mt/yr) in literature due to measurement techniques as well as natural variations, with a more narrow range of approximately between 11.5 to 44.4 Mt/yr (e.g., Eisma & Irion, 1988; Fettweis et al., 2007; Fettweis & Van den Eynde, 2003; Lafite et al., 1993; Van Alphen, 1990; Velegrakis et al., 1997). Eisma & Kalf (1979) and Van Alphen (1990) suggest that about half of this flux is deviated towards the French–Belgian–Dutch coastal zone. Based on the above-mentioned values, this equates to approximately between 5.8 to 22.2 Mt/yr. A small portion of this flux is imported to the WS estuary.

The Western Scheldt Estuary has two estuarine turbidity maxima (ETM). The coastal turbidity maximum at the mouth area near Zeebrugge harbor exists because of sediment trapping due to tidal flow conditions and is maintained by erosion of old mud deposits, mud dredged from Zeebrugge harbor, sediment- and salinity-driven density currents (van Maren et al., 2020). Another ETM exists near Antwerp port which is commonly attributed to a combination of gravitational circulation, tidal pumping, and flocculation (Van Kessel et al., 2011).

Table 5.1. Net mud import (Kt/yr) at the Western Scheldt (WS) mouth and the Belgium-Dutch border reported in literature.

Mud import at the WS mouth (kt/yr)	Year	Reference
600	1969 - 1986	Van Alphen (1990)
100 ± 200	-	Van Maldegem & Vroon (1995)
120	1998-1999	Van Maldegem et al. (1999)
300 to 650	1990, 1995 and 1997-2001	Lefèvre (2000)
333	1994-2010	Dam & Cleveringa (2013)
934	2006	Cronin et al. (2018)
-221	2014	
150 *	1955 to 2020	Elias et al. (2023)
Riverine mud import at the BE-NL border (kt/yr)		
400	1975-1985	Van Maldegem et al. (1993)
153	early 1980s	Baeyens et al. (1997)
160 to 380	1990, 1995 and 1997-2001	Lefèvre (2000)
306	1964-1986	Wartel et al. (2007)
87	1986-1999	
122.5 *	2001 -2011	Vandenbruwaene et al. (2017)

* A dry density of 0.5 ton/m³ was assumed to convert from m³/yr to kt/yr

5.3 MODELING SETUP

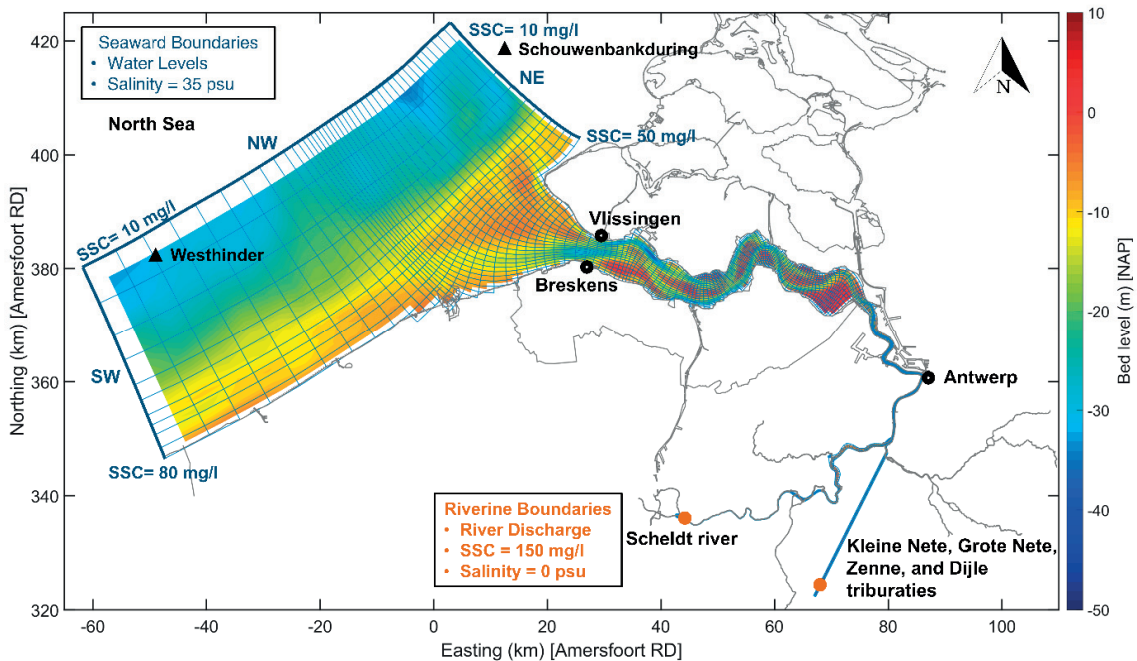


Figure 5.2. The Western Scheldt hydrodynamic model grid and 1964 observed bathymetry (m; Datum: NAP). Light grey lines are the land boundary.

We implement the 3D, process-based, numerical model Delft3D (D3D; Deltares, 2023; Lesser et al., 2004) to compute hydrodynamics, sediment dynamics, and the associated morphological development. The FLOW module in D3D computes the flow by solving the non-steady shallow water equations (continuity and momentum). The model domain covers the Western Scheldt estuary along with a section of the North Sea and the Scheldt River (Figure 5.2). The model grid is a curvilinear grid with variable grid resolution which is based on the NeVla model configuration (e.g. van Maren et al., 2020; Vroom et al., 2015), but with a coarser grid resolution similar to that implemented by van der Wegen & Roelvink (2012). The seaward model boundaries are composed of three sections South West (SW), North West (NW), and North East (NE). The riverine boundaries are represented by two source points at the Scheldt River and its tributaries. Due to grid resolution limitation, we schematized the Scheldt tributaries (Kleine Nete, Grote Nete, Zenne, and Dijle) as one rectangular tributary with approximately similar length and water volume. The model is 3D with 7 vertical sigma layers which follow the bed topography and are equally spaced over the water column. Salinity effects are included by assigning a constant concentration of 35 and 0 psu at the seaward and riverine boundaries, respectively. The initial model domain salinity level (before spin-up) is set to 25 psu.

The hydrodynamics at the seaward boundaries are forced by time-varying water levels which are derived from Delft3D FM (Flexible Mesh) Global Tide and Surge Model (GTSM Model; Muis et al., 2020) using conditions year 2011 as the base case for the No SLR scenario. The GTSM model is also used to simulate linear global SLR scenarios of 0.4, 0.96, 1.67, and 2.63 m (Le Bars et al., 2017) for the period from 2020 to 2100. This results in a modeled local SLR at Westhinder of 0.22, 1.10, 1.96, and 3.02 m, respectively. Robke et al. (2020) provide more information regarding the seaward boundary conditions derivation. We assume constant discharges at the riverine boundaries of 110 m³/s based on the average observed mean discharge of the Scheldt. This is divided equally between the Scheldt River and its tributaries.

The model incorporates both sand ($D_{50} = 200 \mu\text{m}$) and mud fractions ($D_{50} \leq 63 \mu\text{m}$) with mud being mainly present on the intertidal shoals and the more downstream sections of the estuary (which is subjected to low wave attack). Due to the lack of spatial bed composition data, the initial bed composition used for the morphological hindcast simulation is generated using an approach similar to that applied by Van der Wegen et al. (2011) for San Pablo Bay (USA) and Van Maren et al. (2020) for the Western Scheldt. Using 1964 bathymetry with a sandy bed, we performed a 1-year hydrodynamic simulation without morphological updates during which mud enters from the boundaries and distributes across the model domain based on hydrodynamic conditions and sediment supply. At the end of the one-year period, the available sediment mass in the top active sediment layer (0.5 m) reached an approximately dynamic equilibrium state. The mud percentage in the top layer was temporally averaged over the last 29.5 days of the simulation to include spring-neap tidal variations and was used as initial conditions for the morphological simulations. We disregard cells at which notable sediment depletion occurred (e.g., in the channels) resulting in a low ($<200 \text{ kgm}^2$) sediment mass in the seabed.

The Van Rijn (1993) formulations are used to compute the sandy sediment ($D_{50} = 200 \mu\text{m}$) transport for the combined effect of waves and currents for both bedload and suspended load transport. The mud transport is computed using (Partheniades, 1965) cohesive sediment transport formulation. This implementation accounts for the mud impact on the sand erodibility but not vice versa. The applied mud fractions have a critical erosion shear stress ($\tau_{c,e}$) of 0.25 N/m², an erosion parameter (M) of 1.0×10^{-4} , and a settling velocity (w_s) of 0.5 (Mud fraction 1) and 2 mm/s (Mud fraction 2). The use of two settling velocities is to simulate different particle sizes in the system.

Suspended sediment transport is calculated in the D3D by an advection-diffusion solver which includes a sink and source term describing sediment exchange with the bed. The bed stratigraphy comprises a top active 0.5 m sediment layer (transport layer) which interacts with the water column. Bellow that, four 1 m under layers exist along with a

base layer which extends to the non-erodible layer. With erosion, sediment is exported from the top transport layer and replenished from the underlayers to maintain the transport layer thickness. With deposition, sediment is imported to the underlayers after mixing with the top transport layer. The D3D MOR module computes the bed level changes based on the divergence of the sediment transport field. The MORFAC (Roelvink, 2006) approach multiplies the bed level changes with a morphological acceleration factor (MF) to enhance the morphological developments. This approach has been implemented in several long-term morphological studies of tidal systems and showed good results with implementations up to a MF of 400, and lower values when including wave action (Braat et al., 2017; Dissanayake, 2011; Elmilady et al., 2019, 2022; e.g., van der Wegen et al., 2008).

We model 1 hydrodynamic year (355 days) with a MF of 51.59 and 82.54 for the hindcast and forecast period resulting in 48 and 80 years of morphological development, respectively. This approach provides stable morphodynamics with a reasonable computational effort as modeling 1 hydrodynamic year (including wave action) takes about 2 days on a 4-core (2.6 GHz) computer.

Seaward boundaries prescribe an equilibrium sand concentration profile. For simplicity purposes, we assume no variations in the mud concentrations between summer and winter. Constant suspended sediment concentrations (SSC) for the mud fractions are imposed at the model boundaries. A SSC of 80 mg/l and 50 mg/l is applied at the shoreline of the southwestern and northeastern model boundaries, respectively. This is approximately based on seasonally average observed surface SSC maps (Groenenboom, 2015; van Maren et al., 2020). Going offshore, the SSC decreases linearly to 10 mg/l. The concentrations at the seaward boundaries are divided equally between the two mud fractions. We applied a Thatcher-Harleman relaxation time lag (Thatcher & Harleman, 1972) of 120 min to avoid SSC discontinuities at the boundary during turning tides. The coastal boundary option in D3D was implemented to allow for non-perpendicular flow across the boundaries (Deltares, 2017). At the riverine boundaries, only the finer mud fraction ($w_s = 0.5$ mm/s) is imposed with a concentration of 150 mg/l. This concentration was treated as a calibration parameter so that the modeled mud load from the Scheldt is within the reported range in previous literature. We also apply dredging (minimum water depth ≈ 2 m) at the riverine section upstream the confluence of the Scheldt and its tributaries to prevent exaggerated mud accumulation and the clogging of the water pathways.

The implemented initial (1964) hindcast bed level is the observed bathymetry from the Vaklodingen data set (RWS, 2023) measured in 1963, 1964, and for some small sections in 1969. Extensive dredging operations occurred during the hindcast period and are currently ongoing in the Western Scheldt estuary to maintain the navigational channel.

Dredging is simulated in the model and occurs when the bed level at the specified cells exceeds the defined level. The dredging and deposition areas (Figure 5.13; Appendix 4) and the associated dredging depth were defined for the hindcast simulation based on historical operations (starting 1970s) while the dredging operations for the forecast simulation were defined based on the currently applied (2013-2014) in the Western Scheldt (Vroom & Schrijvershof, 2015). Dredging mainly occurs in the deep navigational channel while deposition occurs partly in the vicinity of shoals and partly in some channel areas. In addition to dredging and deposition, at some locations within the estuary, dredged material is mined and extracted from the system.

The Delft3D model is coupled (60-minute interval) with the spectral wave model SWAN (Booij et al., 1999; <http://swanmodel.sourceforge.net/>) in stationary mode to simulate wave action including off-shore wave propagation and wind-wave generation within the model domain. The wave model is forced with constant wave conditions at the seaward boundary representing the measured average significant wave height (H_s ; 1.41 m), wave peak period (T_p ; 6.5 sec), and mean direction (292 degrees) at station Schouwenbank during the period from 1983 (2006 for the wave direction) to 2014 (van der Wegen, van der Werf, et al., 2017). We also implement a constant wind field with a wind speed of 5.5 m/sec and a direction of 261 degrees based on the average measurements at station Vlissingen from 2006 to 2014. The resulting significant wave height (H_{sig}) in the estuary ranges from 0.1 to 0.4 m (Example in Figure 5.14; Appendix 4). Table 5.2 summarizes the main model parameters.

Table 5.2. Summary of the main model parameters.

Parameter	Value
Dimension	3D (7 vertical sigma layers)
Hydrodynamic time step	0.5 min
Wave coupling time step	60 min
Roughness	0.023 s/m ^{1/3}
Horizontal eddy viscosity	1 m ² /s
Horizontal eddy diffusivity	10 m ² /s
Global SLR scenarios	0.4, 0.96, 1.67, and 2.63 m
Local SLR magnitude	0.22, 1.10, 1.96, and 3.02 m
Wind magnitude	5.5 m/s
Wind direction	261°
Transverse bed slope factor (Abn)	100
Streamwise bed slope factor (Abs)	1
Sand diameter (D50)	200 μm
Mud critical erosion shear stress	0.25 N/m ²
Mud erosion parameter (M)	1.0 × 10 ⁻⁴

Parameter	Value
Mud settling velocity	0.5 and 2 mm/s
Morphological acceleration factor (MF)	51.59 (Hindcast) and 82.54 (Forecast)

5.4 HINDCAST

We performed a morphological hindcast and compared it to observed development from 1964 to 2012 (Figure 5.3). The estuary experienced notable morphological development during the hindcast period, with the highest dynamics occurring at the upstream section and bed level changes reaching up to ± 10 m (Figure 5.3a). Dredging activities resulted in a significant deepening of the main navigation channel up to Antwerp port. This includes the Pas van Terneuzen, Gat van Ossensisse, and the Zuidergat channels in which the deepening reached up to 15 m at some locations (please refer to Figure 5.1 for labels). On the other hand, the Middelgat experienced notable sedimentation. The deepest section of Everingen channel as well as its Northern channel bank experienced deposition, while the rest of the channel mainly experienced erosion. The deposition in the Middelgat and the Everingen channel is partly due to the deposition of the dredged material from the main channel. Also, the Hooge Platen, Platen van Ossensisse, Platen van Valkenisse experienced deposition mainly due to deposition activities on top or in the vicinity of the shoals. Land van Saeftinghe, the most landward shoal, experienced quite limited deposition due to its already high elevation. The mouth area experienced lower bed-level dynamics compared to the upstream section, with bed-level changes in the order of ± 5 m. A thin middle stretch of the estuary entrance (Vlissingen-Breskens) experienced erosion while the northern and southern sections mainly experienced deposition.

Model results (Figure 5.3b) show a good reproduction of the observed cumulative sedimentation/erosion trends, albeit with lower spatial (small-scale) variability due to the relatively coarse model grid resolution. The modeled hindcast reproduces the deepening of the main navigation channel along with the sedimentation in the Middelgat and Everingen channels. Shoals (e.g., Hooge Platen, Platen van Ossensisse, and Platen van Valkenisse) experienced deposition. However, at some locations (e.g., Platen van Valkenisse) the deposition is of a higher magnitude and less spread compared to observations. This is due to how deposition activities are modeled. The dumped sediment is supplied to the bed instead of being supplied in the water column as in reality which allows the sediment to spread. Model results underestimate the deposition that occurred at Land van Saeftinghe. Similar to measurements, modeled development shows higher bed level dynamics at the upstream estuary section than the mouth area. Also, model performance is highest at the upstream section which is subjected to the most pronounced dredging activities to maintain the navigation channel depth. The modeled cumulative

dredging volumes ($5.69 \times 10^8 \text{ m}^3$) show a good match to the observed volumes ($4.51 \times 10^8 \text{ m}^3$) during the hindcast period (Figure 5.15; Appendix 4). For the hindcast modeled and measured hypsometries, please refer to Figure 5.16 in Appendix 4.

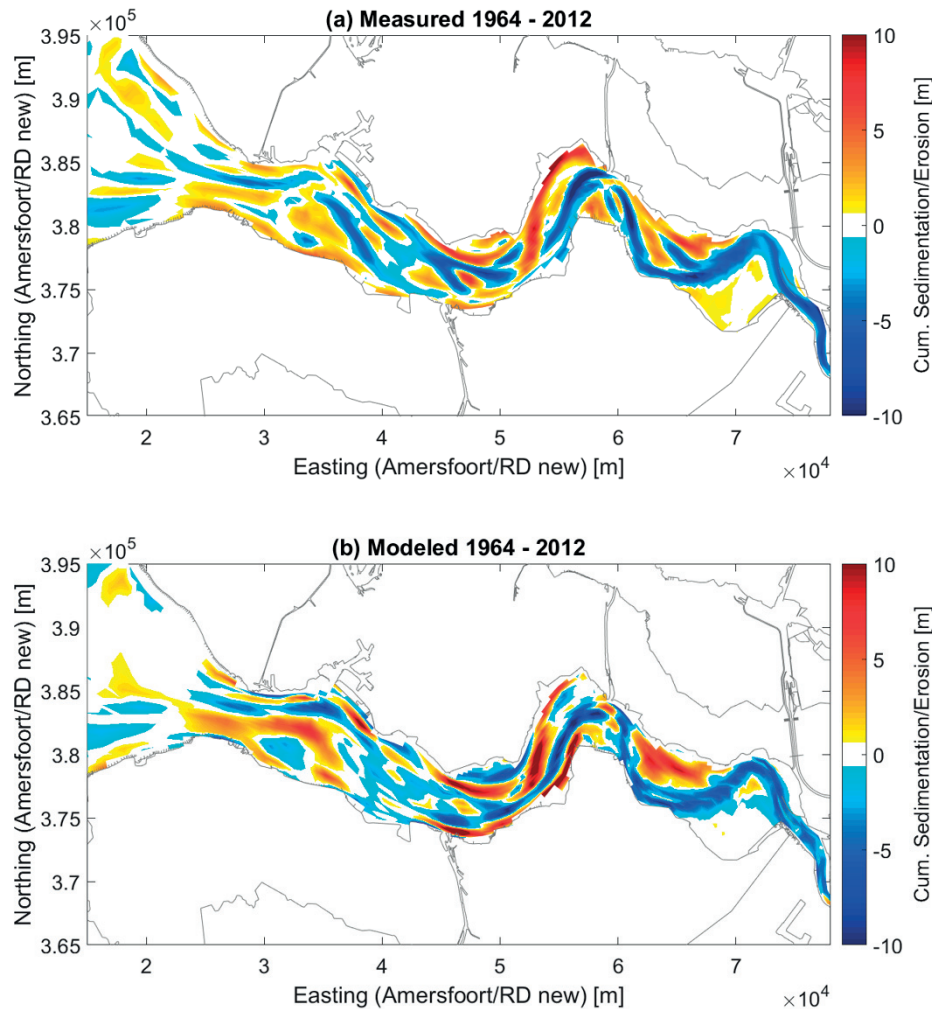


Figure 5.3. (a) Measured, and (b) Modeled cumulative sedimentation/erosion (m) during the hindcast period (1964 to 2012).

Figure 5.4 shows the observed and modeled sediment budget between 1964 and 2012 along with the width-averaged cumulative sedimentation/erosion which occurred during this period. The cross-section locations are inspired by the macrocell concept by Winterwerp et al. 2001, where the basin is subdivided into macrocells each including a major ebb and flood channel circulating the sediment. Measurements (Figure 5.4a) show that the mouth area (Cell 1) along with the downstream section of the estuary (Cell 2) experienced net deposition. The vicinity of the estuary entrance (Vlissingen-Breskens) is depositional. A possible reason is that two main deposition locations are located in the

vicinity of the estuary entrance and the neighboring Hoge Plaaten shoal. The mid-section of the estuary (Cell 3) is mostly a spatially erosional cell that experienced net erosion. On the other hand, Cell 4 is mostly a spatially depositional cell that experienced net deposition. One of the main reasons is that the western side of Cell 4 incorporates a main deposition location for the sediment that is being dredged from the upstream sections of the navigation channel (in Cells 5 and 6). This is reflected in the observed sedimentation in the Middelgaat (Figure 5.3). Cells 5, and 6 are mostly spatially erosional cells that experienced notable net erosion. This is mainly due to intensive dredging activities that occurred in order to deepen the navigation channel up to Antwerp. A portion of this dredged sediment is dumped on top of Platen van Valkenisse, this is the reason for the lower width averaged volume change values in its vicinity. Also, Cell 5 is the area with the highest sand mining. Overall, the estuary experienced net erosion.

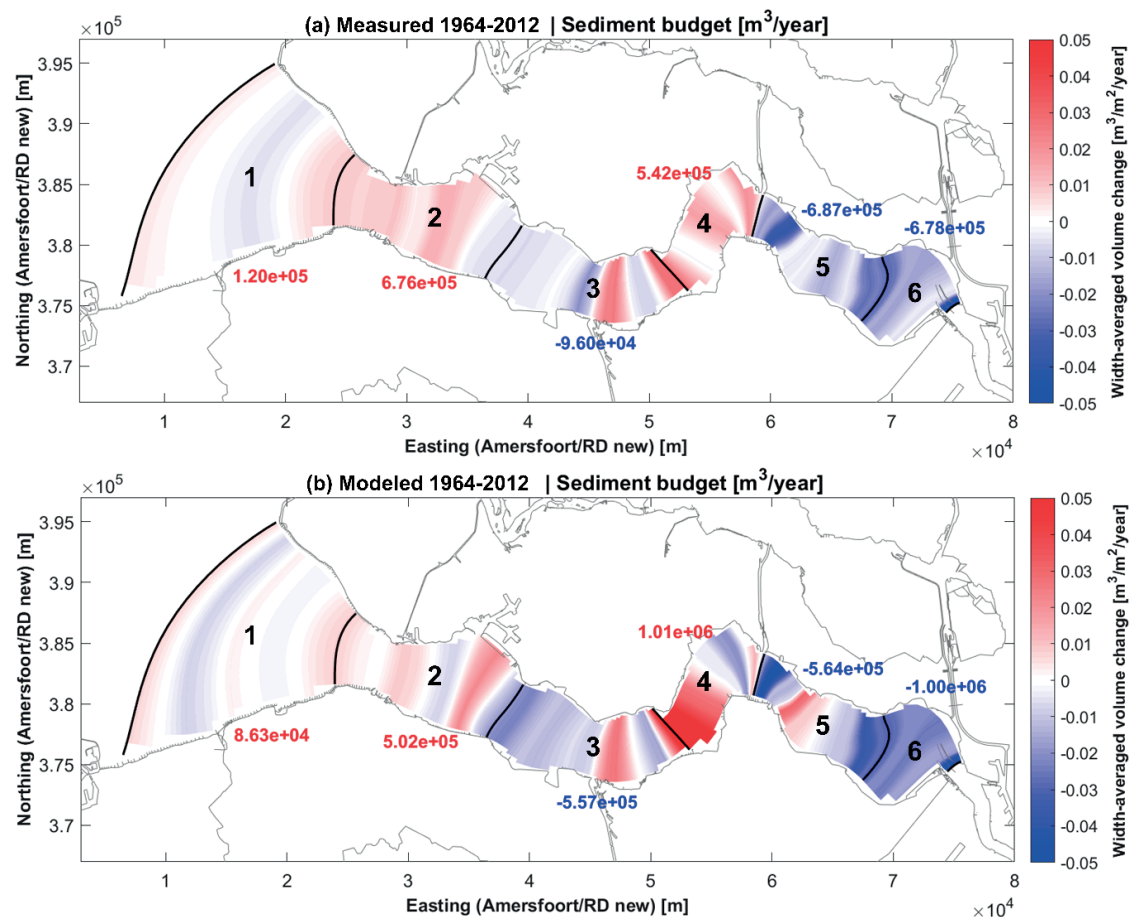


Figure 5.4. (a) Measured, and (b) modeled width-averaged cumulative sediment volume change ($m^3/m^2/yr$) during the hindcast period (1964 to 2012) for 6 cells. The red/blue color indicates sedimentation/erosion, respectively.

The modeled budget Figure 5.4b shows a good resemblance to the observed patterns, albeit with different magnitudes. Cells 1, 2, and 4 are net depositional, while Cells 3, 5, and 6 are net erosional cells. The WS Scheldt estuary's (Cell 2 to 6) modeled net erosion is $0.61 \text{ Mm}^3/\text{yr}$ compared to the observed net erosion of $0.24 \text{ Mm}^3/\text{yr}$.

5.5 FORECAST

We performed an 80-year (2020 – 2100) morphological forecast for the Western Scheldt while implementing different SLR scenarios. The end conditions of the hindcast simulation were used as initial conditions for the forecast simulation. We also explored the forecast with different forcing conditions. In this section, we present the forecast results for two model settings; the base case simulations (Sand-mud) and another simulation that excludes the mud (Sand-only). Figure 5.5 shows the cumulative total (Suspended and bed) sediment transport at Vlissingen – Breskens along with two upstream cross-sections. The Vlissingen – Breskens cross-section is located at the mouth of the estuary and no dredging locations intersect this cross-section. Without SLR, both sand and mud fractions are being imported to the estuary from the North Sea, resulting in a net sediment import. The sand import exists for both simulations, albeit with a higher magnitude in the case of the Sand-only model.

Implementing the SLR scenarios shows that SLR decreases this sand import and shifts it to export for the higher magnitude SLR scenarios (1.10, 1.96, and 3.02 m). SLR also decreases the mud import to the estuary, however, SLR impact is more pronounced for the coarser sandy fraction than that for the finer mud fractions. In addition, the SLR impact on the sand transport is more pronounced for the Sand-only model. For example, the difference in the cumulative sand transport between the 0 m and 3.02 m SLR scenarios is 4.70×10^5 , and 3.79×10^5 for the Sand-only and the Sand-mud simulation, respectively. This is because the mud fractions cause a more cohesive behaviour of the bed which decreases the sand erodibility. The two upstream cross-sections show the same SLR-impact trend as the Vlissingen – Breskens cross-section, albeit at those cross-sections, sand import without SLR is more pronounced and remains import even with the highest SLR scenario.

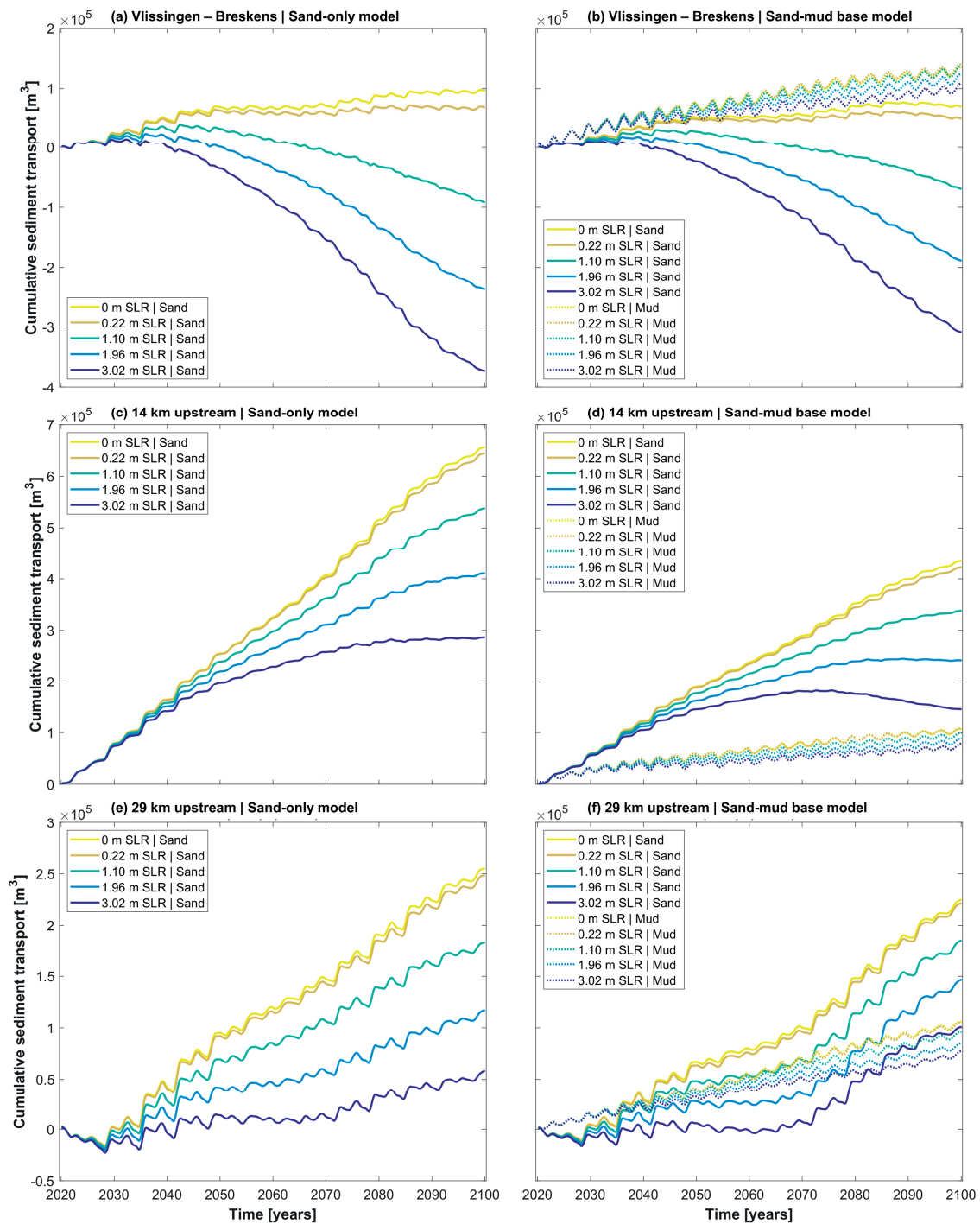


Figure 5.5. The cumulative total (suspended and bed) sediment transport (m^3) during the forecast period through Vlissingen-Breskens cross-section along with two cross-sections at 14 and 29 km upstream; (a, c, and e) Sand-only model, and (b, d, and f) Sand-mud base model. Positive/ negative numbers are import to/export from the estuary, respectively. Sediment volume is based on particle density and excludes voids and the morphological factor.

Figure 5.6 shows the mud transport (Kt/yr) at the estuary bounds and mouth area for the 0 m and 3.02 m SLR scenarios. Going forward, we only present the highest SLR scenario (3.02 m) as it has the most pronounced impact, other scenarios show the same trend, albeit with lower magnitudes. We show the total net mud transport and make a distinction between the marine mud ($w_s = 0.5$ and 2 mm/s) and fluvial mud ($w_s = 0.5$ mm/s). Without SLR, the net total longshore mud transport (17.7 Mt/yr) is northeast-directed. This value falls within the reported range in the literature (5.8 to 22.2 Mt/yr; section 5.2.4). A small portion (≈ 2.5 %) of the marine mud is imported to the Western Scheldt estuary (436 Kt/yr) through the estuary mouth, while about 79 Kt/yr fluvial sediment is exported from the estuary mouth resulting in a net mud import of 356 Kt/yr. On the other hand, the estuary also experiences fluvial mud import (172 Kt/yr) at the Belgium-Dutch border (upstream cross-section). This modeled fluvial mud import falls in the middle of the wide range reported in the literature (87 to 400 Kt/yr; e.g., van Maldegem et al. 1993, Wartel et al. 2007). On the other hand, marine sediment reaches this border and is exported Zeeschedle 16 and 92 Kt/yr, for the fraction with finer and coarser mud fraction, respectively. SLR slightly decreases the mud transport along the longitudinal mud transport along the coast. Mud import to the estuary through its mouth decreases by about 20% from 356 Kt/yr to 288 Kt/yr. The decrease is caused by the reduced import of the larger marine fraction ($w_s = 2$ mm/s), while the finer marine fraction ($w_s = 0.5$ mm/s) experiences larger import and the fluvial mud export slightly increases. At the Belgium-Dutch border, the fluvial mud import increases from 172 to 276 Kt/yr, while the export of the marine mud towards the Zeeschedle decreases. The main reason for the increase of the fluvial mud import with SLR is that the SLR-induced increase in water level reduces the dredging volumes and the associated sand mining at the vicinity of Antwerp port needed to maintain the navigation channel. The fluvial mud (44 Kt/yr) entering from the southwestern seaward cross-section is from the fluvial mud which deposited in the mouth area during the hindcast period and is being circulated in the North Sea.

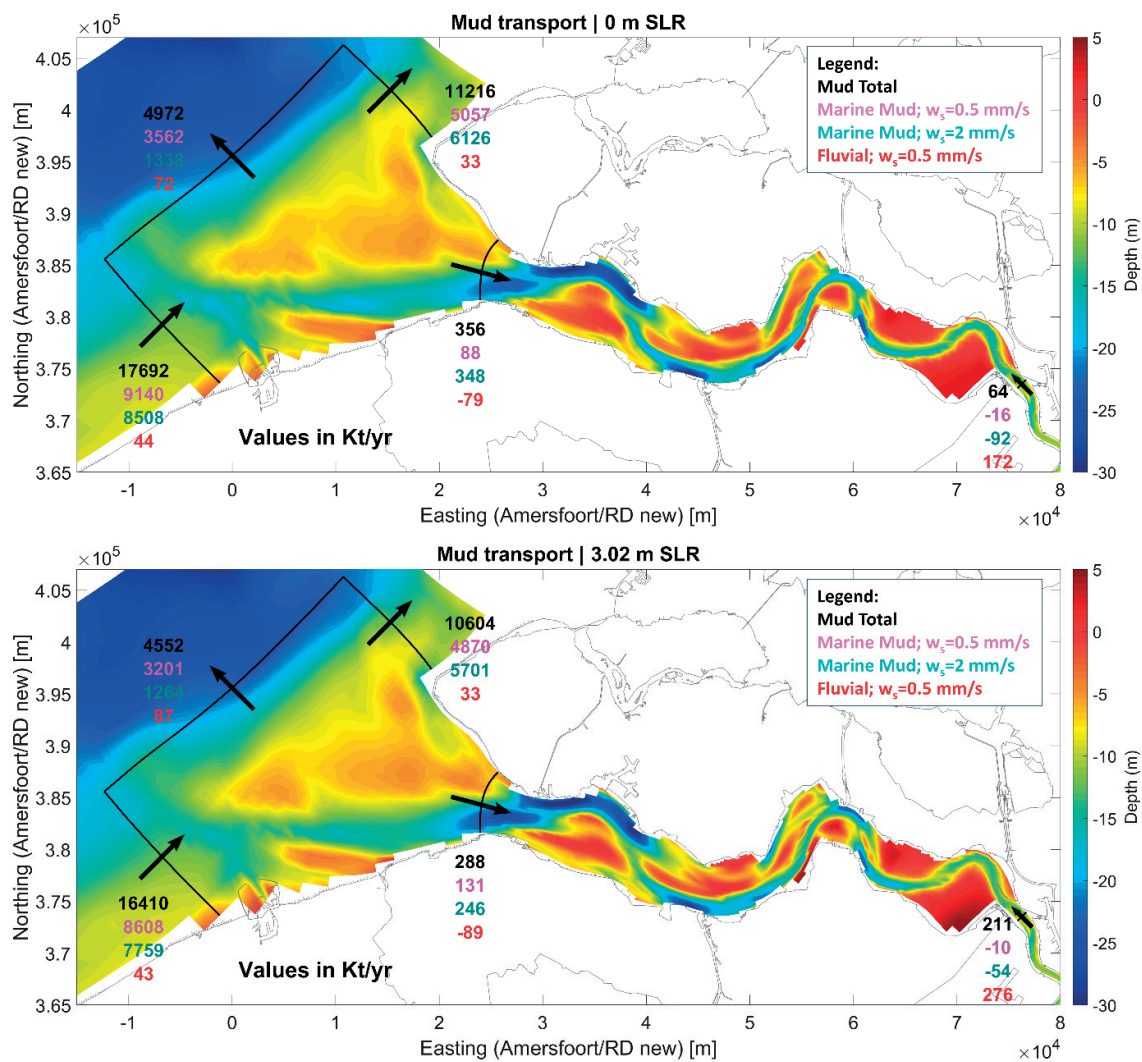


Figure 5.6. The net suspended mud transport (Kt/yr) during the forecast period for the Sand-mud base simulation; (a) 0 m SLR, and (b) 3.02 m SLR. The colored values indicate the total (Black), marine mud (Magenta and Cyan), and fluvial mud (Red). Positive/negative numbers indicate that the direction of transport is the same/opposite to the direction of the arrow, respectively.

Figure 5.7 shows the cumulative sedimentation (m) erosion plots during the forecast period for the Sand-only model and the Sand-mud base model. Independent from the SLR scenario and the mud inclusion, the maximum bed level changes is about 15 m which is mainly due to channel migration. Generally, bed level changes are more pronounced in the western section than that in the eastern section of the estuary. The area around the Hooge Platen experienced notable deposition due to sediment deposition in its vicinity while the neighbouring navigational channel Honte experience notable deepening. The navigational channels Pas v. Teurneuzen and Gat van Ossensisse experienced also

experienced deepening. On the other hand, Everingen channel is not maintained by dredging instead it is a deposition location for sediment dredged from the navigation channels, this resulted in a notable reduction of the channel depth due to large depositional volumes. This is also the case for the Middelgat channel because of a nearby deposition location. Platen van Valkenisse experienced deposition mainly because of sediment deposition on top of the shoal. For the forecast modeled hypsometries of the Sand-only and Sand-mud models, please refer to Figure 5.17 in Appendix 4.

The introduction of SLR results in increased sedimentation in the vicinity of the shoals (e.g., Hooge Platen and Platen van Valkenisse). SLR has a strong impact on the morphodynamics in the western section than the eastern section of the estuary. Pronounced deepening occurred at the estuary mouth. This is also reflected in Figure 5.8 which shows the forecasted width averaged cumulative sedimentation erosion ($\text{m}^3/\text{m}^2/\text{yr}$) along with the sediment budget for 6 cells. SLR causes notable erosion of the western section of Cell 2 (at the estuary mouth). This eroded sediment is transported to Cell 1 which showed much larger deposition in the 3.02 m SLR scenario compared to that for the 0 m SLR scenario. For Cells 3, 4, and 5, SLR results in less deposition/ more erosion. On the other hand, for Cell 6, SLR causes less erosion to the no SLR scenario and only for the Sand-mud model cell 6 turns to be depositional with SLR (Figure 5.8d, Cell 6). This is due to the high mud deposition at the Land van Saeftinge.

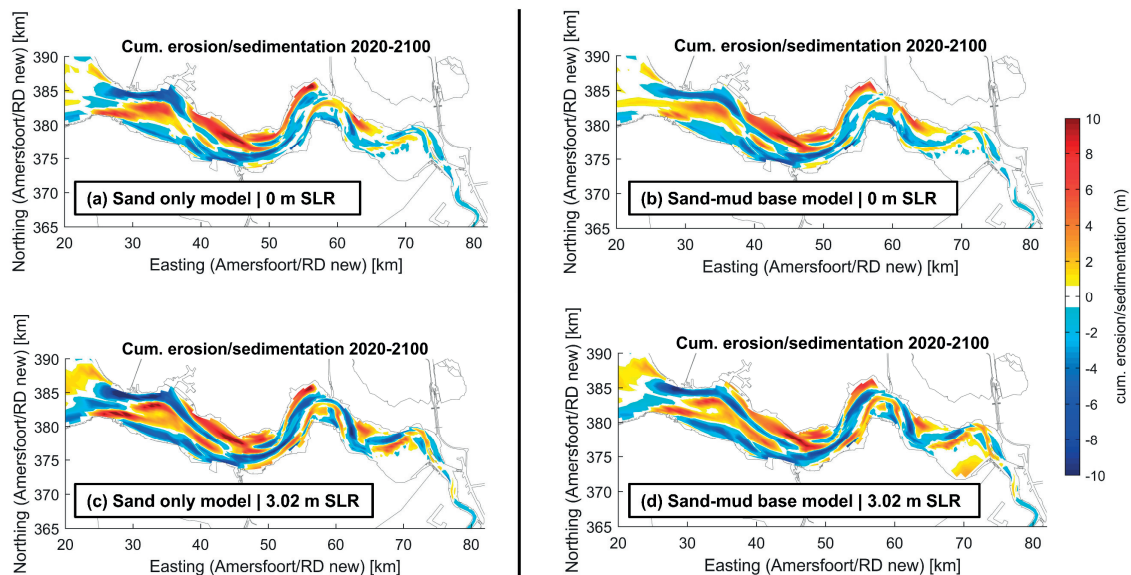


Figure 5.7. Cumulative sedimentation erosion (m) maps during the forecast period (2020 – 2100) for the simulations with the Sand-only and Sand-mud model with (a,b) 0 m, and (c,d) 3.02 m SLR, respectively.

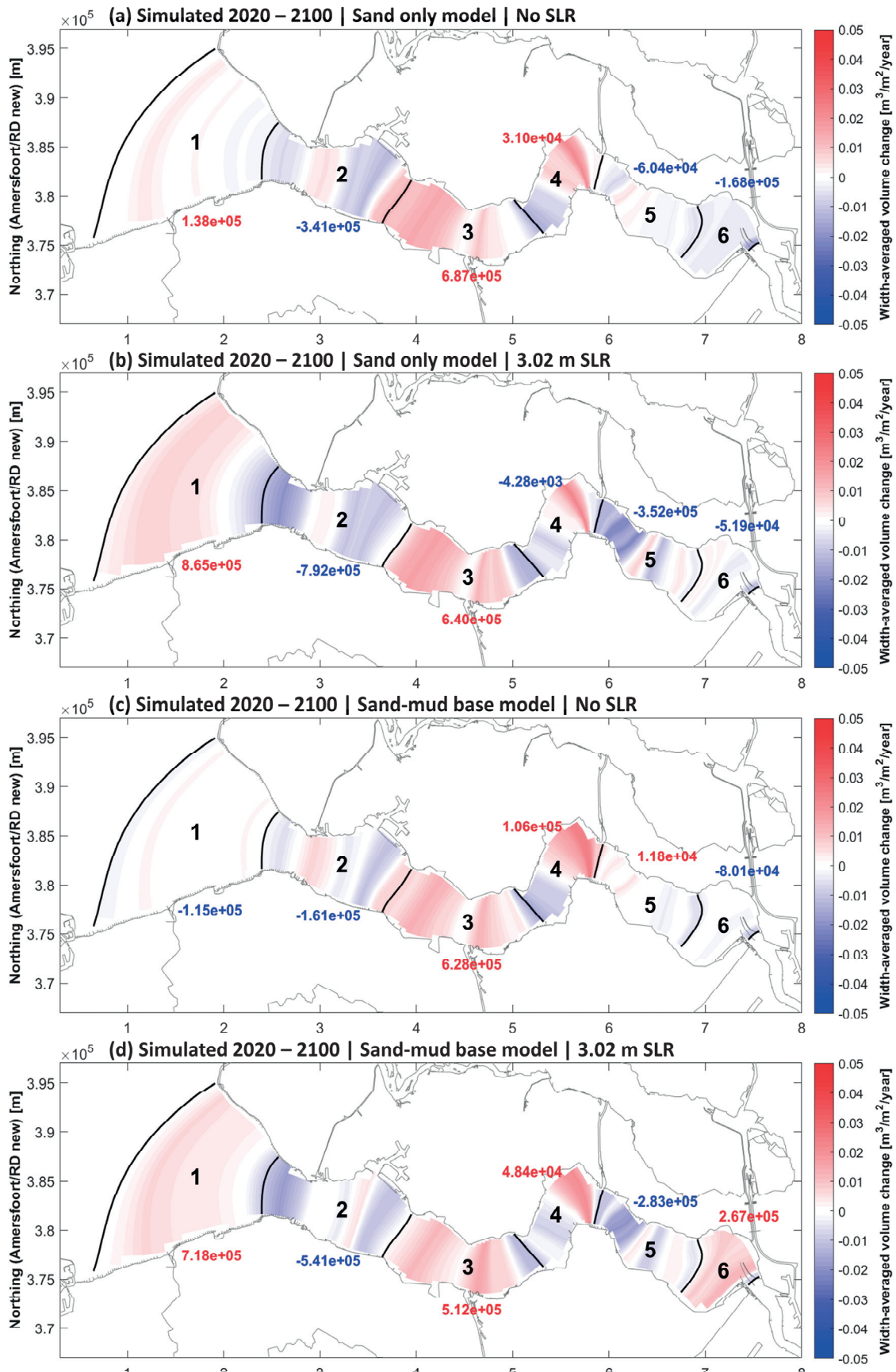


Figure 5.8. Modeled width-averaged cumulative sediment volume change ($m^3/m^2/yr$) during the hindcast period (2020 to 2100) for 6 cells in the Western Scheldt Estuary. (a, and b) Sand-only model (c, and d) Sand-mud base model for the 0 m, and 3.02 m SLR scenarios, respectively. The red/ blue color indicates sedimentation/erosion, respectively.

Intertidal shoals accrete in both the Sand-only and Sand-mud simulations. However, the accretion lags behind SLR resulting in a decline of intertidal area (Figure 5.9a). Without SLR, the intertidal area ($8.74 \times 10^7 m^2$) remains quite constant throughout the forecast period. The 3.02 m SLR scenario causes a 66% and 54% decline to $2.99 \times 10^7 m^2$ and $4.08 \times 10^7 m^2$ for the Sand-only and Sand-mud simulations, respectively. The intertidal shoal volume (Figure 5.9b) behaves similarly, albeit that the Sand-mud model shows less decline in volume suggesting higher and muddier tidal flats. This mud accretion mainly occurs at sheltered, low-energy landward locations with low flow velocities and limited wave action, such as Land van Saeftinge.

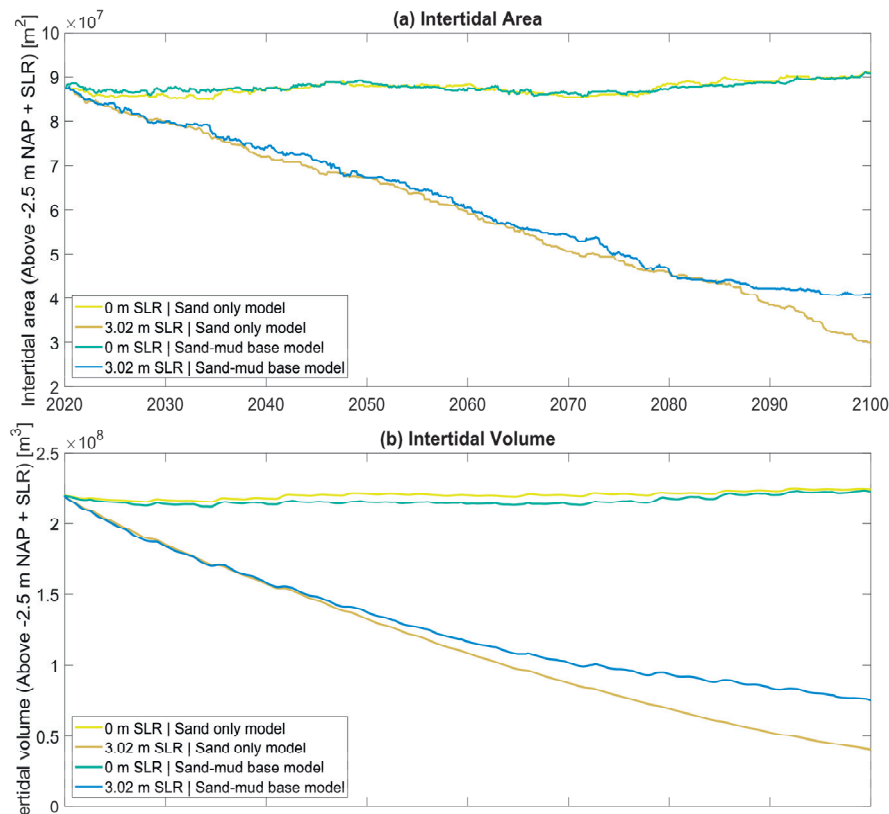


Figure 5.9. Temporal development of the (a) intertidal area (m^2), and (b) intertidal volume during the forecast period for the Sand-only and Sand-mud model.

On the other hand, the presence of mud has a limited impact on shoals located at high-energy seaward locations such as the Hooge Platen. Figure 5.10 shows that SLR causes a flow velocity decline in the deep channels but an increase over the shoals. In addition to

the increase in flow-induced shear stress, the shoals experience a decline in the wave-induced shear stresses due to the increased water depth (Table 5.3). This is especially the case at seaward, high-energy shoal locations where the maximum shear stress on top of the shoals remains high and fairly constant under SLR which hinders mud deposition.

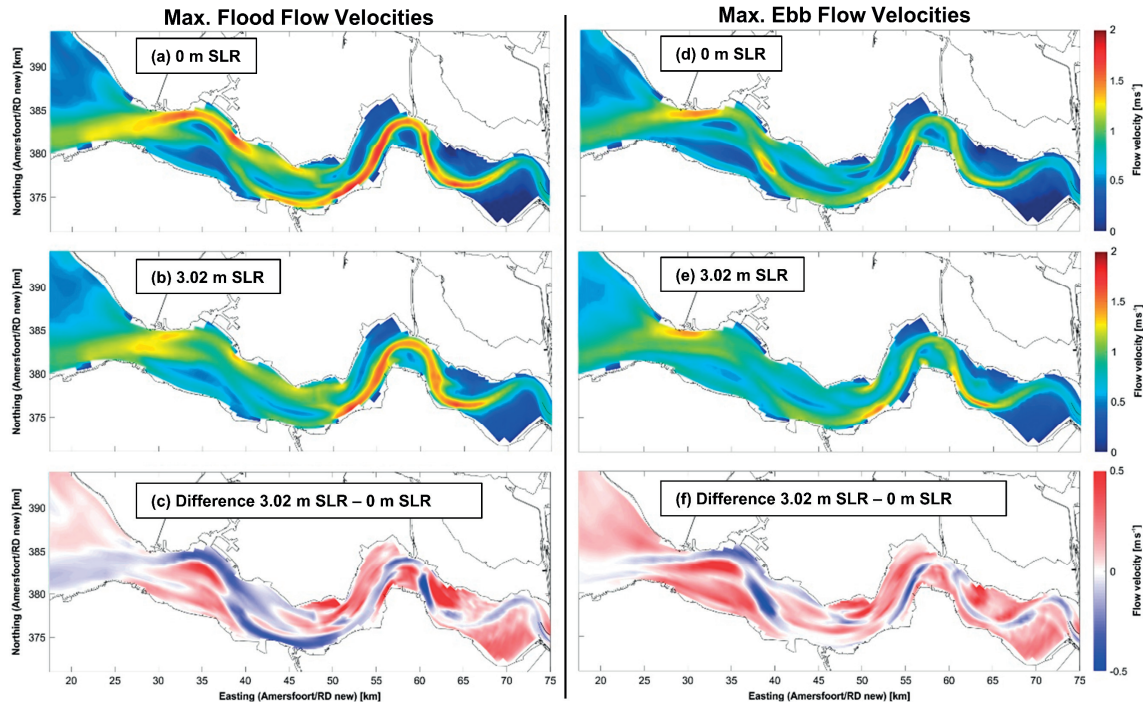


Figure 5.10. Maximum flood (left column; a and b), and ebb (right column; b and e) flow velocities (m/s) in the Western Scheldt during spring tide conditions at the end of the forecast simulation for the 0 m (top row; a and d) and 3.02 m (central row; b and e) SLR scenarios. The bottom row (c and f) shows the difference between the maximum flood and ebb velocities between the 3.02 and 0 m SLR scenario, red/blue colors indicate an increase/decrease in the flow velocities in the case of the 3.02 m SLR scenario.

Table 5.3. Domain integrated and tidally averaged flow, wave, and maximum bed shear stresses (N/m^2) over the shoals (-2.5 m NAP + SLR) during spring tide conditions after 80 years for the Sand-mud model. For simplicity purposes, the maximum bed shear stress is calculated as the summation of the flow and wave-induced bed shear stress.

Parameter	No SLR	3.02 m SLR
Flow shear stress (N/m^2)	0.34	0.71
Wave shear stress (N/m^2)	1.18	0.79
Maximum shear stress (N/m^2)	1.52	1.5

5.5.1 Forecast sensitivity

The model is forced by physical processes and anthropogenic interventions that act non-linearly in driving morphodynamic development. To get a grip on the impact that each of these forcings may have we performed a sensitivity analysis changing a single forcing condition at a time (Figure 5.11).

Without SLR, all forcing conditions except for excluding offshore waves, the Western Scheldt estuary experiences net sediment gain. The magnitude of the accretion varies between the various forcing conditions. SLR decreases the amount of sediment in the system resulting in lower sediment gain or higher loss in case of excluding offshore waves. For the Sand-only and no salinity cases, the system shifts from a depositional to an erosional system. SLR leads to a decrease in the mud import at the estuary's mouth or an increase in the net mud export for excluding salinity or offshore waves.

Comparing the base case (Simulation 1; including mud) to the Sand-only (Simulation 2) shows that mud import to the Western Scheldt is a main contributor to the sediment volume change in the system. Excluding the mud fractions, the system is still depositional (Figure 5.11a; $0.15 \times 10^5 \text{ m}^3/\text{yr}$), albeit with a much lower magnitude compared to the base case (Figure 5.11a; $0.5 \times 10^6 \text{ m}^3/\text{yr}$). A major source of this mud is the import from the estuary's mouth (Figure 5.11b; 356 Kt/yr or $0.71 \times 10^6 \text{ m}^3/\text{yr}$). Sediment volume change in Figure 5.11a is presented as m^3/yr as this is based on actual bed level changes (depositional/erosion). However, the mud transport through the estuary mouth Figure 5.11b is presented as dry weight Kt/yr since not all this mud is deposited in the estuary bed, some mud remains in suspension or is exported from the estuary (To the Sea Scheldt or mined from the domain). To allow for the comparison between the sediment volume change based on the morphology and the contribution of the mud transport through the mouth, within the text we mention the amount in Kt/yr along with the equivalent amount in m^3/yr assuming that all this mud is deposited in the bed. The conversion factor is 2000 which accounts for the porosity (Mud dry bed density= 500 kg/ m^3).

Excluding the salinity effects (Simulation 3) also results in a much lower deposition volume ($0.07 \times 10^6 \text{ m}^3/\text{yr}$). The net mud import at the mouth shifts from import (356 Kt/yr or $0.71 \times 10^6 \text{ m}^3/\text{yr}$) in the base case to export (55 Kt/yr or $0.71 \times 10^6 \text{ m}^3/\text{yr}$) without salinity effects. This also leads to lower mud SSC in the system (Figure 5.12a). The lower mud input to the system is due to the absence of the longitudinal salinity gradient between the North Sea and the Western Scheldt and its associated gravitational circulation processes which enhances the landward transport at the lower portion of the water column where higher SSC prevails and seaward transport at the higher water column portion with lower SSC. Excluding gravitational circulation processes has a much lower impact on the prevailing sand transports.

In the base case simulation, the vertical water column is represented by 7 sigma layers. This number of layers was chosen to provide a reasonable computational effort while capturing the vertical variation of the flow velocities and the associated sediment concentrations. Increasing the number of layers to 14 layers (Simulation 4) shows a similar trend as the base case simulation, albeit with larger volumes. This increase is mainly caused by the larger mud (without SLR, 59 % increase from 356 to 565 Kt/yr) and sand (not shown; without SLR, 32 % increase from 186 to 245 Kt/yr) import at the estuary mouth. Increasing the number of layers to more than 14 layers (20 layers; not shown) had a very limited impact compared to the 14-layer simulation.

Excluding the dredging and deposition operations shows the most pronounced impact on the sediment budget. The estuary experiences a net deposition (1.5×10^6 m³/yr) that is 3 times larger than the accretion in the base case (0.5×10^6 m³/yr). The mud import increasing from 356 to 681 Kt/yr (0.71×10^6 to 1.36×10^6 m³/yr) is the main reason for the higher depositional volumes. The Western Scheldt system becomes muddier and the SSC increases compared to the base case (Figure 5.12b). A possible explanation is that, following the current dredging policy, the base case applies the majority of the deposition at more seaward locations compared to the dredging locations. This decreases the landward transport of mud and favors seaward export of freshly deposited mud. Furthermore, excluding dredging leads to a shallower estuary enhancing flood dominance. In addition to the increase of marine mud import at the mouth, stopping the sediment mining operations close to Antwerp port also results in an increase of the mud input at the Belgium-Dutch border from 64 Kt/yr (Base case) to 165 Kt/yr (Simulation 5), not shown.

Waves, either off-shore or locally wind-generated, also play an important role in the sediment dynamics of the system. Off-shore waves (imposed at the model seaward boundary) dominate the modeled wave climate along the coast and estuary's mouth. While off-shore waves penetrate as far landward as Ossenisse, the modeled wave climate in the estuary is dominated by locally generated wind waves. Excluding the off-shore waves (Simulation 6) causes the system to shift from depositional (0.5×10^6 m³/yr) to erosional (0.33×10^6 m³/yr). Off-shore waves play an important role in the sediment (sand and mud) resuspension at the mouth area and the sediment transport into the estuary. For example, the net mud transport at the estuary mouth shifts from 356 Kt/yr (0.71×10^6 m³/yr) import for the base case to 232 Kt/yr (0.46×10^6 m³/yr) export excluding offshore waves. On the other hand, excluding the locally generated waves (Simulation 7) results in more favourable conditions for mud import which is mainly due to lower prevailing mud SSC in the estuary during ebb tides. In that case, the estuary experiences an approximately 88% increase (0.44×10^6 m³/yr) in net deposition compared to the base case.

5. The impact of mud dynamics on long-term morphodynamic evolution of the Western Scheldt estuary under sea level rise

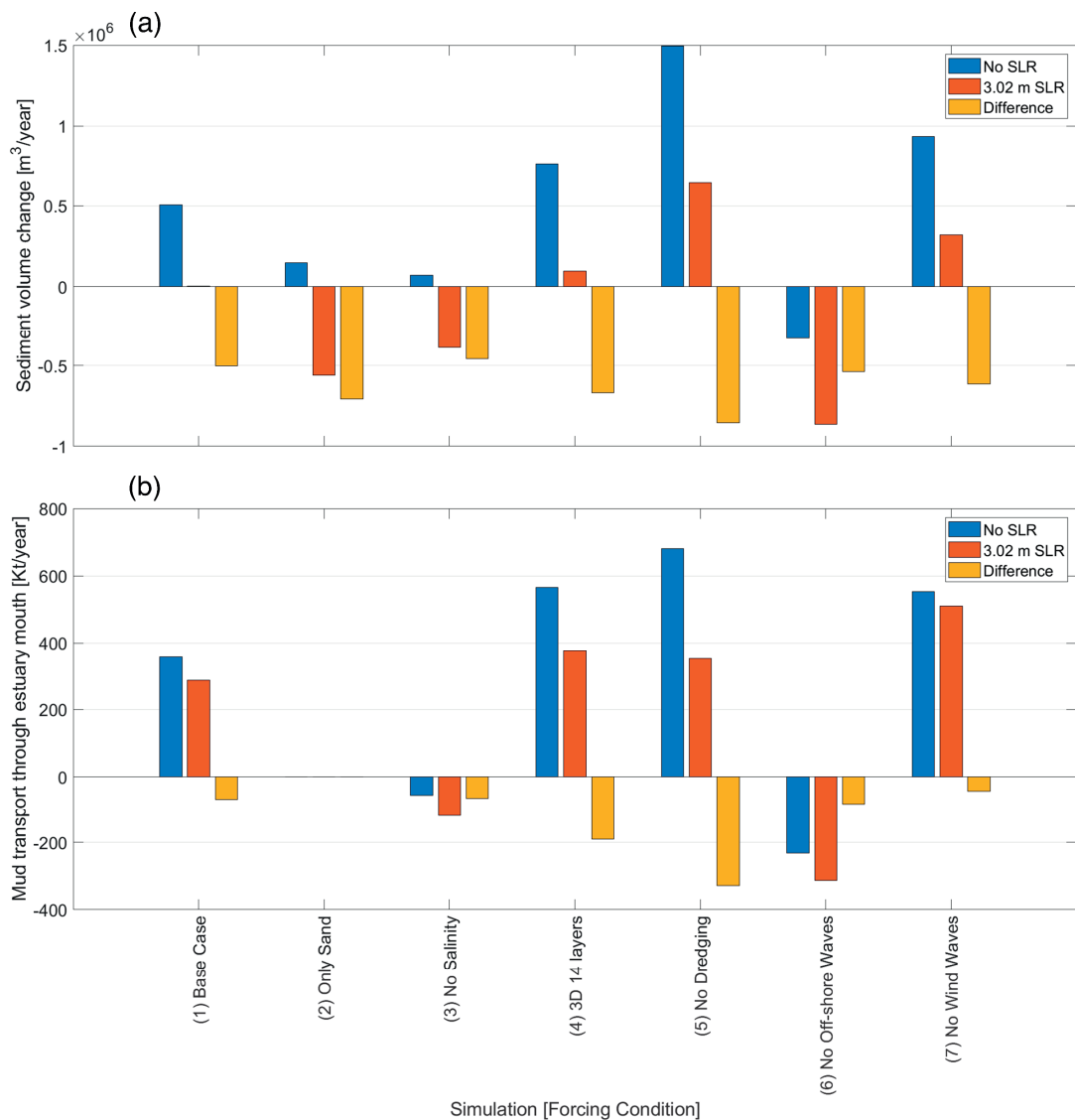


Figure 5.11. Forecast sensitivity analysis for different forcing conditions. (a) Sediment budget ($m^3/year$) of the system (Cell 2 to 6, e.g., Figure 5.8), positive/negative values indicate net sediment gain/loss. (b) Mud transport (Kt/yr) through the estuary mouth (Vlissingen-Breskens), positive/negative values indicate mud import/export.

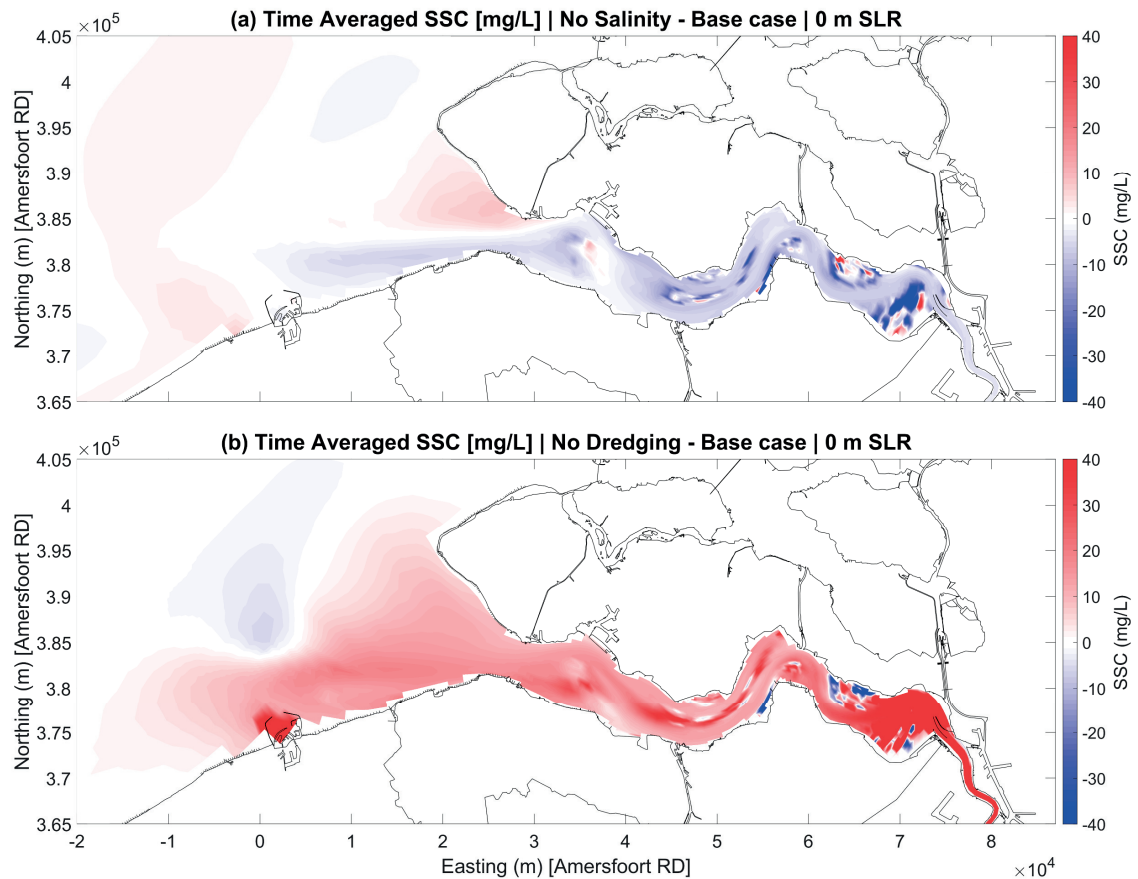


Figure 5.12. Time-averaged (over tidal cycle) and depth-averaged SSC (mg/L) difference between the base case and the (a) No salinity and (b) No Dredging simulation. The presented tidal cycle is during the last spring tide of the forecast simulation. Warm colors indicate higher values than the base case.

5.6 DISCUSSION

5.6.1 Mud impact

Literature (section 5.2.4) and Van Kessel et al., (2023) show a wide range of estimates for the mud dynamics in the WS system varying significantly depending on the investigated period and approach used. In essence, marine mud is imported from the North Sea to the WS, a portion of this mud is transported from the WS to the Sea Scheldt, while net mud accumulation occurs in the WS mainly in secondary channels, estuarine margins, and salt marshes (e.g., Land van Saeftinghe). Also, the Scheldt riverine mud is a sediment source for the WS. Our model reproduces the mud transport trends with values within the range reported in the literature.

We show that the presence of mud reduces the sand dynamics and the associated residual transport magnitudes. The estuary experiences net mud deposition of marine and riverine mud, with marine mud being the main contributor. Mud input is an important part of the WS sediment budget which suggests a trend of the WS becoming muddier over time. Despite that, mud has a relatively limited impact on the morphological development of the channel-shoal patterns which is dominated by local transport/redistribution of the sandy sediment along with dredging and deposition operations.

Our work shows that SLR causes a reduction of the net sediment (sand and mud) input to the system. This finding aligns with R bke et al. (2020) following a similar approach albeit with a higher resolution grid in 2D mode excluding mud. Their work explains this trend as SLR causes the system to become less flood-dominant and even ebb-dominant at some locations which resulted in decreasing the landward and increasing the seaward tide-residual sediment transport. The larger water depth under SLR results in larger cross-sectional areas leading to a decline in both the maximum flood and ebb velocities. However, the decline in the maximum flood velocities is higher than the ebb velocities decline. Our coarser grid, 3D model reproduces this hydrodynamic response and the associated sand dynamics. Implementing sand along with two mud fractions shows that SLR has more impact on the sand fractions than on the mud fractions. Similarly, coarser mud fractions (larger settling velocity) experience a larger impact than finer mud fractions since these latter fractions remain in suspension for a longer duration and are thus less subject to changes in local velocities. Mud helps some intertidal area accrete under SLR. However, this mud accretion mainly occurred at sheltered, low-energy landward locations with low flow velocities and limited wave action, such as Land van Saefinge. On the other hand, at the seaward high-energy shoal locations (e.g., Hooge Platen), the maximum shear stress on top of the shoals remained high and fairly constant under SLR which hindered mud deposition.

Our modeling effort may provide a good estimate for first-order mud dynamics. Still, we recognize that our model may lack complexity which might be relevant to mud dynamics. Areas where known estuarine turbidity maximums (ETMs) exist such as Zeebrugge and Antwerp are merely captured in our model by a slightly higher SSC. Our model does not include the detailed setup such as in short-term (annual) models that would be able to capture the ETMs and seasonal variations in SSC (van Maren et al., 2020). Our model also does not include processes such as flocculation which could be relevant for mud deposition and intertidal area adaptation (e.g., Ganju & Schoellhamer, 2010), or the effect of the easily erodible freshly deposited sediment layer by means of the fluffy layer concept (Van Kessel et al., 2011). Careful consideration should be taken when increasing the complexity as it makes the results harder to interpret.

5.6.2 Sediment balance

The sediment balance of the WS estuary has been the subject of several studies. Utilizing historic bathymetric surveys (1860 to 1955) combined with a 3D subsurface model incorporating both sand and mud fractions, Dam et al., (2022) skilfully derived sediment-type specific sediment budget shows a net exporting estuary (Table 5.4). Their work highlighted the contrasting behaviour of sand export and mud import at the estuary mouth and western section of the estuary, however, their approach does not reveal/include the underlying mechanisms. Our modeling results also show this contrasting Sand-mud behaviour with SLR scenarios (1.10 m and above), but only at the mouth area. SLR-induced changes in residual flow velocities have a more pronounced impact on sand fractions which shifted the residual sand transport from import to export, while it has a relatively lower impact on the finer mud fractions which remained import with the different scenarios.

Table 5.4. *Historical net sediment budget of the Western Scheldt estuary. Negative/positive values indicate sediment loss/gain, respectively.*

	Dam et al., (2022) 1860-1955	Elias et al. (2023) 1955-2005	Elias et al. (2023) 2005-2020
Sand	-1.71 – -2.68 Mm ³ /yr	-1.74 Mm ³ /yr	1.33 Mm ³ /yr
Mud	0.71 – 1.68 Mm ³ /yr	0.04 Mm ³ /yr	0.4 Mm ³ /yr
Total	-1 Mm ³ /yr	-1.70 Mm ³ /yr	1.73 Mm ³ /yr

For the follow-up period (1955 to 2020), Elias et al. (2023) present a comprehensive sediment budget for the Western Scheldt system using a unique series of bathymetric historical data including human interventions such as dredging, disposal, and sand mining. Similar to the 1860 to 1955 period, they show a net sediment volume loss between 1955 to 2005 (Table 5.4) caused by sand mining. Excluding sand mining, the Western Scheldt experiences a net sediment volume gain except for one decade (1994 to 2005) when this import trend temporarily reversed to export. This reversal cannot be explained by changes in hydrodynamic conditions but instead is attributed to anthropogenic influence of large-scale dredging and disposal in the western section of the estuary by main channel deepening and disposal on tidal flats and in secondary channels. Laboratory experiments (e.g., van Dijk et al., 2021) and models (e.g., Röbbke et al., 2020; van Dijk et al., 2021; Wang et al., 2002) highlight the pronounced impact of dredging and dumping operations on the Western Scheldt sediment dynamics. Our work shows that excluding the dredging and deposition operations results in larger net deposition while the main portion of this deposition is due to the larger marine mud import which causes the system to become muddier also leading to an increase in prevailing SSC. Between 2005 to 2020, Elias et al.

(2023) show that the Western Scheldt experienced a net sediment volume gain due to a decrease in sand mining that even stopped in 2014, as well as due to a change of the dredge and deposition strategy in 2010.

Long-term sediment balances based on measurements/deposits (Dam et al., 2022; Elias et al., 2023) provide a trustworthy historical sediment budget whereas modeled budgets like in this study usually include uncertainty ranges and can only approach observed budgets. However, observations do not reveal the underlying mechanisms and do not resolve the complete sand and mud budget. For example, observation-based budgets rely on educated estimates of each fraction contribution at the boundaries and the mud origin (within or outside the basin). In addition, forecasts based on observations only remain hypothetical. Our process-based modeling approach can help with this understanding and also provide insight into the predicted SLR-impact trend.

Observations during the hindcast period show that the system experiences a net erosion of $-0.24 \text{ Mm}^3/\text{yr}$ (Table 5.5). The observed magnitudes differ from those presented by Elias et al. (2023) (Table 5.4) due to differences in the study area boundaries (for example the location of the estuary mouth), grid resolution used for data interpolation, and the investigated period. Our model results capture the erosional trend, albeit the model overestimates the erosion magnitude ($-0.61 \text{ Mm}^3/\text{yr}$).

For the forecast period, our model shows the estuary experiences net accretion ($0.5 \text{ Mm}^3/\text{yr}$) without SLR. This shift from an erosional system during hindcast to a depositional system during the forecast agrees with the observed shift reported by Elias et al. (2023) following 2005. Imposing SLR showed reduced accretion volumes resulting in an almost neutral system, ($0.01 \text{ Mm}^3/\text{yr}$) with the highest SLR scenario (3.02 m). The SLR impact trend of decreasing the sediment volume in the estuary is consistent with the different sensitivity runs.

Table 5.5. *The observed and modeled sediment budget of the Western Scheldt during the hindcast and forecast period, presented in this study. The values presented are based on bed level changes.*

	Hindcast (1964-2012)	Forecast (2020-2100)
Observed	$-0.24 \text{ Mm}^3/\text{yr}$	
Modeled	$-0.61 \text{ Mm}^3/\text{yr}$	
Modeled No SLR		$0.5 \text{ Mm}^3/\text{yr}$
Modeled SLR (3.02 m)		$0.01 \text{ Mm}^3/\text{yr}$

5.6.3 Relevance to other estuaries

It is difficult to generalize the SLR and mud impact findings of this study to other estuaries around the world. The main driver of the morphological evolution and the formation of the channel-shoal system in the Western Scheldt is the interaction between the tidal forcing and the basin geometry (fixed banks and non-erodible layers), as demonstrated by Van der Wegen and Roelvink (2012) and Dam et al., (2016). The WS estuary experiences tidal resonance. Röbbke et al. (2020) show that changes in the resonance length and less friction under larger depth with SLR can play an important role regarding the sediment budget of the estuary. Also, the dredging operations which occur in the WS estuary are very specific to this system. Furthermore, the WS estuary has limited accommodation space for SLR adaptation which, when available for other systems could potentially reduce the adverse changes such as intertidal area drowning (L. Guo et al., 2021; Townend et al., 2021).

5.6.4 Future research

5.6.4.1 Model validation

We performed a morphological hindcast (1964 to 2012) which showed a good reproduction of the observed development trends, albeit with lower spatial (small-scale) variability due to the relatively coarse model grid resolution. Our study could benefit from a more detailed hindcast validation to create more trust in our approach (For example, as Van der Wegen et al., 2011 and Elmilady et al., 2019 for San Pablo Bay, San Francisco Estuary). This includes an examination of the impact of the specified tidal boundary signal on the morphological evolution of the system during the hindcast period and on the SLR impact during the forecast period. Usually, historic bathymetric and bed composition data in such environments are not always available worldwide, however, the data used by Dam et al. (2022) and Elias et al., (2023) for the WS and the constructed sediment budget presents an opportunity for future research to improve the reliability of the modeled sediment budget. Van Kessel et al. (2023) also recommend supplementing this with available SSC data. Still, calibration and validation can be a challenge due to the large number of parameters involved. Also, parameter settings for 2D long-term morphological models are more common in literature (e.g., Dam et al., 2016; Elmilady et al., 2022; Röbbke et al., 2020) and can be different than for 3D models.

5.6.4.2 Model complexity and approach

Models should be complex enough to account for all complexity but simple enough to allow for interpretation (e.g., Kleinhans et al., 2010). Our approach applies a complex process-based approach which allows for processes and complexity to be added. The drawback is computational/postprocessing time and lack of enough validation data (like

enough 3D hydro and mud validation data). Simpler, more schematized, and parametrized models (ASMITA; Jeuken et al. (2003)) can provide more straightforward analyses. Also, at an even more schematized level (Leuven et al., 2019; Nienhuis et al., 2020) provides worldwide assessments of estuarine morphodynamics based on rough schematizations of estuarine plan form based on satellite imagery, although care must be taken in automated processing (Zăinescu et al., 2023). Different approaches should be explored and ideally confirm each other, putting more trust in model results.

Schematized worldwide assessments (e.g., Leuven et al., 2019; Nienhuis et al., 2020) provide better generalization. However, it is yet to be explored if and how estuarine morphodynamics can be sensibly parametrized, or if the variety of complex local conditions (tidal resonance, dredging operations, sediment properties, and wave dynamics) can be accounted for in worldwide assessments. We believe that complex approaches like the current study can help to justify the parametrization of input of more schematized models. We recommend gradually increasing the model complexity with careful consideration, as this makes the results harder to interpret. The implemented coarse-resolution approach allowed for fast computations and sensitivities, however, implementing a higher (e.g., factor 2 \times) can provide a better representation of the intertidal area dynamics (e.g., wave attention; Elmilady et al., 2020) which can be relevant for a better representation of the mud contribution to the SLR adaptation of the intertidal area. However, the level of model detail should not rise to high-resolution models which are developed for much shorter time scales (annual) since comparison with the high-resolution approach of Robke et al. (2024) in the WS and the findings of other relatively coarse-resolution modeling efforts (e.g., Elmilady et al., 2019, 2022) show that model resolution such as implemented in this study are still able to capture the main trends of the long-term morphological evolution. Our model accounts for the mud impact on the sand erodibility but not vice versa. Braat et al., (2017) show the benefit of a more complex two-way feedback sand-mud interaction model. We investigated one sand fraction and two mud fractions. There is value in including another finer sand fraction for a better representation of sediment gradation in the system and its SLR adaptation (e.g., Elmilady et al., 2022). Future studies may explore the impact of consolidation, and flocculation (Z. Zhou et al., 2015). On some shoals (e.g., Land van Saeftinghe) and estuarine margins vegetation exists or is recently developing (e.g., Hooge Platen), there is value in including vegetation for long-term SLR forecasts since vegetated areas play a role in capturing fine sediment.

5.7 CONCLUSIONS

Utilizing a 3D process-based Delft3D numerical modeling, we explored the impact of mud on the long-term morphological evolution of the Western Scheldt Estuary and its

morphological response to sea level rise. Our morphological hindcast (1964 to 2012) showed a good reproduction of the observed erosion and sedimentation patterns, while modeled sediment transport trends are within an order of magnitude.

The hindcast was extended with an 80-year (2020 – 2100) morphological forecast under different SLR scenarios, i.e. 0.22, 1.10, 1.96, and 3.02 m by the end of 2100. SLR causes a reduction of the net sediment (sand and mud) input to the WS system. Changes in the hydrodynamics caused the system to become less flood-dominant and even ebb-dominant at some locations which resulted in decreasing the landward and increasing the seaward tide-residual sediment transport. SLR impact on the sediment transport depends on the SLR magnitude and sediment characteristics. The lowest SLR scenario showed a relatively limited impact compared to the extreme 3.02 m scenario, while the coarser sediment transport (sand) experienced a larger impact than that for the mud fractions.

For the different scenarios, with and without SLR, the estuary experiences net mud (marine and riverine) deposition, with marine mud being the main contributor. The presence of mud caused a more cohesive bed behavior which reduces the sand dynamics/erodibility and the associated residual transports. Mud input is an important part of the WS sediment budget which suggests a trend of the WS becoming muddier over time. Despite that, mud had a relatively limited impact on the morphological development of the channel-shoal patterns which is dominated by local transport/redistribution of the sandy sediment along with dredging and deposition operations.

Mud helped some intertidal area to accrete under SLR. However, this mud accretion mainly occurred at sheltered, low-energy landward locations with low flow velocities and limited wave action, such as Land van Saeftinghe. On the other hand, at the seaward high-energy shoal locations (e.g., Hooge Platen), the maximum shear stress on top of the shoals remained high and fairly constant under SLR which hindered mud deposition.

We performed a sensitivity analysis for the forecast period to have a better understanding of the relevance of the different forcing conditions. Dredging and deposition operations showed the most pronounced impact on the sediment budget, excluding dredging resulted in significantly higher depositional volumes, especially for mud fractions which caused the estuary to become muddier. Excluding the salinity impact and the offshore waves are the only two scenarios where the estuary did not experience marine mud import at its mouth. On the other hand, excluding the relatively smaller wind-generated waves within the estuary resulted in more favorable conditions for mud deposition. Increasing the vertical and horizontal resolution can provide a better representation of the 3D flows and transports. Future work on a more detailed hindcast will enhance trust in the modeling approach.

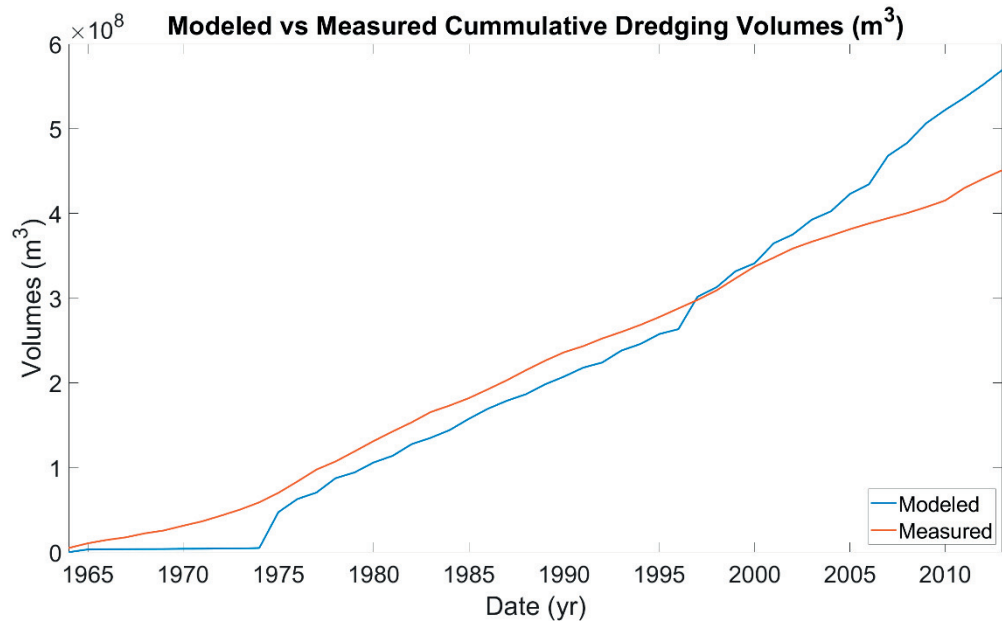


Figure 5.15. Modeled vs Measured cumulative dredging volumes (m^3) during the hindcast period 1964 to 2012.

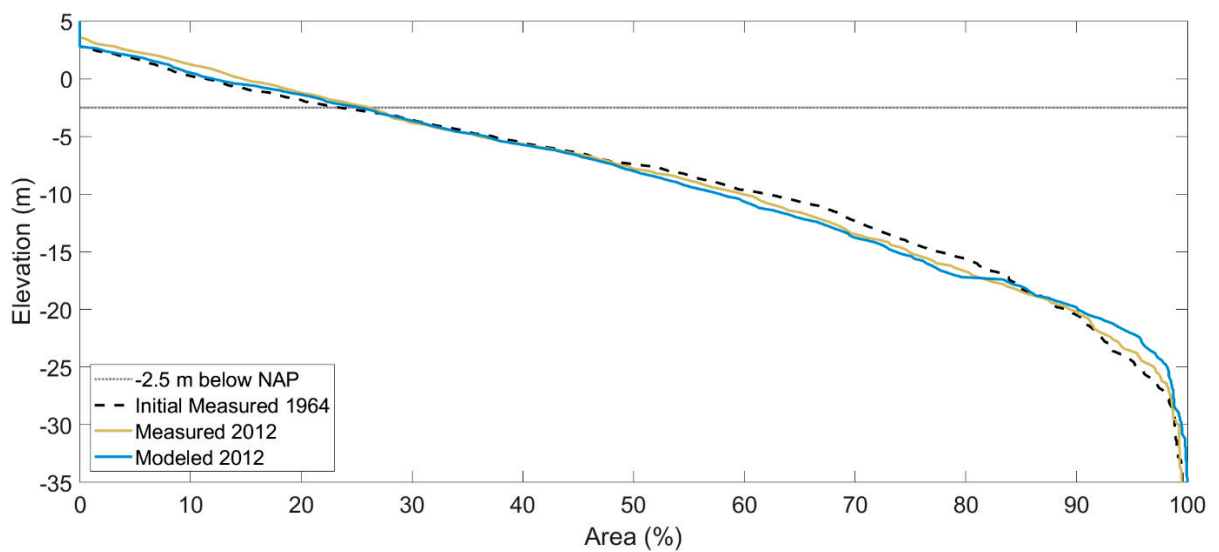


Figure 5.16. Hypsometry curve of the Western Scheldt Estuary: Initial measured 1964, Measured 2012, and Modeled 2012.

5. The impact of mud dynamics on long-term morphodynamic evolution of the Western Scheldt estuary under sea level rise

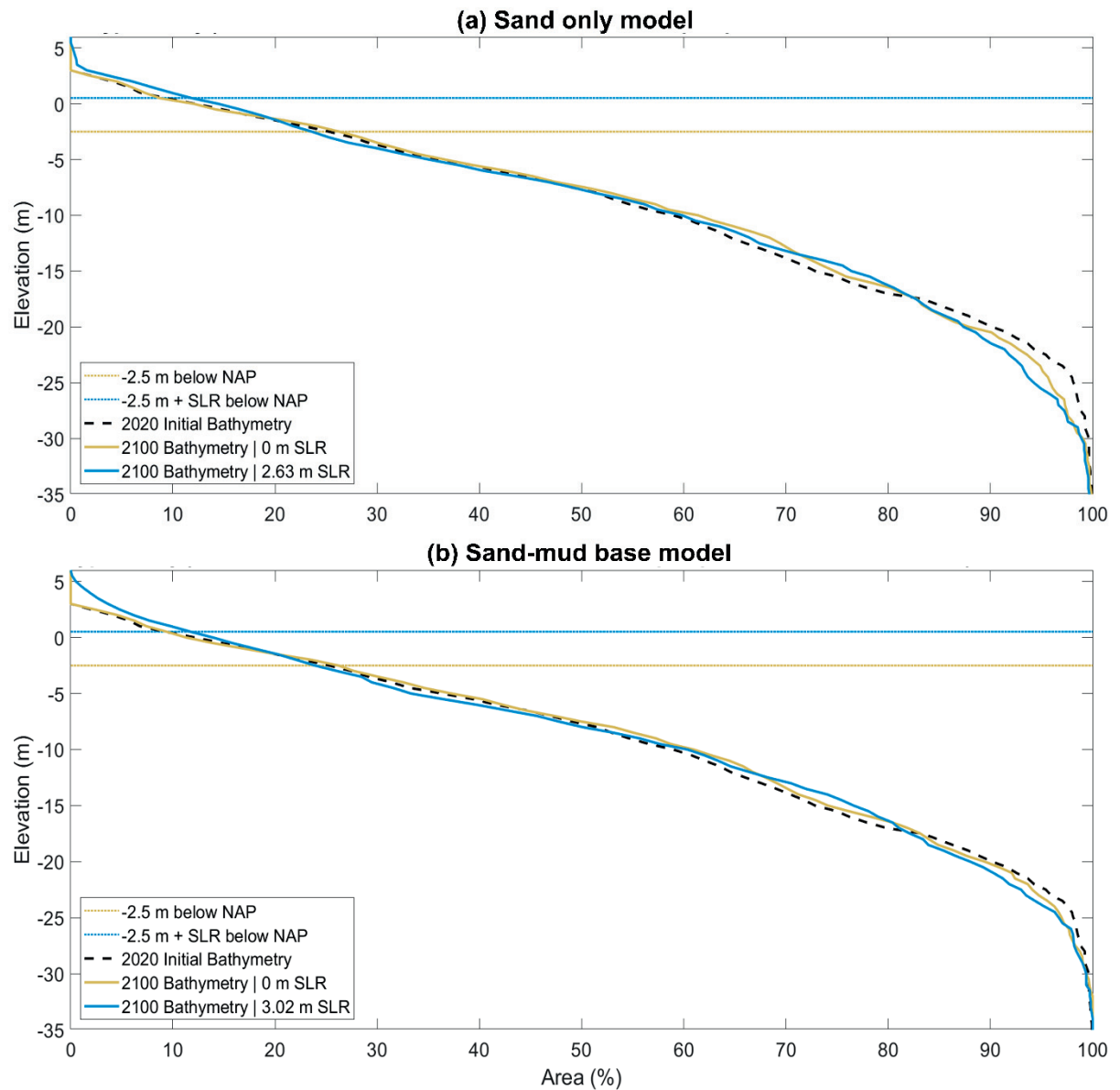


Figure 5.17. Hypsometry curve of the Western Scheldt estuary: Initial 2020, Measured 2100, and Modeled 2100 for (a) Sand-only model and (b) Sand-mud model.

6

CONCLUSIONS & RECOMMENDATIONS

This chapter includes conclusions and recommendations. The concluding section summarizes the main study findings in the form of answers to the research questions. Future research recommendations are also discussed.

6.1 CONCLUSIONS

6.1.1 Introduction

Sea level rise poses a potential threat to the estuarine environment. The morphological evolution of estuaries is crucial to their future, as it is the key aspect that ensures the sustainability of ecological life, ecosystem services, and human welfare. The main aim of this research is to assess SLR impact on the long-term (decades to centuries) morphological development of the estuarine environment, with a main focus on the intertidal area.

A process-based numerical modeling approach using Delft3D is utilized to model the SLR morphodynamic impact, supported by field data and observations. Fundamental studies are performed on idealized setups (*Chapters 2 and 3*) to isolate and investigate some knowledge gaps. This study also examines real case studies of the mud-dominated San Pablo Bay (San Francisco Estuary, USA; *Chapter 4*) and sand-dominated Western Scheldt Estuary (The Netherlands; *Chapter 5*), including a morphological hindcast compared to unique historical bathymetries followed by a forecast towards the end of the 21st century. This section provides answers to the research questions presented in the Introduction chapter (*Chapter 1*).

6.1.2 Answers to research questions

- i. What are the processes required for morphodynamic predictions of sea level rise impact in estuarine environments?**

Forcing conditions and sediment properties in nature vary between different systems depending on local conditions. The contribution of SLR forcing compared to other (changing in) forcings varies case by case. Still, some general answers can be formulated.

Our research implements a process-based modeling approach that allows for adding or excluding forcing conditions and investigating their impact. SLR-induced changes to the tide-driven hydrodynamics and the associated residual sediment transports dominate the morphological response of estuaries to SLR. It is therefore important to implement a representative tidal signal (amplitudes and main constituents). (*Chapters 3 and 5*)

A larger sediment supply results in faster SLR adaptation. Locations near the sediment source experience more accretion both on a large (basin) scale and a small (shoal) scale. There is value in including sediment supply variations between wet and dry seasons. Future SSC levels under SLR and climate change remain an important and uncertain factor contributing to the uncertainty in predictions. (*Chapters 2 to 4*)

Cohesive (mud) and non-cohesive (sand) sediment fractions can behave differently in estuarine environments. Mud fractions are more easily transported and can accelerate the

system's adaptation to SLR, especially at low-energy locations. The SLR-induced changes in residual flow velocities impact the sand transport magnitude and direction more than that for the finer mud fractions. Also, SLR may induce a shift in the composition of transported sand fractions, for example leading to more import of finer sand fractions under SLR. Along these lines also the composition of available bed sediment plays an important role in the morphodynamic adaptation of estuaries. (*Chapters 2 to 5*)

Small, local wind-generated waves have an impact on the estuarine morphology resulting in lower, wider shoals along with wider and shallower channels. At the channel-shoal interface, wave action helps distribute sediment supplied from the channels over the shoals. It also induces sediment resuspension over the shoals. Waves should be included in long-term morphological SLR investigation models with simple parametrization of representative wind condition/s such as presented in this research. Excluding wave action does not fundamentally change the morphodynamic response of the whole system under SLR since tide-residual transports are governing. However, waves provide a better characterization of the morphological features and sediment distribution in the system. (*Chapters 2 and 3*)

Strom events are generally short-lived and recovery is fast compared to SLR timescales and usually do not trigger a fundamental long-term morphological adaptation. Tidal levees (e.g., the Wadden Sea and the Western Scheldt) are other examples of dynamic and short-lived features that develop due to a short-term change in forcing conditions (absence of waves) but vanish if the prevailing wave climate is restored. Including such short-term forcing variations is not needed for SLR investigations. However, including the underlying mechanisms is relevant as shoals' SLR adaptation is a longer-term manifestation of such short-timescale dynamics. (*Chapter 2*)

Salinity/density effects and 3D dynamics are highly relevant especially for the transport of finer mud sediment, albeit sand transports are affected as well. These 3D dynamics may affect the long-term sediment budget and need to be incorporated when studying SLR impact. (*Chapters 4 and 5*)

ii. What is the spatial resolution and time scale required for estuarine morphodynamic predictions of sea level rise impact?

This research investigates different spatial modeling resolutions ranging from high resolution (≈ 20 m) up to coarse resolution (≈ 500 m). The high-resolution approach provided a better comprehension of detailed processes governing the morphological development and SLR adaptation of tidal systems. For example, it enabled modeling and investigating the formation of small-scale tidal levees and the detailed sediment exchange between the deep channels and shoals. However, when performing basin-scale SLR long-term morphological investigations, capturing these detailed small-scale formations and

the detailed structure of the shoals/channels is useful, but not necessary as long as the model includes the underlying governing processes and the resolution solves the main morphodynamic features. Furthermore, the relatively coarse resolution case study models of San Pablo Bay and the Western Scheldt provided a good representation of observed large-scale and long-term morphological development. The “adequate” grid resolution will differ between the different systems. For example, representing the channel-shoal structure in the Western Scheldt estuary requires a higher grid resolution than that for the vast mud flat of San Pablo Bay. Performing a sensitivity for the grid resolution can help in this determination. Model parameter adjustments (e.g., horizontal eddy diffusivity) could be necessary when shifting from a high-resolution to a coarser resolution. (*Chapters 2 to 5*)

The modeling configurations in this study have different spatial scales, ranging from a small-scale, single channel-shoal system to a large-scale, entire estuary system. The small-scale configuration allows for understanding the SLR impact on a morphological element (e.g. shoals) under boundary conditions assumptions such as equilibrium concentrations which are maintained during SLR. However, in real scenarios, this may not be the case. Findings of such configurations should not be applied to entire estuarine systems as they neglect the SLR-induced morphological response of other estuarine elements (e.g., channels or ebb-tidal delta). A large-scale setup incorporating a part of or a whole estuary configuration provides a better representation as it allows for investigating SLR impact on the different estuarine morphological elements along with their interactions and the impact of sediment supply. Also, it captures the impact of the estuarine geometric configuration. (*Chapters 2 to 5*)

The impact of the predicted 21st-century SLR will extend beyond the end of the 21st century. In all our studies, the morphological adaptation lags behind the SLR. Towards the end of the ≈ 100 -year SLR, it is clear that the system’s morphology is still adapting. Extension beyond the 100 years (Chapter 1), showed that even assuming an artificially imposed abrupt stop of the SLR could take the system more than 200 years to recover. Currently, the main interest is in understanding the 21st-century impact, however, there is value in investigating a longer time scale for understanding the complete impact. (*Chapters 2 to 5*)

Due to the computational effort, the application of large-scale morphological process-based models can be limited for performing such investigations. Basin-scale aggregated models (e.g., ASMITA) can be useful for performing these investigations. Delft3D-type of high-resolution modeling could help determine and quantify ASMITA parameters such as sediment exchange factors under conditions of varying supply of multiple sediment fractions under SLR scenarios.

iii. Can we make trustworthy morphodynamic predictions in complex tidal environment case studies?

This thesis shows that morphodynamic process-based models can provide trustworthy hindcasts of observed centennial timescale morphodynamic developments in San Pablo Bay and the Western Scheldt. These case studies provide confidence in the subsequent forecasts. However, this requires a large data set which is usually not available in most estuarine environments. Also, this requires sensitivity analysis, parameter calibration (within comprehensible limits), and some schematizations which are time-consuming for long-term morphological models due to the high computational effort. Process-based models are highly complex and include a great deal of non-linearity, if small issues exist, over time, this will be amplified causing incomprehensible results. Among other research, we show that over the long-time scale, such models can provide logical results and help explain governing processes which supports the trust in this model modeling approach. This is despite the high level of “best guesses” specifications (e.g., process, initial conditions, and parameters) and various schematizations (e.g., model domain, forcing conditions, and morphological acceleration). (*Chapters 4 and 5*)

Models function within a window of tolerance and provide results within a window of probability. The existence of consistent trends also provides confidence. Furthermore, in this study, we examine and can relate some of our modeling results and findings with those reported in the literature using the same and other modeling approaches or based on observations. Ideally, other modeling approaches can confirm our modeling results in future work, giving more trust.

iv. What is the fate of estuarine intertidal area under sea level rise?

In general, intertidal area will experience drowning under SLR despite accretion. The accretion magnitude is always lower than the SLR due to the morphodynamic inertia of the system. The adaptation time lag and the extent of intertidal area loss mainly depend on the SLR magnitude and rate along with the availability and characteristics of the sediment supply. (*Chapters 2 to 5*)

Under extreme SLR scenarios such as 1.67 m and 3.02 m over approximately a century for San Pablo Bay (*Chapter 4*) and the Western Scheldt (*Chapter 5*), the intertidal area experienced a pronounced loss of 91% and 54%, respectively. *Chapter 1* shows that with a constant SLR rate (linear), given the availability of sediment supply, over the long-time scale (century-scale), the intertidal area can reach a new state of dynamic equilibrium in which accretion rates match the SLR rate. Under an accelerating SLR rate (non-linear), intertidal area loss will continue.

Estuarine systems with low sediment supply are more vulnerable to SLR. Mud can accelerate the intertidal area SLR adaptation resulting in larger and more uniform

accretion along with muddier intertidal area under SLR. However, hydrodynamic conditions over intertidal areas could hinder mud deposition such as at the high-energy shoals of the Western Scheldt estuary. Compared to the sand fraction, mud can be more easily resuspended and transported. Similarly, the fine sand fractions also play an important role in the intertidal shoal adaptation. (*Chapters 2 to 5*)

Intertidal area loss poses a greater concern for constrained systems (e.g., sea defenses, urbanization, or geological outcrops) such as the Western Scheldt and the Wadden Sea (Netherlands), and San Francisco Bay (USA) where there is no available space for landward migration to compensate for the drowning intertidal area. On the other hand, in natural unconstrained systems, the intertidal areas could be maintained via marine transgression (lateral expansion or landward migration).

6.2 RECOMMENDATIONS

The models presented in this study can be used as bases for future studies. This includes investigating the potential SLR impact combined with other climate change-induced forcing changes such as sediment supply, river flow, and meteorological conditions. Also, they can provide a tool for developing and accessing mitigation/adaptation measures. Furthermore, this study includes the subtidal area (e.g., channels) but mainly focuses on the intertidal area. There is value in further examination of the SLR impact on the subtidal area.

This study investigates constrained systems with no accommodation space. This is the case for several estuaries and tidal basins around the world due to either due to urbanization (e.g., sea defenses) or geology. However, in natural unconstrained systems, marine transgression (lateral expansion or landward migration) may also occur as a SLR adaptation mechanism. In addition to the active shoal build-up, marine transgression can lead to “passive shoal formation” due to the drowning of the coastal plain causing dry land to shift from the supratidal realm into the intertidal realm. There is value in extending the developed modeling configurations to simulate unconstrained systems and investigate the above-mentioned adaptation mechanism. Also, this provides the possibility for creating inundation/risk maps.

A relatively complex process-based modeling approach is utilized in this study. Simpler, more schematized, and parametrized models can provide more straightforward analyses. They also require less computational effort which makes them a valuable tool for quicker analyses and for investigating more scenarios. Furthermore, schematized worldwide assessments include a wider range of forcing conditions and thus can provide better generalization. However, future investigations should explore if and how estuarine morphodynamics can be sensibly parametrized, or if the variety of complex local conditions can be accounted for in worldwide assessments. In this study, some of our

findings were compared to other behavior-based modeling studies. However, future studies should include a more detailed quantitative comparison of the results for the same system. Ideally, if different approaches confirm each other, this provides more confidence in the results. Also, the process-based approach like in this study can help to quantify the parameter input of more schematized models.

Calibration and validation of process-based models can be a challenge due to the large number of parameters involved. Our Western Scheldt estuary study could benefit from a more detailed validation to create more trust. This includes an examination of the impact of the tidal boundary forcing conditions on the morphological evolution during the hindcast period. Also, it can be supplemented with available historic SSC data. Furthermore, the historic bathymetries, bed composition data, and the constructed sediment budgets in literature present an opportunity for future research to improve the reliability of the modeled sediment budget.

In this study, we mainly focused on SLR impact projections until the end of the 21st century, as this is the time scale of interest for decision-makers. However, the SLR impact and morphological adaption will extend beyond this timescale. Despite the additional computational effort and increased uncertainty, there is value in future longer-term investigations (centuries).

Progressively increasing the complexity of the developed models is beneficial for gaining a deeper understanding of the potential SLR impact. This includes investigating additional geometric modeling configurations. Also, implementing a more complex sand-mud two-way feedback interaction scheme. Furthermore, including flocculation could be relevant for mud deposition and intertidal area adaptation, or the effect of the easily erodible freshly deposited sediment layer utilizing the fluffy layer concept (Van Kessel et al., 2011). Careful consideration should be taken when increasing the complexity gradually as it makes the results harder to interpret.

REFERENCES

- Achete, F. M., van der Wegen, M., Roelvink, D., & Jaffe, B. (2015). A 2-D process-based model for suspended sediment dynamics: a first step towards ecological modeling. *Hydrology and Earth System Sciences*, 19(6), 2837–2857. doi:10.5194/hess-19-2837-2015
- Achete, F., van der Wegen, M., Roelvink, J. A., & Jaffe, B. (2017). How can climate change and engineered water conveyance affect sediment dynamics in the San Francisco Bay-Delta system? *Climatic Change*, 142(3–4), 375–389. doi:10.1007/s10584-017-1954-8
- Adams, P. N., Slingerland, R. L., & Smith, N. D. (2004). Variations in natural levee morphology in anastomosed channel flood plain complexes. *Geomorphology*, 61(1–2), 127–142. doi:10.1016/J.GEOMORPH.2003.10.005
- Ahnert, F. (1960). Estuarine meanders in the Chesapeake Bay area. *Geographical Review*, 50(3), 390–401. doi:10.2307/212282
- Airoldi, L., & Beck, M. (2007). Loss, Status and Trends for Coastal Marine Habitats of Europe. *An Annual Review*, 45, 345–405. doi:10.1201/9781420050943.ch7
- Allen, J. R. L. (1990). The Severn Estuary in southwest Britain: its retreat under marine transgression, and fine-sediment regime. *Sedimentary Geology*, 66(1), 13–28. doi:10.1016/0037-0738(90)90003-C
- Allen, J. R. L., & Duffy, M. J. (1998). Medium-term sedimentation on high intertidal mudflats and salt marshes in the Severn Estuary, SW Britain: The role of wind and tide. *Marine Geology*, 150(1–4), 1–27. doi:10.1016/S0025-3227(98)00051-6
- Asuncion, R. C., & Lee, M. (2017). Impacts of Sea Level Rise on Economic Growth in Developing Asia (ADB Economics Working Paper Series 507). Asian Development Bank. Retrieved from <https://ideas.repec.org/p/ris/adbewp/0507.html>
- Atwater, B. F., Hedel, C. W., & Helley, E. J. (1977). Late Quaternary depositional history, Holocene sea-level changes, and vertical crust movement, southern San Francisco Bay, California (Vol. 1014). Washington, D.C.: US Government Printing Office.
- Baeyens, W., van Eck, B., Lambert, C., Wollast, R., & Goeyens, L. (1997). General description of the Scheldt estuary. *Hydrobiologia*, 366. doi:10.1023/A:1003164009031
- Barnard, P. L., Schoellhamer, D. H., Jaffe, B. E., & McKee, L. J. (2013). Sediment transport in the San Francisco Bay coastal system: an overview. *Marine Geology*, 345, 3–17. doi:10.1016/j.margeo.2013.04.005
- Beets, D. J., & van der Spek, A. J. F. (2000). The Holocene evolution of the barrier and the back-barrier basins of Belgium and the Netherlands as a function of late Weichselian morphology, relative sea-level rise and sediment supply. *Netherlands*

- Journal of Geosciences - Geologie En Mijnbouw, 79(1), 3–16. doi:10.1017/S0016774600021533
- Best, Ü. S. N., Van der Wegen, M., Dijkstra, J., Willemsen, P. W. J. M., Borsje, B. W., & Roelvink, D. J. A. (2018). Do salt marshes survive sea level rise? Modelling wave action, morphodynamics and vegetation dynamics. *Environmental Modelling & Software*, 109, 152–166. doi:10.1016/J.ENVSOF.2018.08.004
- Bever, A. J., & MacWilliams, M. L. (2013). Simulating sediment transport processes in San Pablo Bay using coupled hydrodynamic, wave, and sediment transport models. *Marine Geology*, 345, 235–253. doi:10.1016/j.margeo.2013.06.012
- Blum, M. D., & Roberts, H. H. (2009). Drowning of the Mississippi Delta due to insufficient sediment supply and global sea-level rise. *Nature Geoscience*, 2(7), 488–491. doi:10.1038/ngeo553
- Booij, N., Ris, R. C., & Holthuijsen, L. H. (1999). A third-generation wave model for coastal regions: 1. Model description and validation. *Journal of Geophysical Research: Oceans*, 104(C4), 7649–7666. doi:10.1029/98JC02622
- Bosboom, J., & M. Reniers, A. J. H. (2014). Displacement-based error metrics for morphodynamic models. *Advances in Geosciences*, 39(2009), 37–43. doi:10.5194/adgeo-39-37-2014
- Bosboom, J., Reniers, A. J. H. M., & Luijendijk, A. P. (2014). On the perception of morphodynamic model skill. *Coastal Engineering*, 94, 112–125. doi:10.1016/j.coastaleng.2014.08.008
- Braat, L., van Kessel, T., Leuven, J., & Kleinhans, M. G. (2017). Effects of mud supply on large-scale estuary morphology and development over centuries to millennia. *Earth Surface Dynamics*, 5(4), 617–652. doi:10.5194/esurf-5-617-2017
- Brierley, G. J., Ferguson, R. J., & Woolfe, K. J. (1997). What is a fluvial levee? *Sedimentary Geology*, 114(1–4), 1–9. doi:10.1016/S0037-0738(97)00114-0
- Brinkman, A. G., Ens, B. J., Kersting, K., Baptist, M., Vonk, M., Drent, J., ... Van der Tol, M. W. M. (2001). Modelling the impact of climate change on the Wadden Sea ecosystems. Dutch National Research Programme on Global Air Pollution and Climate Change. Report no.: 410200066. Bilthoven, The Netherlands: National Institute of Public Health and the Environment.
- Carniello, L., Defina, A., Fagherazzi, S., & D’Alpaos, L. (2005). A combined wind wave-tidal model for the Venice lagoon, Italy. *Journal of Geophysical Research: Earth Surface*, 110(4). doi:10.1029/2004JF000232
- Castagno, K. A., Jiménez-Robles, A. M., Donnelly, J. P., Wiberg, P. L., Fenster, M. S., & Fagherazzi, S. (2018). Intense Storms Increase the Stability of Tidal Bays. *Geophysical Research Letters*, 45(11), 5491–5500. doi:10.1029/2018GL078208
- Christie, M. C., Dyer, K. R., & Turner, P. (1999). Sediment flux and bed level

- measurements from a macro tidal mudflat. *Estuarine, Coastal and Shelf Science*, 49(5), 667–688. doi:10.1006/ecss.1999.0525
- Church, J. A., Clark, P. U., Cazenave, A., Gregory, J. M., Jevrejeva, S., Levermann, A., ... Unnikrishnan, A. S. (2013). Sea Level Change. In: *Climate Change 2013: The Physical Science Basis. Contribution of Working Group I to the Fifth Assessment Report of the Intergovernmental Panel on Climate Change*. In T. F. Stocker et al. (Ed.) (pp. 1137–1216). Cambridge, United Kingdom: Cambridge University Press.
- Church, J. A., Gregory, J., White, N., Platten, S., & Mitrovica, J. (2011). Understanding and Projecting Sea Level Change. *Oceanography*, 24(2), 130–143. doi:10.5670/oceanog.2011.33
- Church, J. A., Monselesan, D., Gregory, J. M., & Marzeion, B. (2013). Evaluating the ability of process based models to project sea-level change. *Environmental Research Letters*, 8(1), 014051. doi:10.1088/1748-9326/8/1/014051
- Church, J. A., White, N. J., Konikow, L. F., Domingues, C. M., Cogley, J. G., Rignot, E., ... Velicogna, I. (2011). Revisiting the Earth's sea-level and energy budgets from 1961 to 2008. *Geophysical Research Letters*, 38(18). doi:10.1029/2011GL048794
- Cleveringa, J. (2013). *Ontwikkeling mesoschaal Westerschelde (factsheets). Basisrapport kleinschalige ontwikkeling K-16*. Antwerpen: ARCADIS Nederland BV/International Marine & Dredging Consultants/Deltares/Svašek Hydraulics BV (in Dutch).
- Cloern, J. E., Knowles, N., Brown, L. R., Cayan, D., Dettinger, M. D., Morgan, T. L., ... Jassby, A. D. (2011). Projected Evolution of California's San Francisco Bay-Delta-River System in a Century of Climate Change. *PLoS ONE*, 6(9), e24465. doi:10.1371/journal.pone.0024465
- Coeveld, E. M., Hibma, A., & Stive, M. J. F. (2003). Feedback mechanisms in channel-shoal formation. *Coastal Sediments Conference*, St. Petersburg, FL, USA. (on CD-ROM).
- Conomos, T. J., & Peterson, D. H. (1977). Suspended-particle transport and circulation in San Francisco Bay: an overview. In *Estuarine processes: Circulation, Sediments, and transfer of material in the estuary* (pp. 82–97). Elsevier. doi:10.1016/B978-0-12-751802-2.50014-X
- Cooper, J. A. G. (2003). Anthropogenic impacts on estuaries. *Coastal Zones, Estuaries. Encyclopedia of Life Support Systems (EOLSS)*. Oxford, UK, UNESCO, EOLSS Publishers., 246.
- Council, N. R. (2012). *Sea-Level Rise for the Coasts of California, Oregon, and Washington: Past, Present, and Future*. Lighthouse. doi:10.17226/13389
- Cronin, K., van Kessel, T., & Smits, B. (2018). Update of the LTV model. Report 1202233-000-ZKS-0026. Delft, The Netherlands: Deltares.

- Dam, G., & Cleveringa, J. (2013). De rol van het slib in de sedimentbalans van de Westerschelde. Report G3; 1630/U12376/C/GD. Rotterdam, The Netherlands: Svasek Hydraulics (in Dutch).
- Dam, G., van der Wegen, M., Labeur, R. J., & Roelvink, D. (2016). Modeling centuries of estuarine morphodynamics in the Western Scheldt estuary. *Geophysical Research Letters*, 43(8), 3839–3847. doi:10.1002/2015GL066725
- Dam, G., van der Wegen, M., Taal, M., & van der Spek, A. (2022). Contrasting behaviour of sand and mud in a long-term sediment budget of the Western Scheldt estuary. *Sedimentology*, 69(5), 2267–2283. doi:10.1111/sed.12992
- Dastgheib, A. (2012). Long-term Process-based Morphological Modeling of Large Tidal Basins. PhD Thesis. Delft, The Netherlands: UNESCO-IHE & Delft University of Technology. CRC Press.
- de Alegria-Arzaburu, A. R., Williams, J. J., & Masselink, G. (2011). Application of XBeach to model storm response on a macrotidal gravel barrier. *Coastal Engineering Proceedings*, 1(32), 39. doi:10.9753/icce.v32.sediment.39
- de Haas, T., Pierik, H. J., van der Spek, A. J. F., Cohen, K. M., van Maanen, B., & Kleinans, M. G. (2018). Holocene evolution of tidal systems in The Netherlands: Effects of rivers, coastal boundary conditions, eco-engineering species, inherited relief and human interference. *Earth-Science Reviews*, 177, 139–163. doi:10.1016/j.earscirev.2017.10.006
- de Vet, L. (2020). Intertidal Flats in Engineered Estuaries: On the Hydrodynamics, Morphodynamics, and Implications for Ecology and System Management. PhD Thesis. Delft, The Netherlands: Delft University of Technology.
- de Vet, L., Prooijen, B., & Wang, Z. B. (2017). The differences in morphological development between the intertidal flats of the Eastern and Western Scheldt. *Geomorphology* (Vol. 281). doi:10.1016/j.geomorph.2016.12.031
- de Vriend, H. J. (1996). Mathematical modelling of meso-tidal barrier island coasts. Part I: Empirical and semi-empirical models. In P. L. F. Liu (Ed.), *Advances in coastal and ocean engineering* (2nd ed., pp. 115–149). Singapore: World Scientific Publishing Co.
- de Vriend, H. J., Capobianco, M., Chesher, T., de Swart, H. E., Latteux, B., & Stive, M. J. F. (1993). Approaches to long-term modelling of coastal morphology: A review. *Coastal Engineering*, 21(1–3), 225–269. doi:10.1016/0378-3839(93)90051-9
- de Vriend, H. J., & Ribberink, J. S. (1996). Mathematical modelling of meso-tidal barrier island coasts. Part II: Process-based simulation models. In P. L. F. Liu (Ed.), *Advances in coastal and ocean engineering* (2nd ed., pp. 151–197). Singapore: World Scientific Publishing Co.
- Deltares. (2017). Delft3D-FLOW: Simulation of multi-dimensional hydrodynamic flows and transports phenomena, including sediments. User Manual, Version 3.15,

- Revision 45038. Delft, The Netherlands: Deltares.
- Deltares. (2023). Delft3D-FLOW: Simulation of multi-dimensional hydrodynamic flows and transports phenomena, including sediments. User Manual, Version 4.05, Revision 78411. Delft, The Netherlands: Deltares.
- Depreiter, D., Sas, M., Beirinckx, K., & Liek, G. J. (2013). Dredging works in the Western Scheldt to deepen the navigation channel and to create ecologically valuable areas: Status after 3 years of monitoring. Proceedings WODCON XX - Congress and Exhibition: The Art of Dredging.
- Dissanayake, D. M. P. K. (2011). Modelling Morphological Response of Large Tidal Inlet Systems to Sea Level Rise. PhD Thesis. Delft, The Netherlands: UNESCO-IHE & Delft University of Technology. CRC Press.
- Dissanayake, D. M. P. K., Ranasinghe, R., & Roelvink, J. A. (2009). Effect of Sea Level Rise in Tidal Inlet Evolution: A Numerical Modelling Approach. *Journal of Coastal Research*, 942–946. Retrieved from <http://www.jstor.org/stable/25737925>
- Dronkers, J. (1986). Tidal asymmetry and estuarine morphology. *Netherlands Journal of Sea Research*, 20(2–3), 117–131. doi:10.1016/0077-7579(86)90036-0
- Du, J., Shen, J., Zhang, Y. J., Ye, F., Liu, Z., Wang, Z., ... Wang, H. V. (2018). Tidal Response to Sea-Level Rise in Different Types of Estuaries: The Importance of Length, Bathymetry, and Geometry. *Geophysical Research Letters*, 45(1), 227–235. doi:10.1002/2017GL075963
- Eelkema, M., Wang, Z. B., Hibma, A., & Stive, M. (2013). Morphological effects of the eastern scheldt storm surge barrier on the ebb-tidal delta. *Coastal Engineering Journal*, 55. doi:10.1142/S0578563413500101
- Eisma, D., & Irion, G. (1988). Suspended Matter and Sediment Transport BT - Pollution of the North Sea: An Assessment. In W. Salomons, B. L. Bayne, E. K. Duursma, & U. Förstner (Eds.) (pp. 20–35). Berlin, Heidelberg: Springer Berlin Heidelberg. doi:10.1007/978-3-642-73709-1_2
- Eisma, D., & Kalf, J. (1979). Distribution and particle size of suspended matter in the Southern Bight of the North sea and the Eastern channel. *Netherlands Journal of Sea Research*, 13(2), 298–324. doi:10.1016/0077-7579(79)90008-5
- Elias, E. P. L., & Hansen, J. E. (2013). Understanding processes controlling sediment transports at the mouth of a highly energetic inlet system (San Francisco Bay, CA). *Marine Geology*, 345, 207–220. doi:10.1016/j.margeo.2012.07.003
- Elias, E. P. L., Van der Spek, A. J. F., Wang, Z. B., Cleveringa, J., Jeuken, C. J. L., Taal, M., & Van der Werf, J. J. (2023). Large-scale morphological changes and sediment budget of the Western Scheldt estuary 1955–2020: the impact of large-scale sediment management. *Netherlands Journal of Geosciences*, 102, e12. doi:10.1017/njg.2023.11

- Elmilady, H. (2016). 3D Sediment Dynamics in an Estuarine Strait. MSc Thesis. Delft, The Netherlands: UNESCO-IHE.
- Elmilady, H., van der Wegen, M., Roelvink, D., & Jaffe, B. E. (2019). Intertidal Area Disappears Under Sea Level Rise: 250 Years of Morphodynamic Modeling in San Pablo Bay, California. *Journal of Geophysical Research: Earth Surface*, 124(1), 38–59. doi:10.1029/2018JF004857
- Elmilady, H., van der Wegen, M., Roelvink, D., & van der Spek, A. (2020). Morphodynamic Evolution of a Fringing Sandy Shoal: From Tidal Levees to Sea Level Rise. *Journal of Geophysical Research: Earth Surface*, 125(6), e2019JF005397. doi:10.1029/2019JF005397
- Elmilady, H., van der Wegen, M., Roelvink, D., & van der Spek, A. (2022). Modeling the Morphodynamic Response of Estuarine Intertidal Shoals to Sea-Level Rise. *Journal of Geophysical Research: Earth Surface*, 127(1), e2021JF006152. doi:10.1029/2021JF006152
- Engelund, F., & Hansen, E. (1967). A monograph on sediment transport in alluvial streams. Østervoldgade 10, Copenhagen K: Technical University of Denmark.
- Erikson, L. H., Wright, S. A., Elias, E., Hanes, D. M., Schoellhamer, D. H., & Largier, J. (2013). The use of modeling and suspended sediment concentration measurements for quantifying net suspended sediment transport through a large tidally dominated inlet. *Marine Geology*, 345, 96–112. doi:10.1016/j.margeo.2013.06.001
- Fagherazzi, S., Palermo, C., Rulli, M. C., Carniello, L., & Defina, A. (2007). Wind waves in shallow microtidal basins and the dynamic equilibrium of tidal flats. *Journal of Geophysical Research: Earth Surface*, 112(F2). doi:10.1029/2006JF000572
- Fagherazzi, Sergio, Mariotti, G., Wiberg, P. L., & McGLATHERY, K. J. (2013). Marsh collapse does not require sea level rise. *Oceanography*, 26(3), 70–77. doi:10.5670/oceanog.2013.47
- Fan, D., Li, C., Archer, A., & Wang, P. (2002). Temporal distribution of diastems in deposits of an open-coast tidal flat with high suspended sediment concentrations. *Sedimentary Geology*, 152, 173–181. doi:10.1016/S0037-0738(02)00067-2
- Fettweis, M., Nechad, B., & Van den Eynde, D. (2007). An estimate of the suspended particulate matter (SPM) transport in the southern North Sea using SeaWiFS images, in situ measurements and numerical model results. *Continental Shelf Research*, 27(10), 1568–1583. doi:10.1016/j.csr.2007.01.017
- Fettweis, M., & Van den Eynde, D. (2003). The mud deposits and the high turbidity in the Belgian–Dutch coastal zone, southern bight of the North Sea. *Continental Shelf Research*, 23(7), 669–691. doi:10.1016/S0278-4343(03)00027-X
- Fleming, K. (2000). Glacial Rebound and Sea-level Change Constraints on the Greenland Ice Sheet. PhD Thesis. Australia: Australian National University.

- Fleming, K., Johnston, P., Zwart, D., Yokoyama, Y., Lambeck, K., & Chappell, J. (1998). Refining the eustatic sea-level curve since the Last Glacial Maximum using far- and intermediate-field sites. *Earth and Planetary Science Letters*, 163(1–4), 327–342. doi:10.1016/S0012-821X(98)00198-8
- Flick, R. E., Murray, J. F., & Ewing, L. C. (2003). Trends in United States tidal datum statistics and tide range. *Journal of Waterway, Port, Coastal, and Ocean Engineering*, 129(4), 155–164. doi:10.1061/(ASCE)0733-950X(2003)129:4(155)
- Fokker, P., Van Leijen, F., Orlic, B., Marel, H., & Hanssen, R. (2018). Subsidence in the Dutch Wadden Sea. *Netherlands Journal of Geosciences*, 97, 129–181. doi:10.1017/njg.2018.9
- Fokkink, R. J., Karssen, B., Wang, Z. B., & Langerak, A. (1998). Morphological modelling of the Western Scheldt estuary. *Physics of Estuaries and Coastal Seas*, Balkema, Rotterdam.
- Fredsøe, J. (1984). Turbulent Boundary Layer in Wave-current Motion. *Journal of Hydraulic Engineering*, 110(8), 1103–1120. doi:10.1061/(ASCE)0733-9429(1984)110:8(1103)
- Friedrichs, C. (2011). Tidal Flat Morphodynamics. In *Treatise on Estuarine and Coastal Science* (Vol. 3, pp. 137–170). doi:10.1016/B978-0-12-374711-2.00307-7
- Friedrichs, C., & Aubrey, D. G. (1996, January 1). Uniform Bottom Shear Stress and Equilibrium Hyposometry of Intertidal Flats. *Mixing in Estuaries and Coastal Seas*. doi:10.1029/CE050p0405
- Friedrichs, C., Aubrey, D. G., & Speer, P. E. (1990, January 1). Impacts of Relative Sea-level Rise on Evolution of Shallow Estuaries. *Residual Currents and Long-Term Transport*. doi:10.1029/CE038p0105
- Galbraith, H., Jones, R., Park, R., Clough, J., Herrod-Julius, S., Harrington, B., & Page, G. (2002). Global Climate Change and Sea Level Rise: Potential Losses of Intertidal Habitat for Shorebirds. *Waterbirds*, 25(2), 173–183. doi:10.1675/1524-4695(2002)025[0173:GCCASL]2.0.CO;2
- Ganju, Neil K., Knowles, N., & Schoellhamer, D. H. (2008). Temporal downscaling of decadal sediment load estimates to a daily interval for use in hindcast simulations. *Journal of Hydrology*, 349(3–4), 512–523. doi:10.1016/j.jhydrol.2007.11.026
- Ganju, Neil K., & Schoellhamer, D. H. (2006). Annual sediment flux estimates in a tidal strait using surrogate measurements. *Estuarine, Coastal and Shelf Science*, 69(1–2), 165–178. doi:10.1016/j.ecss.2006.04.008
- Ganju, Neil K., & Schoellhamer, D. H. (2009). Calibration of an estuarine sediment transport model to sediment fluxes as an intermediate step for simulation of geomorphic evolution. *Continental Shelf Research*, 29(1), 148–158. doi:10.1016/j.csr.2007.09.005

- Ganju, Neil K., & Schoellhamer, D. H. (2010). Decadal-timescale estuarine geomorphic change under future scenarios of climate and sediment supply. *Estuaries and Coasts*, 33(1), 15–29. doi:10.1007/s12237-009-9244-y
- Ganju, Neil K., Schoellhamer, D. H., & Jaffe, B. E. (2009). Hindcasting of decadal-timescale estuarine bathymetric change with a tidal-timescale model. *Journal of Geophysical Research: Earth Surface*, 114(4), 1–15. doi:10.1029/2008JF001191
- Ganju, Neil K., Schoellhamer, D. H., Warner, J. C., Barad, M. F., & Schladow, S. G. (2004). Tidal oscillation of sediment between a river and a bay: a conceptual model. *Estuarine, Coastal and Shelf Science*, 60(1), 81–90. doi:10.1016/J.ECSS.2003.11.020
- Ganju, Niel K., & Schoellhamer, D. H. (2008). Lateral variability of the estuarine turbidity maximum in a tidal strait: Chapter 24. *Proceedings in Marine Science*, 9, 339–355. doi:10.1016/S1568-2692(08)80026-5
- Gao, S. (2019). Chapter 10 - Geomorphology and Sedimentology of Tidal Flats. In G. M. E. Perillo, E. Wolanski, D. R. Cahoon, & C. S. B. T.-C. W. Hopkinson (Eds.) (pp. 359–381). Elsevier. doi:10.1016/B978-0-444-63893-9.00010-1
- Geomor team. (1984). Geomorfologische processen Oosterschelde, een pilot study. Nota DDWT-84.006. The Netherlands: Rijkswaterstaat Dienst Getijdewateren (in Dutch). Retrieved from <https://deltaexpertise.nl/images/9/99/GeomorfologischesprocessenOS1984.pdf>
- Geselbracht, L. L., Freeman, K., Birch, A. P., Brenner, J., & Gordon, D. R. (2015). Modeled sea level rise impacts on coastal ecosystems at six major estuaries on Florida's gulf coast: Implications for adaptation planning. *PLoS ONE*, 10(7). doi:10.1371/journal.pone.0132079
- Gilbert, G. K. (1917). Hydraulic-mining debris in the Sierra Nevada. US Government Printing Office.
- Groenenboom, J. (2015). Modelling sand-mud-bed interaction in the Scheldt estuary. MSc thesis. Delft, The Netherlands: Delft University of Technology.
- Guo, L. C. (2014). Modeling estuarine morphodynamics under combined river and tidal forcing. PhD Thesis. Delft, The Netherlands: UNESCO-IHE & Delft University of Technology. CRC Press.
- Guo, L., van der Wegen, M., Roelvink, D., & He, Q. (2015). Exploration of the impact of seasonal river discharge variations on long-term estuarine morphodynamic behavior. *Coastal Engineering*, 95, 105–116. doi:10.1016/j.coastaleng.2014.10.006
- Guo, L., Xu, F., van der Wegen, M., Townend, I., Wang, Z. B., & He, Q. (2021). Morphodynamic adaptation of a tidal basin to centennial sea-level rise: The importance of lateral expansion. *Continental Shelf Research*, 226, 104494. doi:10.1016/j.csr.2021.104494

- Handleman, M. (2015). Earth's Rising Seas. Retrieved May 3, 2023, from <https://svs.gsfc.nasa.gov/11927>
- Harvey, J., Coon, D., & Abouchar, J. (1998). Habitat lost: taking the pulse of estuaries in the Canadian Gulf of Maine. Conservation Council of New Brunswick.
- Hayes, T. P., Kinney, J. J. R., & Wheeler, N. J. M. (1984). California Surface Wind Climatology. Aerometric Data Division, State of California Air Resources Board, Sacramento, California.
- Herrling, G., & Winter, C. (2015). Tidally- and wind-driven residual circulation at the multiple-inlet system East Frisian Wadden Sea. *Continental Shelf Research*, 106, 45–59. doi:10.1016/j.csr.2015.06.001
- Hibma, A. (2004). Morphodynamic modeling of estuarine channel-shoal systems. PhD thesis. Delft, The Netherlands: Delft University of Technology.
- Hibma, A., de Vriend, H. J., & Stive, M. J. F. (2003). Numerical modelling of shoal pattern formation in well-mixed elongated estuaries. *Estuarine, Coastal and Shelf Science*, 57(5–6), 981–991. doi:10.1016/S0272-7714(03)00004-0
- Hirschhäuser, T., Mewis, P., Witting, M., & Zanke, U. (2000). Determination of representative wind situations for the long-term morphology of the Hörnum tidal basin. In *Proceedings of the 4 th ICHE*. Seoul.
- Hoitink, A. J. F. (2003). Flow asymmetry associated with astronomical tides: Implications for the residual transport of sediment. *Journal of Geophysical Research*, 108(C10), 1–8. doi:10.1029/2002JC001539
- Hoitink, A. J. F., Hoekstra, P., & van Maren, D. S. (2003). Flow asymmetry associated with astronomical tides: Implications for the residual transport of sediment. *Journal of Geophysical Research*, 108(C10), 3315. doi:10.1029/2002JC001539
- Houser, C., & Hill, P. (2010). Wave Attenuation across an Intertidal Sand Flat: Implications for Mudflat Development. *Journal of Coastal Research*, 403–411. doi:10.2112/08-1117.1
- Hu, Z., Wang, Z. B., Zitman, T. J., Stive, M. J. F., & Bouma, T. J. (2015). Predicting long-term and short-term tidal flat morphodynamics using a dynamic equilibrium theory. *Journal of Geophysical Research: Earth Surface*, 120(9), 1803–1823. doi:10.1002/2015JF003486
- Ikeda, S. (1982). Lateral Bed Load Transport on Side Slopes. *Journal of the Hydraulics Division*, 108(11), 1369–1373. doi:10.1061/JYCEAJ.0005937
- IPCC. (2013). *Climate change 2013: the physical science basis: Working Group I contribution to the Fifth assessment report of the Intergovernmental Panel on Climate Change*. Cambridge University Press.
- IPCC. (2023). *Technical Summary*. In I. P. on C. C. (IPCC) (Ed.), *Climate Change 2021*

- The Physical Science Basis: Working Group I Contribution to the Sixth Assessment Report of the Intergovernmental Panel on Climate Change (pp. 35–144). Cambridge: Cambridge University Press. doi:10.1017/9781009157896.002
- Ittekkot, V. (1988). Global trends in the nature of organic matter in river suspensions. *Nature*, 332(6163), 436–438. doi:10.1038/332436a0
- Jaffe, B. E., Smith, R. E., & Foxgrover, A. C. (2007). Anthropogenic influence on sedimentation and intertidal mudflat change in San Pablo Bay, California: 1856–1983. *Estuarine, Coastal and Shelf Science*, 73(1–2), 175–187. doi:10.1016/j.ecss.2007.02.017
- Janssen-Stelder, B. (2000). The effect of different hydrodynamic conditions on the morphodynamics of a tidal mudflat in the Dutch Wadden Sea. *Continental Shelf Research*, 20, 1461–1478. doi:10.1016/S0278-4343(00)00032-7
- Jeuken, M., Wang, Z. B., Keiller, D., Townend, I., & Liek, G. A. (2003). Morphological response of estuaries to nodal tide variation. In *International Conference on Estuaries and Coasts* (pp. 166–173). IRTCES.
- Jiang, L., Gerkema, T., Idier, D., Slangen, A. B. A., & Soetaert, K. (2020). Effects of sea-level rise on tides and sediment dynamics in a Dutch tidal bay. *Ocean Science*, 16(2), 307–321. doi:10.5194/os-16-307-2020
- Karl, T. R., Melillo, J. M., Peterson, T. C., & Hassol, S. J. (2009). *Global Climate Change Impacts in the United States: Highlights*. Cambridge University Press.
- Kemp, A. C., Horton, B. P., Donnelly, J. P., Mann, M. E., Vermeer, M., & Rahmstorf, S. (2011). Climate related sea-level variations over the past two millennia. *Proceedings of the National Academy of Sciences*, 108(27), 11017–11022. doi:10.1073/pnas.1015619108
- Kimmerer, W. (2004). *Open Water Processes of the San Francisco Estuary: From Physical Forcing to Biological Responses*. San Francisco Estuary and Watershed Science , 2(1). Retrieved from <http://www.escholarship.org/uc/item/9bp499mv>
- Kleinhans, M. G., Bierkens, M. F. P., & van der Perk, M. (2010). HESS Opinions On the use of laboratory experimentation: “Hydrologists, bring out shovels and garden hoses and hit the dirt.” *Hydrology and Earth System Sciences*, 14(2), 369–382. doi:10.5194/hess-14-369-2010
- KNMI. (2014). *KNMI’14: Climate Change scenarios for the 21st Century – A Netherlands perspective*. De Bilt, The Netherlands: KNMI.
- Knowles, N. (2010). Potential Inundation due to Rising Sea Levels in the San Francisco Bay Region. *San Francisco Estuary and Watershed Science*, 8(1). doi:10.15447/sfew.2010v8iss1art1
- Knowles, N., & Cayan, D. R. (2002). Potential effects of global warming on the Sacramento/San Joaquin watershed and the San Francisco estuary. *Geophysical*

- Research Letters, 29(18), 38-1-38-4. doi:10.1029/2001GL014339
- Kohsiek, L. H. M., Buist, H. J., Misdorp, R., Berg, J. H., & Visser, J. (1988). Sedimentary Processes on a Sandy Shoal in a Mesotidal Estuary (Oosterschelde, The Netherlands). In *Tide-influenced sedimentary environments and facies* (pp. 201–214). doi:10.1007/978-94-015-7762-5_16
- Kopp, R. E., Kemp, A. C., Bittermann, K., Horton, B. P., Donnelly, J. P., Gehrels, W. R., ... Rahmstorf, S. (2016). Temperature-driven global sea-level variability in the Common Era. *Proceedings of the National Academy of Sciences of the United States of America*, 113(11), E1434-41. doi:10.1073/pnas.1517056113
- Kraft, J. C., Yi, H., & Khalequzzaman, M. (1992). Geologic and human factors in the decline of the tidal salt marsh lithosome: the Delaware estuary and Atlantic coastal zone. *Sedimentary Geology*, 80(3–4), 233–246. doi:10.1016/0037-0738(92)90043-Q
- Krone, R. B. (1979). Sedimentation in the San Francisco Bay system. In: Conomos, T.J. (Ed.), *San Francisco Bay: The Urbanized Estuary*. American Association for the Advancement of Science, San Francisco., 85–96.
- Krone, R. B. (1996). Recent sedimentation in the San Francisco Bay system. In: Hollibaugh JT, editor. *San Francisco Bay: the ecosystem*. San Francisco (CA): Pacific Division, American Association for the Advancement of Science., 36–67.
- Kuijper, C., Steijn, R., Roelvink, D., & Kaaij, T. Van der. (2004). Morphological modelling of the Western Scheldt: validation of DELFT3D. Report Z3648 / A1198. Delft, The Netherlands: Delft hydraulics (Deltares). Retrieved from <https://resolver.tudelft.nl/uuid:4fda20a4-1010-4406-84f8-537d3c1c110a>
- Lafite, R., Shimwell, S. J., Nash, L. A., Dupont, J. P., Huault, M. F., Grochowski, N. T. L., ... Collins, M. B. (1993). Sub-Task S1: suspended material fluxes through the Strait of Dover, Hydrodynamics and biogeochemical fluxes in the Eastern Channel: fluxes into the North Sea. *FLUXMANCHE I Second Annual Report*, MAST, 81–106.
- Lai, S., Loke, L. H. L., Hilton, M. J., Bouma, T. J., & Todd, P. A. (2015). The effects of urbanisation on coastal habitats and the potential for ecological engineering: A Singapore case study. *Ocean & Coastal Management*, 103, 78–85. doi:10.1016/j.ocecoaman.2014.11.006
- Latteux, B. (1995). Techniques for long-term morphological simulation under tidal action. *Marine Geology*, 126(1–4), 129–141. doi:10.1016/0025-3227(95)00069-B
- Le Bars, D., Drijfhout, S., & de Vries, H. (2017). A high-end sea level rise probabilistic projection including rapid Antarctic ice sheet mass loss. *Environmental Research Letters*, 12(4), 44013. doi:10.1088/1748-9326/aa6512
- Lefèvre, F. O. B. (2000). Effecten van systeemingrepen op de water- en bodemkwaliteit van de Westerschelde. Report 2000.006. Middelburg, The Netherlands:

- Rijksinstituut voor Kust en Zee/ RIKZ (Rijkswaterstaat) (in Dutch). Retrieved from <https://repository.tudelft.nl/islandora/object/uuid%3A89caf5f2-8a6b-414e-bed5-6f394d3c10f2>
- Leonardi, N., Carnacina, I., Donatelli, C., Ganju, N. K., Plater, A. J., Schuerch, M., & Temmerman, S. (2018). Dynamic interactions between coastal storms and salt marshes: A review. *Geomorphology*, 301, 92–107. doi:10.1016/J.GEOMORPH.2017.11.001
- Lesser, G. R. (2009). An approach to medium-term coastal morphological modelling. PhD Thesis. Delft, The Netherlands: UNESCO-IHE & Delft University of Technology. CRC Press/Balkema.
- Lesser, G. R., Roelvink, D., van Kester, J. A. T. M., & Stelling, G. S. (2004). Development and validation of a three-dimensional morphological model. *Coastal Engineering*, 51(8–9), 883–915. doi:10.1016/j.coastaleng.2004.07.014
- Leuven, J., de Haas, T., Braat, L., & Kleinhans, M. G. (2018). Topographic forcing of tidal sandbar patterns for irregular estuary planforms. *Earth Surface Processes and Landforms*, 43(1), 172–186. doi:10.1002/esp.4166
- Leuven, J., Kleinhans, M., Weisscher, S. A. H., & van der Vegt, M. (2016). Tidal sand bar dimensions and shapes in estuaries. *Earth-Science Reviews*, 161. doi:10.1016/j.earscirev.2016.08.004
- Leuven, J., Pierik, H. J., Vegt, M. van der, Bouma, T. J., & Kleinhans, M. G. (2019). Sea-level-rise-induced threats depend on the size of tide-influenced estuaries worldwide. *Nature Climate Change*, 9(12), 986–992. doi:10.1038/s41558-019-0608-4
- Lewicki, M., & McKee, L. (2010). New methods for estimating annual and long-term suspended sediment loads from small tributaries to San Francisco Bay. *IAHS Publication*, 337(5).
- Lipcius, R. N., Seitz, R. D., Wennhage, H., Bergström, U., & Ysebaert, T. (2013). Ecological value of coastal habitats for commercially and ecologically important species. *ICES Journal of Marine Science*, 71(3), 648–665. doi:10.1093/icesjms/fst152
- Locke, J. L. (1971). Sedimentation and foraminiferal aspects of the recent sediments of San Pablo Bay. MSc thesis. San Jose, California: Fac. of the Dep. of Geol., San Jose State College.
- Lodder, Q. J., Wang, Z. B., Elias, E. P. L., van der Spek, A. J. F., de Looff, H., & Townend, I. H. (2019). Future Response of the Wadden Sea Tidal Basins to Relative Sea-Level rise—An Aggregated Modelling Approach. *Water*. doi:10.3390/w11102198
- Lovelock, C. E., Feller, I. C., Reef, R., Hickey, S., & Ball, M. C. (2017). Mangrove dieback during fluctuating sea levels. *Scientific Reports*, 7(1), 1680. doi:10.1038/s41598-017-01927-6

- Luan, H. L., Ding, P. X., Wang, Z. B., & Ge, J. Z. (2017). Process-based morphodynamic modeling of the Yangtze Estuary at a decadal timescale: Controls on estuarine evolution and future trends. *Geomorphology*, 290, 347–364. doi:10.1016/J.GEOMORPH.2017.04.016
- Luan, H. L., Ding, P. X., Wang, Z. B., Ge, J. Z., & Yang, S. L. (2016). Decadal morphological evolution of the Yangtze Estuary in response to river input changes and estuarine engineering projects. *Geomorphology*, 265, 12–23. doi:10.1016/J.GEOMORPH.2016.04.022
- Maan, D. C., van Prooijen, B. C., Wang, Z. B., & De Vriend, H. J. (2015). Do intertidal flats ever reach equilibrium? *Journal of Geophysical Research: Earth Surface*, 120(11), 2406–2436. doi:10.1002/2014JF003311
- Maan, D. C., van Prooijen, B. C., Zhu, Q., & Wang, Z. B. (2018). Morphodynamic Feedback Loops Control Stable Fringing Flats. *Journal of Geophysical Research: Earth Surface*, 123(11), 2993–3012. doi:10.1029/2018JF004659
- MacKinnon, J., Verkuil, Y. I., & Murray, N. (2012). IUCN situation analysis on East and Southeast Asian intertidal habitats, with particular reference to the Yellow Sea (including the Bohai Sea). International Union for the Conservation of Nature (IUCN).
- MacVean, L., & Lacy, J. R. (2014). Interactions between waves, sediment, and turbulence on a shallow estuarine mudflat. *Journal of Geophysical Research: Oceans*, 119(3), 1534–1553. doi:10.1002/2013JC009477
- Martyr-Koller, R. C., Kernkamp, H. W. J., van Dam, A., van der Wegen, M., Lucas, L. V., Knowles, N., ... Fregoso, T. A. (2017). Application of an unstructured 3D finite volume numerical model to flows and salinity dynamics in the San Francisco Bay-Delta. *Estuarine, Coastal and Shelf Science*, 192, 86–107. doi:10.1016/J.ECSS.2017.04.024
- McKee, L. J., Lewicki, M., Schoellhamer, D. H., & Ganju, N. K. (2013). Comparison of sediment supply to San Francisco Bay from watersheds draining the Bay Area and the Central Valley of California. *Marine Geology*, 345, 47–62. doi:10.1016/J.MARGE.2013.03.003
- Melillo, J. M., Richmond, T. T., & Yohe, G. (2014). Climate Change Impacts in the United States: The Third National Climate Assessment. U.S. Government Printing Office. doi:10.7930/J0Z31WJ2
- Miller, K. G., Kopp, R. E., Horton, B. P., Browning, J. V., & Kemp, A. C. (2013). A geological perspective on sea-level rise and its impacts along the U.S. mid-Atlantic coast. *Earth's Future*, 1(1), 3–18. doi:10.1002/2013EF000135
- Milne, G. A., Long, A. J., & Bassett, S. E. (2005). Modelling Holocene relative sea-level observations from the Caribbean and South America. *Quaternary Science Reviews*, 24(10), 1183–1202. doi:10.1016/j.quascirev.2004.10.005

- Mitsch, W. J., & Gosselink, J. G. (2000). The value of wetlands: importance of scale and landscape setting. *Ecological Economics*, 35(1), 25–33. doi:10.1016/S0921-8009(00)00165-8
- Moftakhari, H. R., Jay, D. A., Talke, S. A., & Schoellhamer, D. H. (2015). Estimation of historic flows and sediment loads to San Francisco Bay, 1849-2011. *Journal of Hydrology*, 529, 1247–1261. doi:10.1016/j.jhydrol.2015.08.043
- Muis, S., Apecechea, M. I., Dullaart, J., de Lima Rego, J., Madsen, K. S., Su, J., ... Verlaan, M. (2020). A High-Resolution Global Dataset of Extreme Sea Levels, Tides, and Storm Surges, Including Future Projections. *Frontiers in Marine Science*, 7. doi:10.3389/fmars.2020.00263
- Murphy, A. H., & Epstein, E. S. (1989). Skill Scores and Correlation Coefficients in Model Verification. *Monthly Weather Review*, 117(3), 572–582. doi:10.1175/1520-0493(1989)117<0572:SSACCI>2.0.CO;2
- Murray, A. B. (2003). Contrasting the goals, strategies, and predictions associated with simplified numerical models and detailed simulations. Washington DC American Geophysical Union Geophysical Monograph Series (Vol. 135). doi:10.1029/135GM11
- Murray, N. J., Clemens, R. S., Phinn, S. R., Possingham, H. P., & Fuller, R. A. (2014). Tracking the rapid loss of tidal wetlands in the Yellow Sea. *Frontiers in Ecology and the Environment*, 12(5), 267–272. doi:10.1890/130260
- Murray, N. J., Phinn, S. R., DeWitt, M., Ferrari, R., Johnston, R., Lyons, M. B., ... Fuller, R. A. (2019). The global distribution and trajectory of tidal flats. *Nature*, 565(7738), 222–225. doi:10.1038/s41586-018-0805-8
- Narayan, S., Beck, M. W., Wilson, P., Thomas, C. J., Guerrero, A., Shepard, C. C., ... Trespalacios, D. (2017). The Value of Coastal Wetlands for Flood Damage Reduction in the Northeastern USA. *Scientific Reports*, 7(1), 9463. doi:10.1038/s41598-017-09269-z
- NASA. (2023a). 1. Global Temperature. Retrieved February 1, 2024, from <https://climate.nasa.gov/vital-signs/global-temperature/?intent=121>
- NASA. (2023b). 2. Global Temperature Anomalies from 1880 to 2022. Retrieved September 1, 2023, from <https://svs.gsfc.nasa.gov/5060/>
- NASA. (2023c). 3. Climate Change: Evidence. Retrieved September 1, 2023, from <https://climate.nasa.gov/evidence/>.
- NASA. (2023d). 4. Carbon Dioxide. Retrieved June 1, 2024, from <https://climate.nasa.gov/vital-signs/carbon-dioxide/?intent=121>
- NASA. (2024). Understanding Sea Level. Retrieved June 1, 2024, from <https://sealevel.nasa.gov/understanding-sea-level/key-indicators/global-mean-sea-level/>

- National Research Council. (2012). *Sea-Level Rise for the Coasts of California, Oregon, and Washington*. Washington, D.C.: National Academies Press. doi:10.17226/13389
- Nicholls, R. J., & Cazenave, A. (2010). Sea-level rise and its impact on coastal zones. *Science*, 328(5985), 1517–1520. doi:10.1126/science.1185782
- Nienhuis, J. H., Ashton, A. D., Edmonds, D. A., Hoitink, A. J. F., Kettner, A. J., Rowland, J. C., & Törnqvist, T. E. (2020, January 23). Global-scale human impact on delta morphology has led to net land area gain. *Nature*. doi:10.1038/s41586-019-1905-9
- NOAA. (2018). NOAA Tides & Currents. Retrieved February 1, 2018, from <https://tidesandcurrents.noaa.gov/map/index.shtml?type=active®ion=California>
- Normark, W. R., Piper, D. J. W., Posamentier, H., Pirmez, C., & Migeon, S. (2002). Variability in form and growth of sediment waves on turbidite channel levees. *Marine Geology*, 192(1–3), 23–58. doi:10.1016/S0025-3227(02)00548-0
- Parris, A., Bromirski, P., Burkett, V., Cayan, D., Culver, M., Hall, J., ... Weiss, J. (2012). *Global Sea Level Rise Scenarios for the US National Climate Assessment*. NOAA Tech Memo OAR CPO-1. Silver Spring, MD: Climate Program Office (CPO).
- Partheniades, E. (1965). Erosion and deposition of cohesive soils. *Journal of the Hydraulics Division*, 91(1), 105–139. doi:10.1061/JYCEAJ.0001165
- Passeri, D. L., Hagen, S. C., Medeiros, S. C., Bilskie, M. V., Alizad, K., & Wang, D. (2015). The dynamic effects of sea level rise on low-gradient coastal landscapes: A review. *Earth's Future*, 3(6), 159–181. doi:10.1002/2015EF000298
- Pelling, M., & Blackburn, S. (2013). *Megacities and the coast: risk, resilience, and transformation*. Routledge. Retrieved from <https://www.routledge.com/Megacities-and-the-Coast-Risk-Resilience-and-Transformation/Pelling-Blackburn/p/book/9780415815123>
- Peri, J., & Šverko, Z. (2015). Economic Impacts of Sea Level Rise Caused By Climate Change. *ToSEE – Tourism in Southern and Eastern Europe*, 3, 285–294.
- Perillo, G. M. E., & Iribarne, O. O. (2003). Processes of tidal channel development in salt and freshwater marshes. *Earth Surface Processes and Landforms*, 28(13), 1473–1482. doi:10.1002/esp.1018
- Pethick, J. (1994). Estuaries and wetlands: function and form. In R. A. Falconer & P. Goodwin (Eds.), *Wetland Management* (pp. 75–87). London, UK: Thomas Telford.
- Philpott, D. (2015). *Critical government documents on the environment*. Bernan Press.
- Portela, L. I. (2006). Calculation of Sediment Delivery from the Guadiana Estuary to the Coastal. *Journal of Coastal Research*, 1819–1823. Retrieved from <http://www.jstor.org/stable/25743075>
- Postma, H. (1957). Size frequency distribution of sands in the Dutch Wadden Sea. *Extrait Des Archives Néerlandaises de Zoologie*, 12(3), 319–349.

- Postma, H. (1961). Transport and accumulation of suspended matter in the Dutch Wadden Sea. *Netherlands Journal of Sea Research*, 1(1), 148–190. doi:10.1016/0077-7579(61)90004-7
- Postma, H. (1967). Sediment transport and sedimentation in the estuarine environment. (G. H. Lauff, Ed.). Washington, DC: American Association for Advancement of Science.
- Postma, H. (1981). Exchange of materials between the North Sea and the Wadden Sea. *Marine Geology*, 40(1), 199–213. doi:10.1016/0025-3227(81)90050-5
- Pritchard, D., & Hogg, A. J. (2003). Cross-shore sediment transport and the equilibrium morphology of mudflats under tidal currents. *Journal of Geophysical Research: Oceans*, 108(C10). doi:10.1029/2002JC001570
- Pritchard, D., Hogg, A. J., & Roberts, W. (2002). Morphological modelling of intertidal mudflats: the role of cross-shore tidal currents. *Continental Shelf Research*, 22(11–13), 1887–1895. doi:10.1016/S0278-4343(02)00044-4
- Ranasinghe, R., Wu, C. S., Conallin, J., Duong, T. M., & Anthony, E. J. (2019). Disentangling the relative impacts of climate change and human activities on fluvial sediment supply to the coast by the world's large rivers: Pearl River Basin, China. *Scientific Reports*, 9(1), 9236. doi:10.1038/s41598-019-45442-2
- Reed, D., van Wesenbeeck, B., Herman, P. M. J., & Meselhe, E. (2018, November 30). Tidal flat-wetland systems as flood defenses: Understanding biogeomorphic controls. *Estuarine, Coastal and Shelf Science*. Academic Press. doi:10.1016/j.ecss.2018.08.017
- Reineck, H.-E., & Singh, I. B. (1980). Tidal Flats BT - Depositional Sedimentary Environments: With Reference to Terrigenous Clastics. In H.-E. Reineck & I. B. Singh (Eds.) (pp. 430–456). Berlin, Heidelberg: Springer Berlin Heidelberg. doi:10.1007/978-3-642-81498-3_26
- Ridderinkhof, H., Van der Ham, R., & Van der Lee, W. (2000). Temporal variations in concentration and transport of suspended sediments in a channel-flat system in the Ems-Dollard estuary. *Continental Shelf Research*, 20(12–13), 1479–1493. doi:10.1016/S0278-4343(00)00033-9
- Ridderinkhof, W., de Swart, H. E., van der Vegt, M., & Hoekstra, P. (2016). Modeling the growth and migration of sandy shoals on ebb-tidal deltas. *Journal of Geophysical Research: Earth Surface*, 121(7), 1351–1372. doi:10.1002/2016JF003823
- Rios-Yunes, D., Tiano, J. C., van Oevelen, D., van Dalen, J., & Soetaert, K. (2023). Annual biogeochemical cycling in intertidal sediments of a restored estuary reveals dependence of N, P, C and Si cycles to temperature and water column properties. *Estuarine, Coastal and Shelf Science*, 282, 108227. doi:10.1016/j.ecss.2023.108227
- Roberts, W., Le Hir, P., & Whitehouse, R. J. . (2000). Investigation using simple mathematical models of the effect of tidal currents and waves on the profile shape

- of intertidal mudflats. *Continental Shelf Research*, 20(10–11), 1079–1097. doi:10.1016/S0278-4343(00)00013-3
- Röbke, B. R., Elmilady, H., van der Wegen, M., & Taal, M. (2020). The long-term morphological response to sea level rise and different sediment strategies in the Western Scheldt estuary (The Netherlands). Report 1210301-009-ZKS-0009. Delft, The Netherlands: Deltares. Retrieved from <https://edepot.wur.nl/539878>
- Roelvink, D. (1993). Dissipation in random wave groups incident on a beach. *Coastal Engineering*, 19(1–2), 127–150. doi:10.1016/0378-3839(93)90021-Y
- Roelvink, D. (2006). Coastal morphodynamic evolution techniques. *Coastal Engineering*, 53(2–3), 277–287. doi:10.1016/j.coastaleng.2005.10.015
- Roelvink, D., & Reniers, A. (2011). *A Guide to Modeling Coastal Morphology (Vol. 12)*. WORLD SCIENTIFIC. doi:10.1142/7712
- Roelvink, D., Reniers, A., van Dongeren, A., van Thiel de Vries, J., McCall, R., & Lescinski, J. (2009). Modelling storm impacts on beaches, dunes and barrier islands. *Coastal Engineering*, 56(11–12), 1133–1152. doi:10.1016/j.coastaleng.2009.08.006
- Rossington, K., & Spearman, J. (2009). Past and future evolution in the Thames Estuary. *Ocean Dynamics*, 59, 709–718. doi:10.1007/s10236-009-0207-4
- Ruhl, C. A., & Schoellhamer, D. H. (2004). Spatial and temporal variability of suspended-sediment concentrations in a shallow estuarine environment. *San Francisco Estuary and Watershed Science*, 2(2). doi:10.15447/sfew.2004v2iss2art1
- RWS—Rijkswaterstaat Ministerie van Infrastructuur en Milieu. (2023). Vaklodgingen. Retrieved from <https://waterinfo-extra.rws.nl/monitoring/morfologie/#h53b817e6-e5cd-49d1-873c-9a0f85d8e416>
- Sampath, D. M. R., Boski, T., Silva, P. L., & Martins, F. A. (2011). Morphological evolution of the Guadiana estuary and intertidal zone in response to projected sea-level rise and sediment supply scenarios. *Journal of Quaternary Science*, 26(2), 156–170. doi:10.1002/jqs.1434
- Schoellhamer, D. H., Ganju, N. K., & Shellenbarger, G. G. (2008). Sediment transport in San Pablo Bay. In D. A. Cacchione & P. A. Mull (Eds.), *Technical Studies for the Aquatic Transfer Facility: Hamilton Wetlands Restoration Project* (pp. 36–107). San Francisco: U.S. Army Corps of Engineers.
- Schramkowski, G. P., Schuttelaars, H. M., & de Swart, H. E. (2002). The effect of geometry and bottom friction on local bed forms in a tidal embayment. *Continental Shelf Research*, 22(11–13), 1821–1833. doi:10.1016/S0278-4343(02)00040-7
- Seiffert, R., Büscher, A., & Hesser, F. (2014). Impact of Sea Level Rise on Estuarine Hydrodynamics. In: Lehfeldt, Rainer; Kopmann, Rebekka (Hg.): *ICHE 2014. Proceedings of the 11th International Conference on Hydroscience & Engineering*. Karlsruhe: Bundesanstalt für Wasserbau. S. 1059-1066.

- Seminara, G., & Tubino, M. (2001). Sand bars in tidal channels. Part 1. Free bars. *Journal of Fluid Mechanics*, 440, 49–74. doi:10.1017/S0022112001004748
- Shepard, C. C., Crain, C. M., & Beck, M. W. (2011). The protective role of coastal marshes: a systematic review and meta-analysis. *PloS One*, 6(11), e27374–e27374. doi:10.1371/journal.pone.0027374
- Sherwood, C. R., & Creager, J. S. (1990). Sedimentary geology of the Columbia River Estuary. *Progress in Oceanography*, 25(1), 15–79. doi:10.1016/0079-6611(90)90003-K
- Smith, B. J. (1965). Sedimentation in the San Francisco Bay system. In *Proc. of the Interagency Sedimentation Conference* (pp. 675–708).
- Smith, R. (2002). Historical Golden Gate tidal series. NOAA Tech. Rep. NOS CO-OPS 035, U.S. Department of Commerce, Washington, D. C.
- Song, S., Wu, Z., Wang, Y., Cao, Z., He, Z., & Su, Y. (2020). Mapping the Rapid Decline of the Intertidal Wetlands of China Over the Past Half Century Based on Remote Sensing. *Frontiers in Earth Science*, 8, 16. doi:10.3389/feart.2020.00016
- Straub, K. M., & Mohrig, D. (2008). Quantifying the morphology and growth of levees in aggrading submarine channels. *Journal of Geophysical Research: Earth Surface*, 113(F3). doi:10.1029/2007JF000896
- Sutherland, J., Peet, A. H., & Soulsby, R. L. (2004). Evaluating the performance of morphological models. *Coastal Engineering*, 51(8–9), 917–939. doi:10.1016/j.coastaleng.2004.07.015
- Sweet, W. V., Kopp, R. E., Weaver, C. P., Obeysekera, J., Horton, R. M., Thieler, E. R., & Zervas, C. (2017). GLOBAL AND REGIONAL SEA LEVEL RISE SCENARIOS FOR THE UNITED STATES. Silver Spring, Maryland, USA: NOAA/NOS Center for Operational Oceanographic Products and Services.
- Takekawa, J. Y., Thorne, K. M., Buffington, K. J., Spragens, K. A., Swanson, K. M., Drexler, J. Z., ... Casazza, M. L. (2013). Final report for sea-level rise response modeling for San Francisco Bay estuary tidal marshes. US Geological Survey.
- Teeter, A. M., Letter, J. V, Jr., Pratt, T. C., Callegan, C. J., & Boyt, W. L. (1997). San Francisco Bay Long-Term Management Strategy (LTMS) for Dredging and Disposal. Report 2. Baywide Suspended Sediment Transport Modeling.
- Temmerman, S., Bouma, T. J., Govers, G., Wang, Z. B., De Vries, M. B., & Herman, P. M. J. (2005). Impact of vegetation on flow routing and sedimentation patterns: Three-dimensional modeling for a tidal marsh. *Journal of Geophysical Research: Earth Surface*, 110(F4). doi:10.1029/2005JF000301
- Thatcher, M. L., & Harleman, D. R. F. (1972). Prediction of unsteady salinity intrusion in estuaries : mathematical model and user's manual. (S. G. P. O. Massachusetts Institute of Technology & N. S. G. P. (U.S.), Eds.). Retrieved from

- <https://repository.library.noaa.gov/view/noaa/9602>
- Thorne, K., Macdonald, G., Guntenspergen, G., Ambrose, R., Buffington, K., Dugger, B., ... Takekawa, J. (2018). U . S . Pacific coastal wetland resilience and vulnerability to sea-level rise, (February), 1–11. doi:10.1126/sciadv.aao3270
- Toorman, E. A. (2000). Cohesive sediment transport modeling: European perspective. In W. H. McAnally & A. J. Mehta (Eds.), *Proceedings of Marine Sciences, Coastal and Estuarine Fine Sediment Processes* (pp. 1–18). Amsterdam, The Netherlands: Elsevier Science. doi:10.1016/S1568-2692(00)80109-6
- Townend, I., Zhou, Z., Guo, L., & Coco, G. (2021). A morphological investigation of marine transgression in estuaries. *Earth Surface Processes and Landforms*, 46(3), 626–641. doi:10.1002/esp.5050
- US EPA. (2018). San Francisco Bay Delta: About the Waterdhed. Retrieved February 1, 2018, from <https://www.epa.gov/sfbay-delta/about-watershed>
- USCG Aux. (2008). Our Ocean Planet. Retrieved June 25, 2016, from <https://web.archive.org/web/20160625131917/http://a11306.uscgaux.info/envIRON.html>
- USGS. (2018). Water Quality of San Francisco Bay. Retrieved February 1, 2018, from <https://sfbay.wr.usgs.gov/access/wqdata/index.html>
- Van Alphen, J. (1990). A mud balance for Belgian-Dutch coastal waters between 1969 and 1986. *Netherlands Journal of Sea Research*, 25, 19–30. doi:10.1016/0077-7579(90)90005-2
- Van Asselen, S., Karssenberg, D., & Stouthamer, E. (2011). Contribution of peat compaction to relative sea-level rise within Holocene deltas. *Geophysical Research Letters*, 38(24), 1–5. doi:10.1029/2011GL049835
- van de Wal, R. S. W., Nicholls, R. J., Behar, D., McInnes, K., Stammer, D., Lowe, J. A., ... White, K. (2022). A High-End Estimate of Sea Level Rise for Practitioners. *Earth's Future*, 10(11), e2022EF002751. doi:10.1029/2022EF002751
- van der Spek, A. (1994). Large-scale evolution of Holocene tidal basins in the Netherlands. PhD thesis. Utrecht, The Netherlands: Utrecht University. CIP-DATA KONINKLIJKE BIBLIOTHEEK, DEN HAAG.
- van der Spek, A. (1997). Tidal asymmetry and long-term evolution of Holocene tidal basins in The Netherlands: simulation of palaeo-tides in the Schelde estuary. *Marine Geology*, 141(1–4), 71–90. doi:10.1016/S0025-3227(97)00064-9
- van der Spek, A., & Beets, D. J. (1992). Mid-Holocene evolution of a tidal basin in the western Netherlands: a model for future changes in the northern Netherlands under conditions of accelerated sea-level rise? *Sedimentary Geology*, 80(3), 185–197. doi:10.1016/0037-0738(92)90040-X

- van der Wegen, M. (2013). Numerical modeling of the impact of sea level rise on tidal basin morphodynamics. *Journal of Geophysical Research: Earth Surface*, 118(2), 447–460. doi:10.1002/jgrf.20034
- van der Wegen, M., Dastgheib, A., Jaffe, B. E., & Roelvink, D. (2011). Bed composition generation for morphodynamic modeling: Case study of San Pablo Bay in California, USA. *Ocean Dynamics*, 61(2–3), 173–186. doi:10.1007/s10236-010-0314-2
- van der Wegen, M., & Jaffe, B. E. (2013a). Does centennial morphodynamic evolution lead to higher channel efficiency in San Pablo Bay, California? *Marine Geology*, 345, 254–265. doi:10.1016/j.margeo.2013.06.020
- van der Wegen, M., & Jaffe, B. E. (2013b). Towards a probabilistic assessment of process-based, morphodynamic models. *Coastal Engineering*, 75, 52–63. doi:10.1016/j.coastaleng.2013.01.009
- van der Wegen, M., & Jaffe, B. E. (2014). Processes governing decadal-scale depositional narrowing of the major tidal channel in San Pablo Bay, California, USA. *Journal of Geophysical Research: Earth Surface*, (119), 1136–1154. doi:10.1002/2013JF002824
- van der Wegen, M., Jaffe, B. E., & Roelvink, D. (2011). Process-based, morphodynamic hindcast of decadal deposition patterns in San Pablo Bay, California, 1856-1887. *Journal of Geophysical Research: Earth Surface*, 116(2), 1–22. doi:10.1029/2009JF001614
- van der Wegen, M., Jaffe, B., Foxgrover, A., & Roelvink, D. (2017). Mudflat Morphodynamics and the Impact of Sea Level Rise in South San Francisco Bay. *Estuaries and Coasts*, 40(1), 37–49. doi:10.1007/s12237-016-0129-6
- van der Wegen, M., & Roelvink, D. (2008). Long-term morphodynamic evolution of a tidal embayment using a two-dimensional, process-based model. *Journal of Geophysical Research: Oceans*, 113(3), 1–23. doi:10.1029/2006JC003983
- van der Wegen, M., & Roelvink, D. (2012). Reproduction of estuarine bathymetry by means of a process-based model: Western Scheldt case study, the Netherlands. *Geomorphology*, 179, 152–167. doi:10.1016/j.geomorph.2012.08.007
- van der Wegen, M., Roelvink, J. A., & Jaffe, B. E. (2019). Morphodynamic Resilience of Intertidal Mudflats on a Seasonal Time Scale. *Journal of Geophysical Research: Oceans*, 124(11), 8290–8308. doi:10.1029/2019JC015492
- van der Wegen, M., van der Werf, J. J., De Vet, P. L. M., & R bke, B. R. (2017). Hindcasting Westerschelde mouth morphodynamics (1963-2011). Report 1210301-001-ZKS-0006. Delft, The Netherlands: Deltares. Retrieved from <http://www.scheldemonitor.nl/nl/imis?module=ref&refid=284224&printversion=1&dropIMISitle=1>
- van der Wegen, M., Wang, Z. B., Savenije, H., & Roelvink, D. J. A. (2008). Long-term morphodynamic evolution and energy dissipation in a coastal plain, tidal embayment.

- Journal of Geophysical Research, 113, 2008 ; doi:10.1029/2007JF000898 (Vol. 113). doi:10.1029/2007JF000898
- van der Werf, J. J., & Briere, C. D. E. (2013). The influence of morphology on tidal dynamics and sand transport in the Scheldt estuary. Report 1207720-000. Delft, The Netherlands: Deltares.
- van Dijk, W. M., Cox, J. R., Leuven, J. R. F. W., Cleveringa, J., Taal, M., Hiatt, M. R., ... Kleinhans, M. G. (2021). The vulnerability of tidal flats and multi-channel estuaries to dredging and disposal. *Anthropocene Coasts*, 4(1), 36–60. doi:10.1139/anc-2020-0006
- Van Eck, B. (1999). *De Scheldeatlas: een beeld van een estuarium*. The Netherlands: Rijkswaterstaat (in Dutch).
- Van Goor, M. A., Zitman, T. J., Wang, Z. B., & Stive, M. J. F. (2003). Impact of sea-level rise on the morphological equilibrium state of tidal inlets. *Marine Geology*, 202(3–4), 211–227. doi:10.1016/S0025-3227(03)00262-7
- van Kessel, T., Vroom, J., & Taal, M. (2023). A conceptual framework for fine sediment dynamics in the Scheldt estuary. Report 11208065-000-ZKS-0010. Delft, The Netherlands: Deltares.
- Van Kessel, T., Winterwerp, H., Van Prooijen, B., Van Ledden, M., & Borst, W. (2011). Modelling the seasonal dynamics of SPM with a simple algorithm for the buffering of fines in a sandy seabed. *Continental Shelf Research*, 31(10, Supplement), S124–S134. doi:10.1016/j.csr.2010.04.008
- van Maanen, B., Coco, G., Bryan, K. R., & Friedrichs, C. T. (2013). Modeling the morphodynamic response of tidal embayments to sea-level rise. *Ocean Dynamics*, 63(11), 1249–1262. doi:10.1007/s10236-013-0649-6
- Van Maldegem, D. C., De Winder, B., & Arends, A. (1999). *Slib in de Westerschelde: een beschrijving van de troebelheid en slibverspreiding in de Westerschelde voor de periode december 1998 tot juli 1999*. Report 99.026. Middelburg, The Netherlands: Rijksinstituut voor Kust en Zee/ RIKZ (Rijkswaterstaat) (in Dutch).
- Van Maldegem, D. C., Mulder, H. P. J., & Langerak, A. (1993). A cohesive sediment balance for the Scheldt estuary. *Netherlands Journal of Aquatic Ecology*, 27(2), 247–256. doi:10.1007/BF02334788
- Van Maldegem, D. C., & Vroom, J. (1995). *Invloed speciëstoring uit haven van Zeebrugge op water- en bodemkwaliteit Westerschelde*. Report 94.049. Middelburg, The Netherlands: Rijksinstituut voor Kust en Zee/ RIKZ (Rijkswaterstaat) (in Dutch).
- van Maren, D. S., Vroom, J., Fettweis, M., & Vanlede, J. (2020). Formation of the Zeebrugge coastal turbidity maximum: The role of uncertainty in near-bed exchange processes. *Marine Geology*, 425, 106186. doi:10.1016/j.margeo.2020.106186
- Van Rijn, L. C. (1993). *Principles of sediment transport in rivers, estuaries and coastal*

- seas (Vol. 1006). Aqua publications Amsterdam.
- Van Rijn, L. C. (2013). Tidal Phenomena in the Scheldt Estuary, part 2. Report 1204410-000. Delft, The Netherlands: Deltares.
- Van Rijn, L. C., Walstra, D. J. R., & Ormondt, M. van. (2004). Description of TRANSPOR2004 and Implementation in Delft3D-ONLINE. Report Z3748.10. Delft, The Netherlands: Delft Hydraulics (Deltares).
- van Veen, J. (1950). Eb-en vloodschaar systemen in de Nederlandse getijwateren. Tijdschrift van Het Koninklijk Nederlandsch Aardrijkskundig Genootschap (Ser. 2) (in Dutch), 67, 303–350.
- van Veen, J., van der Spek, A. J. F., Stive, M. J. F., & Zitman, T. (2005). Ebb and Flood Channel Systems in the Netherlands Tidal Waters. *Journal of Coastal Research*, 1107–1120. doi:10.2112/04-0394.1
- van Vessem, P. (1984a). Selectie meetdagen behoefte van Comor, Hiswa en Doos2. Nota WWKZ-84G.284. The Netherlands: Rijkswaterstaat (in Dutch). Retrieved from <https://figshare.com/s/5f3d76060c39a5f437f8?file=17868722>
- van Vessem, P. (1984b). Selectie meetdagen behoefte van Comor, Hiswa en Doos2. Nota WWKZ-84G.293. The Netherlands: Rijkswaterstaat (in Dutch). Retrieved from <https://figshare.com/s/5f3d76060c39a5f437f8?file=17868722>
- Vandenbruwaene, W., Levy, Y., Plancke, Y., Vanlede, J., Verwaest, T., & Mostaert, F. (2017). Integraal plan Boven-Zeeschelde: Deelrapport 3 – Sedimentbalans Zeeschelde, Rupel en Durme. Versie 5.0. Report WL 13_131. Antwerp, Belgium: Flanders Hydraulics Research (in Dutch).
- Velegrakis, A. F., Bishop, C., Lafite, R., Oikonomou, E. K., Lecouturier, M., & Collins, M. B. (1997). Sub-Task S3: Investigation of meso-and macro-scale sediment transport, Hydrodynamics Biogeochemical Processes and Fluxes in the Channel. FLUXMANCHE II Final Report, MAST II, MAS2CT940089, 128–143.
- Vermeersen, B. L. A., Slangen, A. B. A., Gerkema, T., Baart, F., Cohen, K. M., Dangendorf, S., ... van der Wegen, M. (2018). Sea-level change in the Dutch Wadden Sea. *Netherlands Journal of Geosciences*, 97(3), 79–127. doi:10.1017/njg.2018.7
- Vroom, J., De Vet, P. L. M., & Van der Werf, J. (2015). Validatie Waterbeweging Delft3D NeVla Model Westerscheldemonding. Report 1210301-001-ZKS-0001. Delft, The Netherlands: Deltares (in Dutch).
- Vroom, J., & Schrijvershof, R. (2015). Overzicht van menselijke ingrepen inde westerschelde en haar mondingsgebied in de periode. Report 1210301-001-ZKS-0005. Delft, The Netherlands: Deltares (in Dutch).
- Vroom, J., van der Wegen, M., Martyr-Koller, R. C., & Lucas, L. V. (2017). What Determines Water Temperature Dynamics in the San Francisco Bay-Delta System?

- Water Resources Research, 53(11), 9901–9921. doi:10.1002/2016WR020062
- Wachler, B., Seiffert, R., Rasquin, C., & Kösters, F. (2020). Tidal response to sea level rise and bathymetric changes in the German Wadden Sea. *Ocean Dynamics*, 70(8), 1033–1052. doi:10.1007/s10236-020-01383-3
- Wang, Z. B., Elias, E. P. L., van der Spek, A. J. F., & Lodder, Q. J. (2018). Sediment budget and morphological development of the Dutch Wadden Sea: impact of accelerated sea-level rise and subsidence until 2100. *Netherlands Journal of Geosciences*, 97(3), 183–214. doi:10.1017/njg.2018.8
- Wang, Z. B., Jeuken, C., & de Vriend, H. J. (1999). Tidal asymmetry and residual transport in estuaries. Report Z2749. Delft, The Netherlands: WL|Delft Hydraulics (Deltares).
- Wang, Z. B., Jeuken, M. C. J. ., Gerritsen, H., de Vriend, H. J., & Kornman, B. A. (2002). Morphology and asymmetry of the vertical tide in the Westerschelde estuary. *Continental Shelf Research*, 22(17), 2599–2609. doi:10.1016/S0278-4343(02)00134-6
- Wang, Z. B., & Roelfzema, A. (2001). Long-term morphological modelling for humber estuary with estmorf. In G. Li & Z. Wang (Eds.), *IAHR congress proceedings, hydraulics for maritime engineering* (pp. 229–234). Beijing, China: Tsinghua University Press.
- Wartel, S., Chen, M., van Eck, G. T. M., & van Maldegem, D. (2007). Influence of harbour construction on mud accumulation in the Scheldt estuary. *Aquatic Ecosystem Health & Management*, 10(1), 107–115. doi:10.1080/14634980701194001
- Weather2. (2018). San Pablo Bay Climate History. Retrieved February 1, 2018, from <http://www.myweather2.com/City-Town/United-States-Of-America/California/San-Pablo-Bay/climate-profile.aspx?month=12>
- Wentworth, C. K. (1922). A Scale of Grade and Class Terms for Clastic Sediments. *The Journal of Geology*, 30(5), 377–392. Retrieved from <http://www.jstor.org/stable/30063207>
- Werner, B. T. (2003). Modeling Landforms as Self-Organized, Hierarchical Dynamical Systems. In *Prediction in Geomorphology*. (2003), Geophys. Monogr. Ser., vol. 135, edited by P. R. Wilcock and R. M. Iverson, pp. 133-150, AGU, Washington, D. C. (Vol. 135, pp. 133–150). doi:10.1029/135GM10
- Wilson, M. A., Costanza, R., Boumans, R., & Liu, S. (2005). Integrated assessment and valuation of ecosystem goods and services provided by coastal systems. In *The intertidal ecosystem: the value of Ireland’s shores*. (pp. 1–24). Dublin: Royal Irish Academy. Retrieved from <http://hdl.handle.net/102.100.100/182918?index=1>
- Windfinder. (2018). Wind, Wave & Weather Reports, Forecasts & Statistics Worldwide. Retrieved February 1, 2018, from <https://www.windfinder.com/#12/38.0351/->

122.3273

- Winterwerp, J. c., & Van Kesteren, W. G. M. (2004). 5 - Settling and Sedimentation. In Johan C Winterwerp & W. G. M. B. T.-D. in S. van Kesteren (Eds.), *Introduction to the Physics of Cohesive Sediment in the Marine Environment* (Vol. 56, pp. 121–159). Elsevier. doi:10.1016/S0070-4571(04)80006-2
- Winterwerp, J C, Wang, Z. B., Stive, M. J. F., Arends, A., Jeuken, C., Kuijper, C., & Thoolen, P. M. C. (2001). A new morphological schematization of the Western Scheldt estuary, The Netherlands. In *Proceedings of the 2nd IAHR symposium on River, Coastal and Estuarine Morphodynamics* (pp. 525–533).
- Wright, S. a., & Schoellhamer, D. H. (2004). Trends in the sediment yield of the Sacramento River, California, 1957-2001. *San Francisco Estuary and Watershed Science*, 2(2), 1–14. doi:10.5811/westjem.2011.5.6700
- Yang, S.-L., Friedrichs, C., Shi, Z., Ding, P.-X., Zhu, J., & Zhao, Q.-Y. (2003). Morphological response of tidal marshes, flats and channels of the Outer Yangtze River mouth to a major storm. *Estuaries*, 26(6), 1416–1425. doi:10.1007/BF02803650
- Zăinescu, F., Anthony, E., Vespremeanu-Stroe, A., Besset, M., & Tătui, F. (2023). Concerns about data linking delta land gain to human action. *Nature*, 614(7947), E20–E25. doi:10.1038/s41586-022-05624-x
- Zheng, J., Elmilady, H., Röbbke, B. R., Taal, M., Wang, Z. B., van Prooijen, B. C., ... van der Wegen, M. (2021). The impact of wind-waves and sea level rise on the morphodynamics of a sandy estuarine shoal. *Earth Surface Processes and Landforms*, 46(15), 3045–3062. doi:10.1002/esp.5207
- Zhou, X. (2011). *Morphodynamic Response of Yangtze River Estuary to Sea Level Rise and Human Interferences*. PhD Thesis. Darmstadt, Germany: Technische Universität / Institut für Wasserbau und Wasserwirtschaft.
- Zhou, X., Zheng, J., Doong, D.-J., & Demirbilek, Z. (2013). Sea level rise along the East Asia and Chinese coasts and its role on the morphodynamic response of the Yangtze River Estuary. *Ocean Engineering*, 71, 40–50. doi:10.1016/J.OCEANENG.2013.03.014
- Zhou, Z., Coco, G., Townend, I., Olabarrieta, M., Van Der Wegen, M., Gong, Z., ... Gelfenbaum, G. (2017). Is “morphodynamic equilibrium” an oxymoron? *Earth-Science Reviews*, 165, 257–267. doi:10.1016/j.earscirev.2016.12.002
- Zhou, Z., Coco, G., van der Wegen, M., Gong, Z., Zhang, C., & Townend, I. (2015). Modeling sorting dynamics of cohesive and non-cohesive sediments on intertidal flats under the effect of tides and wind waves. *Continental Shelf Research*, 104, 76–91. doi:10.1016/J.CSR.2015.05.010
- Zhou, Z., Ye, Q., & Coco, G. (2016). A one-dimensional biomorphodynamic model of tidal flats: Sediment sorting, marsh distribution, and carbon accumulation under sea

level rise. *Advances in Water Resources*, 93, 288–302. doi:10.1016/J.ADVWATRES.2015.10.011

- Zhu, B., Li, Y., Yue, Y., Yang, Y., Liang, E., Zhang, C., & Borthwick, A. G. L. (2020). Alternate erosion and deposition in the Yangtze Estuary and the future change. *Journal of Geographical Sciences*, 30(1), 145–163. doi:10.1007/s11442-020-1720-0
- Zhu, Q., van Prooijen, B. C., Wang, Z. B., & Yang, S. L. (2017). Bed-level changes on intertidal wetland in response to waves and tides: A case study from the Yangtze River Delta. *Marine Geology*, 385, 160–172. doi:10.1016/j.margeo.2017.01.003

LIST OF ACRONYMS

2D	Two Dimensional
3D	Three Dimensional
AD	Anno Domini
ASMITA	Aggregated Scale Morphological Interaction between Tidal inlets and the Adjacent coast
BF	Base Flow
BSS	Brier Skill Score
BW	Base Wave
CO ₂	Carbon dioxide
CRS	Cross-section
D3D	Delft3D
D3D FM	Delft3D Flexible mesh
D ₅₀	Mean particle size
dH	Tidal range
ETM	Estuarine Turbidity Maxima
GLM	Generalised Lagrangian Mean
GTSM	Global Tide and Surge Model
H _s	Significant wave height
LIDAR	Light Detection and Ranging
LUN	Lunar spring-neap tidal cycle
LW	Low Water
MF	Morphological factor
MLLW	Mean Low Low Water
MS	Schematized mixed semi-diurnal tidal cycle
MSE	Mean-Squared Error

MSL	Mean Sea Level
NAP	Dutch ordnance level
NASA	National Aeronautics and Space Administration
RCPs	Representative Concentrated Pathway scenarios
RMS	Root Mean Square
SEMs	Semi-empirical models
SLR	Sea Level Rise
SPB	San Pablo Bay
SSC	Suspended Sediment Concentrations
T_p	Significant wave period
UN	United Nations
USA	United States of America
USGS	United States Geological Survey
VNSC	Vlaams-Nederlandse Scheldecommissie
WS	Western Scheldt

LIST OF TABLES

Table 1.1. Sea level rise monitoring parameters on January 16, 2024. Source: NASA (2024).....	10
Table 2.1. The forcing conditions and model parameters investigated in the sensitivity analysis.	58
Table 4.1. Spatially averaged bed level changes between 1983-2103 for the No SLR and for the 3 SLR scenarios relative to the No SLR case.....	118
Table 4.2. Implemented sediment parameters.	132
Table 4.3. Brier Skill Score proposed classification (Sutherland et al., 2004).....	132
Table 5.1. Net mud import (Kt/yr) at the Western Scheldt (WS) mouth and the Belgium-Dutch border reported in literature.	142
Table 5.2. Summary of the main model parameters.	146
Table 5.3. Domain integrated and tidally averaged flow, wave, and maximum bed shear stresses (N/m^2) over the shoals (-2.5 m NAP + SLR) during spring tide conditions after 80 years for the Sand-mud model. For simplicity purposes, the maximum bed shear stress is calculated as the summation of the flow and wave-induced bed shear stress.	157
Table 5.4. Historical net sediment budget of the Western Scheldt estuary. Negative/positive values indicate sediment loss/gain, respectively.	163
Table 5.5. The observed and modeled sediment budget of the Western Scheldt during the hindcast and forecast period, presented in this study. The values presented are based on bed level changes.	164

LIST OF FIGURES

Figure 1.1. Aerial view of Murray River Estuary, Australia. Image source: www.freeaussiestock.com	2
Figure 1.2. The change in the average global surface temperature (°C) from 1880 to 2023 compared to the long-term average from 1951 to 1980. Figure source: NASA (2023a). 4	4
Figure 1.3. The change in global surface temperature (Celsius) for the periods 1880-1884 and 2018-2022 compared to the long-term average from 1951 to 1980. Dark blue color represents areas cooler than average and dark red color represents areas warmer than average. Figure source: NASA (2023b).....	4
Figure 1.4. Historical atmospheric carbon dioxide concentrations (ppm). Figure source: NASA (2023d).....	5
Figure 1.5. Eustatic sea level history along warm and cool periods during the (a) past 900 thousand years and (b) late Quaternary (past 140 years). Figure source: NOAA PaleoClimatology, https://www.ncei.noaa.gov/products/paleoclimatology#sea	8
Figure 1.6. Reconstruction of the sea level curve showing the most recent period of rise and warming during the (A) Post-Glacial era and (B) Holocene era. Figures created by Robert A. Rohde based on data obtained from K. Fleming et al. (1998); K. Fleming (2000); and Milne et al. (2005).....	8
Figure 1.7. Sea level change in the North Atlantic Ocean based on data collected from North Carolina (red line, pink band shows the uncertainty range) compared with a reconstruction of global sea level rise based on tide gauge data (Blue line). Figure source: Adapted from Kemp et al. (2011).....	9
Figure 1.8. Muir Glacier in the Alaska Range. Photographed by William O. Field on 13/08/1941 (Left) and by Bruce F. Molnia on 31/08/2004 (Right). Image source: NSIDC Glacier Photograph Collection, https://nsidc.org/data/glacier_photo/	10
Figure 1.9. Sea level changes (mm) since 1993 as observed by satellite altimeters. The black line shows the measurements, while the blue shade indicates the uncertainty. Figure Source: NASA (2024).....	10
Figure 1.10. Past and projected SLR from 1800 till 2100, relative to year 2000. Estimates from proxy data (1800-1890) are shown in red, observed tidal gauge measurements (1880-2009) shown in blue, and satellite observations (1993-2012) shown in green. The orange line indicates the currently projected range of SLR in 2100 from 1 to 4ft (≈ 0.3 to 1.2 m). The larger range from 0.66 to 6.6 ft (≈ 0.2 to 2.0 m). represents the uncertainties involved in how glaciers and ice sheets will react to climate change. Figure source: Melillo et al. (2014), adapted from Parris et al. (2012) with input from NASA Jet Propulsion Laboratory.....	12

Figure 2.1. (a) Layout and bathymetry (m) of the Western and Eastern Scheldt estuaries with the location of the Galgeplaat indicated. (b) The 1993 Galgeplaat bathymetry (m; Reversed coordinates) showing the location of the 1982-1983 monitoring grid (black rectangle) along with the five cross-sections (CRS1 to CRS5) monitored during 1983-1984 period. (c) Bed-level changes (cm) at 4 cross-sections inside the monitoring grid during the one-year monitoring period (M1) divided into the mean annual gross erosion (Red) and sedimentation (Blue) along with the net annual erosion/sedimentation (Black). (d), (e), and (f) Bed-level changes (cm) at CRS1 to CRS5 (colors correspond to cross-sections in Figure 2.1b) during the monitoring periods of M2, M3, and M4, respectively. The figure was constructed by the digitization of Geomor team (1984), van Vessem (1984a), and (1984b). The bathymetric data (source: Rijkwaterstaat) are with respect to NAP (Dutch Ordnance Level). 31

Figure 2.2. Google Earth satellite images showing small-scale levee formations at the channel-shoal interface in the WS. Note: Large and small images scales (bottom right) are 6 km and 200 m, respectively. 32

Figure 2.3. The left panel shows the 2018 bathymetry (m; reference NAP) of the intertidal zone at the Frisian Inlet of the Wadden Sea obtained from LIDAR imagery (source: Rijkwaterstaat) along with the locations of 8 cross-sections (A1-A8). The right panel shows bed-level profiles for 2018 (black line and solid hatch), and 2012 (blue line). The left and right sides of a cross-section are the seaward and landward sides, respectively. 33

Figure 2.4. Model configuration and initial bathymetry (a) plan-view with the location of the three open model boundaries (black lines) and (b) cross-sectional profile indicating the seaward and landward side along with the MSL, tidal range, wave direction, and initial sediment thickness and properties. 34

Figure 2.5. Modeled (a) equilibrium bathymetry after 200 years and (b) cross-sectionally averaged bed-level profile showing the profile evolution over time towards an equilibrium state. 36

Figure 2.6. Cross-sectional profile showing the initial ($t = 0$ hr, dashed black) and time-varying (black) bed-level, water level (blue), H_s (red), SSC (yellow), bed (magenta) and suspended (green) transport during tidal cycle TCini. Positive and negative transport are landward and seaward directed, respectively. 39

Figure 2.7. Modeled (a) flow (τ_c), wave (τ_w), and maximum (τ_{max}) tidally averaged shear stresses for tidal cycle TCini (dotted) and TCeq (Straight), and (b) wave-induced shear stress (τ_w) during tidal cycle TCeq. Note: For simplicity purposes, τ_w is roughly estimated by the difference between τ_{max} and τ_c 39

- Figure 2.8.** Sensitivity analysis showing the equilibrium profiles corresponding to different forcing conditions. The light blue shading indicates the base-case tidal difference, and the dashed black line indicates the initial profile..... 41
- Figure 2.9.** Cross-sectional bed-level profile after 6 morphological month wave forcing change. 42
- Figure 2.10.** Top panel shows the forecasted bed levels at Years 2100 and 2300 under 1m SLR scenario starting from the 2000 equilibrium profile and 0 m MSL. The bottom panel tracks the SLR and bed-level changes over time at 4 points on the shoal. 44
- Figure 2.11.** Modeled development of intertidal area (m^2) and its inundation over time for (a, and b) different forcing conditions, and (c, and d) different SLR scenarios. 45
- Figure 2.12.** The top panels show SLR and bed-level changes at 4 points on the shoal (see Figure 2.10). The bottom panels show the rates..... 46
- Figure 2.13.** Sensitivity analysis showing the equilibrium profiles corresponding to different parameter values of the (a) wave-induced suspended transport parameter (f_{sw}), minimum depth for sediment computation (SedThr), and wave friction factor (f_w), (b) grid resolution, and (c) morphological factor (MF). The light blue shading indicates the tidal difference, and the dashed black line indicates the initial profile. 57
- Figure 2.14.** Modeled (a) cross-sectional profile of the sedimentation/erosion (m) due to three storm conditions of $T_p=6$ sec and $H_s=1, 1.5$ and 2 m for Storm 1, 2, and 3, respectively. (b) Sedimentation/erosion overtime at two selected points (P1, and P2; see Figure 2.14a x-axis) showing the storm event at $t = 2$ yr and the recovery till $t \approx 12$ yr. 57
- Figure 2.15.** The top panel shows SLR and bed level changes at 4 points on the shoal (see Figure 2.10). The bottom panel shows the rates..... 58
- Figure 3.1.** Model domain and the initial model bathymetry (m)..... 65
- Figure 3.2.** Modeled bathymetry (m) of the high-resolution domain over time for the Flow (left panel) and Wave (right panel) simulations. The white color band is the average low water level ($LW \approx -1.6$ m) which indicates the approximate border between the intertidal (shoal) and subtidal (channels) areas. 66
- Figure 3.3.** (a) Temporal development of τ_{max} (N/m^2) spatially averaged over the whole model domain and over 1m vertical elevation bins. The bin range is with respect to LW and is divided into subtidal bins (-2 to -1 m; grey, and -1 to 0 m; blue), and intertidal bins (0 to 1 m; green, and 1 to 2 m; yellow). Solid and dotted lines correspond to Wave, and Flow simulations, respectively. (b, and c) τ_{max} map of the high-resolution domain at $T = 100$ years for the Wave, and Flow simulations, respectively. The black contour lines indicate the border (LW) between intertidal and subtidal areas..... 67

Figure 3.4. (a) The modeled bathymetry (m) at T = 150 years for the whole model domain. The black box indicates the location of the bottom plot. (b) The tide-residual sediment transport magnitude ($m^3/s/m$) and direction. Arrows are RMS normalized and plotted on a grid with half the model grid resolution to make them more visible. The white contour lines indicate the border (LW) between the intertidal and subtidal areas. 68

Figure 3.5. (a) The initial bathymetry (m) (Wave simulation; T =150 years) along with the location of the two cross-sections (CRS 1, and CRS 2). The modeled bathymetry after 50 years of (b) no waves, (c) Base-case waves, and (d) increased waves. The cross-sectional profile development over time for CRS 1 (e, f, and g), and CRS2 (h, i, and j) for the three wave scenarios. The profiles were chosen parallel to the wind field direction and on the upwind side of the shoals which is subjected to the highest wave attack..... 69

Figure 3.6. The mean sea level (MSL; m) for the implemented SLR scenarios. 70

Figure 3.7. SLR impact on the shoal morphology for the simulation including wind-wave impact (a, b, c, d, and e; Base Wave; BW). (a) The initial shoal elevation (m; with respect to MSL), (b) the shoal elevation (m; w.r.t MSL) after 100 years with no SLR, (c) the shoal elevation (m; w.r.t MSL) after 100 years with a non-linear 0.96 m/century SLR, (d) the difference between the shoal elevation for the SLR and No SLR scenarios (color bar from -0.96 to 0.96 m), and (e) the shoal elevation (m; w.r.t MSL + SLR) corrected with the SLR magnitude. (f) The shoal elevation (m; w.r.t MSL + SLR) corrected with the SLR magnitude (0.96 m) but for the simulation excluding wind-wave impact (Base Flow; BF). The black lines are the elevation contours with 1 m intervals. 71

Figure 3.8. The modeled bathymetry (m) for the Wave Base-case simulation after 100 years with (a) no SLR, and (b) 0.96 m SLR. The black box indicates the location of the below plots. (c, and d) maximum flood velocities, (e, and f) maximum ebb velocities, (g, and h) difference between maximum flood and ebb velocities, and (i, and j) the tide-residual sediment transport magnitude ($m^3/s/m$) and direction. Arrows are RMS normalized and plotted on a grid with half the model grid resolution to make them more visible. The black/white contour lines indicate the border (LW) between the intertidal and subtidal areas. 73

Figure 3.9. Summary of the sensitivity analysis for different forcing conditions showing (a) the shoal volume (m^3 ; w.r.t LW), and (b) the channel volume (m^3 ; w.r.t LW) for the whole model domain for the initial state (blue), after 100 years without SLR (Orange), and after 100 years with SLR (Green). The legend presents the abbreviations used for the different simulations and the description of the varying forcing condition. BF and BW refer to the Base Flow and Base Wave simulations, respectively. 75

Figure 3.10. The temporal development of the shoal (a) and channel (b) volume (m^3) and the shoal (c) and channel (d) area (m^2) for the whole model domain and for the Wave simulations. The solid black line is the No SLR scenario, while the color lines are for the

different SLR scenarios. (e) Schematic showing the shoal and channel definition along with the datums used for the dashed lines (fixed datum; LW), and the solid lines (moving datum; LW+SLR). 77

Figure 3.11. (a, and b) The shoal elevation (m; w.r.t MSL) for the 0.96, and 2.63 m non-linear SLR, respectively. The black arrows in (a) point to the location of the secondary channels. (c, and d) The shoal elevation difference (m) between the SLR and No SLR scenario. The plots are for simulations including wave action. 78

Figure 3.12. (a, and b) The shoal elevation (m; w.r.t MSL) for the No W and W2 wind-wave conditions, respectively. (c, and d) The shoal elevation difference (m) between the SLR and No SLR scenario for each wind-wave condition. 79

Figure 3.13. (a, and c) The elevation difference (m) between the SLR and No SLR scenarios for the sand (BW) and mixture 2 (Mix2) simulations, respectively. The black contour line indicates the border (LW) between the intertidal shoals and channels. (b, and d) The colored solid lines show the temporal development of the width-averaged elevation difference. The dotted line shows the end elevation difference averaged over the whole domain..... 82

Figure 3.14. The mud percentage (%) in the top 0.25 m sediment layer for the simulation with a settling velocity of (a, and b) $w_s = 0.5$ mm/s, and (d, and e) $w_s = 1$ mm/s each without and with SLR, respectively. The difference between the mud percentage (%) for the No SLR and the 0.96 m non-linear SLR scenario for the different settling velocities. The black contour lines indicate the border (LW) between intertidal shoals and channels... 83

Figure 3.15. Satellite image of the Ameland and Frisian Inlet (Wadden Sea, The Netherlands) with the 2011/2012 bathymetry (m; source: Rijkswaterstaat) plotted. (<https://publicwiki.deltares.nl/display/OET/Dataset+documentation+Vaklodingen>) 92

Figure 3.16. Google Earth image of Anderson Inlet and Venus Bay (Victoria, Australia). 92

Figure 3.17. Google Earth image of Otago Harbour (Dunedin, New Zealand). 93

Figure 3.18. Median grain size in the Wadden Sea (The Netherlands). The figure is generated using the Sediment Atlas Wadden Sea. (<https://publicwiki.deltares.nl/display/OET/Dataset+documentation+Sediment+atlas+wadden+sea>) 93

Figure 3.19. SLR impact on the shoal morphology for the simulation excluding wind-wave impact (Base Flow; BF). (a) The initial shoal elevation (m; with respect to MSL), (b) the shoal elevation (m; w.r.t MSL) after 100 years with no SLR, (c) the shoal elevation (m; w.r.t MSL) after 100 years with a non-linear 0.96 m/century SLR, (d) the difference between the shoal elevation for the SLR and No SLR scenarios (color bar from -0.96 to

0.96 m), and (e) the shoal elevation (m; w.r.t MSL + SLR) corrected with the SLR magnitude. The black lines are the elevation contours with 1 m intervals. 94

Figure 3.20. The modeled bathymetry (m) for the Wave Base-case simulation after 100 years with (a) no SLR, and (b) 2.63 m SLR. The black box indicates the location of the below plots. (c, and d) Maximum flood velocities, (e, and f) Maximum ebb velocities, (g, and h) difference between maximum flood and ebb velocities, and (i, and j) the tide-residual sediment transport magnitude (m³/s/m) and direction. Arrows are RMS normalized and plotted on a grid with half the model grid resolution to make them more visible. The black/white contour lines indicate the border (LW) between the intertidal and subtidal areas. 95

Figure 3.21. Depth-averaged velocities during a tidal cycle at a point in the channel for the No SLR (orange) and 2.63 m SLR (blue) scenarios. 96

Figure 3.22. Maximum depth-averaged suspended sediment concentration (SSC; mg/l) for the fine (100 μm) and coarse (250 μm) sand fractions; (a, and b) Initial, (c, and d) after 100 years with no SLR, and (e, and f) after 100 years with a 2.63 m/century SLR. 97

Figure 3.23. The temporal development of the shoal (a) and channel (b) volume (m³) and the shoal (c) and channel (d) area (m²) for the whole model domain and for the Flow simulations. The solid black line is the No SLR scenario, while the color lines are for the different SLR scenarios. (e) Schematic showing the shoal and channel definition along with the datums used for the dashed lines (fixed datum; LW), and the solid lines (moving datum; LW+SLR). 98

Figure 3.24. Hypsometry curves of the (a) Flow, and (b) Waves simulations for the different SLR scenarios. The horizontal dotted lines indicate the border (LW + SLR) between the intertidal and subtidal sections of the hypsometry for the different scenarios. 99

Figure 3.25. The bed level slopes vs elevation (m; w.r.t MSL) in the whole model domain for the simulations without (a) and with (b) wave action and for the different SLR scenarios. The thick solid line indicates the elevation range corresponding to the intertidal section of the shoal. 99

Figure 3.26. (a) Wind speed (m/s) during a wind cycle (48 hours). (b) The spatially averaged wave orbital velocity squared (m²/s²) across the whole model domain during a wind cycle (solid lines). The dashed lines indicate the time average. 100

Figure 4.1. Left panel shows San Francisco Estuary land-boundary. Right panel shows a zoom on San Pablo Bay with its 1856 bathymetry and marsh extent plotted, the thin black line indicates the main channel while the grey dotted line in the middle denotes the division used in this study between the eastern and western side of San Pablo Bay. .. 105

- Figure 4.2.** Schematization of the modeling timeline showing the hindcast (1856-1983) and forecast (1983-2103) along with the associated boundary conditions. The orange, blue, and green lines represent the SSC, river discharge, and sea level, respectively. Sea level is increased for the forecast scenarios with 14%, 50%, and 100% of the total SLR imposed for 2013-2043, 2043-2073, and 2073-2103 periods, respectively. 112
- Figure 4.3.** The top panel shows San Pablo Bay bathymetry (a) 1856 measured, (b) 1983 measured, and (c) 1983 modeled. The middle panel shows (d) difference between 1983 measured and modeled bathymetries, (e) measured, and (f) modeled cumulative sedimentation/erosion from 1856 to 1983. Continuous and dashed lines represent the 0 and 5 m MLLW contour lines, respectively. The observed 1983 contours are shown in red in both (d) and (e). The bottom panels are (g) western and (h) eastern bed level cross-sections shown in (a). 113
- Figure 4.4.** Measured (top panel) and modeled (bottom panel) sedimentation/erosion maps for each period. 114
- Figure 4.5.** Modeled (color shaded) and observed (lines) spatial coverage of the model domain and its changes over time divided between (a) channel (< -5 m MLLW), (b) shoals (0 to -5 m MLLW), and (c) intertidal area (>0 m MLLW) for both the eastern and western sides of San Pablo Bay. Vertical gray lines indicate the end of the wet season runs. Right panel (d) shows the development of the BSS score and its Murphy and Epstein (1989) decomposition throughout the hindcast period compared to the 1856 initial bathymetry. 115
- Figure 4.6.** Top panel shows the cumulative sedimentation/erosion maps from 1983 to 2103 for the (a) No SLR and (b, c, and d) SLR scenarios. Bottom panel shows SLR-induced bed level changes for the (e) 42 cm, (f) 84 cm, and (g) 167 cm SLR scenarios. For example, (f) is the difference between (c) and (a) with the red and blue colors indicating higher and lower bed levels, respectively. 117
- Figure 4.7.** Quarter millennium development of (a) depositional volumes, (b) intertidal area, and (c) channel volume for the No SLR (blue) and the 42 cm (green), 84 cm (purple), 167 cm (red) SLR scenarios. 120
- Figure 4.8.** Hindcast sensitivity results for (a) No Salinity, (b) 2DH-Model, (c) No Waves, and (d) Hindcast SLR. Maps indicate bed level difference between sensitivity run and base case, red and blue color donates higher and lower than base case bed level, respectively. Transects below each map are bed-level cross-sections along CRS shown in (a) for base case (blue) and sensitivity run. Bottom panel (e) shows deposition volumes for the hindcast period. 124
- Figure 4.9.** The Northern San Francisco Bay D3D structured model grid based on the work of van der Wegen et al. (2011a). 130

Figure 5.1. Satellite image and the 2012 Bathymetry of the Western Scheldt Estuary (The Netherlands) with labels of the main morphological features. Figure source: Röbbke et al. (2020). 139

Figure 5.2. The Western Scheldt hydrodynamic model grid and 1964 observed bathymetry (m; Datum: NAP). Light grey lines are the land boundary. 143

Figure 5.3. (a) Measured, and (b) Modeled cumulative sedimentation/erosion (m) during the hindcast period (1964 to 2012). 148

Figure 5.4. (a) Measured, and (b) modeled width-averaged cumulative sediment volume change ($\text{m}^3/\text{m}^2/\text{yr}$) during the hindcast period (1964 to 2012) for 6 cells. The red/blue color indicates sedimentation/erosion, respectively. 149

Figure 5.5. The cumulative total (suspended and bed) sediment transport (m^3) during the forecast period through Vlissingen-Breskens cross-section along with two cross-sections at 14 and 29 km upstream; (a, c, and e) Sand-only model, and (b, d, and f) Sand-mud base model. Positive/ negative numbers are import to/export from the estuary, respectively. Sediment volume is based on particle density and excludes voids and the morphological factor. 151

Figure 5.6. The net suspended mud transport (Kt/yr) during the forecast period for the Sand-mud base simulation; (a) 0 m SLR, and (b) 3.02 m SLR. The colored values indicate the total (Black), marine mud (Magenta and Cyan), and fluvial mud (Red). Positive/negative numbers indicate that the direction of transport is the same/opposite to the direction of the arrow, respectively..... 153

Figure 5.7. Cumulative sedimentation erosion (m) maps during the forecast period (2020 – 2100) for the simulations with the Sand-only and Sand-mud model with (a,b) 0 m, and (c,d) 3.02 m SLR, respectively. 154

Figure 5.8. Modeled width-averaged cumulative sediment volume change ($\text{m}^3/\text{m}^2/\text{yr}$) during the hindcast period (2020 to 2100) for 6 cells in the Western Scheldt Estuary. (a, and b) Sand-only model (c, and d) Sand-mud base model for the 0 m, and 3.02 m SLR scenarios, respectively. The red/ blue color indicates sedimentation/erosion, respectively. 156

Figure 5.9. Temporal development of the (a) intertidal area (m^2), and (b) intertidal volume during the forecast period for the Sand-only and Sand-mud model. 156

Figure 5.10. Maximum flood (left column; a and b), and ebb (right column; b and e) flow velocities (m/s) in the Western Scheldt during spring tide conditions at the end of the forecast simulation for the 0 m (top row; a and d) and 3.02 m (central row; b and e) SLR scenarios. The bottom row (c and f) shows the difference between the maximum flood and ebb velocities between the 3.02 and 0 m SLR scenario, red/blue colors indicate an increase/decrease in the flow velocities in the case of the 3.02 m SLR scenario..... 157

- Figure 5.11.** Forecast sensitivity analysis for different forcing conditions. (a) Sediment budget (m^3/year) of the system (Cell 2 to 6, e.g., Figure 5.8), positive/negative values indicate net sediment gain/loss. (b) Mud transport (Kt/yr) through the estuary mouth (Vlissingen-Breskens), positive/negative values indicate mud import/export..... 160
- Figure 5.12.** Time-averaged (over tidal cycle) and depth-averaged SSC (mg/L) difference between the base case and the (a) No salinity and (b) No Dredging simulation. The presented tidal cycle is during the last spring tide of the forecast simulation. Warm colors indicate higher values than the base case..... 161
- Figure 5.13.** Dredging and disposal polygons in the model and the direction of the operations: (a) Hindcast period (b) Forecast period. 168
- Figure 5.14.** Instantaneous modeled significant wave height (H_{sig}). 168
- Figure 5.15.** Modeled vs Measured cumulative dredging volumes (m^3) during the hindcast period 1964 to 2012. 169
- Figure 5.16.** Hypsometry curve of the Western Schedlt Estuary: Initial measured 1964, Measured 2012, and Modeled 2012..... 169
- Figure 5.17.** Hypsometry curve of the Western Schedlt estuary: Initial 2020, Measured 2100, and Modeled 2100 for (a) Sand-only model and (b) Sand-mud model..... 170

ABOUT THE AUTHOR

Hesham Elmilady was born on September 21st 1990 and grew up in the coastal city of Alexandria, Egypt and has always been fascinated with the coastline and sea. He completed his BSc degree with distinction in Civil Engineering from the Faculty of Engineering, Alexandria University, Egypt in 2012. After graduating, he started working as a lecturer and research assistant at Civil Engineering Department, Faculty of Engineering, Alexandria University.

He moved to the Netherlands and conducted his MSc thesis in IHE Delft within the framework of a joint project (IHE Delft, Deltares, and the USGS) which investigated the sediment dynamics in San Francisco Bay using 3D numerical modeling. He obtained his MSc degree in 2016 with distinction in Coastal Engineering and Port Development at IHE Delft Institute for Water Education, The Netherlands. Following that, he started as a PhD fellow at IHE Delft and an intern at Deltares investigating the potential impact of sea level rise on the long-term morphological evolution of estuaries using the Delft3D process-based numerical model. His PhD research work was funded by the U.S. Geological Survey Priority Ecosystem Science and Coastal and Marine Geology Programs, and the California Delta Science Program as a part of the CASCaDE climate change project (contribution number 80). It was also funded by Deltares Research Funds as a part of their collaboration with the Rijkswaterstaat and the Vlaams-Nederlandse Scheldec commissie (VNCS).

He is married to Sohayla Sheta and they have a 2-year-old daughter, Sarah.

Journals publications

Elmilady, H., van der Wegen, M., Roelvink, D., & Jaffe, B. E. (2019). Intertidal Area Disappears Under Sea Level Rise: 250 Years of Morphodynamic Modeling in San Pablo Bay, California. *Journal of Geophysical Research: Earth Surface*, 124(1), 38–59. doi:10.1029/2018JF004857

Elmilady, H., van der Wegen, M., Roelvink, D., & van der Spek, A. (2020). Morphodynamic Evolution of a Fringing Sandy Shoal: From Tidal Levees to Sea Level Rise. *Journal of Geophysical Research: Earth Surface*, 125(6), e2019JF005397. doi:10.1029/2019JF005397

Elmilady, H., van der Wegen, M., Roelvink, D., & van der Spek, A. (2022). Modeling the Morphodynamic Response of Estuarine Intertidal Shoals to Sea-Level Rise. *Journal of Geophysical Research: Earth Surface*, 127(1), e2021JF006152. doi:10.1029/2021JF006152

Zheng, J., Elmilady, H., Röbbke, B. R., Taal, M., Wang, Z. B., van Prooijen, B. C., ... van der Wegen, M. (2021). The impact of wind-waves and sea level rise on the morphodynamics of a sandy estuarine shoal. *Earth Surface Processes and Landforms*, 46(15), 3045–3062. doi:10.1002/esp.5207

Elmilady, H., et al. (in prep.): The impact of mud dynamics on long-term morphodynamic evolution of the Western Scheldt estuary under sea level rise.

Röbbke, B.R., Elmilady, H., Chaves, M.A., Taal, M. & van der Wegen, M. (in prep.): The relative impact of sea level rise and dredging strategies on the morphodynamic evolution of the Western Scheldt estuary (Netherlands).

Conference proceedings

Jaffe, B., Elmilady, H., Wegen, M., & Fregoso, T. (2023). OBSERVATIONS AND MORPHODYNAMIC MODELING OF DECADE-SCALE MORPHOLOGIC CHANGE IN ESTUARIES UNDER SEA LEVEL RISE. doi:10.1142/9789811275135_0049



*Netherlands Research School for the
Socio-Economic and Natural Sciences of the Environment*

D I P L O M A

for specialised PhD training

The Netherlands research school for the
Socio-Economic and Natural Sciences of the Environment
(SENSE) declares that

***Hesham Mohamed Samy
Elmilady***

born on the 21st of September 1990 in Alexandria, Egypt

has successfully fulfilled all requirements of the
educational PhD programme of SENSE.

Delft, 23 April 2025

SENSE coordinator PhD education

Dr Ir Peter Vermeulen

The SENSE Director

Dr Jampel Dell'Angelo



The SENSE Research School declares that **Hesham Mohamed Samy Elmilady** has successfully fulfilled all requirements of the educational PhD programme of SENSE with a work load of 47.4 EC, including the following activities:

SENSE PhD Courses

- o Environmental research in context (2017)
- o Research in context activity: Organizing and Coordinating IHE NERD NITE 2019 on: Fresh water (Spring), Flood and Drought (Summer), Coastal discovery (Fall), and Water Governance and Society (Winter) (2019)

Selection of Other PhD and Advanced MSc Courses

- o NCK Summer School 2017: Estuarine and Coastal Processes in relation to Coastal Zone Management, Netherlands Centre for Coastal Research (2017)
- o Delft3D Flexible Mesh - Coastal Hydrodynamic Modeling, Deltares (2018)
- o Delft3D Flexible Mesh - Coastal Morphodynamic Modelling, Deltares (2018)
- o Morphodynamic modelling during storm conditions, Deltares (2018)
- o Non-hydrostatic modelling, Deltares (2018)
- o Using Creativity to Maximize Productivity and Innovation in Your PhD, TU Delft (2018)
- o Speedreading and Mindmapping, TU Delft (2018)
- o Discovering Statistics Using SPSS, TU Delft (2018)
- o The Art of Presenting Science, TU Delft (2018)
- o How to become effective in a network conversation, TU Delft (2018)
- o Creative Tools for Scientific Writing, TU Delft (2018)
- o IV International Summer School 2019 on Dynamics of Estuarine and Nearshore Systems, University of Granada and University of Utrecht, Spain (2019)
- o Marketing tools to position yourself confidently in the job market, TU Delft (2020)
- o Teamwork, Leadership and Group Dynamics, TU Delft (2020)
- o Time Management I – Foundation, TU Delft (2020)

Management and Didactic Skills Training

- o Supervising MSc student with thesis (2019-2021)
- o Teaching in the Delft3D course 2019 at IHE Delft course (2019)

Selection of Oral Presentations

- o *Intertidal area disappears under sea-level rise: long-term morphodynamic modelling effort in San Pablo Bay, California.* CERF 2017 Coastal Science at the Inflection Point: Celebrating Successes & Learning from Challenges, 5-9 November 2017, Providence, USA
- o *Investigating the long-term morphological evolution of intertidal shoals and SLR impact.* NCK days, 19-20 March 2020, Texel, The Netherlands
- o *Sea level rise impact on the morphological evolution of intertidal shoals.* Coastal Dynamics 2021, 29-2 July 2021, Delft, The Netherlands.
- o *Mud dynamics and the morphodynamic response of the Western Scheldt estuary to sea level rise.* INTERCOH 2021, 13- 16 September 2021, Delft, The Netherlands

Many estuaries worldwide have intertidal flats and associated unique ecosystems. The fate of these systems under sea level rise (SLR) scenarios is yet unclear. This research aims to investigate SLR impact on the long-term morphodynamic development of the estuarine environment by applying a process-based, numerical modelling approach (Delft3D).

Fundamental explorations with idealized estuarine model setups analyze governing processes, including wind wave dynamics, sediment properties, and grid resolution. Century time scale hindcasts in two case studies - San Pablo Bay (USA) and the Western Scheldt Estuary (Netherlands) – show significant skill in reproducing unique historic bathymetric datasets. Forecasts under various SLR scenarios show that

morphodynamic adaptation lags behind SLR, so that intertidal area declines depending on SLR rate, sediment supply, and sediment properties. Extreme SLR scenarios (1.67 and 3.02 m per century) could result in a 91% and 54% loss of intertidal area in San Pablo Bay and the Western Scheldt, respectively.

The results of this research advances understanding of SLR impact on the morphodynamic evolution of estuaries. They also show that, despite their complexity, process-based models are valuable tools for morphodynamic forecasts. Delft3D-type of models can be used in future studies to investigate potential adaptation measures and to design sustainable estuarine management strategies.